



Provided by the author(s) and University of Galway in accordance with publisher policies. Please cite the published version when available.

Title	Heterocyclic chemistry: Controlled unmasking of nitric oxide and nitroxides
Author(s)	Kielty, Patrick
Publication Date	2019-11-29
Publisher	NUI Galway
Item record	<a href="http://hdl.handle.net/10379/15613">http://hdl.handle.net/10379/15613</a>

Downloaded 2024-04-27T05:40:41Z

Some rights reserved. For more information, please see the item record link above.



# **Heterocyclic Chemistry: Controlled Unmasking of Nitric Oxide and Nitroxides**

Patrick Kiely

*Thesis submitted to the National University of Ireland, Galway  
in fulfilment of the degree of  
Doctor of Philosophy (PhD)*



School of Chemistry  
National University of Ireland, Galway

November 2019

Head of School: Dr. Patrick O'Leary

Supervisors: Dr. Dennis Smith, Dr. Pau Farràs  
and Prof. Fawaz Aldabbagh

*Dedicated to my mother and father*

# Contents

<b>Declaration</b> .....	vii
<b>Abstract</b> .....	ix
<b>Acknowledgements</b> .....	xi
<b>Abbreviations</b> .....	xiii

## **Chapter 1: The Bicyclic 5-5 Ring-Fused Heterocyclic Systems with 1:1**

<b>Heteroatoms</b> .....	1
1.1 Introduction.....	3
1.2 Experimental Structural Methods .....	6
1.3 Thermodynamic Aspects .....	8
1.4 Reactivity of Fully Conjugated Rings .....	9
1.5 Reactivity of Nonconjugated Rings .....	14
1.6 Reactivity of Substituents Attached to Ring Carbon Atoms .....	19
1.7 Examples of Diheteropentalene Ring-Synthesis using TEMPO Nitroxide.....	22
1.8 Synthesis of Particular Classes of Compounds.....	25
1.9 Important Compounds and Applications .....	29
1.10 Chapter 1 References .....	31

## **Chapter 2: Nitric Oxide Donor Furoxans *via* Methylmagnesium Chloride**

<b>Mediated Acetylations of Isosorbide</b> .....	39
2.1 Introduction.....	41
2.2 Chapter Aims and Objectives .....	45
2.3 Results and Discussion .....	46
2.3.1 Acetylation of isosorbide.....	46
2.3.2 Functionalising isosorbide with furoxans.....	51
2.3.3 Nitric oxide (NO) release studies .....	55
2.3.4 Thermal degradation studies.....	57
2.4 Conclusions.....	59
2.5 Future Work.....	59
2.6 Experimental.....	60

2.6.1	Materials .....	60
2.6.2	Measurements .....	60
2.6.3	Synthetic procedures and characterization .....	63
2.7	Chapter 2 Contributions .....	70
2.8	Chapter 2 References .....	70

### **Chapter 3: Visible-Light Unmasking of Quinone Methide Radicals and Nitroxides from Alkoxyamines .....**

3.1	Introduction.....	77
3.2	Chapter Aims and Objectives .....	85
3.3	Results and Discussion .....	86
3.3.1	DFT investigation into TEMPO-Vis reactivity .....	86
3.3.2	Synthesis.....	88
3.3.3	Homolysis of alkoxyamines and bis-alkoxyamines .....	91
3.4	Conclusions.....	102
3.5	Future Work.....	102
3.6	Experimental.....	103
3.6.1	Materials .....	103
3.6.2	Measurements.....	104
3.6.3	Synthetic procedures and characterization .....	108
3.7	Chapter 3 Contributions.....	115
3.8	Chapter 3 References .....	115

### **Chapter 4 .....**

Chapter 4 Layout.....	123
Part 1: The Chemistry of TMIO-Vis.....	125
4.1.1 Introduction .....	125
4.1.2 Results and Discussion .....	127
4.1.2.1 Synthesis of TMIO-coupled benzimidazolequinones.....	127
4.1.2.2 Kinetics of homolysis for TMIO-Vis .....	131
4.1.3 Experimental.....	136
4.1.4 Conclusions .....	141
Part 2: The Chemistry of CF <sub>3</sub> -Bis-TEMPO-Vis .....	142

4.2.1	Introduction .....	142
4.2.2	Results and Discussion .....	143
4.2.2.1	Synthesis of CF <sub>3</sub> -Bis-TEMPO-Vis .....	143
4.2.2.2	Kinetics of homolysis for CF <sub>3</sub> -Bis-TEMPO-Vis .....	146
4.2.3	Experimental .....	149
4.2.4	Conclusions .....	151
Part 3:	2-(Fluoromethyl)-4,7-dimethoxy-1-methyl-1 <i>H</i> -benzimidazole .....	153
4.3.1	Introduction .....	153
4.3.2	Results and Discussion .....	154
4.3.3	Materials and Methods .....	159
4.3.3	Conclusion .....	160
4.4	Chapter 4 References .....	161
<b>Appendix</b>	.....	<b>167</b>
	Supplementary Data for Chapter 2 .....	168
	Chapter 2 Supporting Tables .....	168
	Chapter 2 Supporting Figures .....	173
	Supplementary Data for Chapter 3 .....	177
	Chapter 3 Supporting Tables .....	177
	Chapter 3 Supporting Figure .....	180
	Chapter 3 NMR Spectra .....	181
	Supplementary Data for Chapter 4 .....	186
	Chapter 4 Supporting Table .....	186
	Chapter 4 Supporting Figure .....	187
	Chapter 4 NMR Spectra .....	188
	Conference Proceedings .....	200
	Peer-Reviewed Publications .....	203

## **Declaration**

I declare that the work included in this thesis is my own work, except where stated otherwise, and has not been previously submitted for a degree to this or any other academic institution.

Patrick Kielty

## Abstract

Nitric oxide (NO) is a gaseous free radical with medicinally significant properties. The NO-releasing prodrug, isosorbide-5-mononitrate (**Is5N**), is long established for the treatment of angina pectoris. Nitroxides are organic derivatives of NO, and their release from organic carriers (alkoxyamines) unmasks useful, reactive alkyl radicals. Heterocycles are rich in chemical and biochemical properties that allow a variety of stimuli, including visible-light, to induce NO or nitroxide release.

**Chapter 1:** The bicyclic fused heterocycle isosorbide (1,4:3,6-dianhydro-D-glucitol) is an appropriate substrate for the attachment of NO donor motifs. The broader structural family of isosorbide, the 5-5 ring-fused heterocyclic systems, containing one heteroatom in each ring is reviewed. Conjugated and non-conjugated heterocyclic systems are considered in terms of their reactivity and aromaticity, with the most common ring system, pyrrolo[2,3-*b*]indole, an important structural motif of natural products.

**Chapter 2:** Isosorbide was functionalized with furoxan (1,2,5-oxadiazole 2-oxide) for the first time to give thermally stable adducts that release NO up to 7.5 times faster than **Is5N**. Protection of isosorbide using MeMgCl-mediated acetylation allowed selective alkylation with furoxan bromides. By increasing the amount of MeMgCl, selectivity of acetylation was switched from isosorbide-5-acetate to isosorbide-2-acetate. Reactivity was rationalized in terms of a more stable 5-alkoxide magnesium salt using DFT, and was further validated by the selective deacetylation of isosorbide-2,5-diacetate.

**Chapter 3:** Benzimidazolequinone alkoxyamines with contrasting photochemical properties were prepared by varying the oxidation of one alkoxyamine synthetic precursor. The unmasking of a stabilized quinone methide radical is used to establish room-temperature visible-light activated heterocyclic quinone alkoxyamines and bis-alkoxyamines. This includes the first reported use of visible-light to release up to two equivalents of nitroxide per molecule. 2,2,6,6-Tetramethylpiperidin-1-yloxy (TEMPO) release is consecutive, and at the same rate, from both bis-alkoxyamine moieties.

**Chapter 4:** In part 1, the synthesis and kinetics of alternative 1,1,3,3-tetramethylisoindolin-2-oxyl (TMIO)-based benzimidazolequinone alkoxyamines is investigated. The chemistry of a trifluoromethylated bis-benzimidazolequinone alkoxyamine is explored in part 2, where bis-alkoxyamine photolysis was found to be inhibited by nitroxide-induced quenching at high concentrations. Oxidative, mesolytic cleavage of TEMPO and fluorination of a benzimidazole-alkoxyamine was demonstrated in part 3 using the electrophilic fluorinating reagent, Selectfluor.



## Acknowledgements

Sincere thanks to my supervisors, Dr. Dennis Smith, Dr. Pau Farràs and Prof. Fawaz Aldabbagh, for their unwavering support and guidance throughout my PhD, and for making my research so thoroughly enjoyable.

The Irish Research Council is acknowledged for generous support by means of a scholarship provided through the Enterprise Partnership Scheme, in collaboration with UCB Manufacturing Ireland, Shannon.

Thanks to my Enterprise Mentor, Dr. Peter Cannon, and to Dr. MaryRose Kelleher, Shannon, both of whose help and kindness made for a great collaboration, and thanks to both I enjoyed a fulfilling industrial placement in Shannon.

The contributions of interdisciplinary experts have been key to the realisation of this thesis, and I am grateful to Dr. Michael Carty, who guided us on nitric oxide release studies; Prof. Patrick McArdle, who provided X-ray crystal structures; Dr. Michael Kennedy, who evaluated the thermal stability of our compounds; and to Dr. Richard Singer who performed computational modeling of our new molecules.

To all of the students and staff of the Chemistry Department of NUI Galway, especially the past and present members of the Farràs and Aldabbagh groups, I am forever grateful for your advice and friendship at work and beyond.

Finally, thanks to all of my family and friends for much needed support over these years, with most special thanks reserved for my parents, Margaret and Des, to whom this thesis is dedicated.

## Abbreviations

$\delta$	chemical shift in ppm downfield from TMS
Å	angstrom
°C	degrees Celsius
Ac	acetyl
aq	aqueous
ATR	universal attenuated total reflectance
BDE	bond dissociation energy
Boc	<i>tert</i> -butyloxycarbonyl
BOX	bis(oxazoline)
bs	broad signal
Bu	butyl
BuChE	butyrylcholinesterase
Calcd	calculated
CAN	cerium(IV) ammonium nitrate
CCDC	Cambridge Crystallographic Data Centre
Compd	compound
CPB	chiral phosphate base
CT	charge-transfer
d	doublet
DABCO	1,4-diazabicyclo[2.2.2]octane
DCC	<i>N,N'</i> -dicyclohexylcarbodiimide
DCE	1,2-dichloroethane
DDQ	2,3-dichloro-5,6-dicyano-1,4-benzoquinone
Deg	degraded
DEPT	distortionless enhancement by polarization transfer
DFT	density functional theory
DIPEA	<i>N,N</i> -diisopropylethylamine
DMA	<i>N,N</i> -dimethylacetamide
DMAP	4- <i>N,N</i> -dimethylaminopyridine
DMB	dimethoxybenzimidazole
DMF	<i>N,N</i> -dimethylformamide

DMSO	dimethyl sulfoxide
DNA	deoxyribonucleic acid
DSC	differential scanning calorimetry
EI	electron impact
eq	equation
equiv	equivalents
ESI	electrospray ionization
Et	ethyl
$E_T$	lowest triplet energy level
FID	flame ionization detector
GC	gas chromatography
GC-MS	gas chromatography-mass spectrometry
GST	glutathione- <i>S</i> -transferase
h	hours
h $\nu$	light
HIV	human immunodeficiency virus
HMBC	heteronuclear multiple bond correlation spectroscopy
HOMO	highest occupied molecular orbital
HPLC	high performance liquid chromatography
HPLC-MS	high performance liquid chromatography-mass spectrometry
HRMS	high resolution mass spectrometry
HSQC	heteronuclear single quantum correlation spectroscopy
Hz	hertz
<i>i</i> -	iso
ICHEC	Irish Centre for High-End Computing
IR	infrared
Is5N	isosorbide-5-mononitrate
IsDiN	isosorbide dinitrate
<i>J</i>	coupling constant
LED	light-emitting diode
LUMO	lowest unoccupied molecular orbital
m	multiplet
<i>m</i> -	<i>meta</i> -
M <sup>+</sup>	mass of molecular ion

<i>m</i> -CPBA	<i>m</i> -chloroperoxybenzoic acid
Me	methyl
MHz	megahertz
min	minutes
MMC	mitomycin C
μM	micromolar
mM	millimolar
mp	melting point
MRI	magnetic resonance imaging
MS	mass spectrometry
Ms	mesyl
MTBE	methyl <i>t</i> -butyl ether
<i>m/z</i>	mass-to-charge ratio
NADPH	nicotinamide adenine dinucleotide phosphate hydrogen
NBO	natural bond orbital
NBS	<i>N</i> -bromosuccinimide
NCS	<i>N</i> -chlorosuccinimide
NIS	<i>N</i> -iodosuccinimide
NMP	nitroxide-mediated radical polymerization
NMR	nuclear magnetic resonance
NO	nitric oxide
NQO1	NADPH:quinone oxidoreductase 1
NTO	natural transition orbital
<i>o</i> -	<i>ortho</i> -
OFET	organic field-effect transistor
OLED	organic light-emitting diode
<i>p</i> -	<i>para</i> -
PACT	photoactivated chemotherapy
PBI	pyrrolo[1,2- <i>a</i> ]benzimidazole
PBNF	potassium 4,5-bis(dinitromethyl)furoxanate
PC	personal computer
PDI	polydispersity index
PETN	pentaerythritol tetranitrate
Ph	phenyl

pH	power of hydrogen
PIFA	phenyliodine bis(trifluoroacetate)
PivOH	pivalic acid
PMB	<i>p</i> -methoxybenzyl
PMP	1,2,2,6,6-pentamethylpiperidine
PPL	porcine pancreatic lipase
ppm	parts per million
Pr	propyl
PRE	persistent radical effect
q	quartet
$R_f$	retention factor
ROESY	rotating frame overhauser enhancement spectroscopy
s	singlet
sat	saturated
SET	single electron transfer
$S_H2$	homolytic substitution reaction
SSCE	sodium-saturated calomel electrode
t	triplet
<i>t</i> -	<i>tertiary</i> -
TBA	tribromoacetic acid
TBAI	tetrabutylammonium iodide
TCI	Tokyo Chemical Industry
TD-DFT	time-dependent density functional theory
TEMPO	(2,2,6,6-tetramethylpiperidin-1-yl)oxyl
Tf	triflyl
TFA	trifluoroacetic acid
THF	tetrahydrofuran
TLC	thin layer chromatography
TMIO	1,1,3,3-tetramethylisoindolin-2-oxyl
TOF-MS	time-of-flight mass spectrometer
TPE	tetraphenylethylene
UV	ultraviolet
V	Volt

# Chapter 1

## *A Review of the Literature*

### **The Bicyclic 5-5 Ring-Fused Heterocyclic Systems with 1:1 Heteroatoms**

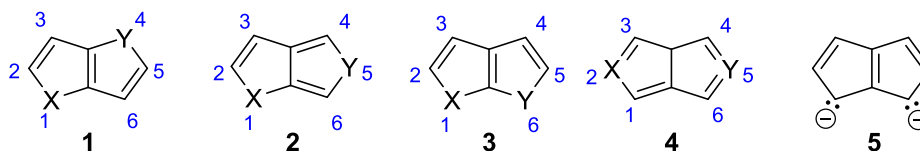
Parts of this chapter will be published in:

Patrick Kielty and Fawaz Aldabbagh, in *Comprehensive Heterocyclic Chemistry IV*, David Black, Janine Cossy, and Christian Stevens, EIC; Elsevier; Fawaz Aldabbagh, Ed; Section 10, Chapter 10.01: Bicyclic 5-5 Systems: Two Heteroatoms 1:1, in press

## 1.1 Introduction

There are described 59 heterocyclic systems possessing two non-bridgehead heteroatoms from Groups 15–17 of the Periodic Table arranged 1:1 in each bicyclic 5-5 ring system. Advances since the 2008 chapter in *Comprehensive Heterocyclic Chemistry III* by Krutošóková and Gracza<sup>1</sup> are detailed herein.

There are four modes of fusion of the 5:5 fused systems, as designated by structures **1–4** (Figure 1.1), which are isoelectronic with the 10- $\pi$ -electron dianion **5**.<sup>2,3</sup> The general classes **1–4** are referred to herein as 1,4-, 1,5-, 1,6- and 2,5-diheteropentalenes respectively. Heteroatoms may be the same or different and include O, N, S, Se, Te, P, As, Sb and I (as a salt). Figures 1.2–1.5 depict the 44 parent heterocycles outlined in the 2008 chapter.<sup>1</sup> There are another 15 new parent systems: **9**,<sup>4,5</sup> **10**,<sup>6</sup> **11**,<sup>7</sup> **12**,<sup>8</sup> **16**,<sup>6</sup> **20**,<sup>9–11</sup> **21–22**,<sup>10</sup> **23**,<sup>8,12–14</sup> **25**,<sup>6</sup> **27**,<sup>15</sup> **35**,<sup>16,17</sup> **45**<sup>6</sup> and **62**<sup>18</sup> containing Se, Te, P, I (as a salt), As and Sb. One di-Te system, **26**,<sup>19</sup> was described prior to 2008, but was not covered in the preceding review.<sup>1</sup> Noteworthy are reviews on 1,4-dihydropyrrolo[3,2-*b*]pyrroles by Janiga and Gryko in 2014,<sup>20</sup> thienothiophenes by Cinar and Ozturk in 2015<sup>21</sup> and thieno[2,3-*b*]indoles by Egorov in 2016.<sup>22</sup> Asymmetric syntheses of pyrrolo[2,3-*b*]indoles bearing a C3a quaternary stereocenter was reviewed by Repka and Reisman in 2013.<sup>23</sup> Exceptions to 10- $\pi$ -electron systems are noted for some 2,5-diheteropentalenes (Figure 1.5), with parent structures **53–56** and **60–64** observed in their more stable, and sometimes partially saturated forms. Indeed, some partially and fully saturated structures of the parent aromatic heterocycles will be discussed in this review. For instance, the naturally derived diol, isosorbide, contains a fully saturated furo[3,2-*b*]furan core and has found application in biopolymers,<sup>24,25</sup> green solvents<sup>26</sup> and vasodilation.<sup>27</sup> The reactivity of non-conjugated systems including isosorbide will be reviewed in section 1.5.



X, Y = O, NH, S, Se, Te, PH, AsH, SbH, I (as a salt)

**Figure 1.1** General structures of 5-5 fused heterocyclic systems containing one heteroatom in each ring.

# Chapter 1

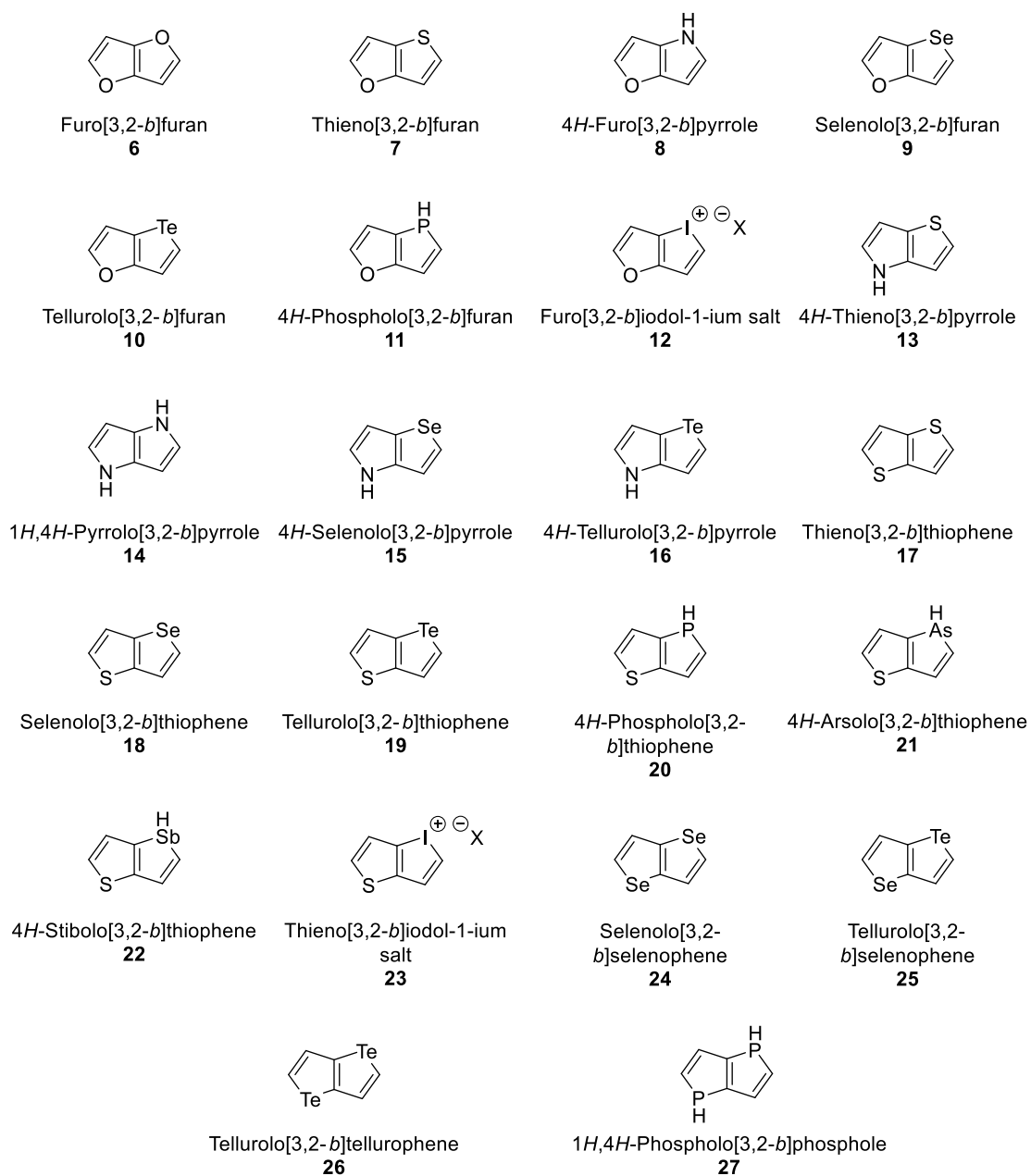


**Figure 1.2** 1,4-Diheteropentalene structures.



## Chapter 1

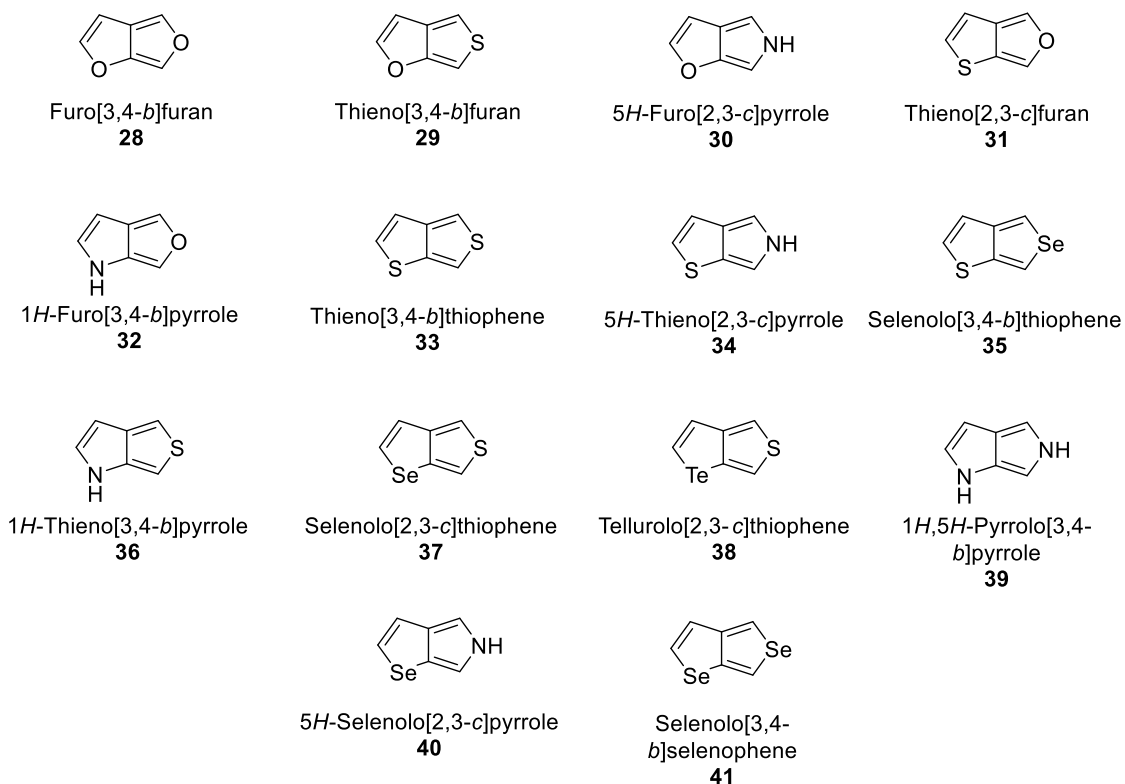


**Figure 1.3** 1,5-Diheteropentalene structures.

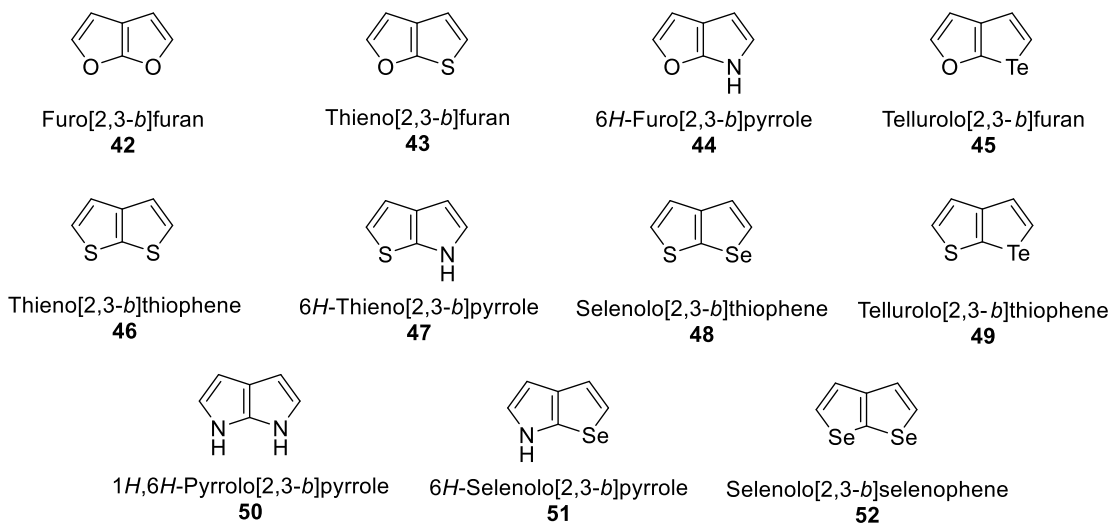


**Figure 1.4** 1,6-Diheteropentalene structures.

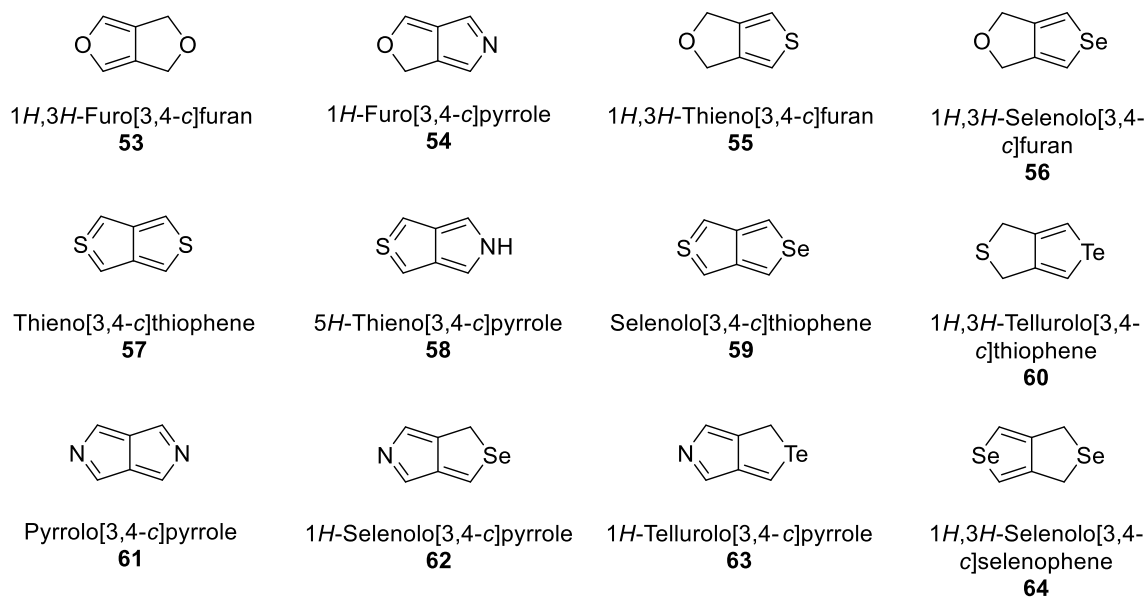


**Figure 1.5** 2,5-Diheteropentalene structures.

## 1.2 Experimental Structural Methods

### 1.2.1 X-Ray Diffraction Studies

A fluorescent  $\pi$ -expanded pyrrolo[3,2-*b*]pyrrole system gives diastereomeric folded and twisted forms inseparable by chiral HPLC (Figure 1.6). DFT suggested a low energy barrier between the conformers.<sup>28</sup> The diastereomers were co-crystallized and their existence revealed using X-ray crystallography.

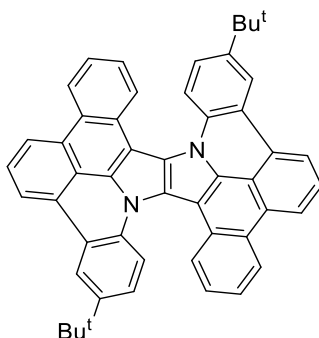
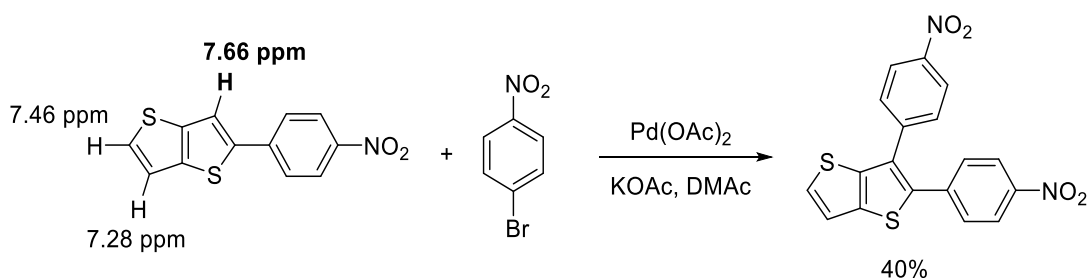


**Figure 1.6** Double-helicene system containing a pyrrolo[3,2-*b*]pyrrole core.<sup>28</sup>

### 1.2.2 NMR Spectroscopy

Selectivity in the Pd-catalysed coupling of 1-bromo-4-nitrobenzene with 2-(4-nitrophenyl)thieno[3,2-*b*]thiophene was explained by the increased acidity of the 3-CH as indicated by a downfield <sup>1</sup>H NMR chemical shift (Scheme 1.1).<sup>29</sup>



**Scheme 1.1**  $^1\text{H}$  NMR evidence to explain selectivity of the Pd-catalysed coupling.<sup>29</sup>

The non-aromatic character of the 20- $\pi$ -electron thieno[3,2-*b*]pyrrole-containing heteroporphyrin **66** was evidenced by the location of the  $^1\text{H}$  NMR chemical shifts (Figure 1.7).<sup>30</sup> The NH protons in **66** appeared in the 9–17 ppm range, while the NH proton signal in thiaporphyrin **65** shifted upfield to a negative  $\delta$  value due to the shielding effect of the macrocyclic aromatic ring current. Furthermore, the five CHs in **66** appeared as five singlets in the 4.82–7.16 ppm region, while the six CHs in **65** appeared as two singlets at 10.13 and 10.14 ppm.

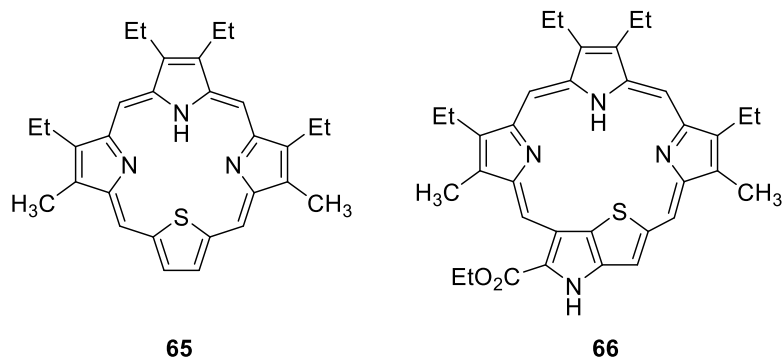


**Figure 1.7** Aromatic thiaporphyrin **65** and non-aromatic thieno[3,2-*b*]thiophene **66**.<sup>30</sup>

Phosphorus-31 NMR spectroscopy was used to assess the electron density around the P-atom in a series of fluorescent phospholo[3,2-*b*]thiophenes (Figure 1.8).<sup>11</sup> A more electropositive phosphorus centre (downfield phosphorus-31 chemical shift) gave rise to greater fluorescence quantum yield.

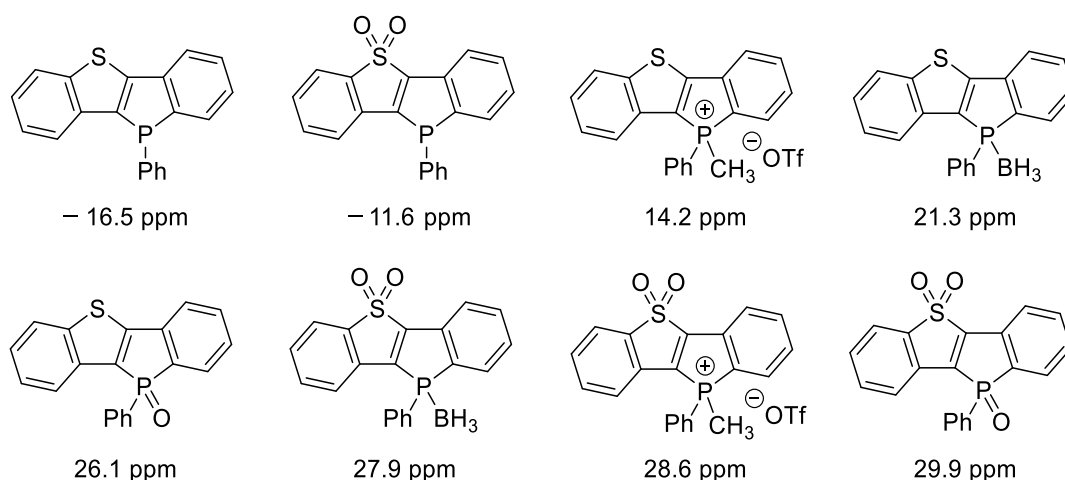
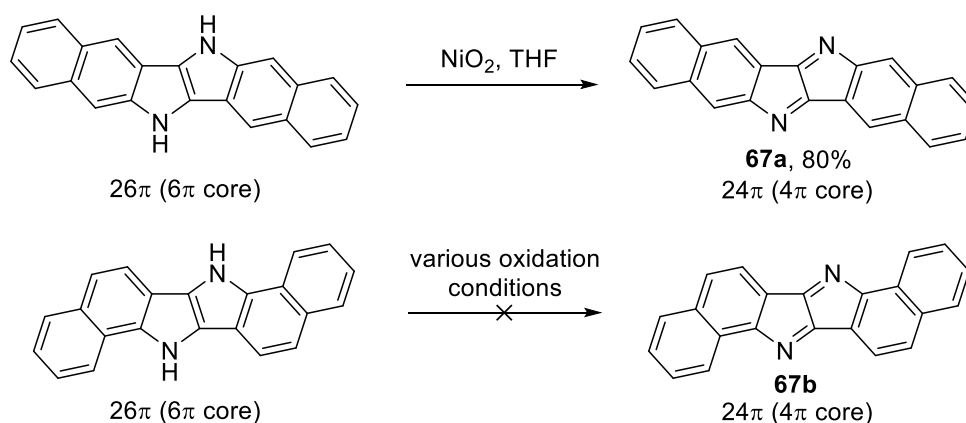


**Figure 1.8**  $^{31}\text{P}$  NMR chemical shifts of fluorescent phospholo[3,2-*b*]thiophenes.<sup>11</sup>

## 1.3 Thermodynamic Aspects

### 1.3.1 Aromaticity

The stabilization of indolo[3,2-*b*]indoles bearing an anti-aromatic core was found to be dependent upon the location of aromatic ring fusion.<sup>31</sup> Benzo[*f*]benzo[5,6]indolo[3,2-*b*]indole **67a** was accessible by oxidation of the dihydro analogue, while its isomer, benzo[*g*]benzo[6,7]indolo[3,2-*b*]indole **67b**, was not isolable (Scheme 1.2). DFT analysis found that the HOMO  $\rightarrow$  LUMO transition was symmetry-allowed for **67a**, implying that the anti-aromatic character is attenuated by the fused benzene rings. The HOMO  $\rightarrow$  LUMO transition for **67b** was symmetry-forbidden, as is typical for anti-aromatic  $4n\pi$ -electron systems.<sup>32</sup> Optimized geometries showed the bond length at the 5-6 fusion points between the pyrrolo[3,2-*b*]pyrrole moiety of **67a** and the naphthalene moieties (1.450 Å) were longer compared to the same fusion points in **67b** (1.405 Å). The latter is an indicator of increased levels of  $\pi$ -delocalization in **67a**.<sup>32</sup>

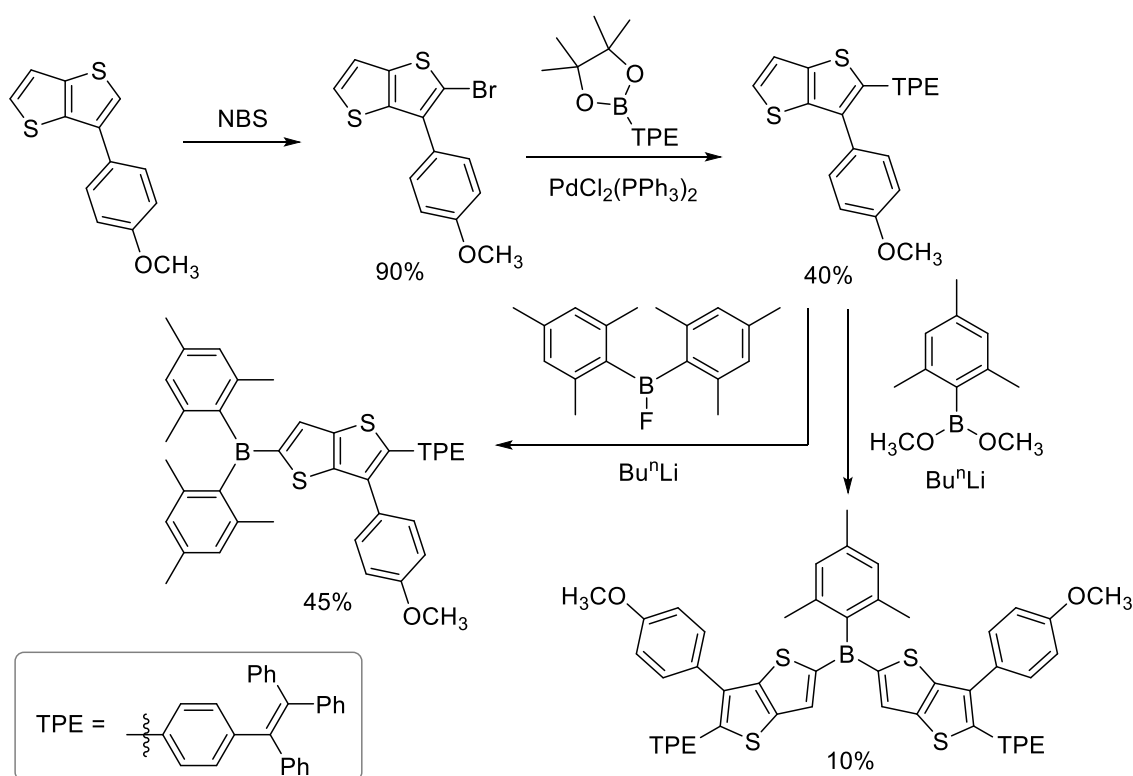


**Scheme 1.2** Aromatic and non-aromatic indolo[3,2-*b*]indoles.<sup>31</sup>

## 1.4 Reactivity of Fully Conjugated Rings

### 1.4.1 1,4-Diheteropentalene Systems

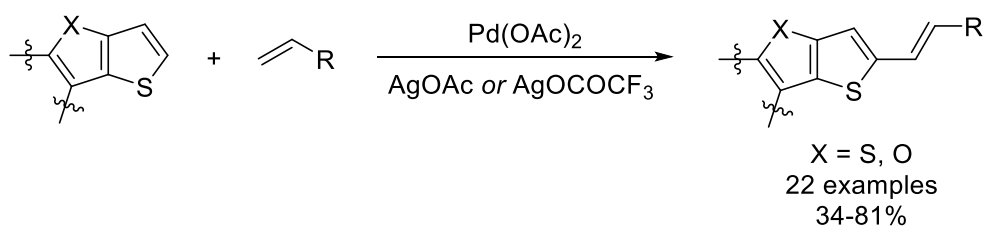
Highly conjugated thieno[3,2-*b*]thiophene derivatives for organic light-emitting diode (OLED) applications were prepared by an initial NBS-mediated bromination at the 2-position of 3-(4-methoxyphenyl)thieno[3,2-*b*]thiophene (Scheme 1.3).<sup>33</sup> This facilitated Suzuki-type coupling with protected boronic acid-functionalized tetraphenylethylene (TPE). Functionalization at the 5-position of the thieno[3,2-*b*]thiophene was completed *via* the *n*-BuLi-promoted attachment of dimesityl borane derivatives.



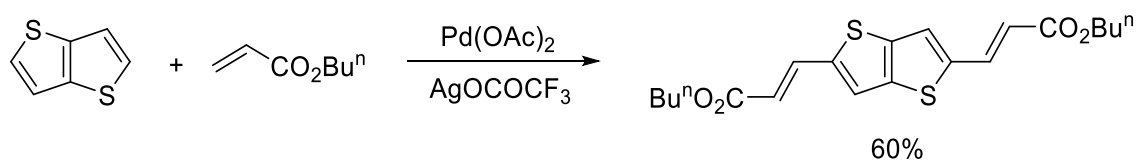
**Scheme 1.3** Thieno[3,2-*b*]thiophenes functionalized with mesityl borane derivatives.<sup>33</sup>

Alkenylation and styrylation of thieno[3,2-*b*]thiophenes and thieno[3,2-*b*]benzo[*b*]furans occurred selectively at the C-2 position in the presence of a Pd catalyst and  $\text{AgOCOCF}_3$  (for alkenylation) or  $\text{AgOAc}$  (for styrylation), and is described as a dehydrogenative Heck reaction (Scheme 1.4).<sup>34</sup> The dialkenylation of thieno[3,2-*b*]thiophene was performed using the same approach (Scheme 1.5).<sup>34</sup>

## Chapter 1

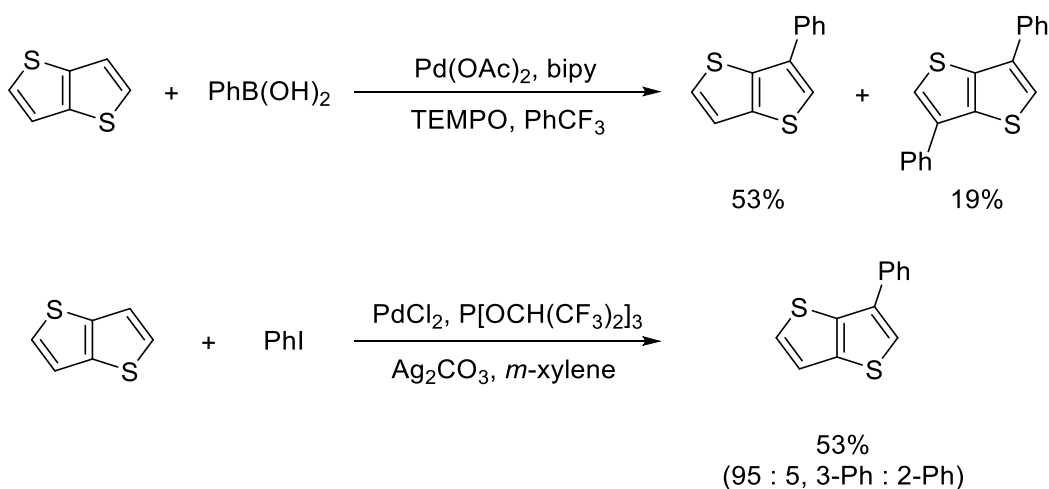


**Scheme 1.4** Synthesis of 2-alkenylated thieno[3,2-*b*]thiophenes and thieno[3,2-*b*]benzo[*b*]furans.<sup>34</sup>



**Scheme 1.5** Synthesis of dialkenylated thieno[3,2-*b*]thiophene.<sup>34</sup>

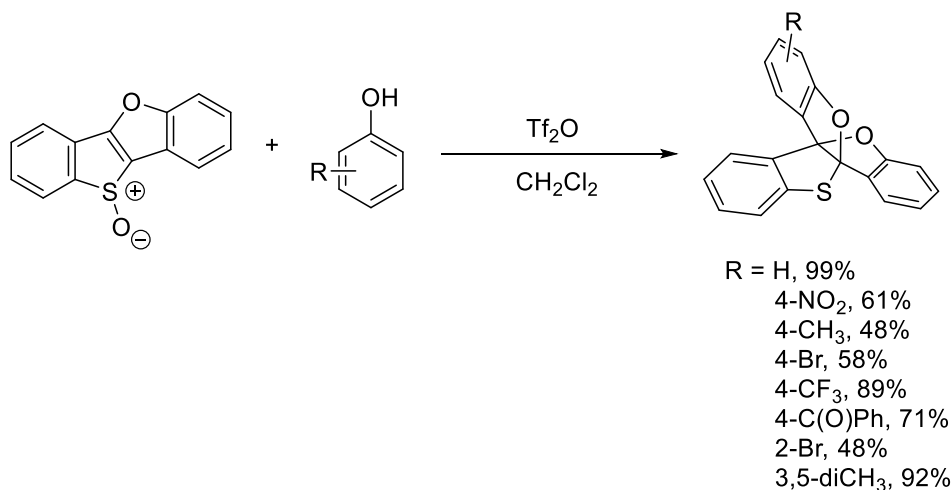
Phenylboronic acid was coupled at the 3-position of thieno[3,2-*b*]thiophene using (2,2,6,6-tetramethylpiperidin-1-yl)oxyl (TEMPO) as an oxidant in  $\alpha,\alpha,\alpha$ -trifluorotoluene, with 3,6-diphenylthieno[3,2-*b*]thiophene isolated in lower yield (Scheme 1.6).<sup>35</sup> Similarly, iodobenzene was used in the Pd-catalyzed arylation of thieno[3,2-*b*]thiophene affording 3-phenylthieno[3,2-*b*]thiophene in 53% yield and 95% purity (5% of 2-phenyl product).<sup>36</sup>



**Scheme 1.6** Synthesis of 3-phenylated and 3,6-diphenylated thieno[3,2-*b*]thiophene.<sup>35,36</sup>

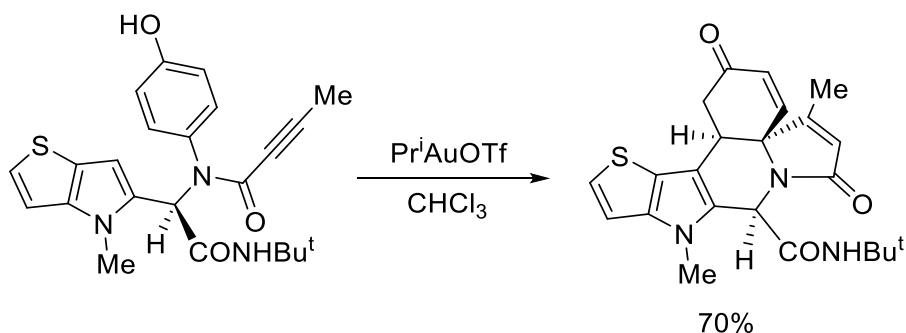
Procter and co-workers synthesized a series of heteropropellane-type compounds by coupling phenols to benzo[*b*]thieno[3,2-*b*]benzo[*b*]furan *S*-oxide in the presence of  $\text{Tf}_2\text{O}$

(Scheme 1.7).<sup>37</sup> Trifluoroacetylation of the *S*-oxide facilitates substitution of phenol, from which a [3,3]-sigmatropic rearrangement and subsequent rearomatisation (loss of H<sup>+</sup>) yielded the thioacetal.



**Scheme 1.7** Synthesis of heteropropellanes from benzo[*b*]thieno[3,2-*b*]benzo[*b*]furan *S*-oxide.<sup>37</sup>

Van der Eycken and co-workers reported a gold-catalyzed domino-cyclization onto C-3 of thieno[3,2-*b*]pyrrole forming a pentacyclic fused system where the attached phenol becomes an  $\alpha,\beta$ -unsaturated ketone (Scheme 1.8).<sup>38</sup>

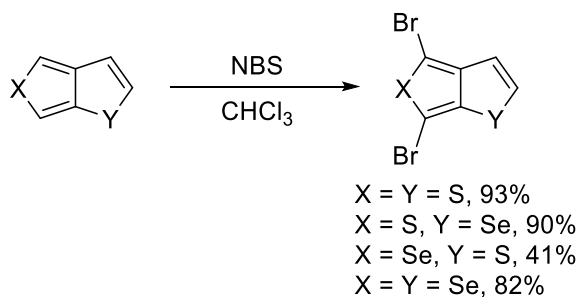


**Scheme 1.8** Domino cyclization onto the C-3 of thieno[3,2-*b*]pyrrole.<sup>38</sup>

#### 1.4.2 1,5-Diheteropentalene Systems

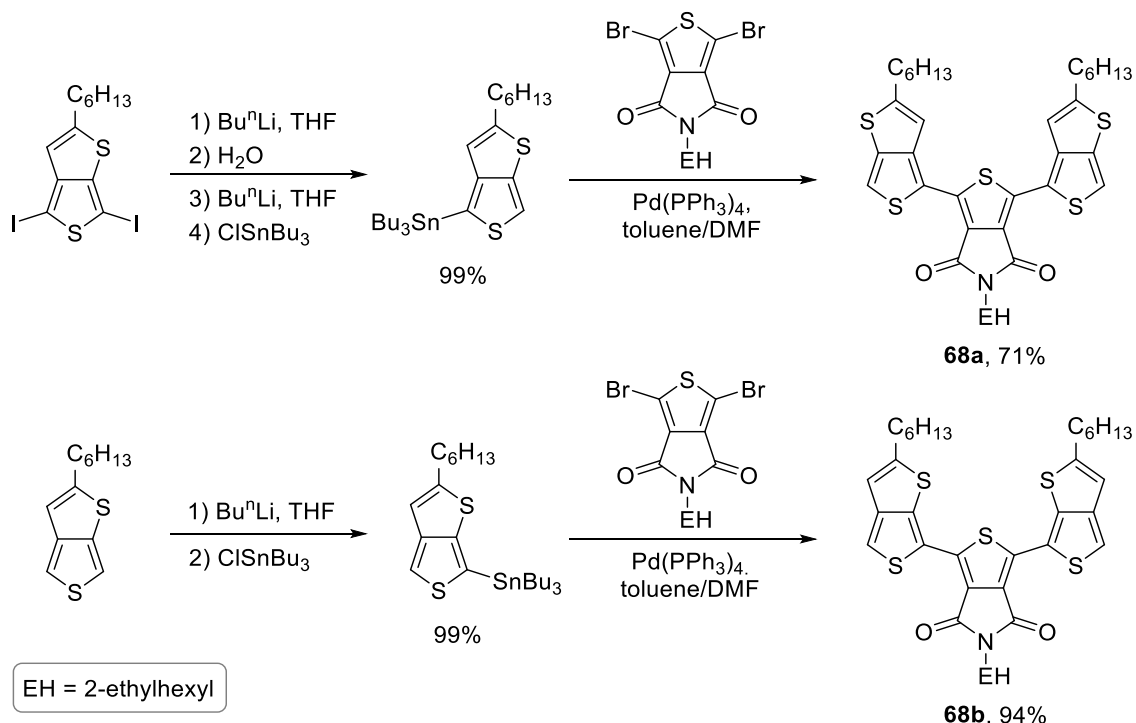
Bendikov and co-workers demonstrated that an NBS-mediated dibromination was selective at the CH-X-CH moiety of *S*- and *Se*-containing 1,5-diheteropentalenes (Scheme 1.9).<sup>16</sup> The low yield for 4,6-dibromoselenolo[3,4-*b*]thiophene was attributed to facile polymerization of the product.

## Chapter 1



**Scheme 1.9** Synthesis of S- and Se-containing 4,6-dibromo(1,5-diheteropentalenes).<sup>16</sup>

Analogous to Scheme 1.9, 2-hexyl-4,6-diiodothiopheno[3,4-*b*]thiophene was synthesized from 2-hexylthieno[3,4-*b*]thiophene using NIS and TFA in  $\text{CHCl}_3$ .<sup>39</sup> Tributyl(2-hexylthieno[3,4-*b*]thiophen-4-yl)stannane was prepared through selective Li/I exchange and addition of  $\text{ClSnBu}_3$  (Scheme 1.10). Stille coupling of the stannane with 1,3-dibromo-5-(2-ethylhexyl)-4*H*-thieno[3,4-*c*]pyrrole-4,6(5*H*)-dione gave terthiophene **68a**. Selective *n*-BuLi deprotonation of 2-hexylthieno[3,4-*b*]thiophene at the 6-position followed by addition of  $\text{ClSnBu}_3$ , and Stille coupling gave the isomeric terthiophene **68b**.

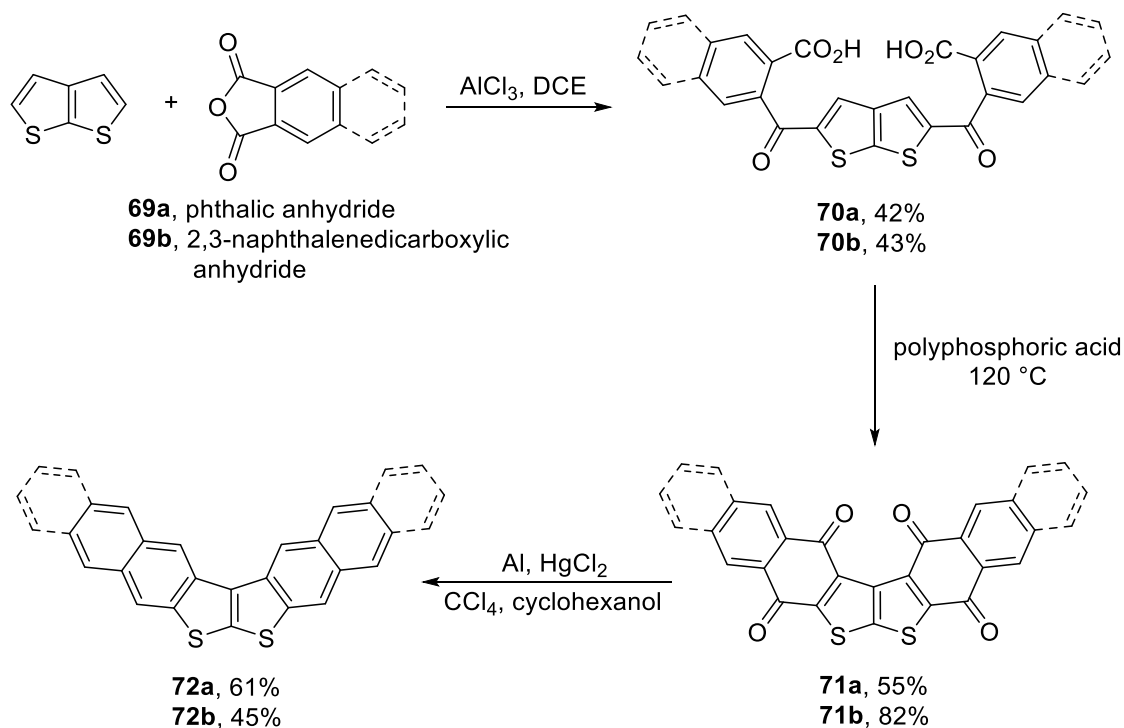


**Scheme 1.10** Synthesis of heterocyclic ring-fused terthiophenes.<sup>39</sup>



### 1.4.3 1,6-Diheteropentalene Systems

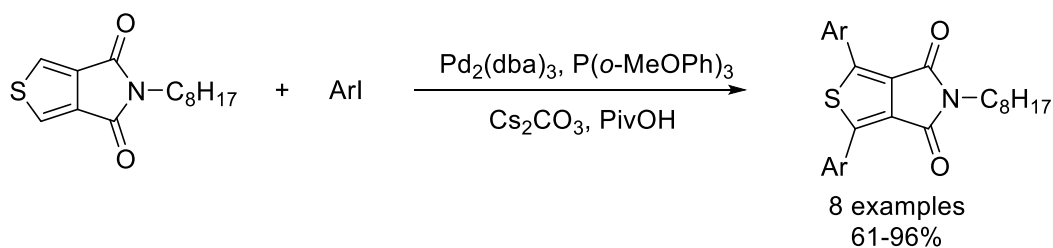
The Friedel-Crafts acylation of thieno[2,3-*b*]thiophene with phthalic anhydride or 2,3-naphthalenedicarboxylic anhydride gave the respective 2,5-diacylated products (Scheme 1.11).<sup>40</sup> Condensation in the presence of polyphosphoric acid gave 1,4-naphthoquinone- and 1,4-anthraquinone-fused thieno[2,3-*b*]thiophenes with subsequent reduction furnishing fully aromatic bent hexacyclic and octacyclic ring-fused systems having organic field-effect transistor (OFET) applications.



**Scheme 1.11** Synthesis of dinaphthalene- and dianthracene-fused thieno[2,3-*b*]thiophenes.<sup>40</sup>

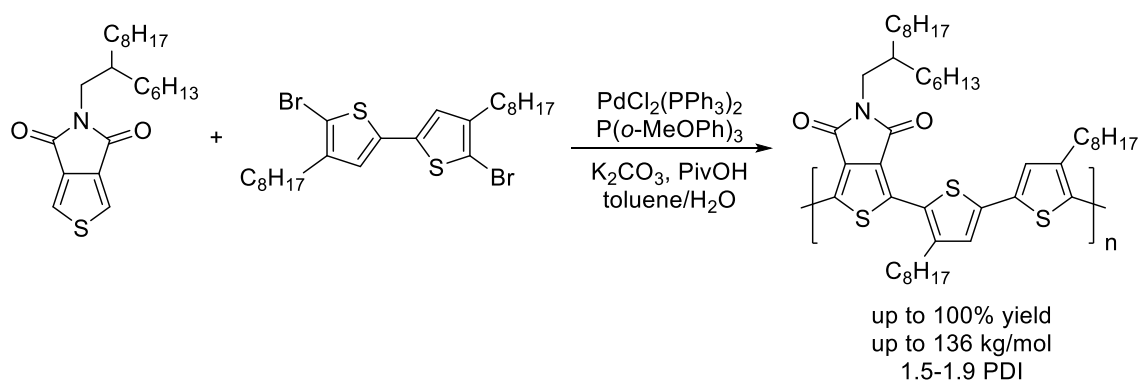
### 1.4.4 2,5-Diheteropentalene Systems

The Pd-catalyzed diarylation of 5-octylthieno[3,4-*c*]pyrrole-4,6-dione was performed under solvent-free conditions in the presence of air to give a series of 1,3-diarylthieno[3,4-*c*]pyrroles having application as semiconductors (Scheme 1.12).<sup>41</sup>



**Scheme 1.12** Synthesis of 1,3-diarylthieno[3,4-*c*]pyrroles.<sup>41</sup>

The copolymerization of a thieno[3,4-*c*]pyrrole-4,6-dione derivative and 5,5'-dibromo-4,4'-dioctyl-2,2'-bithiophene was performed under biphasic conditions in the presence of a Pd catalyst to give a polymer with a fully conjugated backbone. The yield, molecular weight and polydispersity index (PDI) depended on the reagent amounts, temperature, and whether inert or aerated conditions were employed (Scheme 1.13).<sup>42</sup>

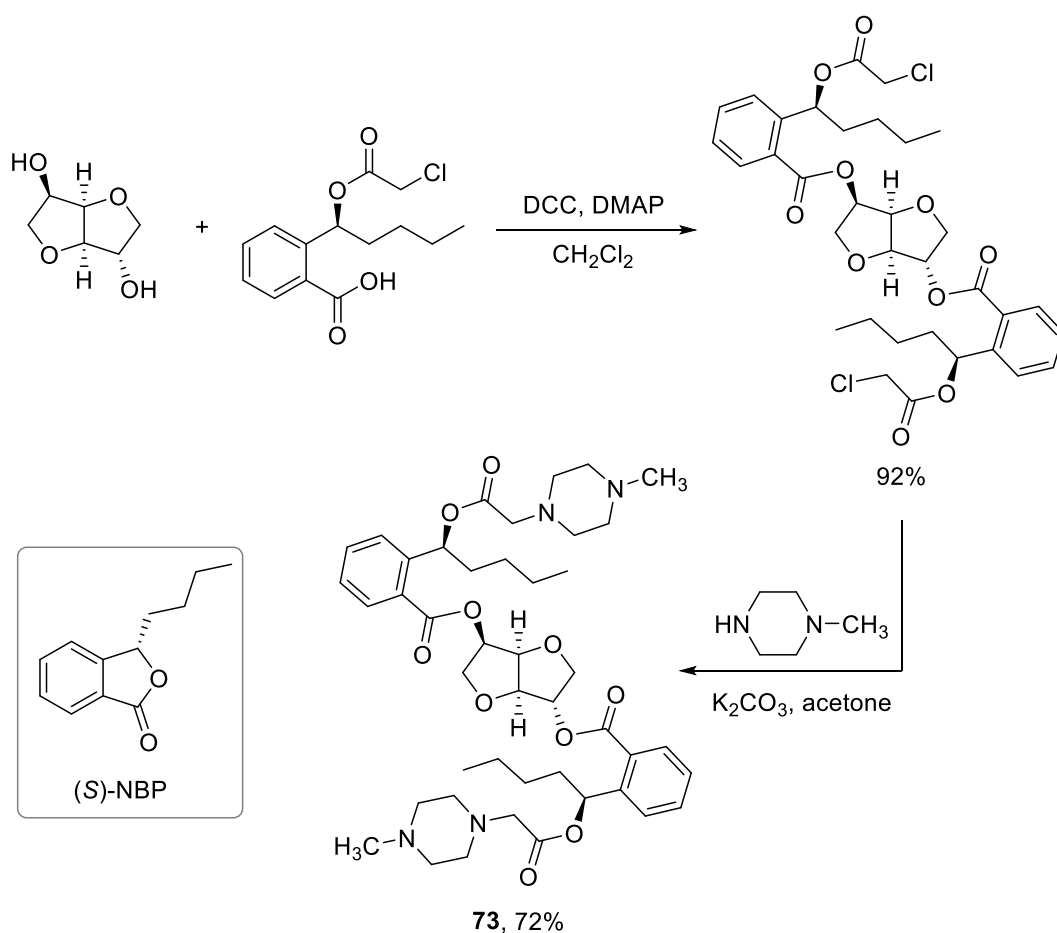


**Scheme 1.13** Synthesis of a thieno[3,4-*c*]pyrrole-containing conjugated polymer.<sup>42</sup>

## 1.5 Reactivity of Nonconjugated Rings

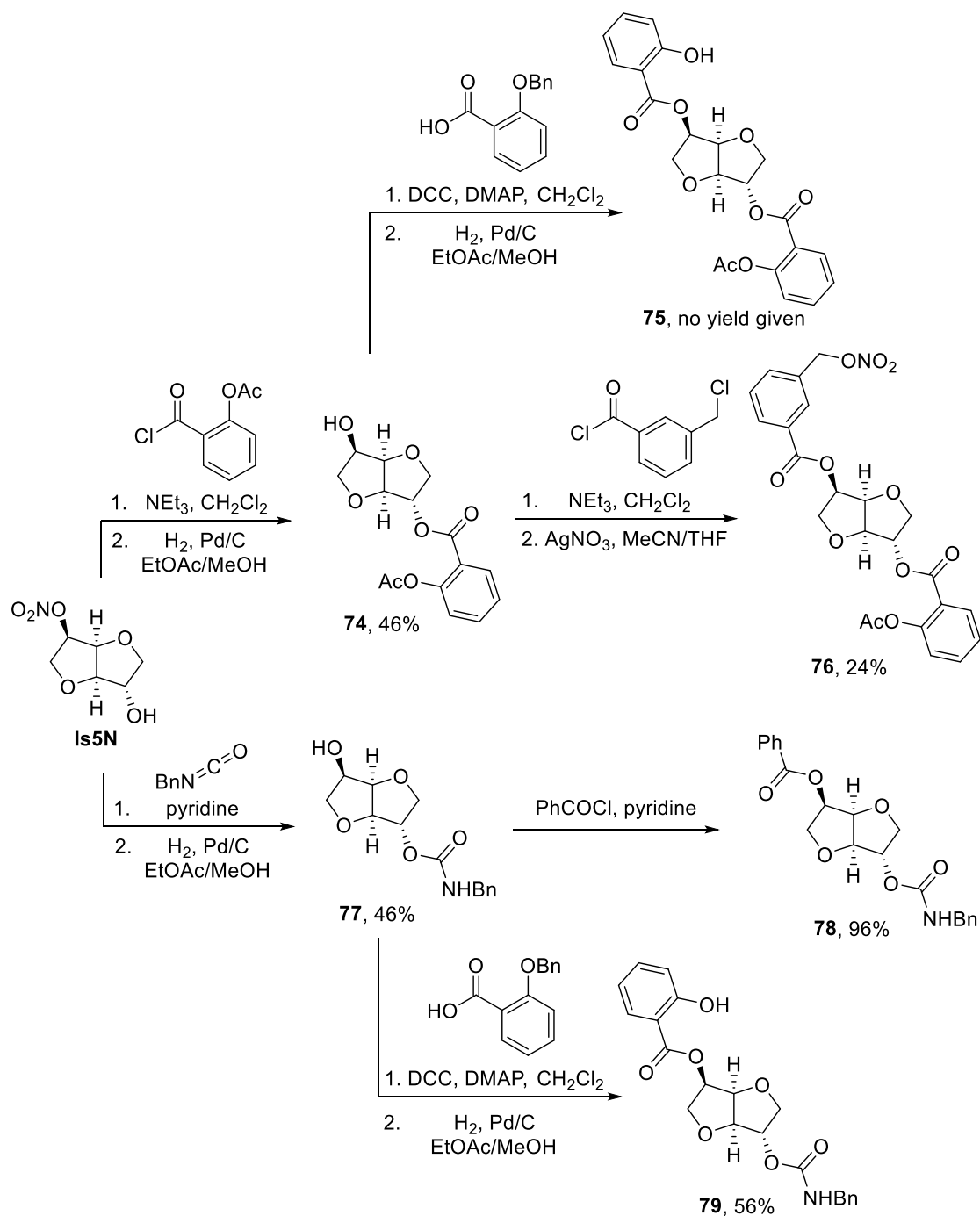
### 1.5.1 1,4-Diheteropentalene Systems

1,4:3,6-Dianhydro-D-glucitol (isosorbide) was di-functionalized with a ring-opened derivative of the anti-ischemic stroke drug (3*S*)-*n*-butylphthalide [(*S*)-NBP] using DCC and DMAP (Scheme 1.14).<sup>43</sup> Aqueous solubility was increased by substitution of *N*-methyl piperazines to give **73**, a compound with superior antiplatelet aggregation effects compared to (*S*)-NBP.



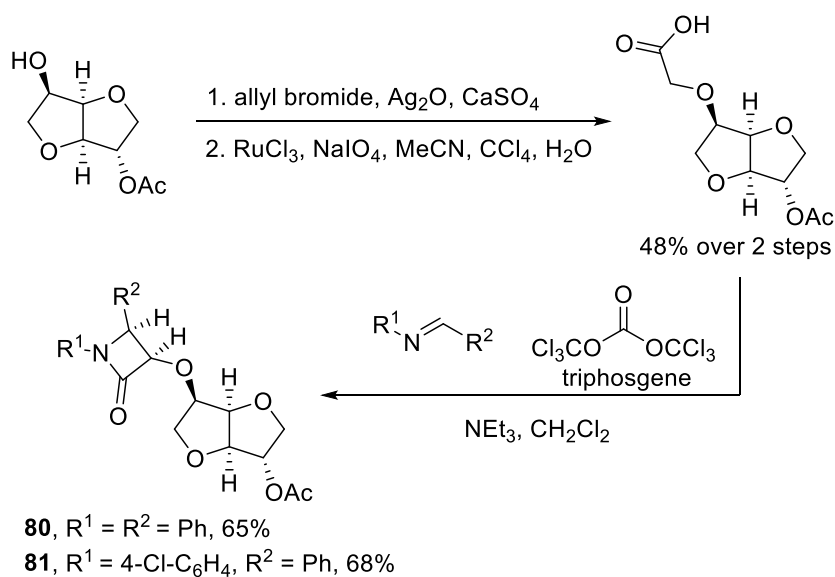
**Scheme 1.14** Synthesis of an isosorbide-based alternative to (S)-NBP.<sup>43</sup>

Esterification of the free OH of isosorbide-5-nitrate (**Is5N**) with acetylsalicyloyl chloride gave isosorbide-2-aspirinate **74** following reductive removal of the nitro group (Scheme 1.15).<sup>44</sup> Coupling adducts at the 5-OH of isosorbide-2-aspirinate were isosorbide-2-aspirinate-5-salicylate **75**, an aspirin prodrug that undergoes almost complete hydrolysis to aspirin in human plasma,<sup>44</sup> and isosorbide-2-aspirinate-5-(3-nitrooxymethyl)benzoate **76**, a dual aspirin and nitric oxide (NO) prodrug.<sup>45</sup> Carbamylation of **Is5N** using benzyl isocyanate, followed by reductive removal of the nitrate ester moiety gave isosorbide-2-benzyl carbamate **77**.<sup>46</sup> Esterification at the 5-OH of **77** gave butyrylcholinesterase (BuChE) inhibitors isosorbide-2-benzyl carbamate-5-esters **78** and **79**.<sup>47</sup>



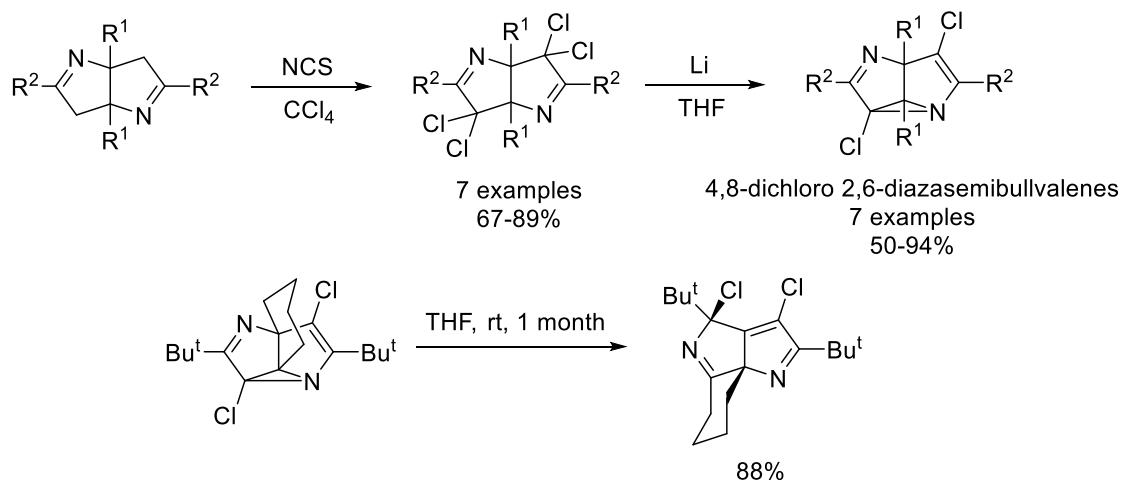
**Scheme 1.15** Synthesis of benzoyl derivatives of isosorbide from **Is5N**.<sup>44-47</sup>

Isosorbide-2-acetate was prepared from isosorbide using AcOH, DCC and DMAP,<sup>48</sup> and was used for the attachment of a short-chain acid at the free 5-OH (Scheme 1.16).<sup>49</sup> Using triphosgene as an acid activator, a diastereoselective [2+2] cycloaddition occurred between the ketene intermediate and imines to give  $\beta$ -lactam-fused isosorbides **80** and **81**. No diastereoselectivity was observed when the analogous  $\beta$ -lactam ring forming procedure was attempted at the 2-position of isosorbide due to insufficient facial differentiation at the cycloaddition transition state.



**Scheme 1.16** Synthesis of  $\beta$ -lactam functionalized isosorbides.<sup>49</sup>

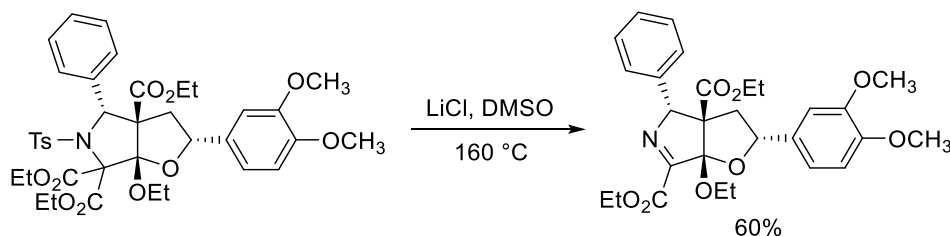
Treatment of 3,3a,6,6a-tetrahydropyrrolo[3,2-*b*]pyrroles with NCS (6 equiv) gave 3,3,6,6-tetrachlorinated products, from which formal loss of Cl<sub>2</sub> induced by lithium metal furnished 4,8-dichloro 2,6-diazasemibullvalenes (Scheme 1.17).<sup>50</sup> The pyrrolo[3,2-*b*]pyrrole core rearranged slowly to a pyrrolo[3,4-*b*]pyrrole initiated by 3-membered ring-opening. Synthesis of the analogous dibromo- and tetrabromo-bipyrrolines from tetrahydro-bipyrroline starting materials was achieved using NBS, with lithium metal treatment furnishing non-brominated and dibrominated 2,6-diazasemibullvalenes.<sup>51</sup> Previously reported syntheses of 2,6-diazasemibullvalenes from pyrrolo[3,2-*b*]pyrroles were reviewed by Xi *et al.* in 2015.<sup>52</sup>



**Scheme 1.17** Synthesis of 2,6-diazasemibullvalenes and rearrangement to a pyrrolo[3,4-*b*]pyrrole core.<sup>50</sup>

### 1.5.2 1,5-Diheteropentalene Systems

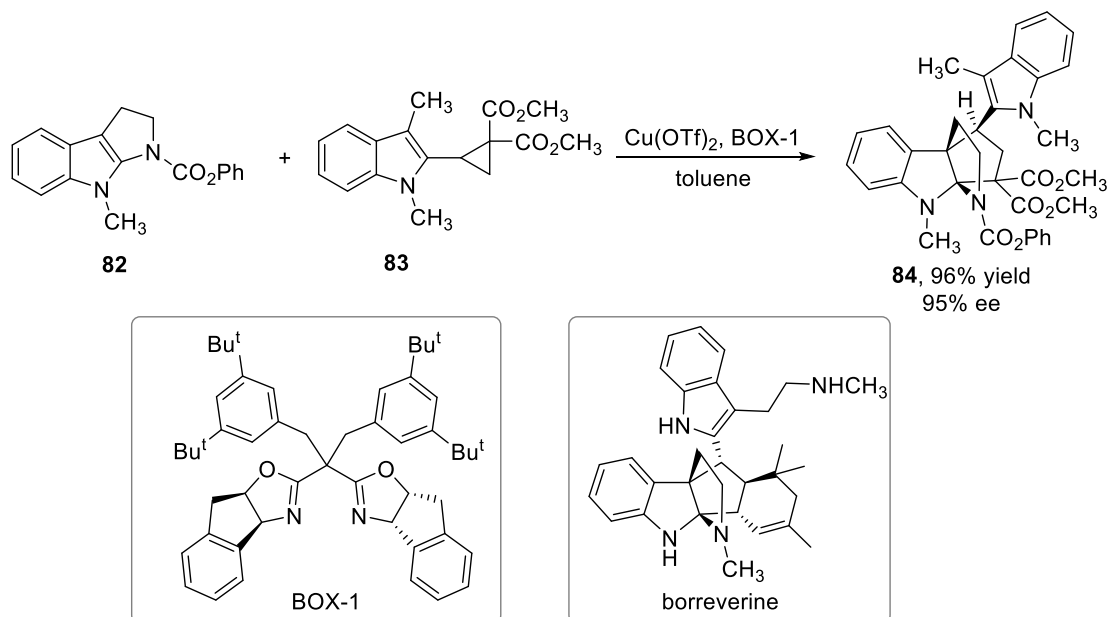
Furo[2,3-*c*]pyrrole underwent mono-decarboxylation and tosyl-group deprotection using lithium chloride at high temperatures (Scheme 1.18).<sup>53</sup>



**Scheme 1.18** Non-conjugated furo[2,3-*c*]pyrrole reactivity.<sup>53</sup>

### 1.5.3 1,6-Diheteropentalene Systems

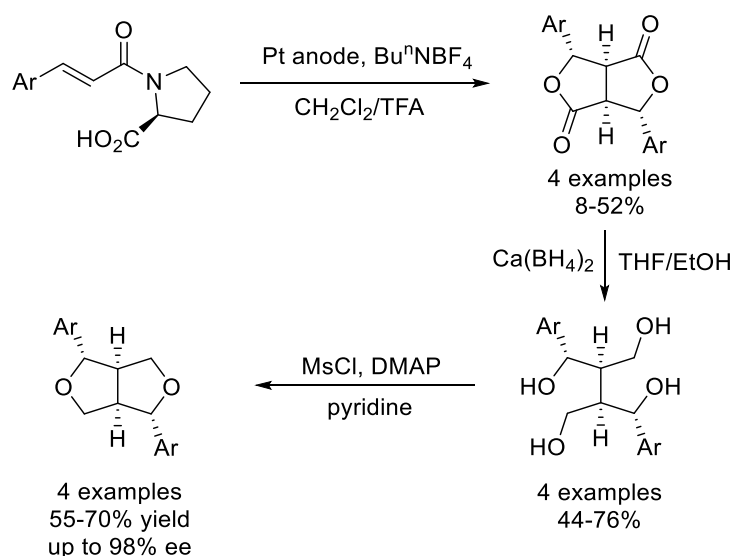
A Cu-catalyzed [3+2] enantioselective cycloaddition of pyrrolo[2,3-*b*]indole **82** onto indole-2-substituted cyclopropane **83** was performed in the presence of a bis(oxazoline) (BOX) ligand to give tetracyclic-fused compound **84** (Scheme 1.19)<sup>54</sup> bearing core structural similarity to the natural product, borreverine.<sup>55</sup>



**Scheme 1.19** Cycloaddition of an indole-2-substituted cyclopropane.<sup>54</sup>

### 1.5.4 2,5-Diheteropentalene Systems

Bis lactones were derived from L-proline-coupled cinnamic acid derivatives through electrochemical oxidative dimerization (Scheme 1.20).<sup>56</sup> The carbonyl groups were removed by reductive ring-opening, enabling ether formation to give a series of tetrahydro-1*H*,3*H*-furo[3,4-*c*]furans.

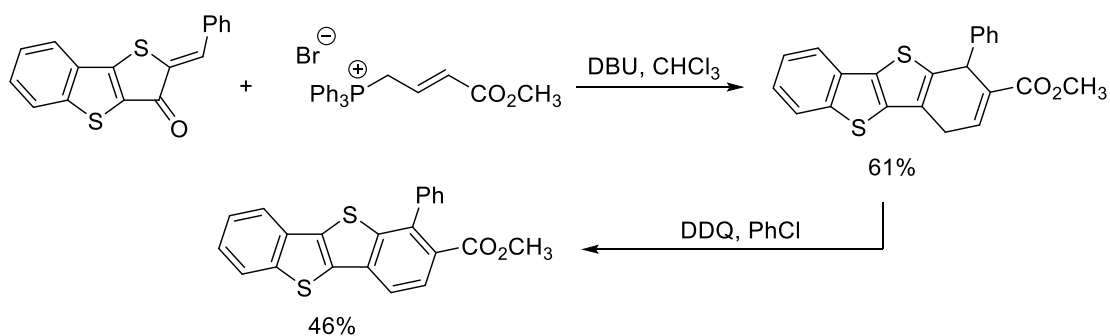


**Scheme 1.20** Synthesis of tetrahydro-1*H*,3*H*-furo[3,4-*c*]furans.<sup>56</sup>

## 1.6 Reactivity of Substituents Attached to Ring Carbon Atoms

### 1.6.1 1,4-Diheteropentalene Systems

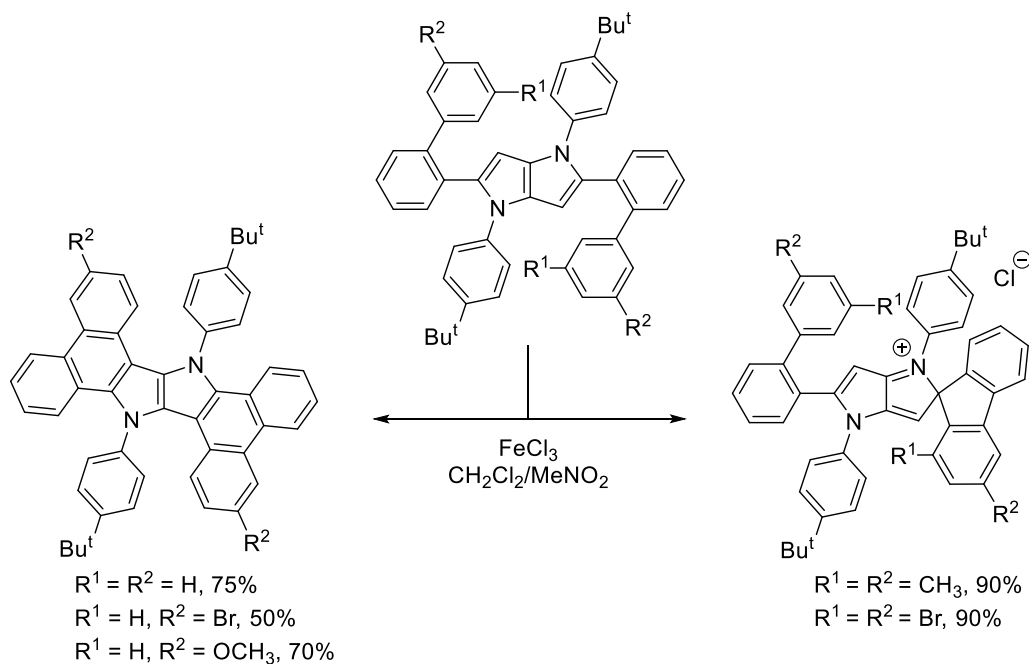
Thioaurone-type thieno[3,2-*b*]benzo[*b*]thiophene gave a 1,4-dihydroarene-fused tetracyclic fused system upon reaction with an allylic phosphonium salt (Scheme 1.21).<sup>57</sup> Aromatization using 2,3-dichloro-5,6-dicyano-1,4-benzoquinone (DDQ) gave a benzo[*b*]thieno[3,2-*b*]benzo[*b*]thiophene derivative in 46% yield.



**Scheme 1.21** Synthesis of a benzo[*b*]thieno[3,2-*b*]benzo[*b*]thiophene derivative from styryl substituents.<sup>57</sup>

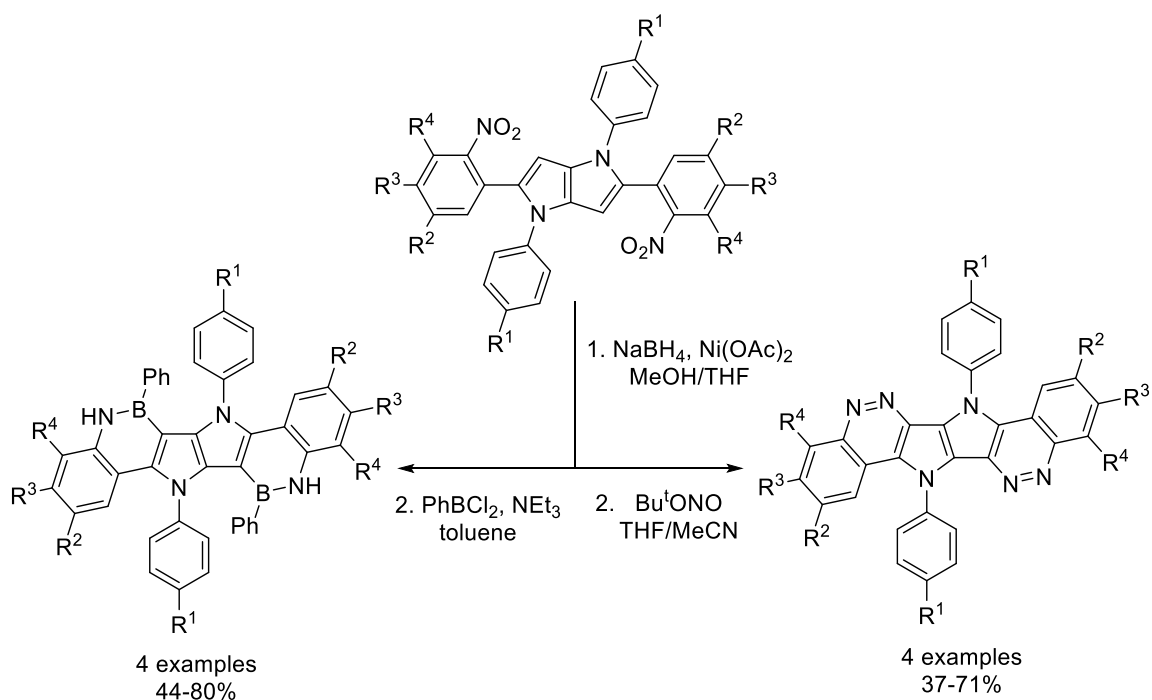
Steric hindrance in the pyrrolo[3,2-*b*]pyrrole system was the deciding factor in the oxidative synthesis to give either the more conjugated blue light-emitting ring-fused system or red light-emitting spiro-fused cationic  $\pi$ -system (Scheme 1.22).<sup>58</sup>

## Chapter 1



**Scheme 1.22** Ring-closure of aryl ring substituents on pyrrolo[3,2-*b*]pyrroles.<sup>58</sup>

Reduction of the nitrophenyl groups in tetraarylpyrrolo[3,2-*b*]pyrroles to their respective anilines was followed by reaction with dichlorophenylborane to provide fluorescent BN-heteroacene derivatives (Scheme 1.23).<sup>59</sup> Reaction of the anilines with *t*-butylnitrite gave non-emitting dicinnolino-fused pyrrolo[3,2-*b*]pyrroles.

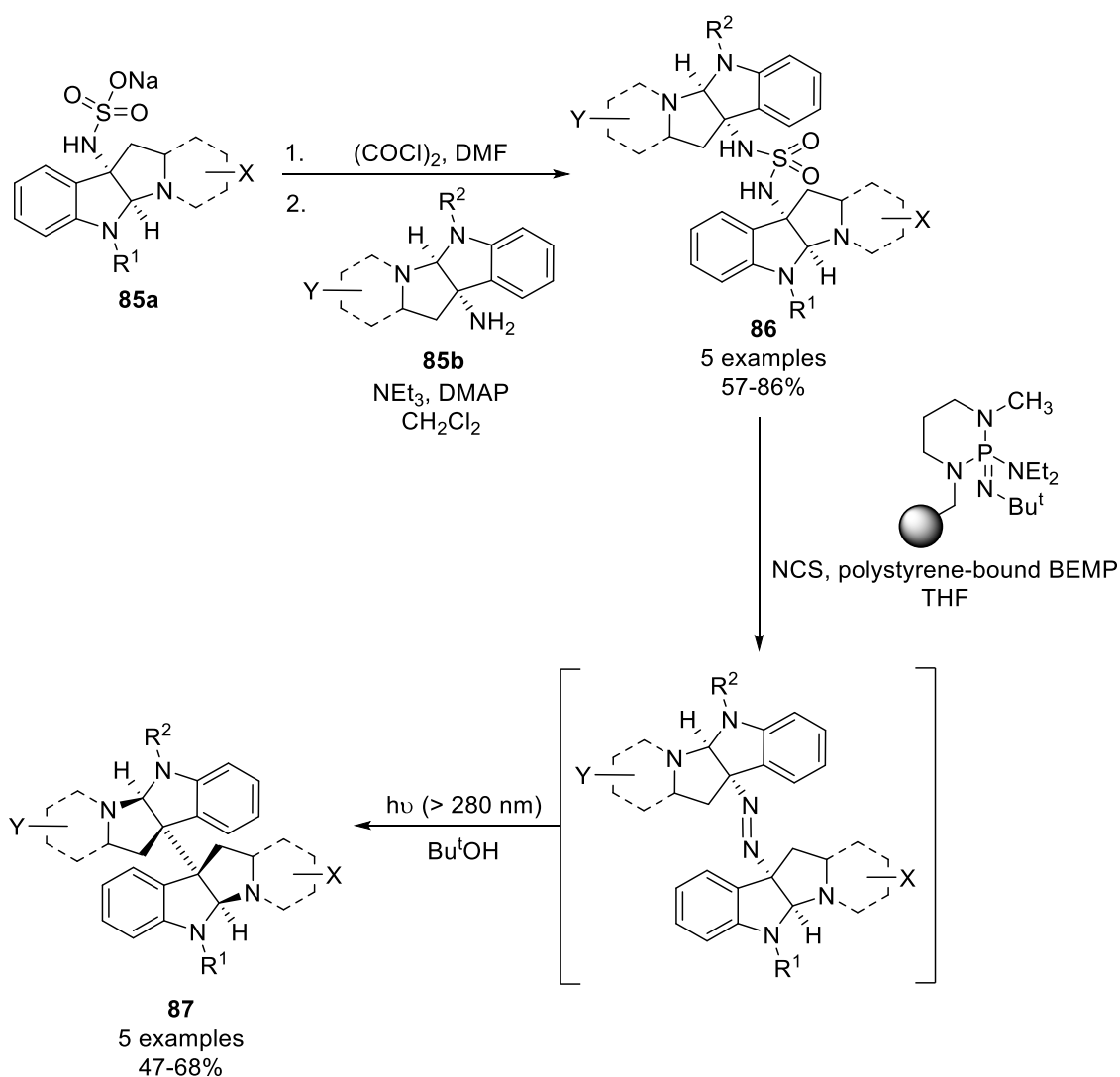


**Scheme 1.23** Synthesis using nitrophenyl substituents on pyrrolo[3,2-*b*]pyrroles.<sup>59</sup>



## 1.6.2 1,6-Diheteropentalene Systems

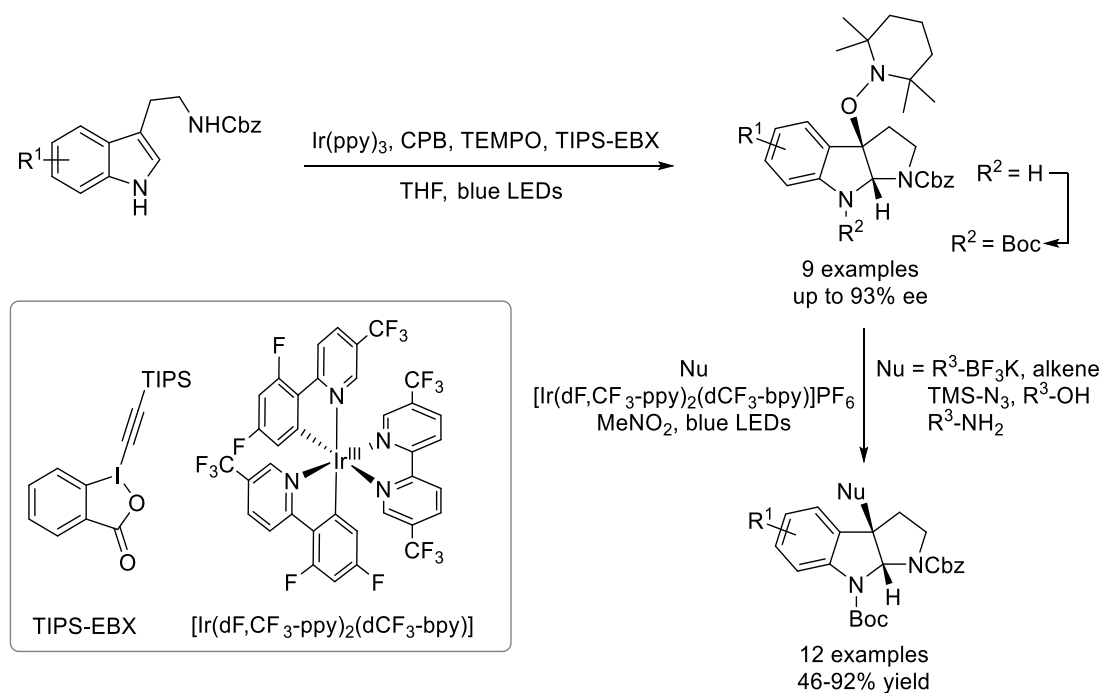
Dimeric hexahydropyrrolo[2,3-*b*]indoles connected at their respective C3a positions are common in natural products.<sup>60-62</sup> Sulfamate salt **85a** was coupled with the dissimilar cyclotryptamine **85b** using oxalyl chloride to give asymmetrical sulfamide **86** (Scheme 1.24).<sup>63</sup> Oxidation and subsequent loss of SO<sub>2</sub> generated the diazene *in situ*, which upon photoinduced expulsion of N<sub>2</sub> furnished the heterodimer **87**.



**Scheme 1.24** Synthesis using sulfamate substituents on hexahydropyrrolo[2,3-*b*]indoles.<sup>63</sup>

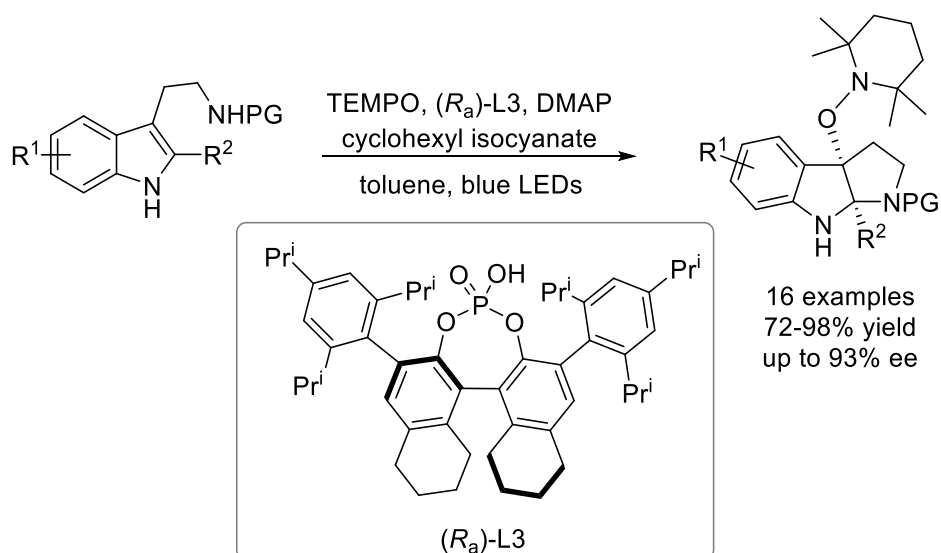
## 1.7 Examples of Diheteropentalene Ring-Synthesis using TEMPO Nitroxide

TEMPO has been employed in the photoredox-catalyzed synthesis of pyrrolo[2,3-*b*]indole alkoxyamines. The field of photoredox catalysis has flourished in recent years.<sup>64–66</sup> The process is centred on the single-electron oxidation/reduction of organic substrates by the visible-light-induced excited state of Ir or Ru complexes. Photocatalytic oxidation of tryptamines in the presence of full equivalents of TEMPO and a chiral phosphate base (CPB) delivered enantioenriched nitroxide-substituted hexahydropyrrolo[2,3-*b*]indoles, with electron and proton acceptance by the hypervalent iodine reagent TIPS-EBX fulfilling the catalytic cycle (Scheme 1.25).<sup>67</sup> Mesolytic cleavage of the alkoxyamine bond was effected by an Ir catalyst, generating TEMPO free radical and a tertiary pyrroloindoline carbocation, which was susceptible to addition by a range of nucleophiles.



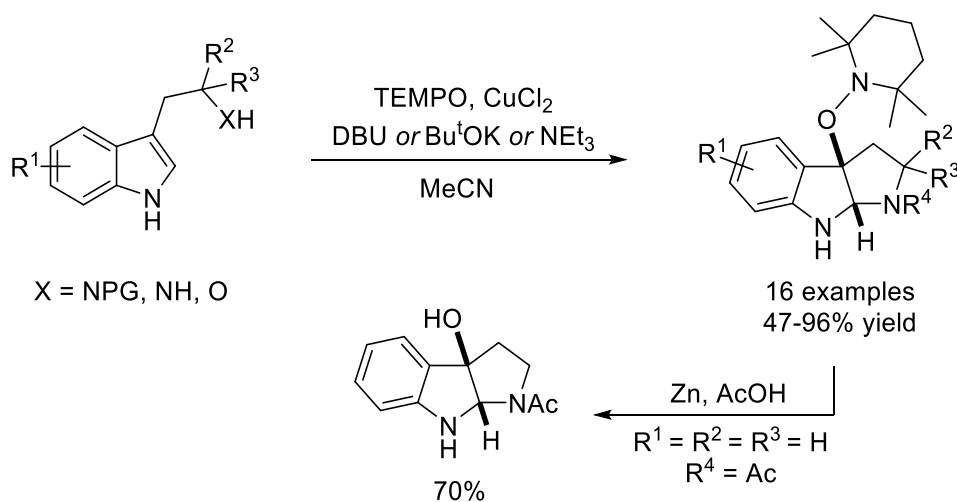
**Scheme 1.25** Synthesis of C3a-substituted pyrroloindolines *via* C3a-alkoxyamines.<sup>67</sup>

The Ir-photocatalyst was not required in the work of Xia *et al.*, with TEMPO being directly excited by visible light, oxidizing 1*H*-tryptamines *via* hydrogen atom transfer and trapping of the intermediate radical in the presence of a chiral phosphoric acid to give analogous enantioenriched hexahydropyrrolo[2,3-*b*]indole alkoxyamines (Scheme 1.26).<sup>68</sup>



**Scheme 1.26** Enantioselective synthesis of C3a-alkoxyamine substituted hexahydropyrrolo[3,2-*b*]indoles.<sup>68</sup>

A Cu-catalyzed racemic synthesis with TEMPO of hexahydropyrrolo[2,3-*b*]indole alkoxyamines was reported,<sup>69</sup> with reductive hydroxylation allowing replacement of TEMPO (Scheme 1.27).

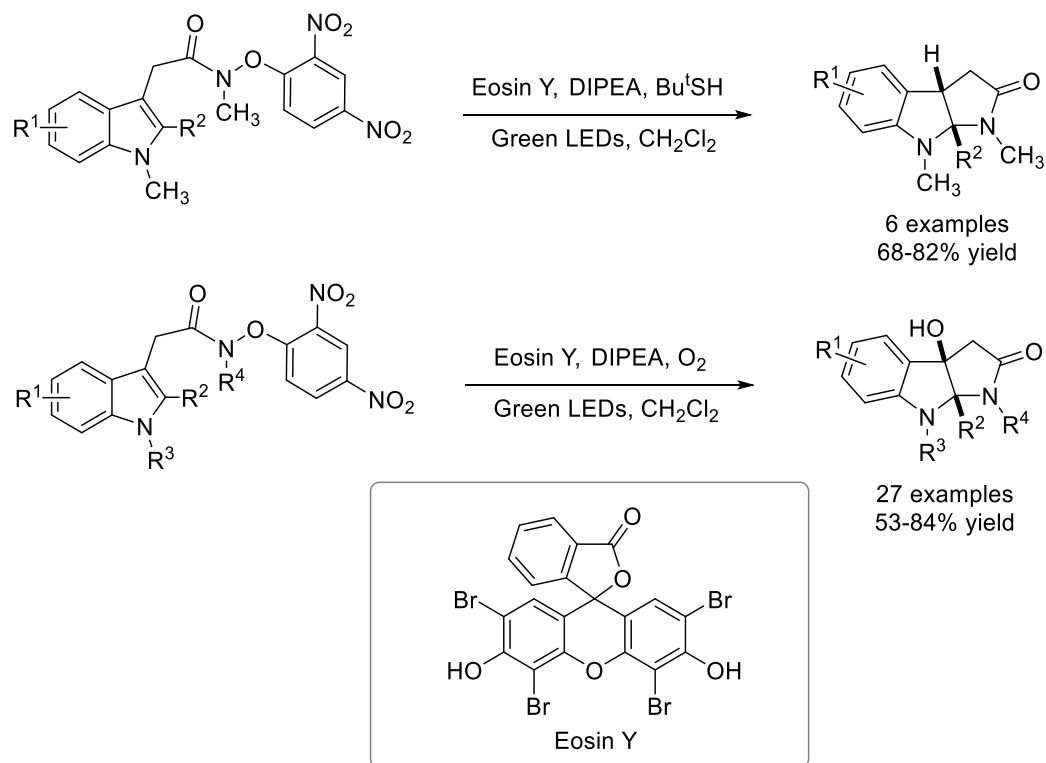


**Scheme 1.27** Racemic synthesis of C3a-alkoxyamine substituted hexahydropyrrolo[3,2-*b*]indoles.<sup>69</sup>

A metal-free photoredox catalyzed synthesis of pyrroloindolines is described by Wang *et al.*, replacing the metal photocatalyst by Eosin Y (Scheme 1.28).<sup>70</sup> Photocatalyzed

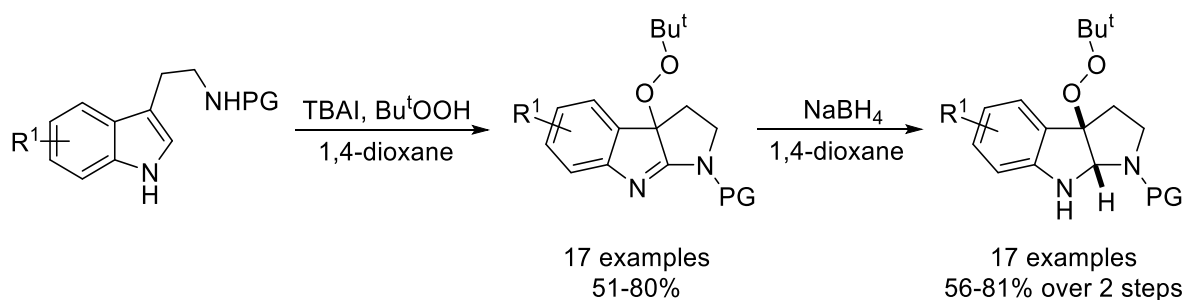
## Chapter 1

reduction of an electron-poor aryloxy group on tryptamides generated an amidyl radical, which cyclized 5-*endo*-trig onto the adjacent indole. By including either a hydrogen donor or O<sub>2</sub>, pyrroloindolines are isolated bearing either H or OH groups at the C3a position respectively.



**Scheme 1.28** Synthesis of hexahydropyrrolo[3,2-*b*]indoles using Eosin Y.<sup>70</sup>

Oxidative cyclization of tryptamines using alkylperoxidation is an alternative to TEMPO methods forming C3a-peroxy pyrrolo[2,3-*b*]indolenines (Scheme 1.29).<sup>71</sup> A sequential reduction step gave C3a-peroxyhexahydropyrrolo[2,3-*b*]indoles.<sup>72</sup>



**Scheme 1.29** Synthesis of peroxypyrroloindolenines and peroxylhexahydropyrrolo[3,2-*b*]indoles.<sup>71,72</sup>

## 1.8 Synthesis of Particular Classes of Compounds

This section focuses on the synthesis of natural products containing the subject heterocyclic systems. The electrochemical dimerization of cinnamic acid derivatives (Section 1.5.4) was applied to the syntheses of furofuran lignins (Figure 1.13).<sup>56</sup>

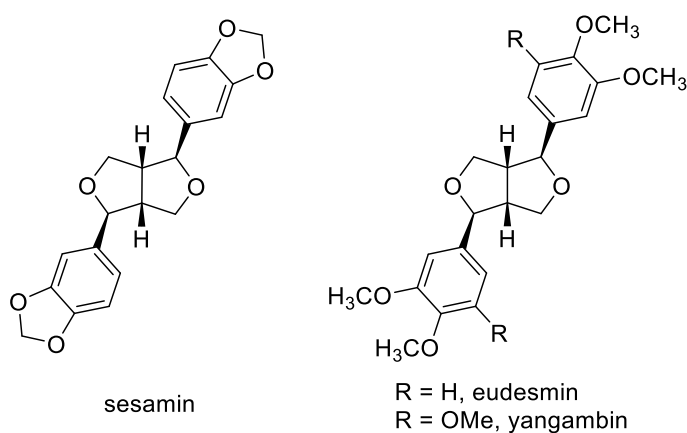
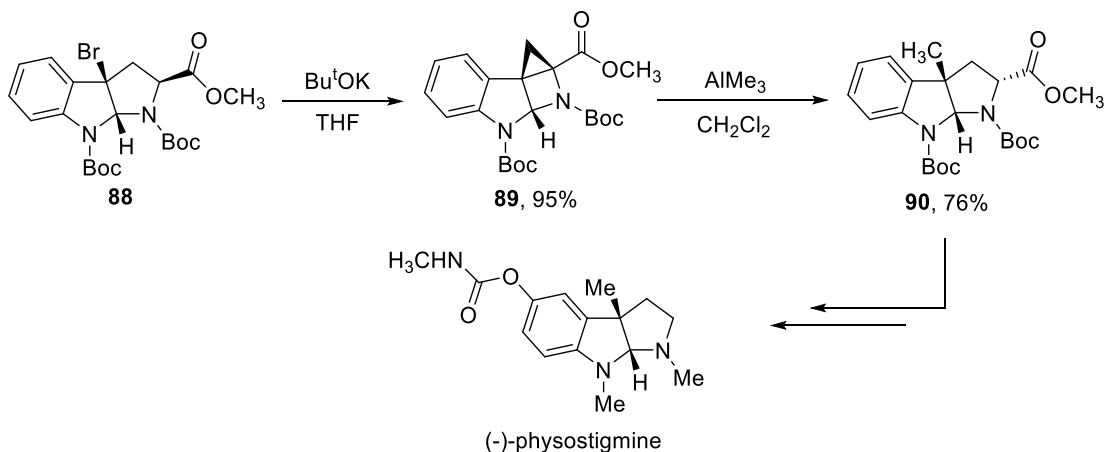


**Figure 1.13** Furofuran lignins.<sup>56</sup>

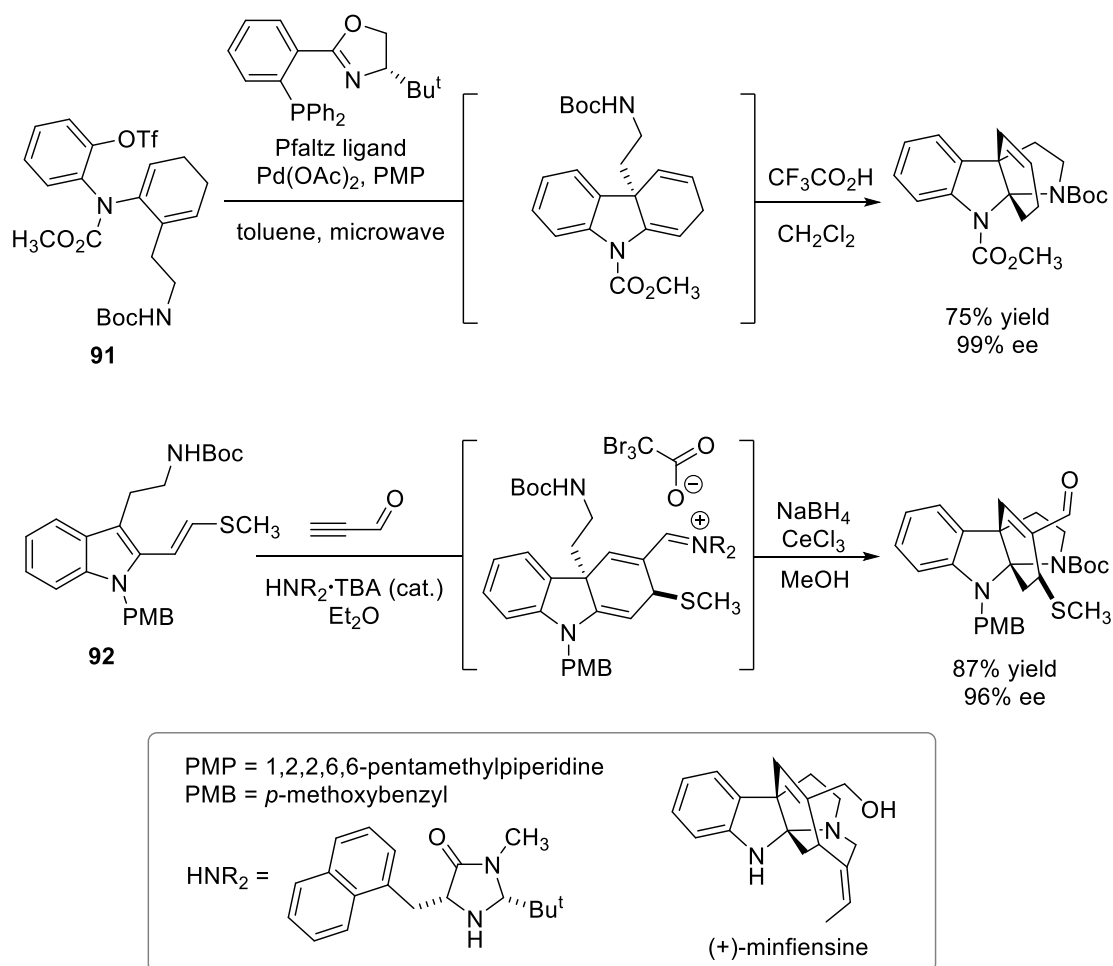
Bromopyrrolo[2,3-*b*]indoline **88** is readily available in a single step in high diastereoselectivity from the corresponding tryptophan derivative, and was converted to cyclopropylazetoidindoline **89** using base (Scheme 1.30).<sup>73</sup> Treatment of **89** with AlMe<sub>3</sub> gave pyrrolo[2,3-*b*]indoline **90**, as part of a synthesis towards the anticholinergic agent and natural product, (-)-physostigmine.



**Scheme 1.30** Synthesis of an intermediate towards (-)-physostigmine.<sup>73</sup>

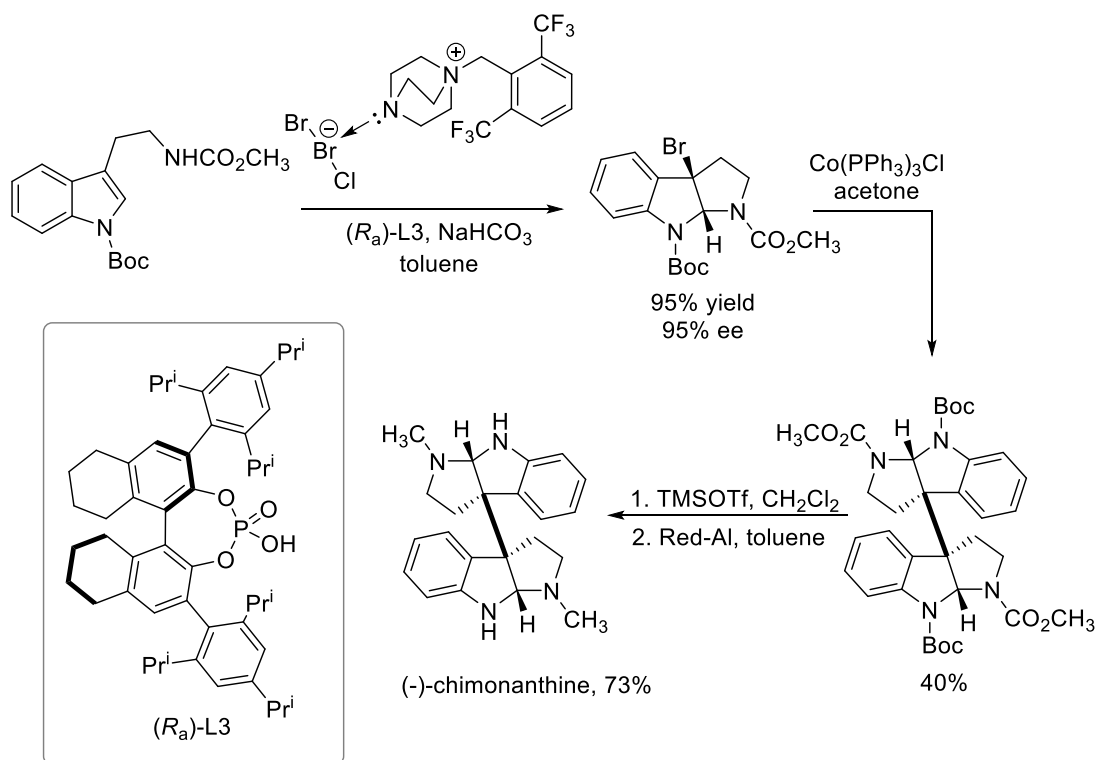
## Chapter 1

Several methods are reported for the total synthesis of *Strychnos minfiensis* derived alkaloid, ( $\pm$ )-minfiensine,<sup>74-80</sup> which contains a pyrrolidino[2,3-*b*]indoline core.<sup>81</sup> Overman and co-workers disclosed the first enantioselective total synthesis of (+)-minfiensine (Scheme 1.31).<sup>82</sup> The key step is the asymmetric Heck cyclization of triflate **91** forming the pyrrolidino[2,3-*b*]indoline core using the Pfaltz ligand.<sup>83</sup> The Jiao group also used a chiral Pd-catalyst for enantioselective formation of the core pyrrolidino[2,3-*b*]indoline system as part of their (+)-minfiensine total synthesis.<sup>84</sup> MacMillan *et al.* described an organocatalyzed enantioselective synthesis of (+)-minfiensine, with the pyrrolidino[2,3-*b*]indoline ring-forming step involving an acetylenic [4+2] cycloaddition onto 2-allyl tryptamine **92**, while application of Luche reduction conditions facilitated detachment of the chiral amine catalyst (Scheme 1.31).<sup>85</sup>



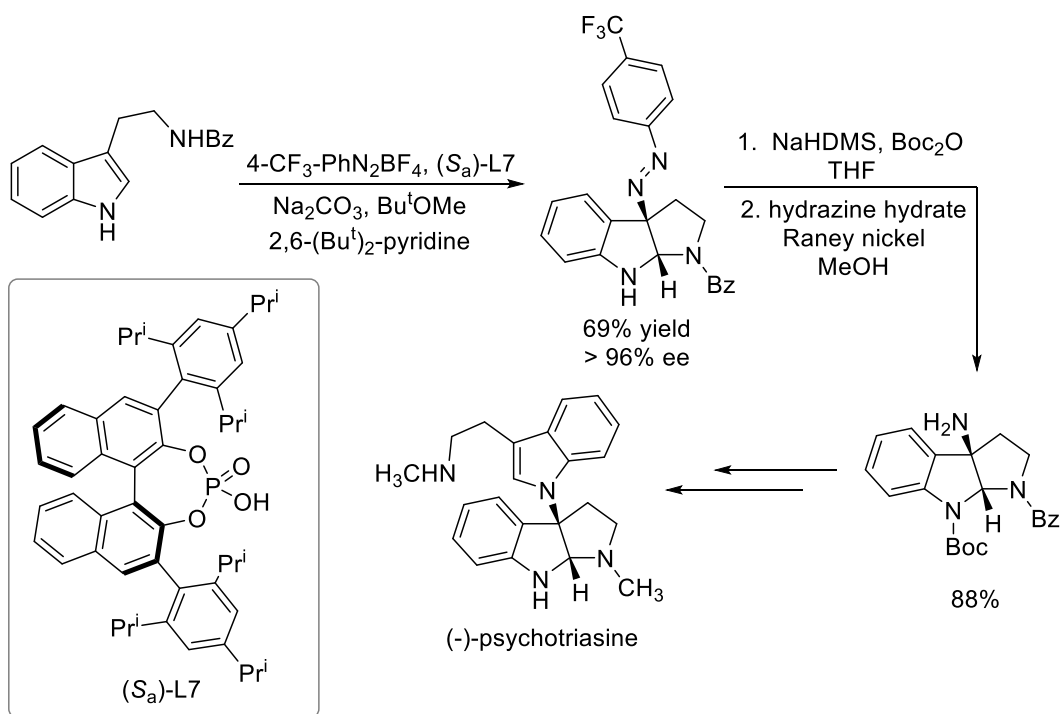
**Scheme 1.31** Asymmetric syntheses of (+)-minfiensine.<sup>82,85</sup>

Ma *et al.* demonstrated the bromocyclization of protected tryptamines using a chiral phosphoric acid catalyst and a DABCO-derived bromine salt to give 3a-bromohexahydropyrrolo[2,3-*b*]indoles,<sup>86</sup> which, upon dimerization using the established method of Co-catalysis,<sup>87-89</sup> deprotection and methylation, gave the natural product (-)-chimonanthine (Scheme 1.32).



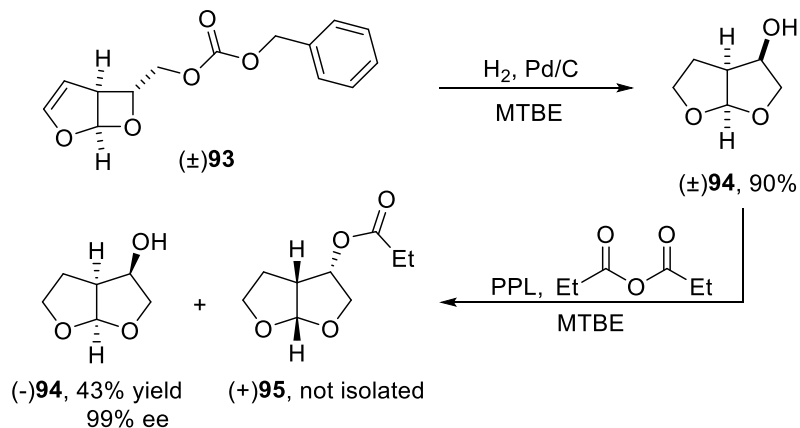
**Scheme 1.32** Synthesis of (-)-chimonanthine.<sup>86</sup>

The key steps in the synthesis of (-)-psychotriasine were the enantioselective cyclization of C3a-diazinated benzoyl-protected tryptamine followed by the Raney nickel-catalyzed reduction to the amine using hydrazine hydrate (Scheme 1.33).<sup>90</sup>



**Scheme 1.33** Enantioselective transformation of tryptamine towards (-)-psychotriazine.<sup>90</sup>

The fully saturated (3*R*,3*aS*,6*aR*)-hexahydrofuro[2,3-*b*]furan-3-ol moiety (-)**94** is a common structural feature of several potent (IC<sub>50</sub> < 5 nM) HIV protease inhibitors including Darunavir,<sup>91</sup> Brexanavir,<sup>92</sup> and GS-8374.<sup>93</sup> Opatz and co-workers started their synthesis of (-)**94** from oxetane (±)**93** (Scheme 1.34).<sup>94</sup> Single step reductive conditions facilitated alkene hydrogenation, carboxybenzyl deprotection, and oxetane ring expansion to give hexahydrofuro[2,3-*b*]furan (±)**94** in 90% yield. The porcine pancreatic lipase (PPL) catalyzed acylation of (+)**94** enabled isolation of the desired 3*R*-enantiomer (-)**94**.



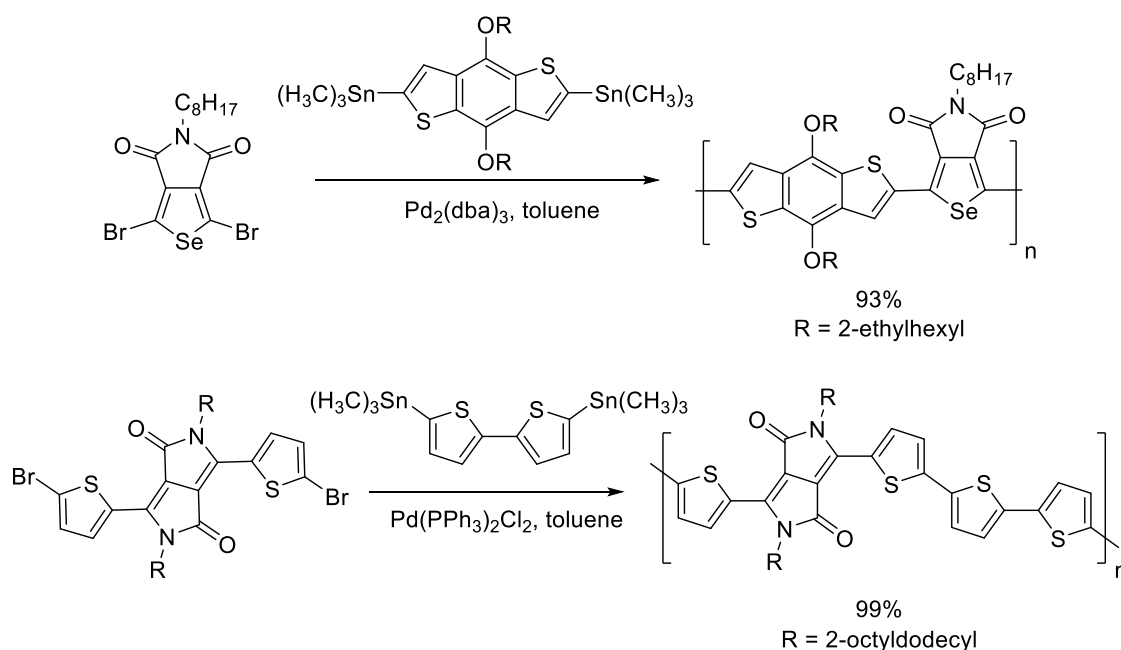
**Scheme 1.34** Synthesis of hexahydrofuro[2,3-*b*]furan-3-ol (-)**102**.<sup>94</sup>



## 1.9 Important Compounds and Applications

As evidenced in this review, heterocyclic compounds consisting of two fused five-membered heterocycles with 1:1 placement of heteroatoms have a myriad of applications. Diheteropentalenes, particularly those bearing N and/or O atoms, are found in many natural products with several total syntheses or key ring-forming steps detailed in this review.

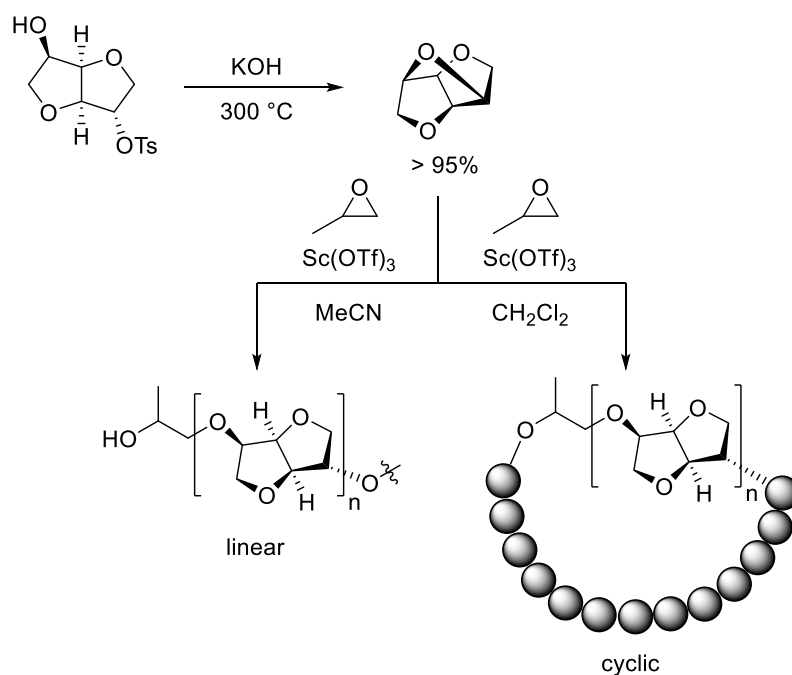
In materials science, the shift to renewable solar energies has promoted research into new efficient semiconductors, and highly conjugated (often polymeric) diheteropentalenes having a low band gap are of immense interest.<sup>16,21,95–99</sup> Stille couplings of selenolo[3,4-*c*]pyrrole<sup>18</sup> and pyrrolo[3,4-*c*]pyrrole<sup>100</sup> systems onto bithiophenes give donor-acceptor polymer semiconductors (Scheme 1.35).



**Scheme 1.35** Synthesis of donor-acceptor polymer semiconductors.<sup>18,100</sup>

The fully-saturated biomass-derived scaffold, isosorbide, is extensively studied for the preparation of chiral, non-toxic and generally environmentally-friendly polymers.<sup>24,25</sup> As a recent synthetic example, the scandium triflate-mediated ring-opening polymerization of 1,4:2,5:3,6-trianhydro-D-mannitol (derived from isosorbide-2-tosylate) provided linear or cyclic polymers depending on the solvent employed (Scheme 1.36).<sup>101</sup>

## Chapter 1



**Scheme 1.36** Controlling the architecture in isosorbide-based polymers.<sup>101</sup>

The chemistry of the diheteropentalenes remains respected and explored, with research continuing into aromaticity, spectroscopy and reactivity, most often with diverse applications in mind.

### 1.10 Chapter 1 References

1. Krutošóková, A.; Gracza, T. In *Comprehensive Heterocyclic Chemistry III*; Katritzky, A. R., Ramsden, C. A., Scriven, E. F. V., Taylor, R. J. K., Eds.; Elsevier: Oxford, 2008; Vol. 10, p 1–64. <https://doi.org/10.1016/B978-008044992-0.00901-9>.
2. Katz, T. J.; Rosenberger, M. *J. Am. Chem. Soc.* **1962**, *84*, 865–866. <https://doi.org/10.1021/ja00864a038>.
3. Katz, T. J.; Rosenberger, M.; O'Hara, R. K. *J. Am. Chem. Soc.* **1964**, *86*, 249–252. <https://doi.org/10.1021/ja01056a030>.
4. Machara, A.; Kozmík, V.; Pojarová, M.; Dvořáková, H.; Svoboda, J. *Collect. Czech. Chem. Commun.* **2009**, *74*, 785–798. <https://doi.org/10.1135/cccc2009001>.
5. Neto, J. S. S.; Iglesias, B. A.; Back, D. F.; Zeni, G. *Adv. Synth. Catal.* **2016**, *358*, 3572–3585. <https://doi.org/10.1002/adsc.201600759>.
6. Wu, B.; Melvina; Wu, X.; Lee Yeow, E. K.; Yoshikai, N. *Chem. Sci.* **2017**, *8*, 4527–4532. <https://doi.org/10.1039/C7SC01162H>.
7. Takahashi, M.; Nakano, K.; Nozaki, K. *J. Org. Chem.* **2015**, *80*, 3790–3797. <https://doi.org/10.1021/jo502889r>.
8. Wang, M.; Wei, J.; Fan, Q.; Jiang, X. *Chem. Commun.* **2017**, *53*, 2918–2921. <https://doi.org/10.1039/C6CC09201B>.
9. Wu, N. M.-W.; Ng, M.; Lam, W. H.; Wong, H.-L.; Yam, V. W.-W. *J. Am. Chem. Soc.* **2017**, *139*, 15142–15150. <https://doi.org/10.1021/jacs.7b08333>.
10. Matsumura, M.; Muranaka, A.; Kurihara, R.; Kanai, M.; Yoshida, K.; Kakusawa, N.; Hashizume, D.; Uchiyama, M.; Yasuike, S. *Tetrahedron* **2016**, *72*, 8085–8090. <https://doi.org/10.1016/j.tet.2016.10.048>.
11. Ren, Y.; Baumgartner, T. *J. Am. Chem. Soc.* **2011**, *133*, 1328–1340. <https://doi.org/10.1021/ja108081b>.
12. Wu, B.; Yoshikai, N. *Angew. Chem. Int. Ed.* **2015**, *54*, 8736–8739. <https://doi.org/10.1002/anie.201503134>.
13. Wang, M.; Fan, Q.; Jiang, X. *Org. Lett.* **2016**, *18*, 5756–5759. <https://doi.org/10.1021/acs.orglett.6b03078>.
14. Wang, M.; Chen, S.; Jiang, X. *Org. Lett.* **2017**, *19*, 4916–4919. <https://doi.org/10.1021/acs.orglett.7b02388>.

## Chapter 1

---

15. Fukazawa, A.; Hara, M.; Okamoto, T.; Son, E.-C.; Xu, C.; Tamao, K.; Yamaguchi, S. *Org. Lett.* **2008**, *10*, 913–916. <https://doi.org/10.1021/ol7030608>.
16. Patra, A.; Wijsboom, Y. H.; Leitus, G.; Bendikov, M. *Chem. Mater.* **2011**, *23*, 896–906. <https://doi.org/10.1021/cm102395v>.
17. Dey, T.; Navarathne, D.; Invernale, M. A.; Berghorn, I. D.; Sotzing, G. A. *Tetrahedron Lett.* **2010**, *51*, 2089–2091. <https://doi.org/10.1016/j.tetlet.2010.02.036>.
18. Beaupré, S.; Pron, A.; Drouin, S. H.; Najari, A.; Mercier, L. G.; Robitaille, A.; Leclerc, M. *Macromolecules* **2012**, *45*, 6906–6914. <https://doi.org/10.1021/ma3011894>.
19. Sashida, H.; Yasuike, S. *J. Heterocycl. Chem.* **1998**, *35*, 725–726. <https://doi.org/10.1002/jhet.5570350337>.
20. Janiga, A.; Gryko, D. T. *Chem. Asian J.* **2014**, *9*, 3036–3045. <https://doi.org/10.1002/asia.201402367>.
21. Cinar, M. E.; Ozturk, T. *Chem. Rev.* **2015**, *115*, 3036–3140. <https://doi.org/10.1021/cr500271a>.
22. Egorov, D. I. *Chem. Heterocycl. Compd.* **2016**, *52*, 779–781. <https://doi.org/10.1007/s10593-016-1964-x>.
23. Repka, L. M.; Reisman, S. E. *J. Org. Chem.* **2013**, *78*, 12314–12320. <https://doi.org/10.1021/jo4017953>.
24. Fenouillot, F.; Rousseau, A.; Colomines, G.; Saint-Loup, R.; Pascault, J. P. *Prog. Polym. Sci.* **2010**, *35*, 578–622. <https://doi.org/10.1016/j.progpolymsci.2009.10.001>.
25. Rose, M.; Palkovits, R. *ChemSusChem* **2012**, *5*, 167–176. <https://doi.org/10.1002/cssc.201100580>.
26. Tundo, P.; Aricò, F.; Gauthier, G.; Rossi, L.; Rosamilia, A. E.; Bevinakatti, H. S.; Sievert, R. L.; Newman, C. P. *ChemSusChem* **2010**, *3*, 566–570. <https://doi.org/10.1002/cssc.201000011>.
27. Ignarro, L. J.; Napoli, C.; Loscalzo, J. *Circ. Res.* **2002**, *90*, 21–28. <https://doi.org/10.1161/hh0102.102330>.
28. Krzeszewski, M.; Kodama, T.; Espinoza, E. M.; Vullev, V. I.; Kubo, T.; Gryko, D. T. *Chem. Eur. J.* **2016**, *22*, 16478–16488. <https://doi.org/10.1002/chem.201603282>.

## Chapter 1

---

29. Ha Vuong, T. M.; Villemin, D.; Nguyen, H.-H.; Le, T. T.; Dang, T. T.; Nguyen, H. *Chem. Asian J.* **2017**, *12*, 2819–2826. <https://doi.org/10.1002/asia.201700562>.
30. Chang, Y.; Chen, H.; Zhou, Z.; Zhang, Y.; Schütt, C.; Herges, R.; Shen, Z. *Angew. Chem. Int. Ed.* **2012**, *51*, 12801–12805. <https://doi.org/10.1002/anie.201204954>.
31. Qiu, L.; Zhuang, X.; Zhao, N.; Wang, X.; An, Z.; Lan, Z.; Wan, X. *Chem. Commun.* **2014**, *50*, 3324–3327. <https://doi.org/10.1039/C3CC49418G>.
32. Kawase, T.; Fujiwara, T.; Kitamura, C.; Konishi, A.; Hirao, Y.; Matsumoto, K.; Kurata, H.; Kubo, T.; Shinamura, S.; Mori, H.; Miyazaki, E.; Takimiya, K. *Angew. Chem. Int. Ed.* **2010**, *49*, 7728–7732. <https://doi.org/10.1002/anie.201003609>.
33. Emin Cinar, M.; Ozturk, T. *Org. Commun.* **2018**, *11*, 68–74. <https://doi.org/10.25135/acg.oc.45.18.05.103>.
34. Morita, T.; Satoh, T.; Miura, M. *Org. Lett.* **2015**, *17*, 4384–4387. <https://doi.org/10.1021/acs.orglett.5b02246>.
35. Kirchberg, S.; Tani, S.; Ueda, K.; Yamaguchi, J.; Studer, A.; Itami, K. *Angew. Chem. Int. Ed.* **2011**, *50*, 2387–2391. <https://doi.org/10.1002/anie.201007060>.
36. Ueda, K.; Yanagisawa, S.; Yamaguchi, J.; Itami, K. *Angew. Chem. Int. Ed.* **2010**, *49*, 8946–8949. <https://doi.org/10.1002/anie.201005082>.
37. He, Z.; Shrivess, H. J.; Fernández-Salas, J. A.; Abengózar, A.; Neufeld, J.; Yang, K.; Pulis, A. P.; Procter, D. J. *Angew. Chem. Int. Ed.* **2018**, *57*, 5759–5764. <https://doi.org/10.1002/anie.201801982>.
38. He, Y.; Li, Z.; Robeyns, K.; Van Meervelt, L.; Van der Eycken, E. V. *Angew. Chem. Int. Ed.* **2018**, *57*, 272–276. <https://doi.org/10.1002/anie.201710592>.
39. Zhang, C.; Zang, Y.; Gann, E.; McNeill, C. R.; Zhu, X.; Di, C.-a.; Zhu, D. *J. Am. Chem. Soc.* **2014**, *136*, 16176–16184. <https://doi.org/10.1021/ja510003y>.
40. Ogawa, Y.; Takiguchi, E.; Mamada, M.; Kumaki, D.; Tokito, S.; Katagiri, H. *Tetrahedron Lett.* **2017**, *58*, 963–967. <https://doi.org/10.1016/j.tetlet.2017.01.074>.
41. Punzi, A.; Capozzi, M. A. M.; Di Noja, S.; Ragni, R.; Zappimbulso, N.; Farinola, G. M. *J. Org. Chem.* **2018**, *83*, 9312–9321. <https://doi.org/10.1021/acs.joc.8b01284>.
42. Grenier, F.; Goudreau, K.; Leclerc, M. *J. Am. Chem. Soc.* **2017**, *139*, 2816–2824. <https://doi.org/10.1021/jacs.6b12955>.

## Chapter 1

---

43. Wang, X.; Wang, L.; Li, T.; Huang, Z.; Lai, Y.; Ji, H.; Wan, X.; Xu, J.; Tian, J.; Zhang, Y. *J. Med. Chem.* **2013**, *56*, 3078–3089. <https://doi.org/10.1021/jm4001693>.
44. Moriarty, L. M.; Lally, M. N.; Carolan, C. G.; Jones, M.; Clancy, J. M.; Gilmer, J. F. *J. Med. Chem.* **2008**, *51*, 7991–7999. <https://doi.org/10.1021/jm801094c>.
45. Jones, M.; Inkielewicz, I.; Medina, C.; Santos-Martinez, M. J.; Radomski, A.; Radomski, M. W.; Lally, M. N.; Moriarty, L. M.; Gaynor, J.; Carolan, C. G.; Khan, D.; O’Byrne, P.; Harmon, S.; Holland, V.; Clancy, J. M.; Gilmer, J. F. *J. Med. Chem.* **2009**, *52*, 6588–6598. <https://doi.org/10.1021/jm900561s>.
46. Carolan, C. G.; Dillon, G. P.; Gaynor, J. M.; Reidy, S.; Ryder, S. A.; Khan, D.; Marquez, J. F.; Gilmer, J. F. *J. Med. Chem.* **2008**, *51*, 6400–6409. <https://doi.org/10.1021/jm800564y>.
47. Carolan, C. G.; Dillon, G. P.; Khan, D.; Ryder, S. A.; Gaynor, J. M.; Reidy, S.; Marquez, J. F.; Jones, M.; Holland, V.; Gilmer, J. F. *J. Med. Chem.* **2010**, *53*, 1190–1199. <https://doi.org/10.1021/jm9014845>.
48. Čeković, Ž.; Tokić, Z. *Synthesis* **1989**, 610–612. <https://doi.org/10.1055/s-1989-27332>.
49. Shaikh, A. L.; Kale, A. S.; Shaikh, M. A.; Puranik, V. G.; Deshmukh, A. R. A. S. *Tetrahedron* **2007**, *63*, 3380–3388. <https://doi.org/10.1016/j.tet.2007.02.022>.
50. Zhan, M.; Zhang, S.; Huang, Z.; Xi, Z. *Org. Lett.* **2015**, *17*, 1026–1029. <https://doi.org/10.1021/acs.orglett.5b00136>.
51. Huang, Z.; Zhan, M.; Zhang, S.; Luo, Q.; Zhang, W.-X.; Xi, Z. *Org. Chem. Front.* **2017**, *4*, 1785–1788. <https://doi.org/10.1039/C7QO00287D>.
52. Zhang, S.; Zhang, W.-X.; Xi, Z. *Acc. Chem. Res.* **2015**, *48*, 1823–1831. <https://doi.org/10.1021/acs.accounts.5b00190>.
53. Ghosh, A.; Pandey, A. K.; Banerjee, P. *J. Org. Chem.* **2015**, *80*, 7235–7242. <https://doi.org/10.1021/acs.joc.5b00705>.
54. Xiong, H.; Xu, H.; Liao, S.; Xie, Z.; Tang, Y. *J. Am. Chem. Soc.* **2013**, *135*, 7851–7854. <https://doi.org/10.1021/ja4042127>.
55. Pousset, J. L.; Cavé, A.; Chiaroni, A.; Riche, C. *J. Chem. Soc., Chem. Commun.* **1977**, 261–262. <https://doi.org/10.1039/C39770000261>.
56. Mori, N.; Furuta, A.; Watanabe, H. *Tetrahedron* **2016**, *72*, 8393–8399. <https://doi.org/10.1016/j.tet.2016.10.058>.

## Chapter 1

---

57. Li, K.; Yu, A.; Meng, X. *Org. Lett.* **2018**, *20*, 1106–1109. <https://doi.org/10.1021/acs.orglett.8b00028>.
58. Krzeszewski, M.; Świder, P.; Dobrzycki, Ł.; Cyrański, M. K.; Danikiewicz, W.; Gryko, D. T. *Chem. Commun.* **2016**, *52*, 11539–11542. <https://doi.org/10.1039/C6CC05904J>.
59. Tasiar, M.; Gryko, D. T. *J. Org. Chem.* **2016**, *81*, 6580–6586. <https://doi.org/10.1021/acs.joc.6b01209>.
60. Barrow, C. J.; Sedlock, D. M. *J. Nat. Prod.* **1994**, *57*, 1239–1244. <https://doi.org/10.1021/np50111a008>.
61. Takahashi, C.; Minoura, K.; Yamada, T.; Numata, A.; Kushida, K.; Shingu, T.; Hagishita, S.; Nakai, H.; Sato, T.; Harada, H. *Tetrahedron* **1995**, *51*, 3483–3498. [https://doi.org/10.1016/0040-4020\(95\)00102-E](https://doi.org/10.1016/0040-4020(95)00102-E).
62. Varoglu, M.; Corbett, T. H.; Valeriote, F. A.; Crews, P. *J. Org. Chem.* **1997**, *62*, 7078–7079. <https://doi.org/10.1021/jo970568z>.
63. Movassaghi, M.; Ahmad, O. K.; Lathrop, S. P. *J. Am. Chem. Soc.* **2011**, *133*, 13002–13005. <https://doi.org/10.1021/ja2057852>.
64. Narayanam, J. M. R.; Stephenson, C. R. J. *Chem. Soc. Rev.* **2011**, *40*, 102–113. <https://doi.org/10.1039/B913880N>.
65. Prier, C. K.; Rankic, D. A.; MacMillan, D. W. C. *Chem. Rev.* **2013**, *113*, 5322–5363. <https://doi.org/10.1021/cr300503r>.
66. M. Gurry and F. Aldabbagh, *Org. Biomol. Chem.* **2016**, *14*, 3849–3862. <https://doi.org/10.1039/C6OB00370B>.
67. Gentry, E. C.; Rono, L. J.; Hale, M. E.; Matsuura, R.; Knowles, R. R. *J. Am. Chem. Soc.* **2018**, *140*, 3394–3402. <https://doi.org/10.1021/jacs.7b13616>.
68. Liang, K.; Tong, X.; Li, T.; Shi, B.; Wang, H.; Yan, P.; Xia, C. *J. Org. Chem.* **2018**, *83*, 10948–10958. <https://doi.org/10.1021/acs.joc.8b01597>.
69. Deng, X.; Liang, K.; Tong, X.; Ding, M.; Li, D.; Xia, C. *Org. Lett.* **2014**, *16*, 3276–3279. <https://doi.org/10.1021/ol501287x>.
70. Wu, K.; Du, Y.; Wei, Z.; Wang, T. *Chem. Commun.* **2018**, *54*, 7443–7446. <https://doi.org/10.1039/C8CC03575J>.
71. Li, Y.; Li, L.; Lu, X.; Bai, Y.; Wang, Y.; Wu, Y.; Zhong, F. *Chem. Commun.* **2019**, *55*, 63–66. <https://doi.org/10.1039/C8CC08866G>.
72. Lu, X.; Bai, Y.; Li, Y.; Shi, Y.; Li, L.; Wu, Y.; Zhong, F. *Org. Lett.* **2018**, *20*, 7937–7941. <https://doi.org/10.1021/acs.orglett.8b03509>.

## Chapter 1

---

73. Espejo, V. R.; Li, X.-B.; Rainier, J. D. *J. Am. Chem. Soc.* **2010**, *132*, 8282–8284. <https://doi.org/10.1021/ja103428y>.
74. Shen, L.; Zhang, M.; Wu, Y.; Qin, Y. *Angew. Chem. Int. Ed.* **2008**, *47*, 3618–3621. <https://doi.org/10.1002/anie.200800566>.
75. Li, G.; Padwa, A. *Org. Lett.* **2011**, *13*, 3767–3769. <https://doi.org/10.1021/ol201320v>.
76. Leverett, C. A.; Li, G.; France, S.; Padwa, A. *J. Org. Chem.* **2016**, *81*, 10193–10203. <https://doi.org/10.1021/acs.joc.6b00771>.
77. Liu, P.; Wang, J.; Zhang, J.; Qiu, F. G. *Org. Lett.* **2011**, *13*, 6426–6428. <https://doi.org/10.1021/ol2027224>.
78. Yu, Y.; Li, G.; Jiang, L.; Zu, L. *Angew. Chem. Int. Ed.* **2015**, *54*, 12627–12631. <https://doi.org/10.1002/anie.201505173>.
79. Ji, W.; Yao, L.; Liao, X. *Org. Lett.* **2016**, *18*, 628–630. <https://doi.org/10.1021/acs.orglett.5b03421>.
80. Zhang, C.; Ji, W.; Liu, Y. A.; Song, C.; Liao, X. *J. Nat. Prod.* **2018**, *81*, 1065–1069. <https://doi.org/10.1021/acs.jnatprod.7b00873>.
81. Massiot, G.; Thépenier, P.; Jacquier, M.-J.; Le Men-Olivier, L.; Delaude, C. *Heterocycles* **1989**, *29*, 1435–1438. <https://doi.org/10.3987/COM-89-4987>.
82. Dounay, A. B.; Overman, L. E.; Wroblewski, A. D. *J. Am. Chem. Soc.* **2005**, *127*, 10186–10187. <https://doi.org/10.1021/ja0533895>.
83. Loiseleur, O.; Meier, P.; Pfaltz, A. *Angew. Chem. Int. Ed.* **1996**, *35*, 200–202. <https://doi.org/10.1002/anie.199602001>.
84. Zhang, Z.-X.; Chen, S.-C.; Jiao, L. *Angew. Chem. Int. Ed.* **2016**, *55*, 8090–8094. <https://doi.org/10.1002/anie.201602771>.
85. Jones, S. B.; Simmons, B.; MacMillan, D. W. C. *J. Am. Chem. Soc.* **2009**, *131*, 13606–13607. <https://doi.org/10.1021/ja906472m>.
86. Xie, W.; Jiang, G.; Liu, H.; Hu, J.; Pan, X.; Zhang, H.; Wan, X.; Lai, Y.; Ma, D. *Angew. Chem. Int. Ed.* **2013**, *52*, 12924–12927. <https://doi.org/10.1002/anie.201306774>.
87. Kim, J.; Ashenhurst, J. A.; Movassaghi, M. *Science* **2009**, *324*, 238–241. <https://doi.org/10.1126/science.1170777>.
88. Kim, J.; Movassaghi, M. *J. Am. Chem. Soc.* **2010**, *132*, 14376–14378. <https://doi.org/10.1021/ja106869s>.



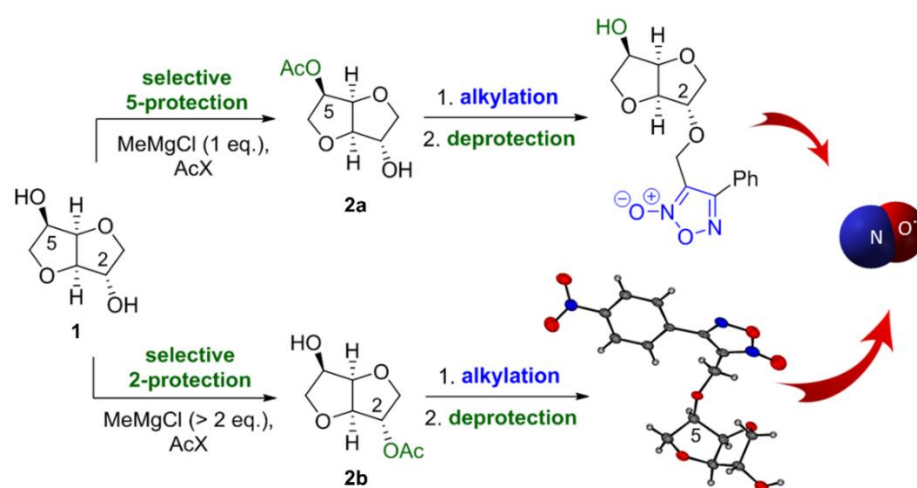
## Chapter 1

---

89. Movassaghi, M.; Schmidt, M. A. *Angew. Chem. Int. Ed.* **2007**, *46*, 3725–3728. <https://doi.org/10.1002/anie.200700705>.
90. Li, Q.; Xia, T.; Yao, L.; Deng, H.; Liao, X. *Chem. Sci.* **2015**, *6*, 3599–3605. <https://doi.org/10.1039/C5SC00338E>.
91. Deeks, E. D. *Drugs* **2014**, *74*, 99–125. <https://doi.org/10.1007/s40265-013-0159-3>.
92. Miller, J. F.; Andrews, C. W.; Brieger, M.; Furfine, E. S.; Hale, M. R.; Hanlon, M. H.; Hazen, R. J.; Kaldor, I.; McLean, E. W.; Reynolds, D.; Sammond, D. M.; Spaltenstein, A.; Tung, R.; Turner, E. M.; Xu, R. X.; Sherrill, R. G. *Bioorg. Med. Chem. Lett.* **2006**, *16*, 1788–1794. <https://doi.org/10.1016/j.bmcl.2006.01.035>.
93. Cihlar, T.; He, G.-X.; Liu, X.; Chen, J. M.; Hatada, M.; Swaminathan, S.; McDermott, M. J.; Yang, Z.-Y.; Mulato, A. S.; Chen, X.; Leavitt, S. A.; Stray, K. M.; Lee, W. A. *J. Mol. Biol.* **2006**, *363*, 635–647. <https://doi.org/10.1016/j.jmb.2006.07.073>.
94. Sevenich, A.; Liu, G.-Q.; Arduengo, A. J.; Gupton, B. F.; Opatz, T. *J. Org. Chem.* **2017**, *82*, 1218–1223. <https://doi.org/10.1021/acs.joc.6b02588>.
95. Liu, Z.; Sun, J.; Zhu, Y.; Liu, P.; Zhang, L.; Chen, J.; Huang, F.; Cao, Y. *Sci. China Chem.* **2015**, *58*, 267–275. <https://doi.org/10.1007/s11426-014-5223-7>.
96. Wada, Y.; Asada, Y.; Ikai, T.; Maeda, K.; Kuwabara, T.; Takahashi, K.; Kanoh, S. *ChemistrySelect* **2016**, *1*, 703–709. <https://doi.org/10.1002/slct.201600205>.
97. Peters, G. M.; Tovar, J. D. *J. Am. Chem. Soc.* **2019**, *141*, 3146–3152. <https://doi.org/10.1021/jacs.8b12617>.
98. Ikai, T.; Kojima, R.; Katori, S.; Yamamoto, T.; Kuwabara, T.; Maeda, K.; Takahashi, K.; Kanoh, S. *Polymer* **2015**, *56*, 171–177. <https://doi.org/10.1016/j.polymer.2014.11.033>.
99. Yamamoto, T.; Ikai, T.; Katori, S.; Kuwabara, T.; Maeda, K.; Koganezawa, T.; Takahashi, K.; Kanoh, S. *J. Polym. Sci., Part A: Polym. Chem.* **2015**, *53*, 1586–1593. <https://doi.org/10.1002/pola.27589>.
100. Li, Y.; Sonar, P.; Singh, S. P.; Soh, M. S.; van Meurs, M.; Tan, J. *J. Am. Chem. Soc.* **2011**, *133*, 2198–2204. <https://doi.org/10.1021/ja1085996>.
101. Saxon, D. J.; Nasiri, M.; Mandal, M.; Maduskar, S.; Dauenhauer, P. J.; Cramer, C. J.; LaPointe, A. M.; Reineke, T. M. *J. Am. Chem. Soc.* **2019**, *141*, 5107–5111. <https://doi.org/10.1021/jacs.9b00083>.

# Chapter 2

## Nitric Oxide Donor Furoxans *via* Methylmagnesium Chloride Mediated Acetylations of Isosorbide



Parts of this chapter are published in:

“Selective Methylmagnesium Chloride Mediated Acetylations of Isosorbide: A Route to Powerful Nitric Oxide Donor Furoxans”

Patrick Kielty, Dennis A. Smith, Peter Cannon, Michael P. Carty,  
Michael Kennedy, Patrick McArdle, Richard J. Singer  
and Fawaz Aldabbagh

*Organic Letters*, **2018**, *20*, 3025–3029

DOI: [10.1021/acs.orglett.8b01060](https://doi.org/10.1021/acs.orglett.8b01060)

## 2.1 Introduction

Nitric oxide (NO) is a gaseous free radical with myriad medical applications. Although useful when administered as a gas,<sup>1</sup> NO has found most application when released from donor molecules. NO has anti-cancer,<sup>2</sup> antibiotic<sup>3</sup> and wound healing properties,<sup>4</sup> but its greatest application is as a vasodilator.<sup>5,6</sup> Clinically available nitrate esters like nitroglycerin, pentaerythritol tetranitrate (**PETN**), isosorbide dinitrate (**IsDiN**) and isosorbide-5-mononitrate (**Is5N**) are prescribed to patients suffering from angina pectoris (Figure 2.1), where NO induces relaxation of vascular smooth muscle to reduce blood pressure.<sup>7,8</sup> NO release is triggered by thiol groups, either in the form of free thiol (cysteine), as part of an enzyme or as the glutathione cofactor of glutathione-*S*-transferase (GST).<sup>7,9</sup> Nitrate esters, however, are well-known explosives, raising safety concerns during manufacture.<sup>10</sup> **IsDiN**, a particularly hazardous side product in the synthesis of **Is5N**,<sup>11</sup> is mixed with lactose to enable safer handling and storage.<sup>12</sup>

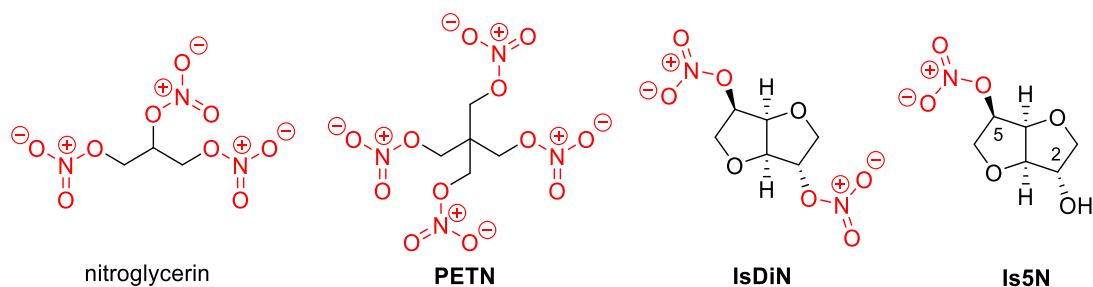


**Figure 2.1** Clinically available nitrate esters.

Furoxans (1,2,5-oxadiazole 2-oxides) are heralded as alternative NO-donors.<sup>13–19</sup> Cassella-Hoechst discovered **CAS 1609** (Figure 2.2) to be a potent and long-lasting vasodilator.<sup>14</sup> Over the same period of dosage, **Is5N** showed development of a significant amount of nitrate tolerance,<sup>17</sup> a common drawback among nitrate esters.<sup>9,20,21</sup> Similarly, phenylsulfonylfuroxan **CHF 2363** exerted a potent vasodilatory effect and strong inhibition of platelet aggregation.<sup>22</sup> Furoxans, too, have been designed as highly energetic molecules, with potassium 4,5-bis(dinitromethyl)furoxanate (**PBNF**) displaying high detonation performance as a green alternative to lead-based primary explosives.<sup>23</sup>

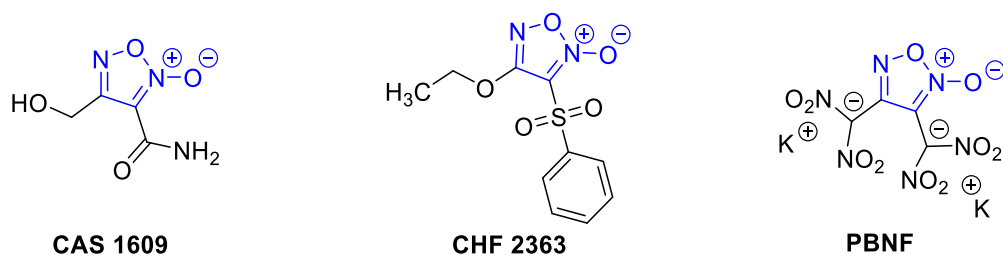
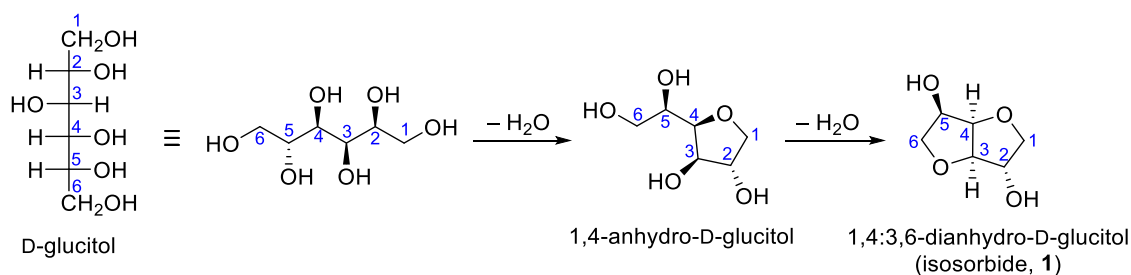


**Figure 2.2** Nitric oxide donor furoxans, **CAS 1609**<sup>14</sup> and **CHF 2363**,<sup>22</sup> and explosive **PBNF**.<sup>23</sup>

Isosorbide (**1**) is a renewable feedstock, produced *via* the double dehydration of D-glucitol,<sup>24</sup> which itself arises from the Raney-nickel catalysed hydrogenation of D-glucose.<sup>24,25</sup> “Isosorbide” is a trivial name and is not recommended by IUPAC, with “1,4:3,6-dianhydro-D-glucitol” assigned as the correct nomenclature. The parent alditol of isosorbide, D-glucitol, is named by changing the suffix “-ose” in the name of the corresponding aldose (glucose) to “-itol”. The first dehydration of D-glucitol forms 1,4-anhydro-D-glucitol, where “anhydro-“ denotes the loss of water, and the locants “1,4” identify the two hydroxyl groups involved in the elimination (Scheme 2.1). A second dehydration forms 1,4:3,6-dianhydro-D-glucitol (isosorbide) where the locants “3,6” denote the two hydroxyl groups involved in this second dehydration.



**Scheme 2.1** Double dehydration of D-glucitol in the production of isosorbide (**1**).

Apart from the nitrate esters, there are few valuable derivatives of **1** due to difficulties in selective functionalization and substitution at the 2- and 5-hydroxyl groups.<sup>26</sup> Selective 5-functionalization of isosorbide, **1**, remains a significant challenge due to the two non-equivalent *exo* 2-OH and *endo* 5-OH groups. The more nucleophilic nature of the 5-OH is attributed to activation *via* H-bonding with the oxygen of the adjacent cycle (Figure 2.3).<sup>27,28</sup>

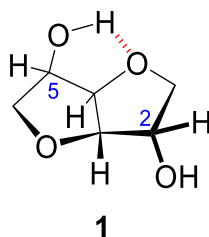
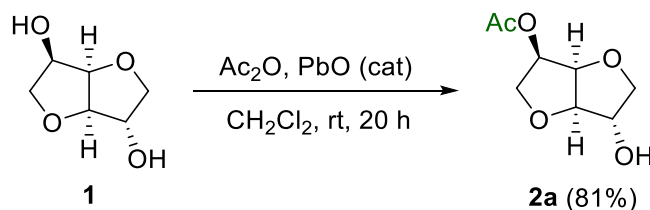


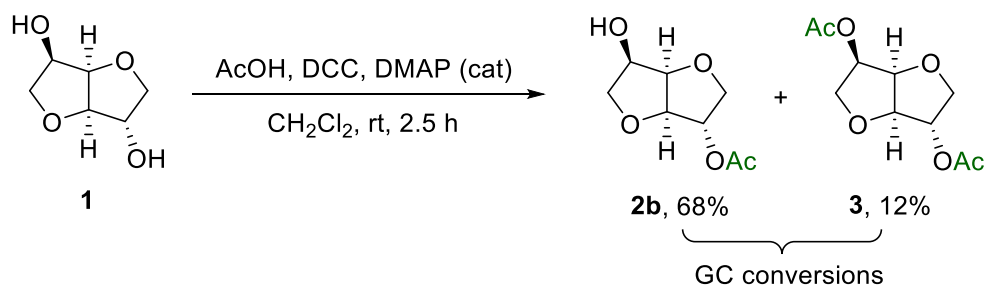
**Figure 2.3** Intramolecular hydrogen-bonding at the 5-OH of **1**.

Despite the difference in reactivity, base-mediated acetylations and alkylations are unreliable and low yielding, with the only reported selective acetylation of **1** using harmful PbO in Ac<sub>2</sub>O to give isosorbide-5-acetate (**2a**, Scheme 2.2).<sup>29,30</sup> A more recent metal-catalyzed method describes acetylation of **1** to give 54% yield of a 4.2 : 1 mixture of **2a** : isosorbide-2-acetate (**2b**) using Sc(OTf)<sub>3</sub> and Ac<sub>2</sub>O.<sup>31</sup> The non-catalyzed acetylation of **1** using Ac<sub>2</sub>O alone (1 equiv) at 120 °C gave poor selectivity of monoacetylation, with **2a** being marginally favoured (23% yield) over **2b** (14% yield).<sup>32</sup>



**Scheme 2.2** Lead-catalyzed synthesis of isosorbide-5-acetate **2a**.<sup>29,30</sup>

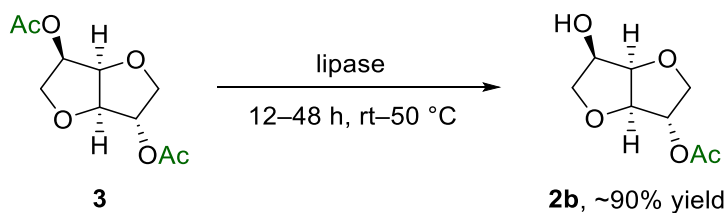
Previously reported syntheses of isosorbide-2-acetate **2b** are inadequately selective with significant draw-backs. Čeković and Tokić described a preparation of **2b** from **1** in 68% conversion by GC, but required the use of DCC coupling reagent with AcOH and DMAP, making for poor atom economy (Scheme 2.3).<sup>33</sup>



**Scheme 2.3** AcOH and DCC-mediated synthesis of isosorbide-2-acetate **2b**.<sup>33</sup>

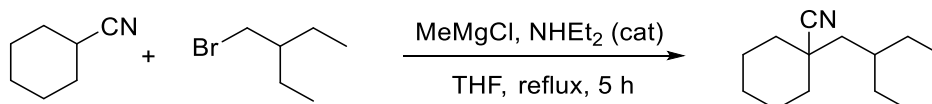
## Chapter 2

Stoss describes a procedure by which 85–95% pure **2b** may be obtained by distillation from an acid catalysed transesterification mixture of the isosorbide-acetates.<sup>34</sup> The method, however, requires access to low pressures (0.1 mbar) and the product purity depends on the quality of the fractional distillation column used and the reflux ratio. More specialized enzyme-mediated acetylation of **1**, and enzyme-mediated hydrolysis of isosorbide-2,5-diacetate **3** have been reported (Scheme 2.4).<sup>35–37</sup>



**Scheme 2.4** Enzyme-mediated synthesis of isosorbide-2-acetate **2b**.<sup>35–37</sup>

Inexpensive MeMgCl has found applications as a non-nucleophilic base, including in the Roche AG industrial deprotonation of diethylamine catalyst and subsequent  $\alpha$ -deprotonation of nitriles (Scheme 2.5).<sup>38</sup> The MeMgCl/diethylamine deprotonation strategy was more recently used for the insertion of up to two and three alkyl groups onto phenylacetonitrile and acetonitrile respectively.<sup>39</sup>

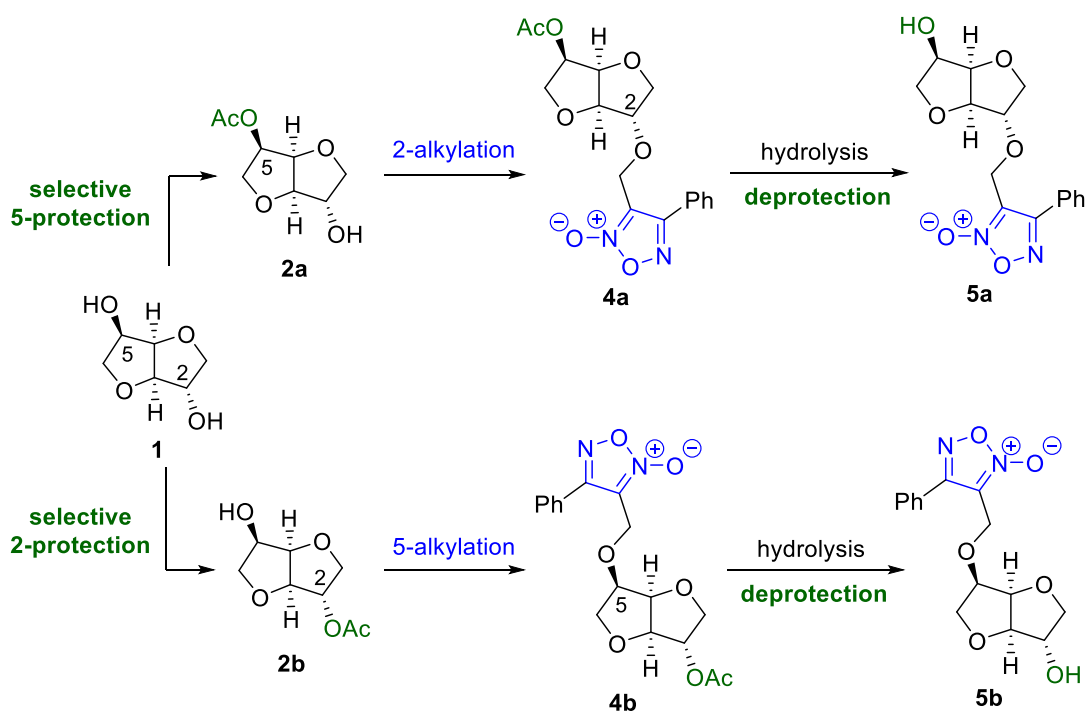


**Scheme 2.5** Roche AG patented MeMgCl-mediated deprotonation of cyclohexanecarbonitrile.<sup>38</sup>

## 2.2 Chapter Aims and Objectives

In this chapter, we aim to:

- Combine furoxan with isosorbide to give isosorbide-5-furoxan (**5a**) and its isomer, isosorbide-2-furoxan (**5b**). In doing so, we aim to provide a simple and selective MeMgCl-mediated acetylation protection-deprotection protocol for scaffold **1** (Scheme 2.6).
- Evaluate the rate and extent of NO release from isosorbide-furoxans and compare with the established drug, **Is5N**.
- Examine the thermal stability of isosorbide-furoxans and compare with **Is5N**.



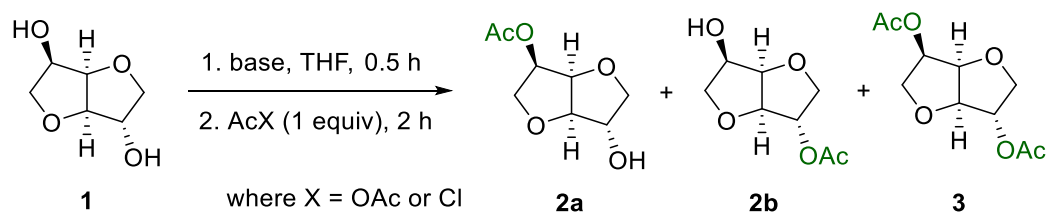
**Scheme 2.6** Protection-deprotection of isosorbide **1** allowing selective functionalization with furoxan.

## 2.3 Results and Discussion

### 2.3.1 Acetylation of isosorbide

NaH and *n*-BuLi in combination with Ac<sub>2</sub>O gave low conversions with little selectivity toward the 2- or 5-positions of isosorbide **1** (Table 2.1). MeMgCl (1.1 equiv) and Ac<sub>2</sub>O provided high conversion and selectivity for acetylation at the 5-position (as indicated by GC, Figure 2.4), with 5-acetate **2a** isolated in 73% yield. By simply increasing the amount of MeMgCl (> 2 equiv), a switch in selectivity of acetylation was achieved with the isomeric 2-acetate **2b** formed as the major product in a ratio of 45 : 1 over **2a**. Conversion was low, however, and replacing Ac<sub>2</sub>O with more reactive AcCl enabled near complete conversion of **1** to **2b** in 78% isolated yield, with trace levels (< 0.5%) of isomer **2a** detected by GC (Figure 2.5).

**Table 2.1** Optimizing the formation of **2a** and **2b**.



base (equiv)	AcX	temp	<b>1</b> (%) <sup>a</sup>	<b>2a</b> (%) <sup>b</sup>	<b>2b</b> (%) <sup>b</sup>	<b>3</b> (%) <sup>b</sup>
none	Ac <sub>2</sub> O	reflux	94	4	2	-
NaH (1.1)	Ac <sub>2</sub> O	reflux	47	30	8	15
NaH (2.8)	AcCl	0 °C	56	9	11	24
<i>n</i> -BuLi (1.1)	Ac <sub>2</sub> O	reflux	24	40	12	25
<i>n</i> -BuLi (2.0)	AcCl	0 °C	47	9	-	44
MeMgCl (1.1)	AcCl	reflux	24	52	7	17
MeMgCl (1.1)	Ac <sub>2</sub> O	0 °C	39	45	7	9
MeMgCl (1.1)	Ac <sub>2</sub> O	reflux	10	76 (73) <sup>c</sup>	2	13
MeMgCl (2.8)	Ac <sub>2</sub> O	reflux	43	1	45	11
MeMgCl (2.8)	AcCl	0 °C	6	-	82 (78) <sup>c</sup>	12

<sup>a</sup>Conversion determined by gravimetry (see experimental section). <sup>b</sup>Conversion determined by GC. <sup>c</sup>Isolated yield.



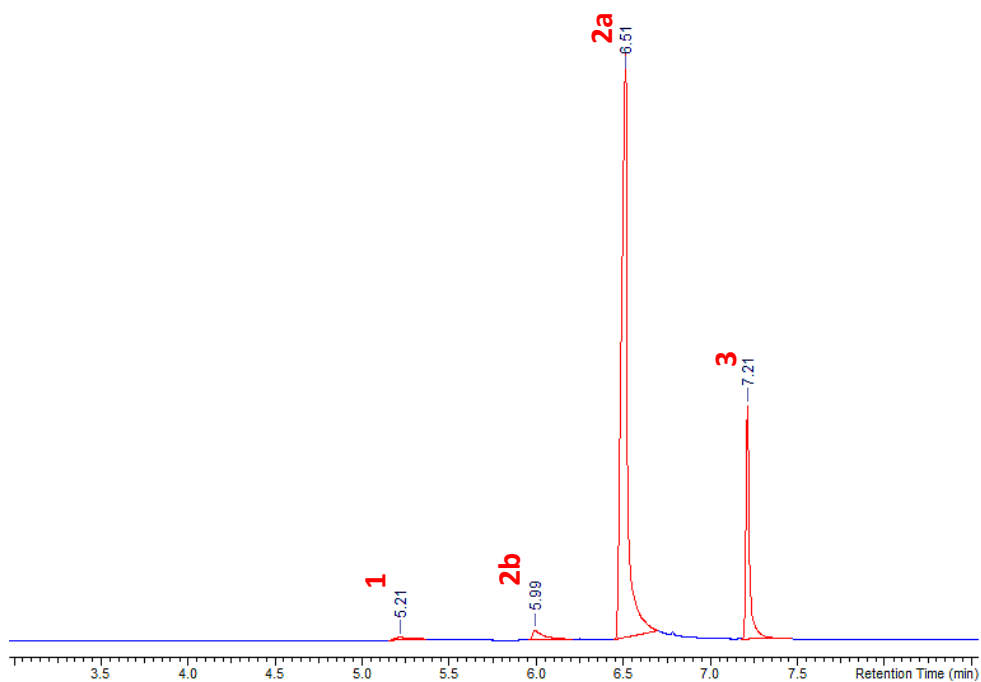


**Figure 2.4** GC chromatogram corresponding to the experiment using isosorbide **1** (1 equiv), MeMgCl (1.1 equiv) and Ac<sub>2</sub>O (1 equiv) at reflux for 2 h. **2a** conversion is 76%.

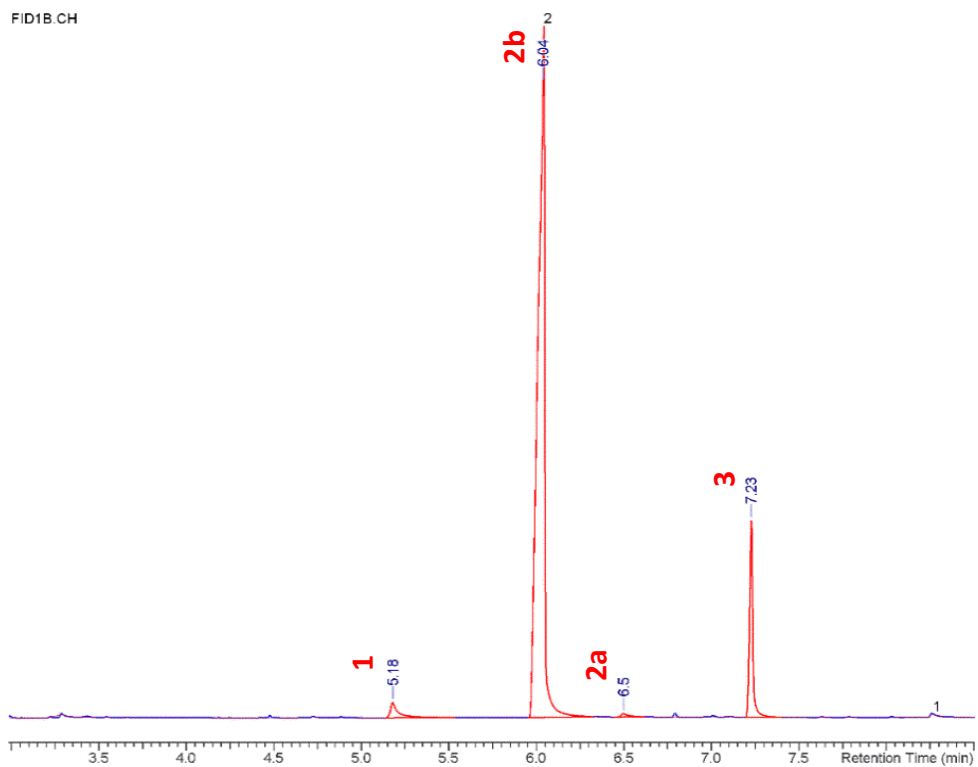
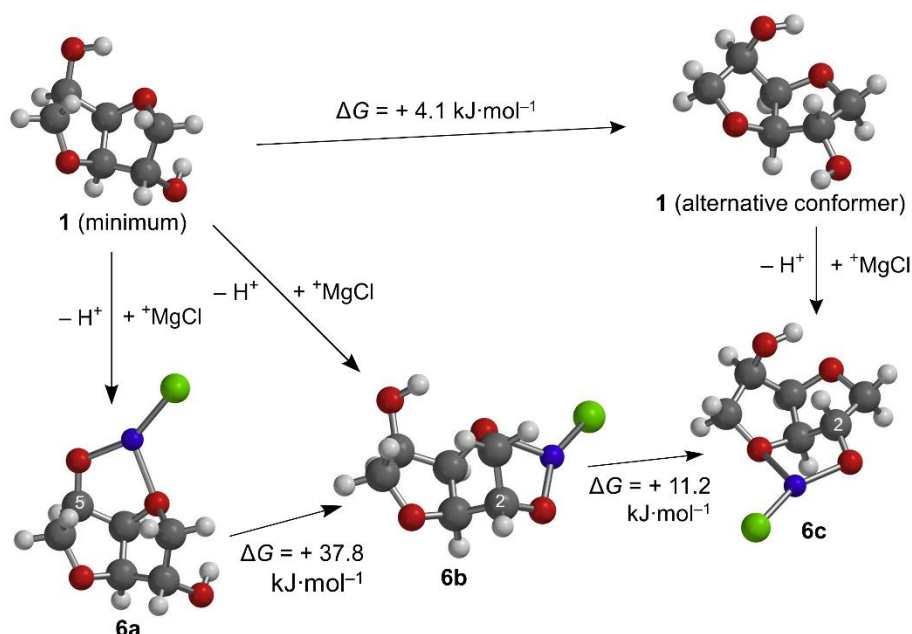


**Figure 2.5** GC chromatogram corresponding to the experiment using isosorbide **1** (1 equiv), MeMgCl (2.8 equiv) and AcCl (1 equiv) at 0 °C for 2 h. **2b** conversion is 82%.

DFT modelling was used to investigate this remarkable selectivity of deprotonation by comparing the stability of the  $^+\text{MgCl}$  complexes; isosorbide-5-alkoxide **6a** and 2-alkoxide **6c** (Scheme 2.7) formed through ethereal (THF-like)<sup>40,41</sup> chelation to the adjacent ring oxygen atom of isosorbide. DFT was carried out in the gas phase, since solvent effects (the role of THF) would not affect the relative energies of the observed isosorbide complexes. All model energies are given in Table A2.1 in the appendix. Two conformations of **1** were of interest; the minimum energy model and an alternative conformer 4.1 kJ·mol<sup>-1</sup> higher in energy. As previously reported,<sup>27,28</sup> H-bonding was observed between the 5-OH and the ethereal O atom of the adjacent ring, with the distance between the H atom and the acceptor ring-O atom measuring 2.13 and 2.05 Å for the minimum energy and alternative conformer respectively. The distance between the 2-OH donor and the closest ring-O acceptor was 2.60 and 3.20 Å for the minimum energy and alternative conformer respectively, suggesting that a weak H-bond at the 2-OH may be the source of the greater stability of the minimum energy structure. Starting from the minimum energy conformer **1**, coordination of the  $^+\text{MgCl}$  ion was preferred at the 5-alkoxide **6a** by 49.0 kJ·mol<sup>-1</sup> over the strained 2-alkoxide **6c**. The greater stability of **6a** arises from more effective  $^+\text{MgCl}$  coordination to the oxygen atom on the adjacent ring,



**Scheme 2.7** DFT of proposed alkoxide intermediates from the reaction of isosorbide **1** with  $\text{MeMgCl}$ . All geometry optimizations were performed using Gaussian 16W/GaussView 6 with DFT B3LYP functional in the gas phase and a 6-311G (2d,p) basis set. Mg and Cl atoms displayed in blue and green respectively.

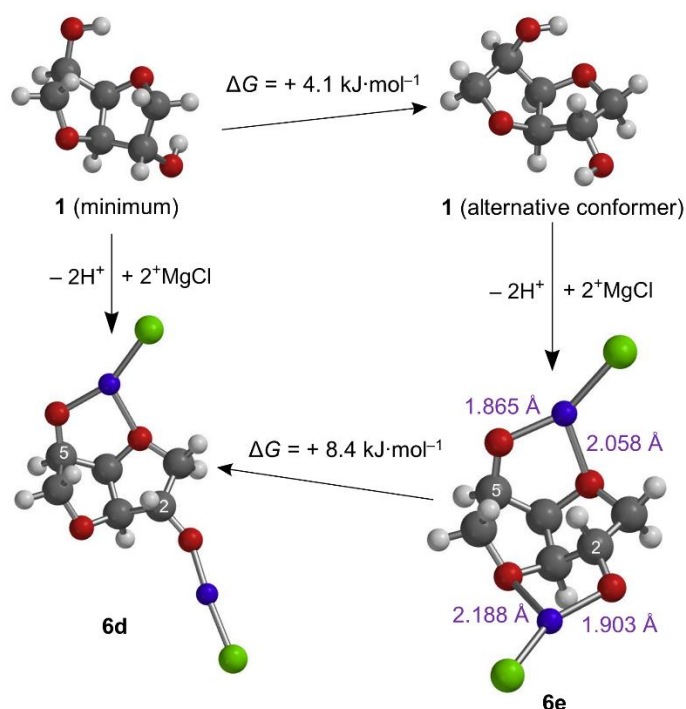
with steric hindrance from the isosorbide junction 3,4-hydrogens affecting coordination in complex **6c**. The energy minimum conformation of **1** preferentially gave 2-alkoxide complex **6b**, with ethereal  $^+\text{MgCl}$  coordination within the same ring, over 2-alkoxide **6c** by  $11.2 \text{ kJ}\cdot\text{mol}^{-1}$ . Moreover,  $^+\text{MgCl}$  coordination to 2-alkoxide **6c** was only possible using the higher energy alternative conformer of **1**. The enhanced stability of 5-alkoxide **6a** over 2-alkoxide complexes **6b** and **6c** was reflected in shorter  $\text{Mg}^+\cdots\text{OR}(\text{alkoxide})$  and  $\text{Mg}^+\cdots\text{OR}_2(\text{ether})$  bond distances (Table 2.2).

**Table 2.2** DFT model bond distances.

	$\text{Mg}^+\cdots\text{OR}$ distance ( $\text{\AA}$ ) <sup>a</sup>	$\text{Mg}^+\cdots\text{OR}_2$ distance ( $\text{\AA}$ ) <sup>b</sup>
<b>6a</b>	1.862	2.075
<b>6b</b>	1.872	2.167
<b>6c</b>	1.898	2.158

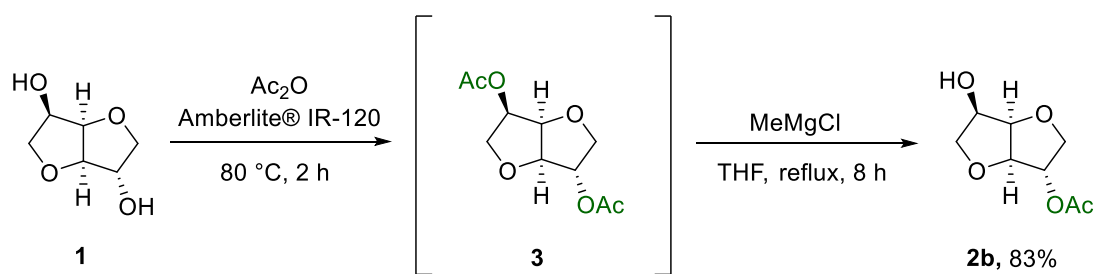
<sup>a</sup>Bond distance between  $\text{Mg}^+$  atom and  $\text{O}^-$  alkoxide atom (Scheme 2.7). <sup>b</sup>Bond distance between  $\text{Mg}^+$  atom and ethereal O atom of the adjacent/same ring (Scheme 2.7).

Upon addition of  $> 2$  equiv of  $\text{MeMgCl}$ , both the 2- and 5- OHs of **1** were deprotonated, and acetylation occurred at the less stable, more reactive 2-alkoxide, delivering a switch in selectivity to give **2b**. DFT modelling supported the greater stabilization of  $^+\text{MgCl}$  at the 5-alkoxide in the 2,5-dialkoxide complex with shorter bond lengths between  $\text{Mg}^+\cdots\text{OR}(\text{alkoxide})$  and  $\text{Mg}^+\cdots\text{OR}_2(\text{ether})$  compared with  $^+\text{MgCl}$  coordination at the 2-position (Scheme 2.8).



**Scheme 2.8** DFT models of dialkoxide complexes **6d** and the energy minimum **6e**. Bond lengths for **6e** are shown in purple, describing a more stable  $^+\text{MgCl}$  complex at the 5-alkoxide. Level of theory as described in Scheme 2.7.

Using the principle of forming the more thermodynamically stable  $^+\text{MgCl}$  intermediate (i.e. the 5-alkoxide, analogous to **6a**), a selective mono-deacetylation of isosorbide-2,5-diacetate **5** with  $\text{MeMgCl}$  (1.3 equiv) was carried out (Scheme 2.9). Demonstrating no apparent barriers to further scale-up, the multi-gram synthesis of isosorbide-2-acetate (**2b**) was achieved in 83% yield without the requirement for chromatography with diacetate **3** formed *in situ* from **1** using  $\text{Ac}_2\text{O}$  and Amberlite® IR-120 as an acid catalyst. Previously reported syntheses of **3** have used undesirable solvents like pyridine,<sup>42</sup> or required more harsh conditions (120 °C for 5 h).<sup>35</sup>



**Scheme 2.9** Synthesis of isosorbide-2-acetate, **2b**, via deacetylation of diacetate **3**.

DFT calculations validated the favourable deacetylation of the 5-acetate in **3**, giving rise to 5-alkoxide **6g**, which was energetically more stable than the equivalent 2-alkoxide **6f** by 66.5 kJ·mol<sup>-1</sup>. The shorter bond lengths between the Mg<sup>+</sup>···OR(alkoxide) and Mg<sup>+</sup>···OR<sub>2</sub>(ether) in **6f** vs **6g** complemented the observed trend in energy values (Figure 2.6).

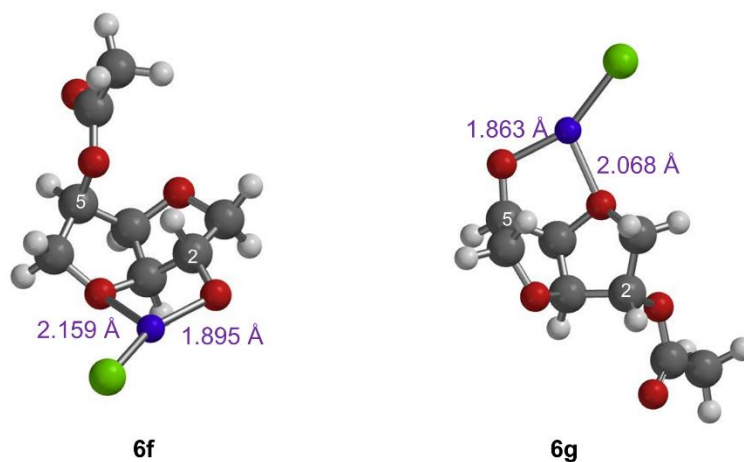
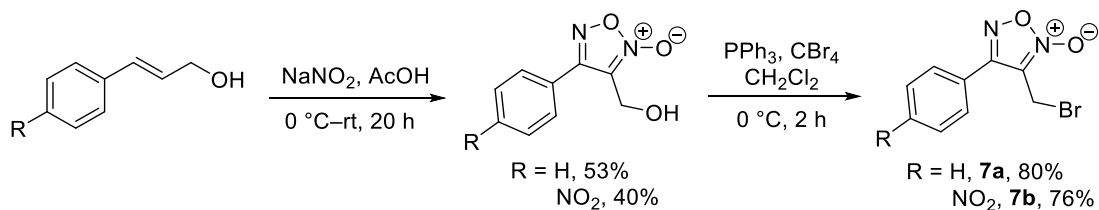


**Figure 2.6** DFT-optimized geometries of 5-acetate-2-alkoxide **6f** and 2-acetate-5-alkoxide **6g**. Level of theory as described in Scheme 2.7.

### 2.3.2 Functionalising isosorbide with furoxans

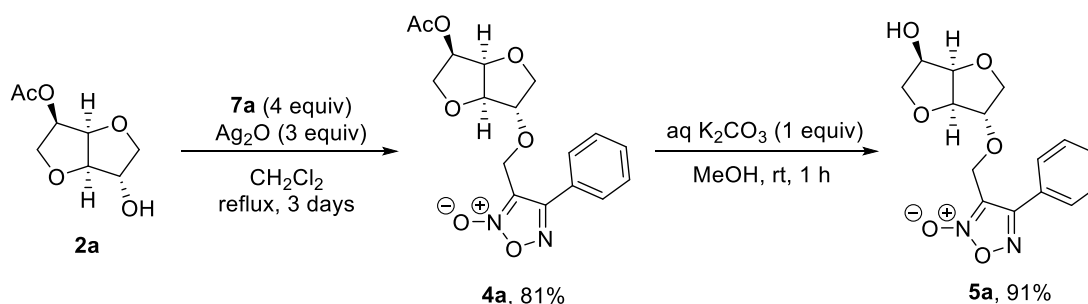
With the 2- or 5-positions on isosorbide effectively blocked through acetylation, functionalization of the available hydroxyl with furoxan was now possible. Furoxan electrophiles **7a-7b** were readily prepared in two steps from their respective cinnamyl alcohols (Scheme 2.10). (2-Oxido-4-phenyl-1,2,5-oxadiazol-3-yl)methanol was prepared as reported by Hopf *et al.*<sup>43</sup> [4-(4-Nitrophenyl)-2-oxido-1,2,5-oxadiazol-3-yl]methanol was prepared in 40% yield by reaction of 4-nitrocinnamyl alcohol with NaNO<sub>2</sub> (3.5 equiv) for 16 h, which was a modification of the procedure by Schiefer *et al.*<sup>18</sup> 3-(Bromomethyl)-2-oxido-4-phenyl-1,2,5-oxadiazole (**7a**) was synthesized by Tang *et al.* in 85% yield from the methanol-substituted furoxan using PBr<sub>3</sub> and imidazole in CH<sub>2</sub>Cl<sub>2</sub>.<sup>19</sup> In our hands, **7a** was prepared in comparable yield *via* the facile Appel reaction, as was the novel furoxan electrophile, 3-(bromomethyl)-4-(4-nitrophenyl)-2-oxido-1,2,5-oxadiazole (**7b**).

## Chapter 2



**Scheme 2.10** Synthesis of furoxan electrophiles from cinnamyl alcohols.

Alkylation of isosorbide-2- and 5-acetate with the furoxan bromides **7a** and **7b** was mediated by Ag<sub>2</sub>O. The traditional Williamson ether synthesis using NaH was not feasible due to the sensitivity of acetate groups to strongly basic conditions.<sup>44</sup> Reaction of 5-acetate **2a** with bromide **7a** yielded isosorbide-5-acetate-2-furoxan **4a** in 81% yield (Scheme 2.11) with furoxan attachment at the *exo*-position confirmed by X-ray crystallography (Figure 2.7). Deprotection of 5-acetate **4a** through basic hydrolysis afforded isosorbide-2-furoxan **5a** in 91% yield.



**Scheme 2.11** Synthesis of isosorbide-2-furoxan **5a** from isosorbide-5-acetate **2a**.

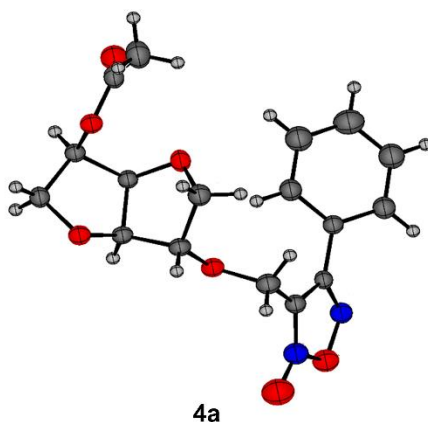
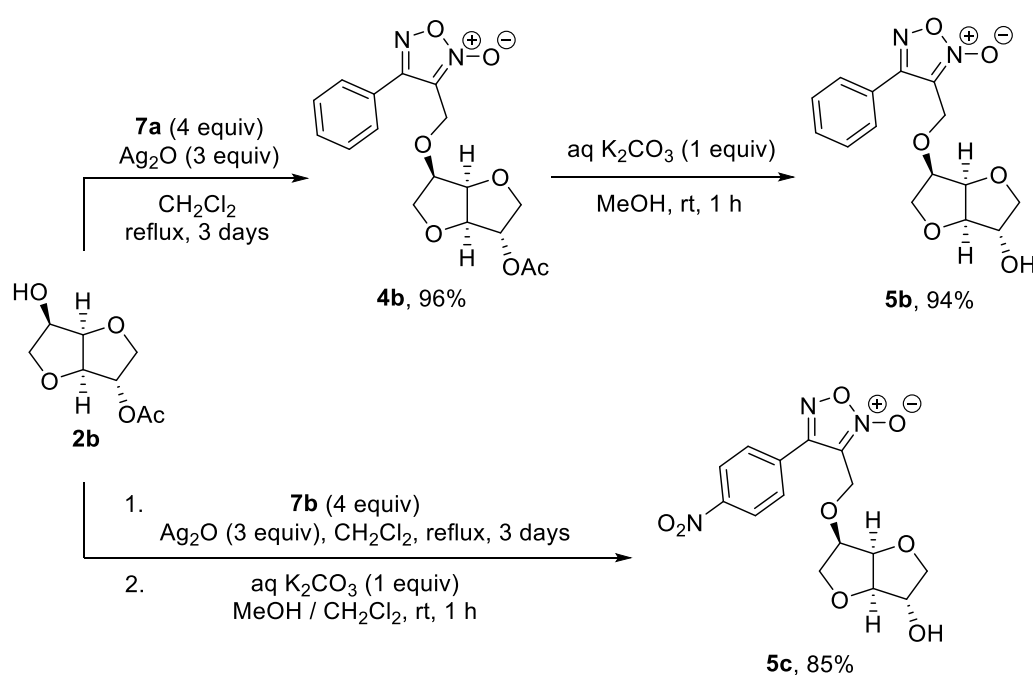


**Figure 2.7** X-ray crystal structure of isosorbide-2-acetate-5-furoxan **4a**.

Similarly, synthesis of furoxan isomer **5b** from 2-acetate **2b** via isosorbide-2-acetate-5-furoxan **4b** occurred in an overall 90% yield over two steps of alkylation and deprotection (Scheme 2.12). It is known that NO production can be increased by substituting the furoxan ring with electron-withdrawing groups, such as nitrobenzene, which effectively increase susceptibility to addition of activating thiols (such as cysteine).<sup>15</sup> Therefore, in a quest to increase the activity of isosorbide-5-furoxan, the preparation of *p*-nitro derivative **5c** was carried out from isosorbide-2-acetate **2b** and bromide **7b** (Scheme 2.12). *p*-Nitrophenyl-substituted furoxan **5c** was isolated in 85% yield without the requirement for isolation of the intermediate isosorbide-2-acetate-5-furoxan.



**Scheme 2.12** Synthesis of isosorbide-5-furoxans **5b** and **5c** from isosorbide-2-acetate **2b**.

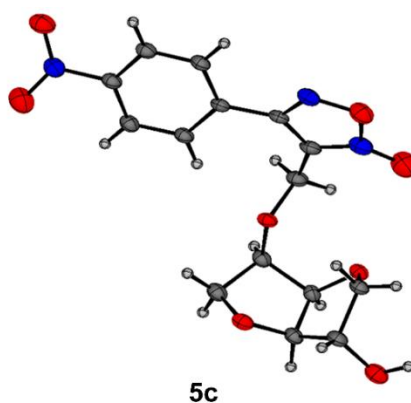
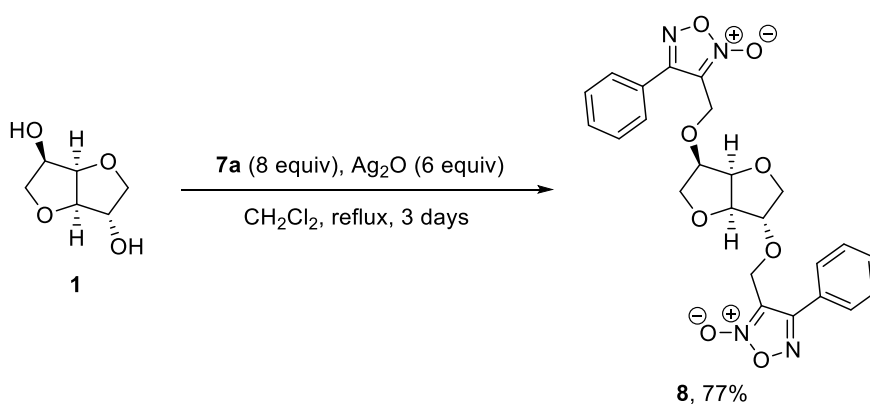


**Figure 2.8** X-ray crystal structure depicting one of the two molecules in the asymmetric unit cell of isosorbide-5-furoxan **5c**.

## Chapter 2

To further increase the level of NO-release, isosorbide was functionalized with two furoxan moieties. The preparation of isosorbide-2,5-difuroxan **8** was achieved in 77% isolated yield by facile alkylation of **1** with **7a** in the presence of Ag<sub>2</sub>O (Scheme 2.13). The X-ray crystal structure of bis-adduct **8** was obtained (Figure 2.9), and like the other two crystal structures (of **4a** and **5c**) provided a clear visual representation of the 2-*exo* and 5-*endo* isosorbide attachments (Figures 2.7–2.9). H-bonding in the lattice only occurred in **5c** (illustrated by the dashed bonds in Figure A2.1 in the appendix) due to the isosorbide hydroxyl being deacetylated.



**Scheme 2.13** Synthesis of isosorbide-2,5-difuroxan **8**.

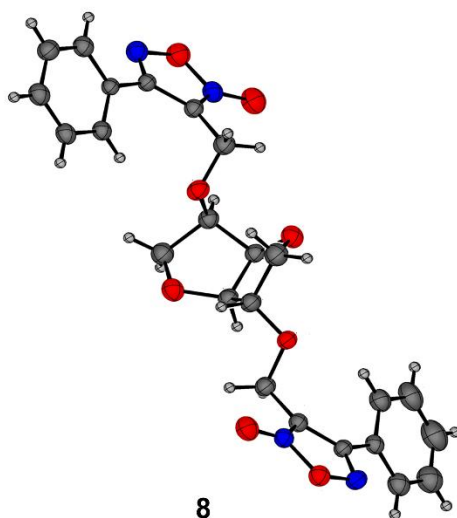
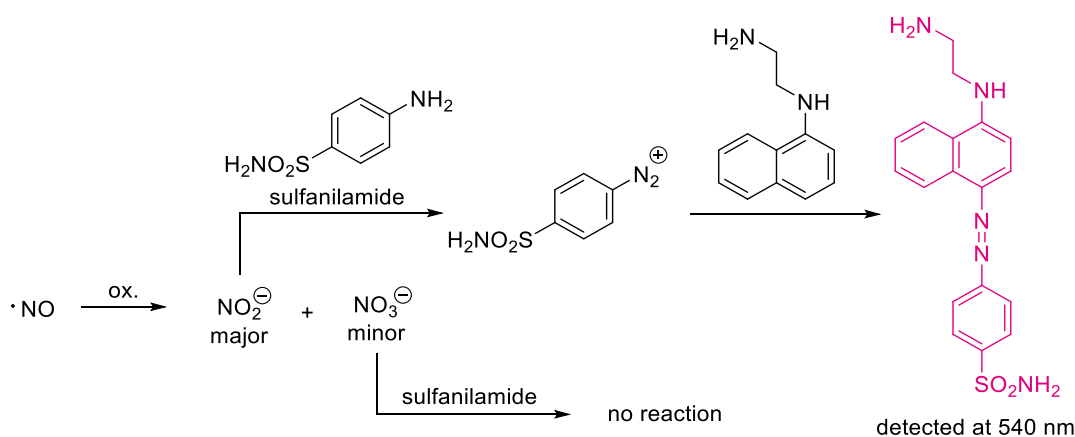


**Figure 2.9** X-ray crystal structure of isosorbide-2,5-difuroxan **8**.



### 2.3.3 Nitric oxide (NO) release studies

NO-release from our isosorbide furoxans was quantitatively measured along with that of the commercial vasodilator, **Is5N**. Furoxans have long been known to release NO upon reaction with thiols, including cysteine.<sup>13,16</sup> DFT calculations supported the addition of a sulfanyl radical onto the C=N bond of the furoxan followed by expulsion of NO,<sup>45</sup> although others give alternative thiolate addition mechanisms,<sup>13,16</sup> which are energetically less favourable.<sup>45</sup> NO-release holds a reasonable correlation with vascular tissue relaxation in a series of furoxans.<sup>13,16,17</sup> NO is, however, never measured directly due to rapid oxidation in aqueous and biological fluids to nitrite ( $\text{NO}_2^-$ ) and nitrate ( $\text{NO}_3^-$ ).<sup>13,16,18</sup> The amount of NO released is commonly evaluated through  $\text{NO}_2^-$  measurement using the Griess assay (Scheme 2.14),<sup>46</sup> in the presence of excess cysteine with the amount of  $\text{NO}_3^-$  produced deemed less significant. Using this approach,  $\text{NO}_2^-$  production from isosorbide-furoxans **4a**, **5a–5c** and **8** was quantitatively monitored by regular sampling (Figure 2.10), which indicated a 3–7.5 fold greater rate of release than **Is5N** ( $k_{\text{obs}}$ , Table 2.3). After 12 h a significant slowdown for most furoxans was observed, apart from isosorbide-2,5-difuroxan **8**, which sustained NO-release over a longer period. This plateau allowed measurement of the extent of  $\text{NO}_2^-$  production after 24 hours (Table 2.3).



**Scheme 2.14** Griess assay for detection of  $\text{NO}_2^-$  arising from NO.

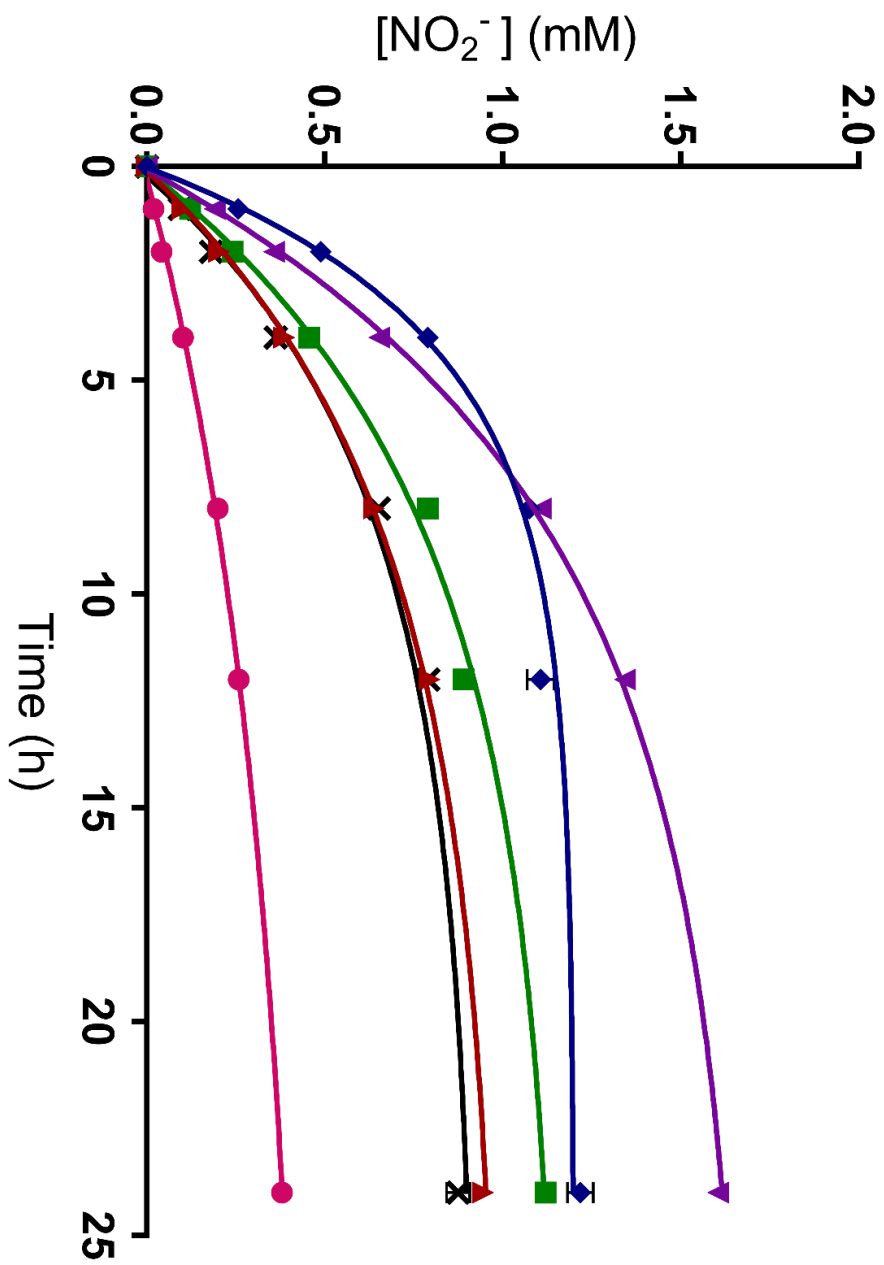


**Figure 2.10** Kinetics of  $\text{NO}_2^-$  production from 2 mM solutions of **4a** (—\*), **5a** (—■), **5b** (—□), **5c** (—◇), **8** (—▽) and **Is5N** (—●). Exponential lines of best fit were plotted using GraphPad Prism® software.

**Table 2.3** Extent and rate of NO release.

NO donor	NO <sub>2</sub> <sup>-</sup> produced (mol %) <sup>a</sup>	NO <sub>2</sub> <sup>-</sup> + NO <sub>3</sub> <sup>-</sup> produced (mol %) <sup>b</sup>	<i>k</i> <sub>obs</sub> (h <sup>-1</sup> ) <sup>c</sup>
<b>4a</b>	43.8 ± 1.7	45.2 ± 1.6	0.081
<b>5a</b>	56.0 ± 1.0	61.7 ± 3.5	0.098
<b>5b</b>	47.3 ± 1.4	47.4 ± 0.7	0.079
<b>5c</b>	60.9 ± 1.8	67.5 ± 1.6	0.195
<b>8</b>	80.3 ± 1.1	94.5 ± 4.0	0.136
<b>Is5N</b>	19.0 ± 0.6	19.0 ± 1.2	0.026

<sup>a</sup>Determined by Griess assay after 24 h incubation of 2.0 mM solutions with excess L-cysteine at 37 °C. <sup>b</sup>Samples of solutions after 24 h incubated with nitrate reductase prior to performing Griess assay. <sup>c</sup>Rate constant (*k*<sub>obs</sub>) for NO<sub>2</sub><sup>-</sup> production calculated by linear regression analysis of 0–4 h data points for **5c** and 0–8 h data points for all other compounds in Figure 2.10.

A thorough approach was used with combined NO<sub>2</sub><sup>-</sup> and NO<sub>3</sub><sup>-</sup> measured. Nowadays, this is possible using a commercially available colorimetric assay that measures total available NO<sub>2</sub><sup>-</sup> after reduction of NO<sub>3</sub><sup>-</sup> to NO<sub>2</sub><sup>-</sup> by NADPH in the presence of the enzyme, nitrate reductase.<sup>47</sup> Moreover, NO<sub>3</sub><sup>-</sup> levels were significant for some furoxans (Table 2.3), especially the most reactive compounds, highlighting the need for analysis. The *p*-nitrophenyl-substituted derivative furoxan **5c** had a significantly higher rate of NO-release, with this compound being the most active, with 2–2.5 times greater rate of NO<sub>2</sub><sup>-</sup> production compared to isosorbide-2- and 5-furoxans **5a** and **5b**. High concentrations of NO have been related to anti-cancer activity for some furoxans.<sup>48,49</sup> The acetate group of **4a** appeared to hinder NO-release with a slower rate, as well as a smaller total amount of NO produced compared to its hydrolyzed derivative **5a**. As expected, substituting both available hydroxyls on isosorbide with furoxan in **8** almost doubled the extent of NO production, but the rate of NO-release was below that of the most reactive mono-substituted isosorbide furoxan **5c**. Isosorbide-2-furoxan **5a** gave higher levels of NO-release compared to its isomer **5b**, and pharmacologically they would be expected to behave differently as shown by the drug **Is5N**, which is less potent than isosorbide-2-mononitrate (**Is2N**), as a vasodilator.<sup>50</sup>

### 2.3.4 Thermal degradation studies

As a useful predictor of the explosive potential of isosorbide-2-furoxan (**5a**) and isosorbide-5-furoxan (**5b**), the oxygen balance test was performed, based solely on the molecular formula of the compound of interest (Equation 2.1, below).<sup>51</sup> The test was

## Chapter 2

formulated in 1949 by Lothrop and Handrick, who drew upon the large volume of quantitative data collected from explosive research during World War II.<sup>52</sup> It describes

$$\text{Oxygen Balance} = \frac{[-1600(2x - \frac{y}{2} - z)]}{M_w} \quad \text{for } C_xH_yNO_z \quad (2.1)$$

the ability of a compound to self-oxidize, with a value of zero indicating that there is the perfect amount of C, O and H atoms present to form CO<sub>2</sub> and H<sub>2</sub>O upon degradation. Negative values imply that there is an insufficient amount of oxidizing atoms and an external oxidant is required for decomposition. Compounds having an oxygen balance around zero, specifically between + 80 and – 120, are deemed high risk explosives.<sup>51</sup> Indeed, the value for **Is5N**, – 88, lies within this hazardous range. Replacement of the nitrate group on **Is5N** with furoxan brings the oxygen balance outside of the hazardous range to – 160. As a comparison, the furoxan **PBNF**, designed as a primary explosive,<sup>23</sup> has an oxygen balance of + 4.3, implying almost perfect self-oxidation and powerful explosivity.

Differential Scanning Calorimetry (DSC) was used for assessment of thermally induced energy release,<sup>53</sup> which allows deductions regarding safe handling in comparison with **Is5N**, which is classified as an explosive.<sup>54</sup> The onset temperature for thermal degradation of phenyl furoxans (**5a**, **5b** and **8**) is less accessible at 66–94 °C above that of **Is5N** (Table 2.4). Similarly, the degradation exotherms peaked 61–73 °C above that of **Is5N**. The energy released from such exothermic events was lower for the phenyl furoxans by 1086–1614 J/g. The most active NO-releasing furoxan, *p*-nitrophenyl furoxan **5c** is safer than **Is5N** with a significantly higher onset and peak temperature by almost 32 °C and 41 °C respectively, and with an energy release 1099 J/g lower.

**Table 2.4** Thermal degradation.<sup>a</sup>

NO donor	onset temp (°C) <sup>b</sup>	peak temp (°C) <sup>c</sup>	energy release (J/g) <sup>d</sup>
5a	231.0	271.8	1122.0
5b	202.9	261.4	1474.5
5c	168.3	241.7	1636.9
8	217.9	273.7	1649.5
Is5N	136.7	200.4	2735.8

<sup>a</sup>DSC was performed using 1.7–4.6 mg of samples in a high pressure crucible, heating at 5 °C/min. <sup>b</sup>Temperature at which the exothermic event begins. <sup>c</sup>Temperature of maximal heat release. <sup>d</sup>Calculated by integration.

### 2.4 Conclusions

Inexpensive MeMgCl-mediated acetylation has afforded an effective and simple protection-deprotection for both hydroxyls of isosorbide. The switch in selectivity was achieved by altering the stoichiometry of MeMgCl. DFT investigations concluded that a more favorable stabilization of the Mg cation at the 5-position of isosorbide was central to the observed selectivity. Subsequent functionalization with furoxan gave powerful nitric oxide donors with vastly higher rates and amounts of NO<sub>x</sub> produced compared to the commercial vasodilator, **Is5N**. Despite the enhanced rate of cysteine-induced NO-release, isosorbide-furoxans are safer to handle than **Is5N**. The research in this chapter was published in Organic Letters in 2018.<sup>55</sup>

### 2.5 Future Work

The vasodilatory effects of the isosorbide-furoxans compared to **Is5N** will be assessed by measuring the relaxation of pre-contracted endothelium denuded strips of rat aorta. The NO dependence of any effects observed will be evaluated in the presence of NO scavengers such as oxyhaemoglobin. The isosorbide protection strategy disclosed is of interest to our funding partners, Avara Pharmaceutical Services Ltd, and the selective synthesis of isosorbide-2-acetate is considered to be the key step in an improved industrial synthesis of the currently marketed drug, **Is5N**.

### 2.6 Experimental

#### 2.6.1 Materials

Isosorbide **1** was used as received from Avara Pharmaceutical Services, Shannon, Ireland. All other solvents and reagents were used as received from Sigma-Aldrich. MeMgCl was used as received as a 3 M solution in THF. THF was freshly distilled over Na/benzophenone. CH<sub>2</sub>Cl<sub>2</sub> was freshly distilled over CaH<sub>2</sub>. (2-Oxido-4-phenyl-1,2,5-oxadiazol-3-yl)methanol was prepared as reported by Hopf *et al.*<sup>43</sup> [4-(4-Nitrophenyl)-2-oxido-1,2,5-oxadiazol-3-yl]methanol was prepared in 40% yield by reaction of 4-nitrocinnamyl alcohol with NaNO<sub>2</sub> (3.5 equiv) for 16 h, which was a modification of the procedure by Schiefer *et al.*<sup>18</sup> 3-(Bromomethyl)-2-oxido-4-phenyl-1,2,5-oxadiazole (**7a**) was reported by Tang *et al.*,<sup>19</sup> but was prepared in the same manner as 3-(bromomethyl)-4-(4-nitrophenyl)-2-oxido-1,2,5-oxadiazole (**7b**), detailed below. Thin layer chromatography (TLC) was performed on Merck TLC Silica gel 60 F<sub>254</sub> plates using a UV lamp for visualization. For TLC analytes lacking UV activity (**1**, **2a**, **2b**, **3**), staining was performed by spraying a solution of H<sub>2</sub>SO<sub>4</sub> (10% v/v in MeOH) followed by brief heating. Column chromatography was performed using silica gel, pore size 60 Å, 230–400 mesh particle size, 40–63 µm particle size. NO release was measured using Nitrite/Nitrate Assay Kit, which was used as received from Sigma-Aldrich.

#### 2.6.2 Measurements

**DFT calculations:** All geometry optimisations were performed using Gaussian 16W/GaussView 6,<sup>56</sup> which was performed with DFT B3LYP functional and a 6-311G (2d,p) basis set on a Windows 10 PC. Model images were rendered in Spartan® software.<sup>57</sup> Formation of <sup>+</sup>MgCl complexes to the two lowest energy conformations of isosorbide alkoxides were explored. Model energies are reported in Table A2.1 in the appendix.

**Gas chromatography (GC) and conversion measurements:** GC analysis was performed on an Agilent 6890 equipped with FID (flame ionization detector) operating at 250 °C with air flow and H<sub>2</sub> flow set to 200 and 30 mL/min respectively. The stationary phase consisted of a HP-5, 30 m, ID 0.25 mm, film thickness 0.25 µm column. Helium was used as carrier gas at a flow rate of 1.2 mL/min. The injector was heated at 160 °C and the column oven followed the below temperature program.

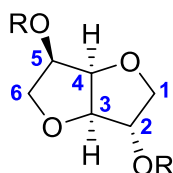
## Chapter 2

heating rate (°C/min)	temperature (°C)	hold time (min)	run time (min)
0.00	100	2.00	2.00
20.00	220	0.00	8.00
40.00	300	2.00	12.00

GC was used for analysis of acetylation reaction mixtures (Table 2.1, Figure 2.4 and 2.5). The difference in detector response between each of the four analytes, **1**, **2a**, **2b** and **3**, was deemed insignificant from analysis of equal weight mixtures allowing conversions to be taken directly from integration percent reports. As a hydrophilic diol, **1** was soluble in the aqueous layer upon acidic workup. GC analysis was performed on the organic extracts and only trace amounts of **1** were detected. The amount of unreacted **1** (content of **1** in both phases) was deduced from the observed yield following evaporation of organic extracts.

**Melting point and infrared spectroscopy:** Melting points were measured on a Stuart Scientific melting point apparatus SMP1. Infrared spectra were recorded using a Perkin-Elmer Spec 1 with ATR attached.

**Nuclear magnetic resonance (NMR spectroscopy):** NMR spectra were recorded using a JEOL ECX 400 MHz instrument equipped with a DEC AXP 300 computer workstation. The chemical shifts were recorded in ppm relative to SiMe<sub>4</sub>. <sup>13</sup>C NMR data were collected at 100 MHz with complete proton decoupling. NMR assignments were supported by DEPT and <sup>1</sup>H-<sup>1</sup>H and <sup>1</sup>H-<sup>13</sup>C correlation. Hydroxyl peaks were confirmed by D<sub>2</sub>O exchange. Characterizations are given according to the numbering of isosorbide below.



In the <sup>1</sup>H NMR, there was no observed coupling between H-2 and H-3, since the dihedral angle is close to 90°. The H-2 and H-3 dihedral angle within the energy minimum conformer of **1** derived from DFT was estimated as 83.0°. For the same reason, there was no observed coupling between H-2 and one of the CH<sub>2</sub>-1 hydrogen atoms, since the dihedral angle is 85.0°. NMR spectra are available on the ACS Publications website at <https://doi.org/10.1021/acs.orglett.8b01060>.<sup>55</sup>

## Chapter 2

---

**High resolution mass spectrometry (HRMS):** HRMS was carried out using ESI time-of-flight mass spectrometer (TOFMS) in positive or negative mode using a Waters LCT Mass Spectrometry instrument. The precision of all accurate mass measurements was better than 5 ppm. In the case of **7b**, the formic acid adduct  $[M + \text{CH}_2\text{O}_2 - \text{H}]^-$  was formed due to the presence of formic acid used to aid protonation in ESI in the mobile phase.

**Single crystal X-ray diffraction:** Single crystal data was collected using an Oxford Diffraction Xcalibur system operated using the CrysAlisPro software and the data collection temperature was controlled at 150 K using a Cryojet system from Rigaku Oxford Diffraction. The crystal structures were solved using ShelxT version 2014/5,<sup>58</sup> and refined using ShelxL version 2017/1,<sup>59</sup> both of which were operated within the Oscale software package.<sup>60</sup> Crystallographic data for compounds **4a**, **5c** and **8** have been deposited with the Cambridge Crystallographic Data Centre with deposit numbers CCDC 1830485, CCDC 1830483, and CCDC 1830484 respectively. This data is available free of charge *via* [www.ccdc.cam.ac.uk/data\\_request/cif](http://www.ccdc.cam.ac.uk/data_request/cif) (or from the Cambridge Crystallographic Data Centre, 12 Union Road, Cambridge CB2 1EZ, U.K.; fax +44 1223 336033; or e-mail [deposit@ccdc.cam.ac.uk](mailto:deposit@ccdc.cam.ac.uk)).

**NO release:** *Quantification of  $[\text{NO}_2^-]$*  Griess reagent was prepared by making a solution of sulfanilamide (2.00 g, 11.6 mmol), *N*-(1-naphthyl)ethylenediamine dihydrochloride (0.10 g, 0.39 mmol), and  $\text{H}_3\text{PO}_4$  (5 mL, 85%) up to 50 mL using phosphate buffer solution (pH 7.4, 50 mM). NO release was induced by addition of isosorbide-furoxan or **Is5N** (200  $\mu\text{L}$ , 4 mM) in MeCN to L-cysteine (200  $\mu\text{L}$ , 200 mM) in phosphate buffer solution (pH 7.4, 50 mM). The solution was incubated at 37 °C for 24 h. Aliquots (4  $\mu\text{L}$ ) were taken in triplicate at various time intervals and diluted to 100  $\mu\text{L}$  using phosphate buffer solution in a 96 well plate. The Griess reagent above (100  $\mu\text{L}$ ) was added, the solution agitated, and incubated at room temperature for 10 min.  $[\text{NO}_2^-]$  was quantified by measuring absorbance at 540 nm using a Biotek Powerwave XS2 plate reader. A  $[\text{NO}_2^-]$  calibration curve was plotted by triplicate analysis of standard solutions of  $\text{NaNO}_2$  (0-80  $\mu\text{M}$ ) in phosphate buffer solution.  $\text{NO}_2^-$  production was not observed in the absence of L-cysteine.

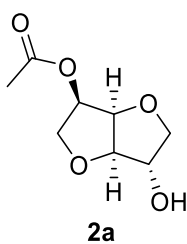
*Quantification of  $[\text{NO}_3^- + \text{NO}_2^-]$  (total  $[\text{NO}]$ )* After 24 h incubation of samples described above, an aliquot (4  $\mu\text{L}$ ) of the sample was diluted to 80  $\mu\text{L}$  using phosphate buffer solution (pH 7.4, 50 mM) followed by addition of nitrate reductase and enzyme



cofactor (10  $\mu\text{L}$  of each, prepared according to manufacturer's instruction) in a 96 well plate in triplicate. The solution was agitated then incubated at 25  $^{\circ}\text{C}$  for 2 h, according to manufacturer's instruction. Griess reagent (100  $\mu\text{L}$ , as prepared above) was added, the solution agitated then incubated at room temperature for 10 min. The absorbance was measured as above. The value obtained corresponds to  $[\text{NO}_2^- + \text{NO}_3^-]$ . A  $[\text{NO}_2^- + \text{NO}_3^-]$  calibration curve was plotted by triplicate analysis of standard solutions of  $\text{NaNO}_3$  (0–80  $\mu\text{M}$ ) in phosphate buffer solution with nitrate reductase and enzyme cofactor (10  $\mu\text{L}$  of each) following incubation at 25  $^{\circ}\text{C}$  for 2 h. A series of control experiments involving incubation of nitrate reductase and enzyme cofactor with isosorbide-furoxan/**Is5N** in the absence of L-cysteine resulted in no detectable NO release from the test compounds. The small amounts of MeCN used during the enzyme assay did not inhibit the action of nitrate reductase, as confirmed in a  $\text{NaNO}_3$  reduction experiment performed in the presence of MeCN, and in the absence of MeCN.

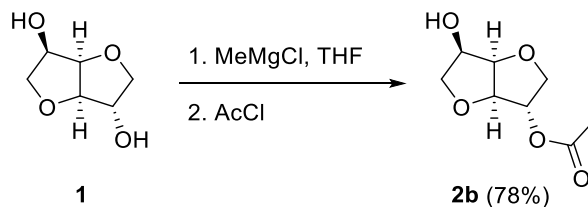
**Thermal stability:** Differential scanning calorimetry (DSC) was performed on a Mettler TA 4000 using high pressure crucible cells. Samples of 1.7–4.6 mg were scanned at a rate of 5  $^{\circ}\text{C}/\text{min}$  in the range of 25–400  $^{\circ}\text{C}$ . See Figure A2.2–A2.6 in the appendix for DSC results.

### 2.6.3 Synthetic procedures and characterization

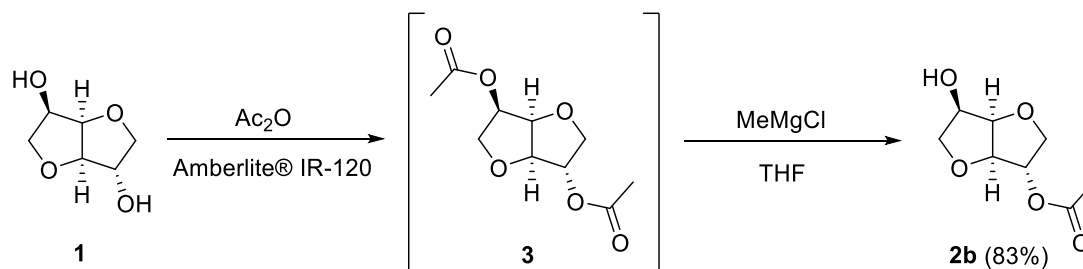


**5-O-Acetyl-1,4:3,6-dianhydro-D-glucitol (isosorbide-5-acetate) 2a;**  $\text{MeMgCl}$  (2.51 mL, 7.53 mmol) was added dropwise to a stirred solution of **1** (1.00 g, 6.84 mmol) in THF (70 mL) at room temperature. The mixture was heated at reflux for 30 min.  $\text{Ac}_2\text{O}$  (0.65 mL, 6.84 mmol) was added dropwise, and the solution stirred at the same temperature for 2 h. The reaction was quenched with HCl (5%, 10 mL), saturated  $\text{Na}_2\text{CO}_3$  solution (80 mL) added and extracted using  $\text{CH}_2\text{Cl}_2$  ( $5 \times 40$  mL). The organic extracts were combined, dried ( $\text{MgSO}_4$ ) and evaporated to dryness. The residue was analysed using GC, indicating 76% conversion to **2a**. Column chromatography using gradient

elution with EtOAc and hexanes gave **2a** (0.936 g, 73%) as a pale yellow oil;  $R_f$  0.37 (7 : 3 EtOAc : hexanes) with spectral data consistent with the literature.<sup>32</sup>

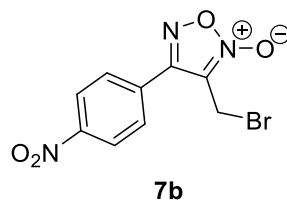


**2-O-Acetyl-1,4:3,6-dianhydro-D-glucitol (isosorbide-2-acetate) 2b via acetylation of 1;** MeMgCl (6.38 mL, 19.20 mmol) was added dropwise to a stirred solution of **1** (1.00 g, 6.84 mmol) in THF (70 mL) at 0 °C. After 30 min, AcCl (0.49 mL, 6.84 mmol) was added dropwise, and the solution stirred at the same temperature for 2 h. The reaction was quenched with HCl (5%, 10 mL) and extracted using CH<sub>2</sub>Cl<sub>2</sub> (5 × 40 mL). The organic extracts were combined, dried (MgSO<sub>4</sub>) and evaporated to dryness. The residue was analysed using GC, indicating 82% conversion to **2b**. Column chromatography using gradient elution with EtOAc and hexanes gave **2b** (0.999 g, 78%) as a white solid;  $R_f$  0.33 (3 : 2 EtOAc : hexanes) with spectral data consistent with the literature,<sup>32</sup> mp 74–75 °C (mp<sup>33</sup> 74 °C).

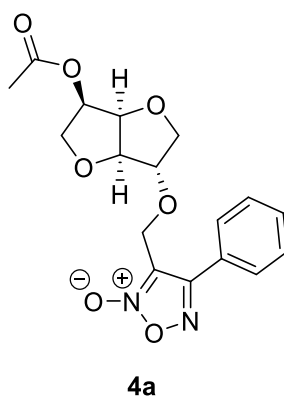


**2-O-Acetyl-1,4:3,6-dianhydro-D-glucitol (isosorbide-2-acetate) 2b via deacetylation of 3;** Ac<sub>2</sub>O (8.1 mL, 85.5 mmol) was added dropwise to a stirred mixture of **1** (5.00 g, 34.2 mmol) and Amberlite® IR-120 (H form, 0.50 g) at 80 °C. Stirring was continued at the same temperature for 2 h. The solution was filtered, toluene (2 × 25 mL) added and evaporated to give a pale yellow residue, which was dissolved in THF (30 mL). MeMgCl (14.8 mL, 44.5 mmol) was added dropwise to the stirred solution at room temperature, and was heated at reflux for 8 h. The reaction was quenched with HCl (5%, 50 mL) and extracted using CH<sub>2</sub>Cl<sub>2</sub> (5 × 50 mL). The organic extracts were combined, dried (MgSO<sub>4</sub>) and evaporated to dryness. The residue was analysed using GC, indicating 88%

conversion to **2b**. The residue was recrystallized from toluene to give **2b** (5.329 g, 83%) as a white solid with spectral data and melting point consistent with the above.



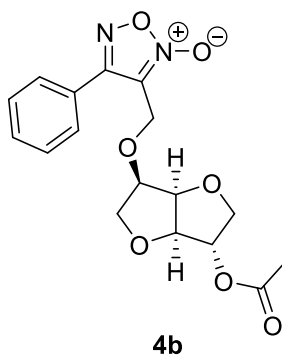
**3-(Bromomethyl)-4-(4-nitrophenyl)-2-oxido-1,2,5-oxadiazole 7b**; PPh<sub>3</sub> (1.647 g, 6.28 mmol) was added to a stirred solution of CBr<sub>4</sub> (2.082 g, 6.28 mmol) and [4-(4-nitrophenyl)-2-oxido-1,2,5-oxadiazol-3-yl]methanol (1.240 g, 5.23 mmol) in CH<sub>2</sub>Cl<sub>2</sub> (75 mL) at 0 °C. Stirring was continued at the same temperature for 2 h. The solution was evaporated and the residue purified by column chromatography using Et<sub>2</sub>O and hexanes to give **7b** (1.195 g, 76%) as a pale yellow solid; mp 110–111 °C; *R<sub>f</sub>* 0.25 (1 : 9 Et<sub>2</sub>O : hexanes);  $\nu_{\text{max}}$  (neat, cm<sup>-1</sup>) 3100, 3043, 2986, 1579 (NO<sub>2</sub>), 1538, 1457, 1424, 1352 (NO<sub>2</sub>), 1238, 1213, 1117, 1033; <sup>1</sup>H NMR (400 MHz, CDCl<sub>3</sub>)  $\delta_{\text{H}}$  4.42 (2H, s), 8.03 (2H, d, *J* = 8.8 Hz), 8.45 (2H, d, *J* = 8.8 Hz); <sup>13</sup>C NMR (100 MHz, CDCl<sub>3</sub>)  $\delta_{\text{C}}$  16.9 (CH<sub>2</sub>), 112.9 (C), 124.9 (CH), 128.8 (CH), 131.8, 149.6, 153.9 (all C); HRMS (ESI) *m/z* [M + CH<sub>2</sub>O<sub>2</sub> - H]<sup>-</sup>, C<sub>10</sub>H<sub>7</sub>N<sub>3</sub>O<sub>6</sub>Br calcd. 343.9518, observed 343.9525.



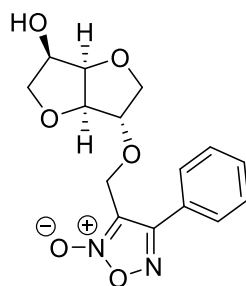
**5-O-Acetyl-1,4:3,6-dianhydro-2-O-[(2-oxido-4-phenyl-1,2,5-oxadiazol-3-yl)methyl]-D-glucitol (isosorbide-5-acetate-2-furoxan) 4a**; Bromide **7a** (1.020 g, 4.0 mmol), Ag<sub>2</sub>O (0.696 g, 3.0 mmol) and **2a** (0.188 g, 1.0 mmol) in CH<sub>2</sub>Cl<sub>2</sub> (10 mL) were stirred at reflux in the absence of light for 3 days. The mixture was filtered through Celite<sup>®</sup>, evaporated and purified by column chromatography using EtOAc and hexanes to give colourless oil. This was triturated using MeOH to give **4a** (0.295 g, 81%) as a white solid; mp 99–

## Chapter 2

100 °C;  $R_f$  0.29 (3 : 7 EtOAc : hexanes);  $\nu_{\max}$  (neat,  $\text{cm}^{-1}$ ) 2983, 2947, 2869, 1744 (C=O), 1613, 1598, 1578, 1466, 1370, 1244, 1087, 1020;  $^1\text{H}$  NMR (400 MHz,  $\text{CDCl}_3$ )  $\delta_{\text{H}}$  2.07 (3H, s,  $\text{CH}_3$ ), 3.73 (1H, dd,  $J = 5.2, 9.8$  Hz, H-6'), 3.84–3.90 (2H, m), 4.01 (1H, d,  $J = 10.5$  Hz, H-1'), 4.12 (1H, d,  $J = 3.4$  Hz, H-2), 4.47 (1H, d,  $J = 5.2$  Hz, H-3), 4.55 (2H, AB-q,  $J = 12.6$  Hz,  $\text{CH}_2$ ), 4.76 (1H, t,  $J = 5.2$  Hz, H-4), 5.09 (1H, q,  $J = 5.2$  Hz, H-5), 7.47–7.53 (3H, m), 7.74–7.77 (2H, m);  $^{13}\text{C}$  NMR (100 MHz,  $\text{CDCl}_3$ )  $\delta_{\text{C}}$  20.8 ( $\text{CH}_3$ ), 59.1 ( $\text{CH}_2$ ), 70.3 ( $\text{CH}_2$ -1), 72.6 ( $\text{CH}_2$ -6), 74.0 (CH-5), 80.7 (CH-4), 84.1 (CH-2), 85.8 (CH-3), 112.5 (C), 126.2 (C), 127.8, 129.5, 131.5 (all CH), 157.2 (C), 170.4 (C=O); HRMS (ESI)  $m/z$   $[\text{M} + \text{H}]^+$ ,  $\text{C}_{17}\text{H}_{19}\text{N}_2\text{O}_7$  calcd. 363.1192, observed 363.1190.

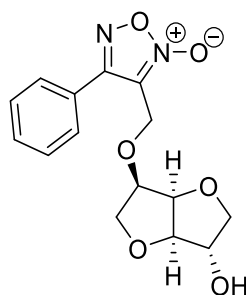


**2-O-Acetyl-1,4:3,6-dianhydro-5-O-[(2-oxido-4-phenyl-1,2,5-oxadiazol-3-yl)methyl]-D-glucitol (isosorbide-2-acetate-5-furoxan) 4b**; Bromide **7a** (1.020 g, 4.0 mmol),  $\text{Ag}_2\text{O}$  (0.696 g, 3.0 mmol) and **2b** (0.188 g, 1.0 mmol) in  $\text{CH}_2\text{Cl}_2$  (10 mL) were stirred at reflux in the absence of light for 3 days. The mixture was filtered through Celite<sup>®</sup>, evaporated and purified by column chromatography using EtOAc and hexanes to give **4b** (0.347 g, 96%) as a colourless oil;  $R_f$  0.23 (1 : 3 EtOAc : hexanes);  $\nu_{\max}$  (neat,  $\text{cm}^{-1}$ ) 2974, 2877, 1743 (C=O), 1596, 1578, 1481, 1458, 1368, 1232, 1081, 1057, 1017;  $^1\text{H}$  NMR (400 MHz,  $\text{CDCl}_3$ )  $\delta_{\text{H}}$  2.07 (3H, s,  $\text{CH}_3$ ), 3.68 (1H, dd,  $J = 6.7, 9.3$  Hz, H-6'), 3.93–4.05 (3H, m), 4.20 (1H, td,  $J = 4.9, 6.7$  Hz, H-5), 4.53 (1H, d,  $J = 4.9$  Hz, H-3), 4.73 (2H, AB-q,  $J = 11.9$  Hz,  $\text{CH}_2$ ), 4.76 (1H, t,  $J = 4.9$  Hz, H-4), 5.16 (1H, d,  $J = 3.5$  Hz, H-2), 7.50–7.56 (3H, m), 7.87–7.90 (2H, m);  $^{13}\text{C}$  NMR (100 MHz,  $\text{CDCl}_3$ )  $\delta_{\text{C}}$  21.0 ( $\text{CH}_3$ ), 60.3 ( $\text{CH}_2$ ), 70.9 ( $\text{CH}_2$ -6), 73.8 ( $\text{CH}_2$ -1), 78.4 (CH-2), 80.6 (2  $\times$  CH), 86.5 (CH-3), 112.9 (C), 126.3 (C), 128.0, 129.4, 131.5 (all CH), 157.4 (C), 170.1 (C=O); HRMS (ESI)  $m/z$   $[\text{M} + \text{H}]^+$ ,  $\text{C}_{17}\text{H}_{19}\text{N}_2\text{O}_7$  calcd. 363.1192, observed 363.1186.



5a

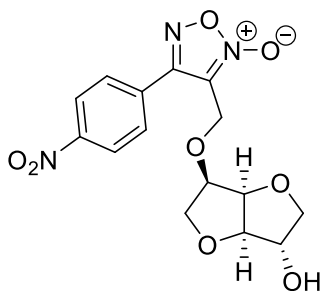
**1,4:3,6-Dianhydro-2-O-[(2-oxido-4-phenyl-1,2,5-oxadiazol-3-yl)methyl]-D-glucitol (isosorbide-2-furoxan) 5a**; Aq  $\text{K}_2\text{CO}_3$  (5 mL, 0.18 M, 0.90 mmol) was added to **4a** (0.326 g, 0.90 mmol) in MeOH (10 mL) and stirred for 1 h at room temperature.  $\text{H}_2\text{O}$  (10 mL) was added and the mixture was extracted with  $\text{CH}_2\text{Cl}_2$  ( $3 \times 30$  mL). The organic extracts were combined, dried ( $\text{MgSO}_4$ ), evaporated and purified by column chromatography using EtOAc and hexanes to give **5a** (0.262 g, 91%) as a white solid; mp 108–109 °C;  $R_f$  0.26 (1 : 1 EtOAc : hexanes);  $\nu_{\text{max}}$  (neat,  $\text{cm}^{-1}$ ) 3407 (OH), 2929, 2871, 1596, 1577, 1479, 1456, 1433, 1336, 1249, 1074, 1010;  $^1\text{H}$  NMR (400 MHz,  $\text{CDCl}_3$ )  $\delta_{\text{H}}$  2.60 (1H, d,  $J = 7.1$  Hz, OH), 3.57 (1H, dd,  $J = 5.7, 9.5$  Hz, H-6'), 3.85–3.92 (2H, m), 4.11 (1H, d,  $J = 10.5$  Hz, H-1), 4.18 (1H, d,  $J = 3.6$  Hz, H-2), 4.26–4.32 (1H, m, H-5), 4.51 (1H, d,  $J = 4.7$  Hz, H-3), 4.60 (2H, AB-q,  $J = 12.5$  Hz,  $\text{CH}_2$ ), 4.61 (1H, t,  $J = 4.7$  Hz, H-4), 7.51–7.59 (3H, m), 7.78–7.81 (2H, m);  $^{13}\text{C}$  NMR (100 MHz,  $\text{CDCl}_3$ )  $\delta_{\text{C}}$  59.2 ( $\text{CH}_2$ ), 72.3 (CH-5), 72.8 ( $\text{CH}_2$ -1), 73.8 ( $\text{CH}_2$ -6), 82.0 (CH-4), 84.5 (CH-2), 85.6 (CH-3), 112.4 (C), 126.3 (C), 127.8, 129.5, 131.5 (all CH), 157.1 (C); HRMS (ESI)  $m/z$   $[\text{M} - \text{H}]^-$ ,  $\text{C}_{15}\text{H}_{15}\text{N}_2\text{O}_6$  calcd. 319.0930, observed 319.0923.



5b

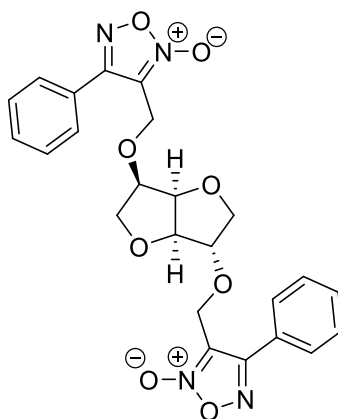
**1,4:3,6-Dianhydro-5-O-[(2-oxido-4-phenyl-1,2,5-oxadiazol-3-yl)methyl]-D-glucitol (isosorbide-5-furoxan) 5b**; Prepared according to the procedure for **5a** to give **5b** (0.271 g, 94%) as a colourless oil;  $R_f$  0.22 (1 : 1 EtOAc : hexanes);  $\nu_{\text{max}}$  (neat,  $\text{cm}^{-1}$ ) 3422 (OH), 2946, 2877, 1595, 1577, 1458, 1267, 1123, 1071, 1012;  $^1\text{H}$  NMR (400 MHz,

CDCl<sub>3</sub>)  $\delta_{\text{H}}$  2.60–2.87 (1H, bs, OH), 3.62 (1H, dd,  $J = 6.7, 9.3$  Hz, H-6'), 3.85–3.92 (3H, m), 4.16 (1H, td,  $J = 4.7, 6.7$  Hz, H-5), 4.28 (1H, d,  $J = 2.4$  Hz, H-2), 4.41 (1H, d,  $J = 4.7$  Hz, H-3), 4.72 (2H, AB-q,  $J = 12.8$  Hz, CH<sub>2</sub>), 4.75 (1H, t,  $J = 4.7$  Hz, H-4), 7.48–7.55 (3H, m), 7.85–7.88 (2H, m); <sup>13</sup>C NMR (100 MHz, CDCl<sub>3</sub>)  $\delta_{\text{C}}$  60.2 (CH<sub>2</sub>), 70.8 (CH<sub>2</sub>-6), 75.8 (CH<sub>2</sub>-1), 76.5 (CH-2), 80.2 (CH-4), 80.7 (CH-5), 88.8 (CH-3), 113.0 (C), 126.2 (C), 128.0, 129.4 and 131.5 (all CH), 157.4 (C); HRMS (ESI)  $m/z$  [M – H]<sup>–</sup>, C<sub>15</sub>H<sub>15</sub>N<sub>2</sub>O<sub>6</sub> calcd. 319.0930, observed 319.0921.



5c

**1,4:3,6-Dianhydro-5-O-[[4-(4-nitrophenyl)-2-oxido-1,2,5-oxadiazol-3-yl]methyl]-D-glucitol (isosorbide-5-*p*-nitrophenyl-furoxan) 5c**; Bromide **7b** (1.080 g, 3.60 mmol), **2b** (0.170 g, 0.90 mmol), and Ag<sub>2</sub>O (0.626 g, 2.70 mmol) in CH<sub>2</sub>Cl<sub>2</sub> (10 mL) were stirred at reflux in the absence of light for 3 days. The solution was filtered through Celite<sup>®</sup> and evaporated to dryness. The residue was dissolved in MeOH/CH<sub>2</sub>Cl<sub>2</sub> (30 mL, 5/1), aq K<sub>2</sub>CO<sub>3</sub> (25 mL, 0.036 M, 0.90 mmol) added, and the mixture stirred for 1 h at room temperature. H<sub>2</sub>O (50 mL) was added and extracted using CH<sub>2</sub>Cl<sub>2</sub> (3 × 40 mL). The organic extracts were combined, dried (MgSO<sub>4</sub>), evaporated, and purified by column chromatography using EtOAc and hexanes to give a pale orange oil which crystallized on standing to give **5c** (0.280 g, 85%) as a pale orange solid; mp 58–60 °C;  $R_f$  0.60 (2 : 3 EtOAc : hexanes);  $\nu_{\text{max}}$  (neat, cm<sup>–1</sup>) 3423 (OH), 3098, 2877, 1727, 1594 (NO<sub>2</sub>), 1523, 1453, 1350 (NO<sub>2</sub>), 1295, 1267, 1196, 1071, 1010; <sup>1</sup>H NMR (400 MHz, CDCl<sub>3</sub>)  $\delta_{\text{H}}$  2.18–2.42 (1H, bs, OH), 3.63 (1H, dd,  $J = 6.8, 9.3$  Hz, H-6'), 3.92 (2H, d,  $J = 2.3$  Hz), 3.95 (1H, dd,  $J = 6.8, 9.3$  Hz, H-6''), 4.21 (1H, td,  $J = 4.7, 6.8$  Hz, H-5), 4.30–4.37 (1H, bs, H-2), 4.46 (1H, d,  $J = 4.7$  Hz, H-3), 4.73 (2H, AB-q,  $J = 12.8$  Hz, CH<sub>2</sub>), 4.74 (1H, t,  $J = 4.7$  Hz, H-4), 8.17 (2H, d,  $J = 9.0$  Hz), 8.36 (2H, d,  $J = 9.0$  Hz); <sup>13</sup>C NMR (100 MHz, CDCl<sub>3</sub>)  $\delta_{\text{C}}$  60.2 (CH<sub>2</sub>), 70.7 (CH<sub>2</sub>-6), 75.9 (CH<sub>2</sub>-1), 76.5 (CH-2), 80.1 (CH-4), 81.1 (CH-5), 88.9 (CH-3), 112.5 (C), 124.5, 129.2 (both CH), 132.2, 149.4, 155.6 (all C); HRMS (ESI)  $m/z$  [M – H]<sup>–</sup>, C<sub>15</sub>H<sub>14</sub>N<sub>3</sub>O<sub>8</sub> calcd. 364.0781, observed 364.0784.



8

**1,4:3,6-Dianhydro-2,5-bis-O-[(2-oxido-4-phenyl-1,2,5-oxadiazol-3-yl)methyl]-D-glucitol (isosorbide-2-5-difuroxan) 8**; Bromide **7a** (2.040 g, 8.0 mmol), Ag<sub>2</sub>O (1.390 g, 6.0 mmol) and **1** (0.146 g, 1.0 mmol) in CH<sub>2</sub>Cl<sub>2</sub> (10 mL) were stirred at reflux in the absence of light for 3 days. The mixture was filtered through Celite®, evaporated and purified by column chromatography using EtOAc and hexanes to give **8** (0.379 g, 77%) as a white solid; mp 96-98 °C; *R*<sub>f</sub> 0.13 (1 : 4 EtOAc : hexanes); *v*<sub>max</sub> (neat, cm<sup>-1</sup>) 2936, 2877, 1595, 1577, 1480, 1457, 1427, 1267, 1082, 1011; <sup>1</sup>H NMR (400 MHz, CDCl<sub>3</sub>) δ<sub>H</sub> 3.67 (1H, dd, *J* = 6.6, 9.3 Hz, H-6'), 3.91–3.95 (2H, m), 4.03 (1H, d, *J* = 10.5 Hz, H-1'), 4.14 (1H, d, *J* = 3.4 Hz, H-2), 4.19 (1H, td, *J* = 4.7, 6.6 Hz, H-5), 4.56 (1H, d, *J* = 4.7 Hz, H-3), 4.58 (2H, AB-q, *J* = 12.5 Hz, CH<sub>2</sub>), 4.72 (2H, AB-q, *J* = 12.8 Hz, CH<sub>2</sub>), 4.73 (1H, t, *J* = 4.7 Hz, H-4), 7.50–7.58 (6H, m), 7.79 (2H, dd, *J* = 1.7, 7.9 Hz), 7.89 (2H, dd, *J* = 1.7, 7.9 Hz); <sup>13</sup>C NMR (100 MHz, CDCl<sub>3</sub>) δ<sub>C</sub> 59.2, 60.3 (both CH<sub>2</sub>), 70.9 (CH<sub>2</sub>-1), 72.9 (CH<sub>2</sub>-6), 80.6 (CH-4 and CH-5), 84.4 (CH-2), 86.4 (CH-3), 112.5, 112.9, 126.2, 126.3 (all C), 127.8, 128.0, 129.4, 129.5, 131.5, 131.5 (all CH), 157.2 (C), 157.4 (C); HRMS (ESI) *m/z* (M – H)<sup>-</sup>, C<sub>24</sub>H<sub>21</sub>N<sub>4</sub>O<sub>8</sub> calcd. 493.1359, observed 493.1348.

### 2.7 Chapter 2 Contributions

Sincere thanks to Dr. Michael Kennedy and Mary Kennedy (SPDS, Tarbert, Co. Kerry, Ireland) for performing the DSC experiments, to Prof. Patrick McArdle (NUI Galway) for X-ray crystallography, and to Dr. Richard Singer (Kingston University) for DFT calculations on the O-magnesiated isosorbide structures.

### 2.8 Chapter 2 References

1. Carpenter, A. W; Schoenfisch, M. H. *Chem. Soc. Rev.* **2012**, *41*, 3742–3752. <https://doi.org/10.1039/C2CS15273H>.
2. Xu, W.; Liu, L. Z.; Loizidou, M.; Ahmed, M.; Charles, I. G. *Cell Res.* **2002**, *12*, 311–320. <https://doi.org/10.1038/sj.cr.7290133>.
3. Jones, M. L.; Ganopolsky, J. G.; Labbé, A.; Wahl, C.; Prakash, S. *Appl. Microbiol. Biotechnol.* **2010**, *88*, 401–407. <https://doi.org/10.1007/s00253-010-2733-x>.
4. Witte, M. B.; Barbul, A. *Am. J. Surg.* **2002**, *183*, 406–412. [https://doi.org/10.1016/S0002-9610\(02\)00815-2](https://doi.org/10.1016/S0002-9610(02)00815-2).
5. Lundberg, J. O.; Weitzberg, E.; Gladwin, M. T. *Nat. Rev. Drug Discovery* **2008**, *7*, 156–167. <https://doi.org/10.1038/nrd2466>.
6. Bohlen, H. G. *Compr. Physiol.* **2015**, *5*, 803–828. <https://doi.org/10.1002/cphy.c140052>.
7. Thatcher, G. R. J. *Chem. Soc. Rev.* **1998**, *27*, 331–337. <https://doi.org/10.1039/A827331Z>.
8. Ignarro, L. J.; Napoli, C.; Loscalzo, J. *Circ. Res.* **2002**, *90*, 21–28. <https://doi.org/10.1161/hh0102.102330>.
9. Mayer, B.; Beretta, M. *Br. J. Pharmacol.* **2008**, *155*, 170–184. <https://doi.org/10.1038/bjp.2008.263>.
10. Boschan, R.; Merrow, R. T.; van Dolah, R. W. *Chem. Rev.* **1955**, *55*, 485–510. <https://doi.org/10.1021/cr50003a001>.
11. Shixiao, W.; Yongji, G.; Jie, H.; Yanshun, L.; Qinghua, H. *CN Patent* **2014**, CN103641840.



## Chapter 2

---

12. Reddy, G. O.; Rao, A. S. *J. Hazard. Mater.* **1992**, *32*, 87–104. [https://doi.org/10.1016/0304-3894\(92\)85107-C](https://doi.org/10.1016/0304-3894(92)85107-C).
13. Medana, C.; Ermondi, G.; Fruttero, R.; Di Stilo, A.; Ferretti, C.; Gasco, A. *J. Med. Chem.* **1994**, *37*, 4412–4416. <https://doi.org/10.1021/jm00051a020>.
14. Bohn, H.; Brendel, J.; Martorana, P. A.; Schonafinger, K. *Br. J. Pharmacol.* **1995**, *114*, 1605–1612. <https://doi.org/10.1111/j.1476-5381.1995.tb14946.x>.
15. Ferioli, R.; Folco, G. C.; Ferretti, C.; Gasco, A. M.; Medana, C.; Fruttero, R.; Civelli, M.; Gasco, A. *Br. J. Pharmacol.* **1995**, *114*, 816–820. <https://doi.org/10.1111/j.1476-5381.1995.tb13277.x>.
16. Sorba, G.; Medana, C.; Fruttero, R.; Cena, C.; Di Stilo, A.; Galli, U.; Gasco, A. *J. Med. Chem.* **1997**, *40*, 463–469. <https://doi.org/10.1021/jm960379t>.
17. Gasco, A.; Fruttero, R.; Sorba, G.; Di Stilo, A.; Calvino, R. *Pure Appl. Chem.* **2004**, *76*, 973–981. <https://doi.org/10.1351/pac200476050973>.
18. Schiefer, I.T.; VandeVrede, L.; Fa', M.; Arancio, O.; Thatcher, G. R. J. *J. Med. Chem.* **2012**, *55*, 3076–3087. <https://doi.org/10.1021/jm201504s>.
19. Tang, W.; Xie, J.; Xu, S.; Lv, H.; Lin, M.; Yuan, S.; Bai, J.; Hou, Q.; Yu, S. *J. Med. Chem.* **2014**, *57*, 7600–7612. <https://doi.org/10.1021/jm5007534>.
20. Hinz, B.; Schröder, H. *Biochem. Biophys. Res. Commun.* **1998**, *252*, 232–235. <https://doi.org/10.1006/bbrc.1998.9630>.
21. Needleman, P.; Johnson, E. M. *J. Pharmacol. Exp. Ther.* **1973**, *184*, 709.
22. Civelli, M.; Giossi, M.; Caruso, P.; Razzetti, R.; Bergamaschi, M.; Bongrani, S.; Gasco, A. *Br. J. Pharmacol.* **1996**, *118*, 923–928.
23. He, C.; Shreeve, J. M. *Angew. Chem. Int. Ed.* **2016**, *55*, 772–775. <https://doi.org/10.1002/anie.201509209>.
24. Dussenne, C.; Delaunay, T.; Wiatz, V.; Wyart, H.; Suisse, I.; Sauthier, M. *Green Chem.* **2017**, *19*, 5332–5344. <https://doi.org/10.1039/C7GC01912B>.
25. Gallezot, P.; Cerino, P. J.; Blanc, B.; Flèche, G.; Fuertes, P. *J. Catal.* **1994**, *146*, 93–102. [https://doi.org/10.1016/0021-9517\(94\)90012-4](https://doi.org/10.1016/0021-9517(94)90012-4).
26. Rose, M.; Palkovits, R. *ChemSusChem* **2012**, *5*, 167–176. <https://doi.org/10.1002/cssc.201100580>.
27. Szeja, W. *J. Chem. Soc., Chem. Commun.* **1981**, 215–216. <https://doi.org/10.1039/C39810000215>.
28. Che, P.; Lu, F.; Nie, X.; Huang, Y.; Yang, Y.; Wang, F.; Xu, J. *Chem. Commun.* **2015**, *51*, 1077–1080. <https://doi.org/10.1039/C4CC08467E>.

## Chapter 2

---

29. Stoss, P.; Merrath, P.; Schlüter, G. *Synthesis* **1987**, 1987, 174–176. <https://doi.org/10.1055/s-1987-27878>.
30. Abenhaïm, D.; Loupy, A.; Munnier, L.; Tamion, R.; Marsais, F.; Quéguiner, G. *Carbohydr. Res.* **1994**, 261, 255–266. [https://doi.org/10.1016/0008-6215\(94\)84022-9](https://doi.org/10.1016/0008-6215(94)84022-9).
31. Gallagher, J. J.; Hillmyer, M. A.; Reineke, T. M. *ACS Sustain. Chem. Eng.* **2015**, 3, 662–667. <https://doi.org/10.1021/sc5008362>.
32. Lavergne, A.; Moity, L.; Molinier, V.; Aubry, J.-M. *RSC Adv.* **2013**, 3, 5997–6007. <https://doi.org/10.1039/C3RA40205C>.
33. Čeković, Ž.; Tokić, Z. *Synthesis* **1989**, 1989, 610–612. <https://doi.org/10.1055/s-1989-27332>.
34. Stoss, P. *U.S. Pat.* **1983**, 4371703.
35. Zhu, S.-G.; Huang, J.-X.; Zhang, G.-M.; Chen, S.-X.; Zhang, F.-L. *Org. Process Res. Dev.* **2018**, 22, 1548–1552. <https://doi.org/10.1021/acs.oprd.8b00310>.
36. Roy, A.; Chawla, H. P. S. *Enzyme Microb. Technol.* **2001**, 29, 490–493. [https://doi.org/10.1016/S0141-0229\(01\)00425-2](https://doi.org/10.1016/S0141-0229(01)00425-2).
37. Seemayer, R.; Bar, N.; Schneider, M. P. *Tetrahedron: Asymmetry* **1992**, 3, 1123–1126. [https://doi.org/10.1016/S0957-4166\(00\)82092-3](https://doi.org/10.1016/S0957-4166(00)82092-3).
38. Harnett, G. J.; Hayes, J.; Reents, R.; Smith, D. A.; Walsh, A. *U.S. Pat.* **2012**, US20120071683.
39. Gbadebo, O.; Smith, D.; Harnett, G.; Donegan, G.; O'Leary, P. *Eur. J. Org. Chem.* **2018**, 2018, 7037–7045. <https://doi.org/10.1002/ejoc.201801462>.
40. Guggenberger, L. J.; Rundle, R. E. *J. Am. Chem. Soc.* **1968**, 90, 5375–5378. <https://doi.org/10.1021/ja01022a007>.
41. Peltzer, R. M.; Eisenstein, O.; Nova, A.; Cascella, M. J. *J. Phys. Chem. B* **2017**, 121, 4226–4237. <https://doi.org/10.1021/acs.jpcc.7b02716>.
42. Cope, A. C.; Shen, T. Y. *J. Am. Chem. Soc.* **1956**, 78, 5916–5920. <https://doi.org/10.1021/ja01603a055>.
43. Hopf, H.; Mourad, A.-F. E.; Jones, P. G. *Beilstein J. Org. Chem.* **2010**, 6, No. 68. <https://doi.org/10.3762/bjoc.6.68>.
44. Greene, T. W.; Wuts, P. G. M. Protection for the Hydroxyl Group, Including 1,2- and 1,3-Diols. In *Protective Groups in Organic Synthesis*; Wiley-VCH: New York, **1999**; pp 17–245. <https://doi.org/10.1002/0471220574.ch2>.

45. Burov, O. N.; Kletskii, M. E.; Fedik, N. S.; Lisovin, A. V.; Kurbatov, S. V. *Chem. Heterocycl. Compd.* **2015**, *51*, 951–960. <https://doi.org/10.1007/s10593-016-1804-z>.
46. Coneski, P. N.; Schoenfisch, M. H. *Chem. Soc. Rev.* **2012**, *41*, 3753–3758. <https://doi.org/10.1039/C2CS15271A>.
47. Hevel, J. M.; Marletta, M. A. Nitric-oxide Synthase Assays. In *Methods in Enzymology*; Packer, L., Ed.; Academic Press: San Diego, **1994**; Vol. 233, pp 250–258. [https://doi.org/10.1016/S0076-6879\(94\)33028-X](https://doi.org/10.1016/S0076-6879(94)33028-X).
48. Han, C.; Huang, Z.; Zheng, C.; Wan, L.; Zhang, L.; Peng, S.; Ding, K.; Ji, H.; Tian, J.; Zhang, Y. *J. Med. Chem.* **2013**, *56*, 4738–4748. <https://doi.org/10.1021/jm400463q>.
49. Liu, M.-M.; Chen, X.-Y.; Huang, Y.-Q.; Feng, P.; Guo, Y.-L.; Yang, G.; Chen, Y. *J. Med. Chem.* **2014**, *57*, 9343–9356. <https://doi.org/10.1021/jm500613m>.
50. Wendt, R. L. *J. Pharmacol. Exp. Ther.* **1972**, *180*, 732–742.
51. Shanley, E. S.; Melhem, G. A. *Process Saf. Prog.* **1995**, *14*, 29–31. <https://doi.org/10.1002/prs.680140105>.
52. Lothrop, W. C.; Handrick, G. R. *Chem. Rev.* **1949**, *44*, 419–445. <https://doi.org/10.1021/cr60139a001>.
53. Frurip, D. J.; Elwell, T. *Process Saf. Prog.* **2007**, *26*, 51–58. <https://doi.org/10.1002/prs.10167>.
54. Butler, A. R.; Pearson, R. J. Vasodilators for Biological Research. In *Nitric Oxide Donors*; Wang, P. G., Cai, T. B., Taniguchi, N., Eds.; Wiley-VCH: Weinheim, **2005**; pp 201–231.
55. KIELTY, P.; SMITH, D. A.; CANNON, P.; CARTY, M. P.; KENNEDY, M.; McARDLE, P.; SINGER, R. J.; ALDABBAGH, F. *Org. Lett.* **2018**, *20*, 3025–3029. <https://doi.org/10.1021/acs.orglett.8b01060>.
56. Frisch, M. J.; Trucks, G. W.; Schlegel, H. B.; Scuseria, G. E.; Robb, M. A.; Cheeseman, J. R.; Scalmani, G.; Barone, V.; Petersson, G. A.; Nakatsuji, H.; Li, X.; Caricato, M.; Marenich, A. V.; Bloino, J.; Janesko, B. G.; Gomperts, R.; Mennucci, B.; Hratchian, H. P.; Ortiz, J. V.; Izmaylov, A. F.; Sonnenberg, J. L.; Williams-Young, D.; Ding, F.; Lipparini, F.; Egidi, F.; Goings, J.; Peng, B.; Petrone, A.; Henderson, T.; Ranasinghe, D.; Zakrzewski, V. G.; Gao, J.; Rega, N.; Zheng, G.; Liang, W.; Hada, M.; Ehara, M.; Toyota, K.; Fukuda, R.; Hasegawa, J.; Ishida, M.; Nakajima, T.; Honda, Y.; Kitao, O.; Nakai, H.; Vreven,

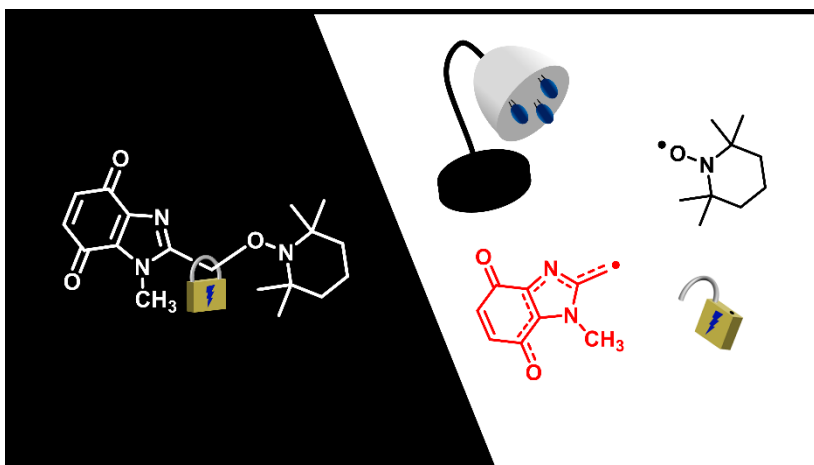
## Chapter 2

---

- T.; Throssell, K.; Montgomery, J. A., Jr.; Peralta, J. E.; Ogliaro, F.; Bearpark, M. J.; Heyd, J. J.; Brothers, E. N.; Kudin, K. N.; Staroverov, V. N.; Keith, T. A.; Kobayashi, R.; Normand, J.; Raghavachari, K.; Rendell, A. P.; Burant, J. C.; Iyengar, S. S.; Tomasi, J.; Cossi, M.; Millam, J. M.; Klene, M.; Adamo, C.; Cammi, R.; Ochterski, J. W.; Martin, R. L.; Morokuma, K.; Farkas, O.; Foresman, J. B.; Fox, D. J. Gaussian 16W, Revision A.03, Gaussian, Inc., Wallingford CT, 2016.
57. Spartan '10, version 1.1.0 Wavefunction Inc., Irvine CA, 2010.
58. Sheldrick, G. *Acta Crystallogr. Sect. A: Found. Crystallogr.* **2015**, *71*, 3–8. <https://doi.org/10.1107/S2053273314026370>.
59. Sheldrick, G. *Acta Crystallogr. Sect. C: Cryst. Struct. Commun.* **2015**, *71*, 3–8. <https://doi.org/10.1107/S2053229614024218>.
60. McArdle, P. *J. Appl. Crystallogr.* **2017**, *50*, 320–326. <https://doi.org/10.1107/S1600576716018446>.

# Chapter 3

## Visible-Light Unmasking of Quinone Methide Radicals and Nitroxides from Alkoxyamines



Parts of this chapter are published in:

“Visible-Light Unmasking of Heterocyclic Quinone Methide Radicals from Alkoxyamines”

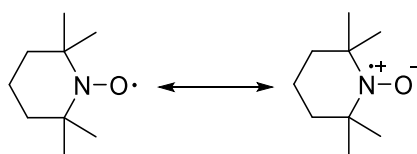
Patrick Kielty, Pau Farràs, Patrick McArdle, Dennis A. Smith  
and Fawaz Aldabbagh

*Chemical Communications*, 2019, Advance article

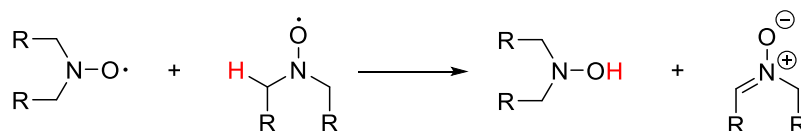
DOI: [10.1039/C9CC08261A](https://doi.org/10.1039/C9CC08261A)

### 3.1 Introduction

Nitroxides are bench-stable free radicals, with (2,2,6,6-tetramethylpiperidin-1-yl)oxyl, or TEMPO, being the most widely used and commercially available nitroxide. The stability of TEMPO arises from the resonance stabilization of the unpaired electron across the NO moiety, resulting in a  $\pi_{\text{N-O}}$  three-electron bond, with the spin density of the unpaired electron residing mainly on the O atom (Scheme 3.1).<sup>1</sup> Dimerization of nitroxides is prevented due to the unfavourable thermodynamics of the NO–ON bond,<sup>2</sup> and the absence of a hydrogen atom  $\alpha$  to the N atom prevents disproportionation of the nitroxide to the corresponding hydroxylamine and nitrene (Scheme 3.2).<sup>3</sup>



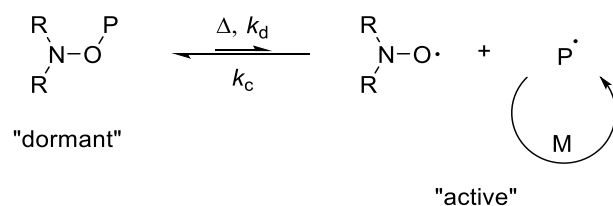
**Scheme 3.1** Resonance stabilization of TEMPO nitroxide.



**Scheme 3.2** Disproportionation of nitroxides bearing  $\alpha$ -hydrogens.<sup>3</sup>

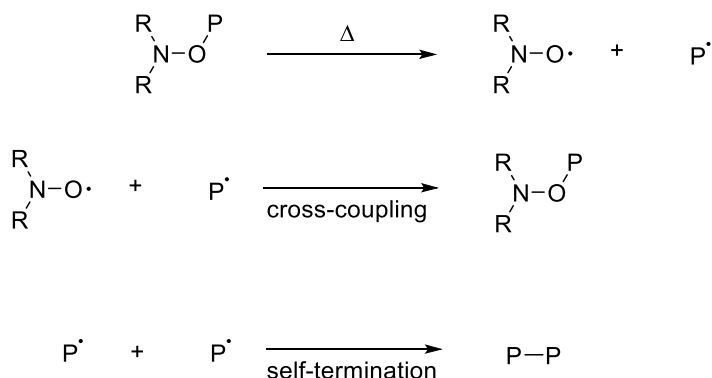
Nitroxides mask reactive carbon-centred radicals in the form of alkoxyamines. Thermal homolysis of alkoxyamines forms the basis for the popular nitroxide-mediated radical polymerization (NMP), a well-established method of controlled/living polymerization delivering polymers with low polydispersity indices (Scheme 3.3).<sup>4</sup> The rate of thermal homolysis of alkoxyamines ( $k_d$ ) is several orders of magnitude slower than the reverse recombination rate ( $k_c$ ), thus ensuring that the concentration of reactive radicals in the active monomer-consuming step is lower than for conventional, uncontrolled radical polymerizations.

## Chapter 3



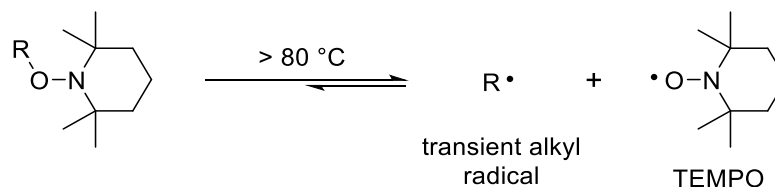
**Scheme 3.3** The reversible dissociation of a polymeric alkoxyamine into nitroxide and polymer radical. P = polymer, M = monomer.

The persistent radical effect (PRE)<sup>5</sup> regulates carbon-centred radical concentration by an initial build up in nitroxide concentration during the early stages of NMP (Scheme 3.4). In the early stages of NMP, the concentration of thermally-derived nitroxide and alkyl radicals is equal. However, owing to self-termination reactions of low molecular weight alkyl radicals, the relative concentration of non-self-terminating nitroxide increases. Alkyl and polymer radicals are thus regulated by the excess of free nitroxide that accumulated, and termination processes become insignificant.



**Scheme 3.4** The persistent radical effect in NMP.<sup>5</sup>

TEMPO has found wide-ranging application in synthesis and catalysis,<sup>6,7</sup> spin labelling,<sup>8</sup> fluorescence,<sup>9</sup> magnetic resonance imaging (MRI),<sup>10</sup> electrochemistry,<sup>11</sup> organic radical batteries,<sup>12</sup> high-tech polymers,<sup>13</sup> and radical scavenging.<sup>14</sup> Homolysis of TEMPO-alkoxyamines is traditionally achieved *via* thermal activation, which usually requires temperatures in excess of 80 °C (Scheme 3.5),<sup>15</sup> but there have been attempts at controlled/living NMP using photodissociation of alkoxyamines.<sup>16-18</sup> Bis- or bifunctional alkoxyamines are useful for the synthesis of A-B-A type block co-polymers, however homolysis has only been achieved by thermal means at temperatures between 70–140 °C (Figure 3.1).<sup>19-22</sup>



**Scheme 3.5** Traditional thermal activation of alkoxyamines.

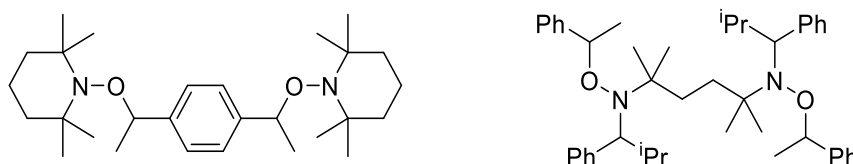
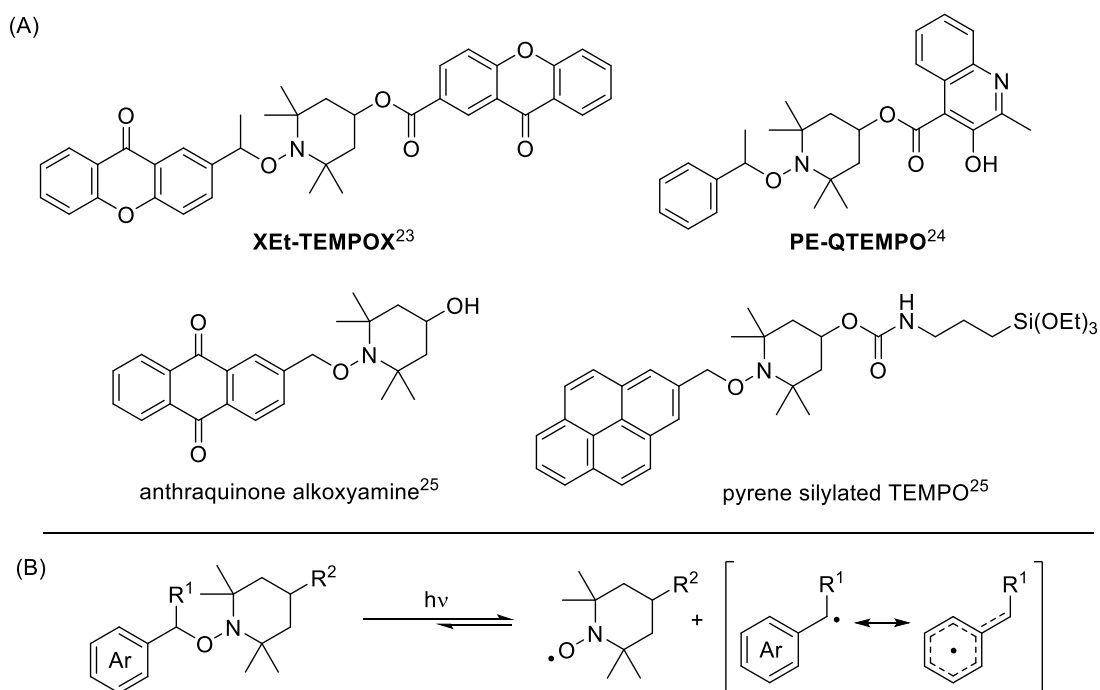


**Figure 3.1** Thermally activated bis-alkoxyamines.<sup>19,22</sup>

From a biomedical applications perspective, alkoxyamine activation at or near physiological temperature is essential. Low or ambient temperature alkoxyamine activation using UV/visible-light has been reported using highly conjugated derivatives of 4-hydroxy-TEMPO (4-OH-TEMPO),<sup>18,23-25</sup> including **XEt-TEMPOX**<sup>23</sup> and **PE-QTEMPO** (Scheme 3.6A).<sup>24</sup> Guillaneuf and co-workers coupled benzylic

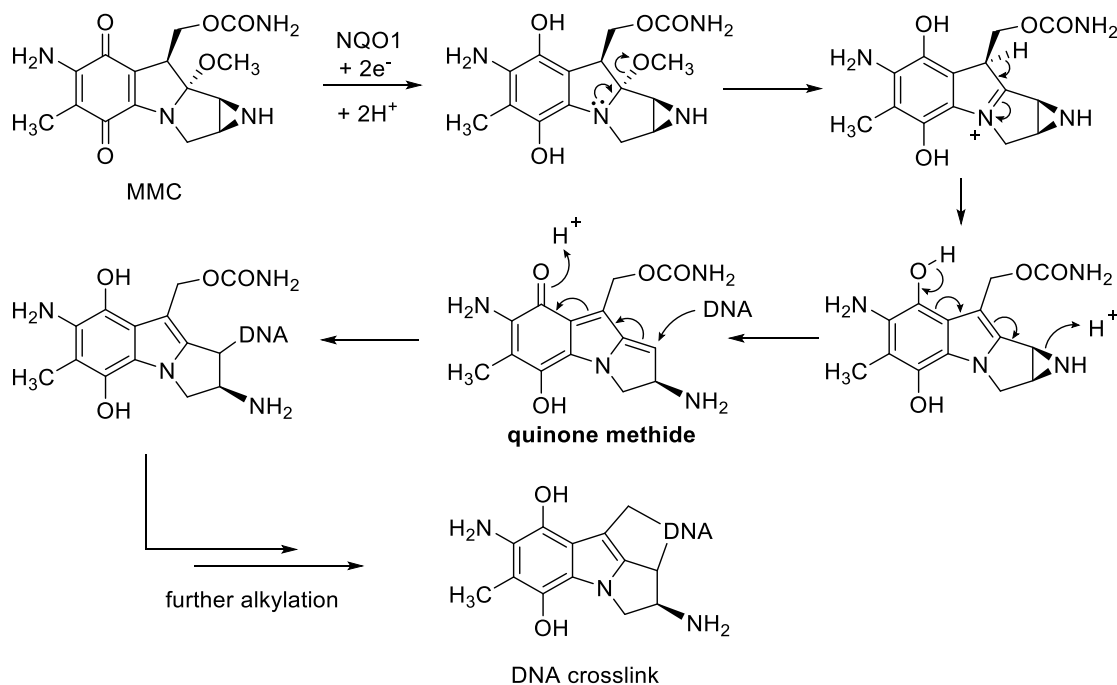


**Scheme 3.6** (a) Light-sensitive alkoxyamines with (b) homolysis driven by the formation of stabilized benzyl radicals.



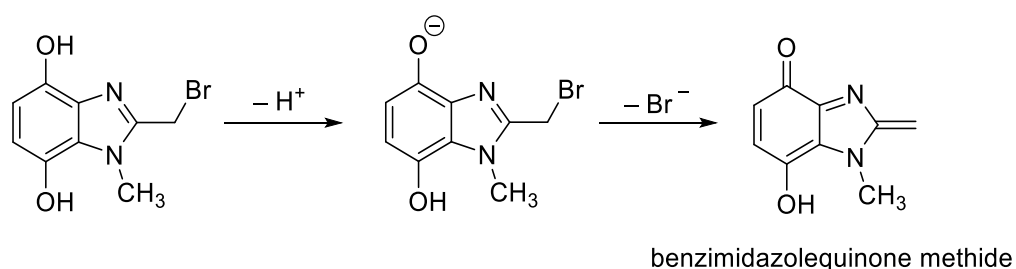
## Chapter 3

derivatives of naphthalene, benzophenone, coumarin, anthraquinone and pyrene with 4-OH-TEMPO to give a series of UV/visible-light sensitive alkoxyamines.<sup>25</sup> The quinone methide radical-forming anthraquinone adduct displayed the fastest dissociation, and the silylated TEMPO pyrene alkoxyamine was used to generate micropatterned surfaces *via* thermal exchange with polystyrene alkoxyamines. For reported light-sensitive alkoxyamines,<sup>18,23–25</sup> the formation of thermodynamically stabilized benzylic radicals promotes the loss of TEMPO (Scheme 3.6B). Comparably, the generation of a quinone methide drives the bioreductive elimination of the carbamate functionality of the chemotherapeutic mitomycin C (MMC) to give a reactive site for cross-linking with DNA (Scheme 3.7 and 3.8). Activation of MMC occurs *via* NADPH:quinone oxidoreductase 1 (NQO1) mediated two-electron reduction (Scheme 3.7)<sup>26</sup> or by NADPH-cytochrome P450 reductase (CP450) mediated one-electron reduction (Scheme 3.8).<sup>27,28</sup> Both mechanisms result in DNA crosslinking, however the one-electron reduction of MMC to the semiquinone radical is rapidly reversed in the presence of O<sub>2</sub>,<sup>29</sup> and thus, the route proceeds under hypoxic conditions.



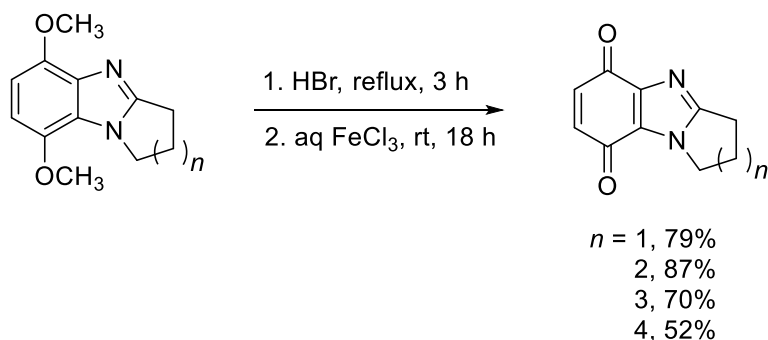
**Scheme 3.7** Two-electron bioreductive DNA crosslinking by MMC.<sup>26</sup>





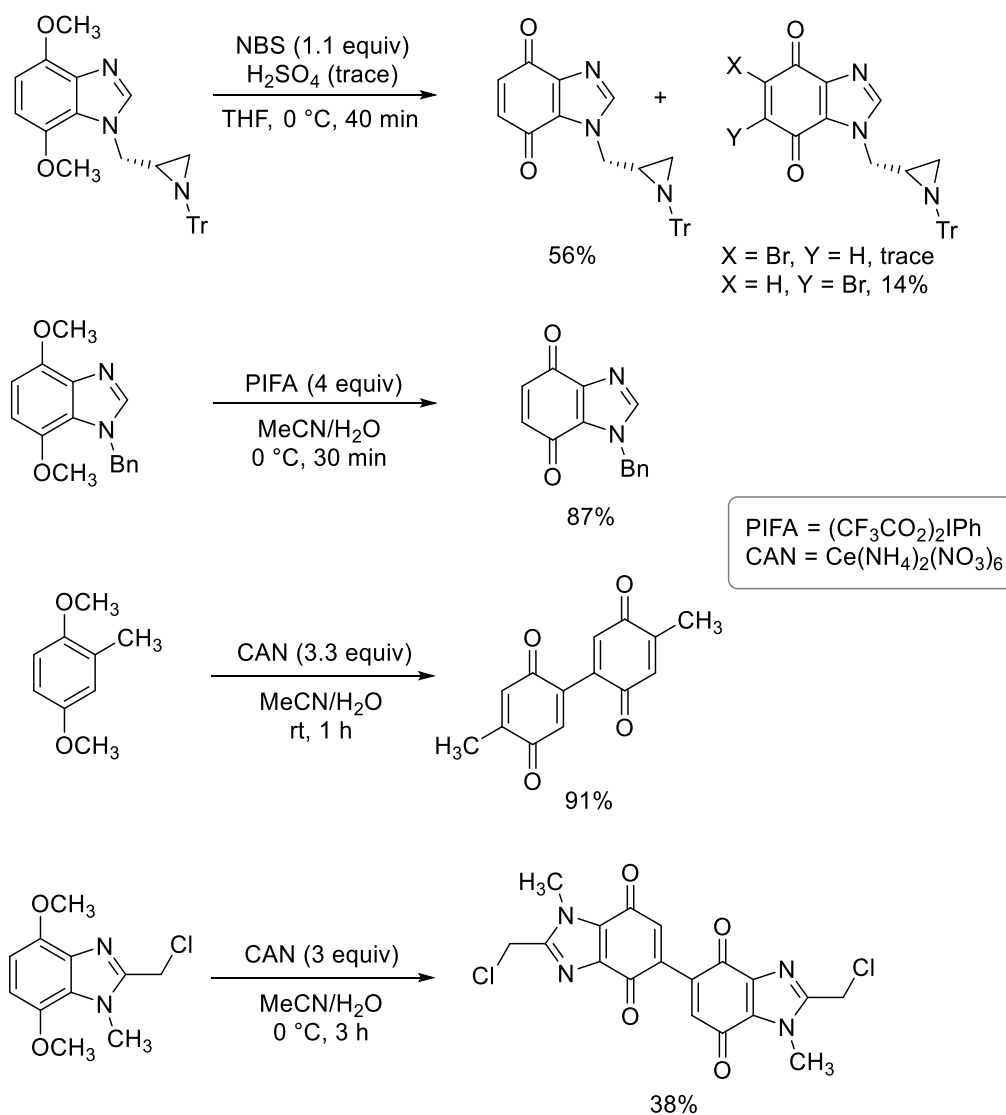
**Scheme 3.10** pH-Mediated benzimidazolequinone methide formation.<sup>31</sup>

The most common synthetic route to benzimidazolequinones is *via* oxidation of 4,7-dimethoxybenzimidazole precursors. A two-step procedure involving demethylation of both methyl ether groups in refluxing HBr followed by FeCl<sub>3</sub>-mediated oxidation yields the benzimidazolequinone,<sup>32</sup> though the procedure is undesirable in the presence of other acid-sensitive moieties (Scheme 3.11).



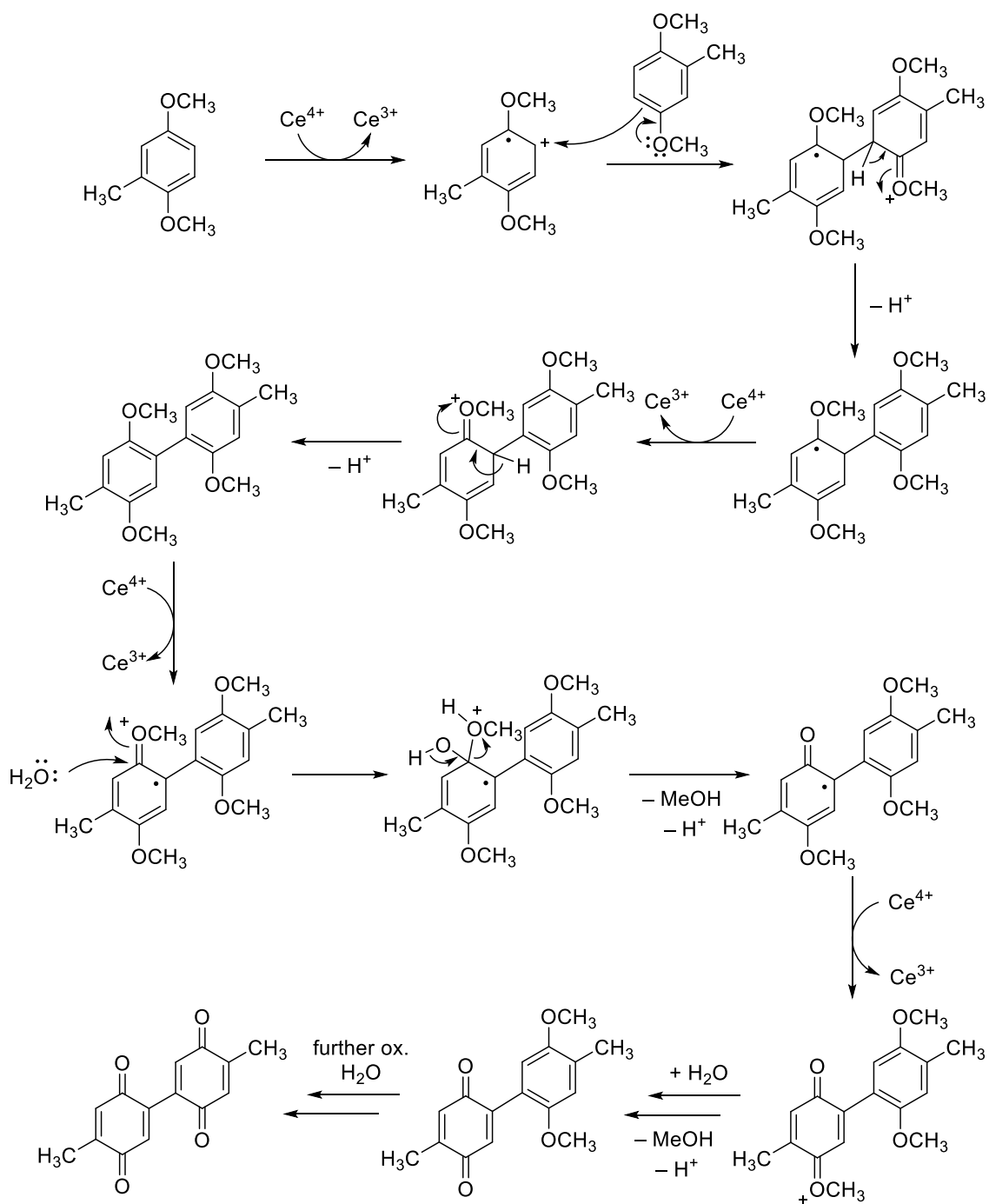
**Scheme 3.11** Benzimidazolequinone synthesis using HBr/FeCl<sub>3</sub>.<sup>32</sup>

Stronger oxidants circumvent the acidic demethylation step, offering a one-step oxidation from dimethoxybenzimidazoles to the quinone (Scheme 3.12). NBS in combination with a trace amount of H<sub>2</sub>SO<sub>4</sub> was used to oxidize dimethoxybenzimidazoles containing an acid sensitive aziridine pendant to benzimidazolequinones with minor amounts of brominated product given.<sup>33</sup> Bis-[(trifluoroacetoxy)iodo]benzene (PIFA) has been used to effect the same oxidative transformation of two analogous 4,7-dimethoxyindoles.<sup>34,35</sup> Oxidative dimerization of dimethoxybenzenes to diquinones is most often achieved through the use of ceric ammonium nitrate (CAN),<sup>36</sup> and one report exists of a benzimidazolequinone dimer in low yield.<sup>37</sup>



**Scheme 3.12** One-step oxidation of dimethoxybenzimidazoles to benzimidazolequinones.<sup>33,34,36,37</sup>

Given that oxidative dimerization of quinones does not occur using CAN,<sup>36</sup> dimerization is proposed to occur upon one-electron oxidation of dimethoxybenzene,<sup>38</sup> with C-C bond formation following nucleophilic addition of another molecule of the electron-rich aromatic (Scheme 3.13). The role of water in oxidative demethylation to give benzimidazolequinones has been confirmed using isotopic labelling experiments.<sup>39</sup>

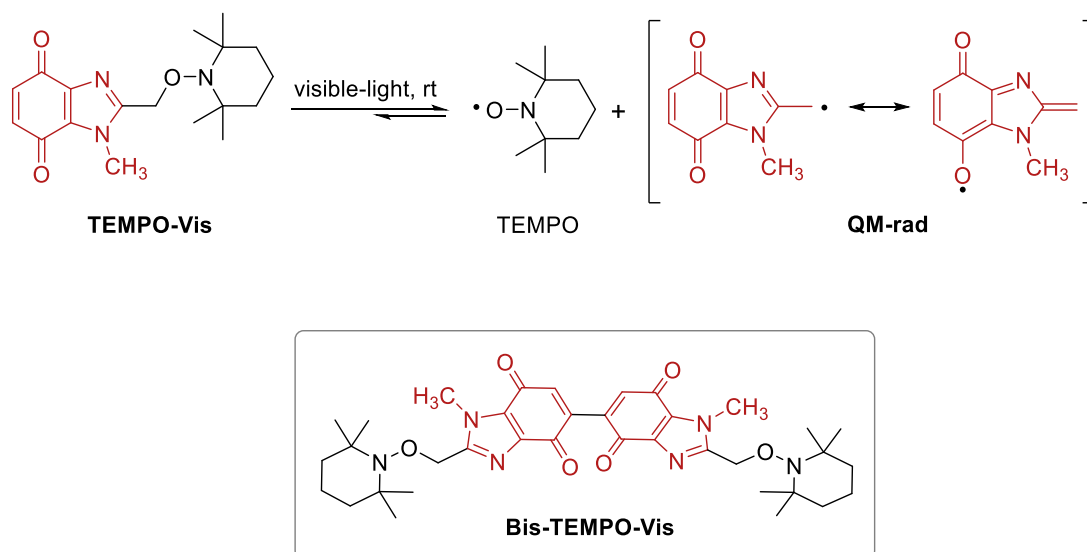


**Scheme 3.13** Mechanism of CAN-mediated dimerization of dimethoxybenzene to diquinone.

### 3.2 Chapter Aims and Objectives

In this chapter, we aim to:

- Establish visible-light active nitroxide-releasing benzimidazolequinone alkoxyamines and bis-alkoxyamines. **TEMPO-Vis** and **Bis-TEMPO-Vis** alkoxyamines are proposed based on the formation of a stabilized quinone methide-type radical (Scheme 3.13).
- Prepare visible-light active benzimidazolequinone alkoxyamines *via* oxidation of a dimethoxybenzimidazole alkoxyamine precursor.
- Tune the light activity of a bis-alkoxyamine by synthetic deactivation of one of its two benzimidazolequinone chromophores.
- Characterize the visible-light release kinetics of TEMPO nitroxide from **TEMPO-Vis** and **Bis-TEMPO-Vis**.

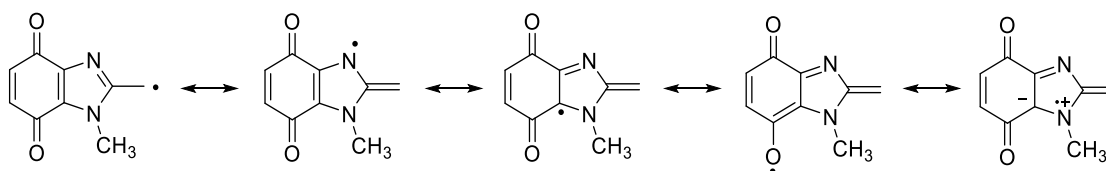


**Scheme 3.13** Controllable unmasking of quinone methide radicals using visible-light.

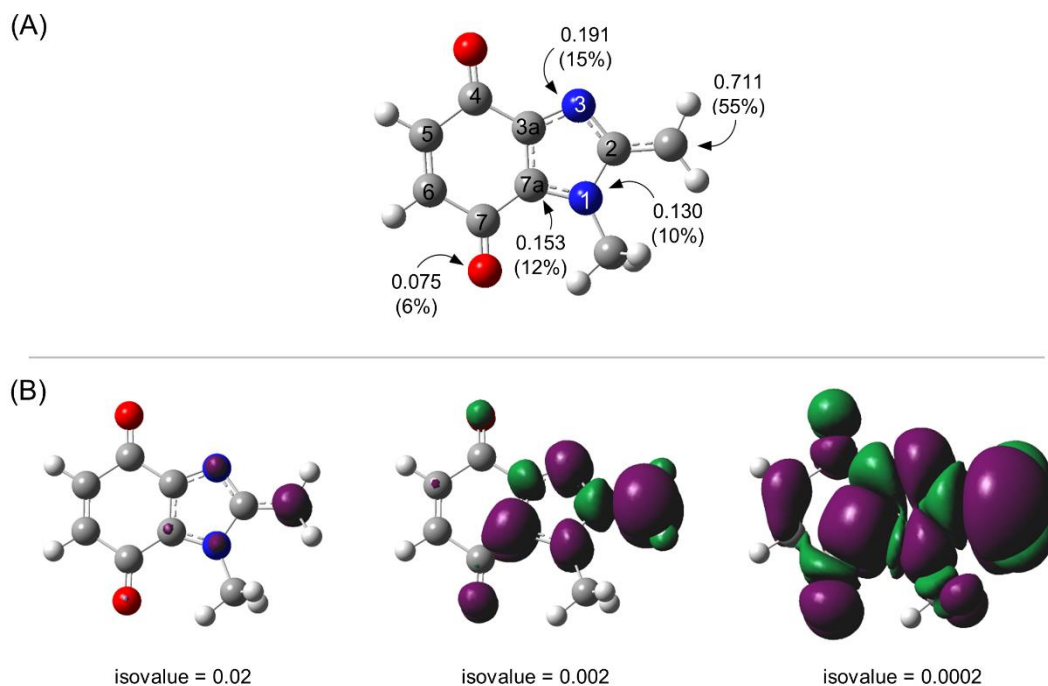
### 3.3 Results and Discussion

#### 3.3.1 DFT investigation into TEMPO-Vis reactivity

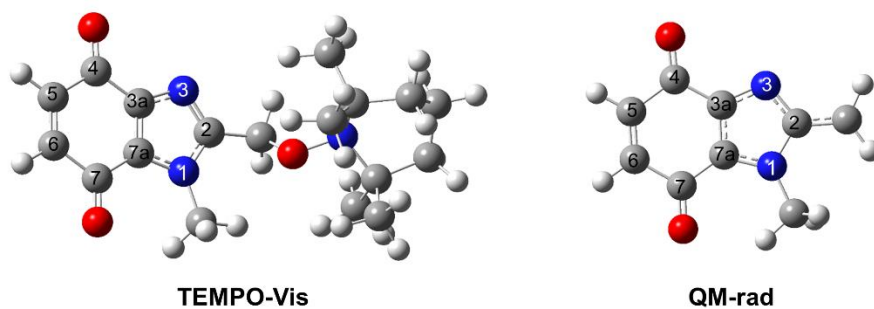
The premise for the room temperature homolysis of **TEMPO-Vis** was obtained through DFT investigation of the level of delocalization of the unpaired electron in **QM-rad**. DFT supported the traditional resonance structures (Scheme 3.10) with significant distribution of spin density into the benzimidazolequinone ring system, including onto the quinone 7O-atom (Figure 3.3). The largest positive spin density resides on the exocyclic C-atom (55%), as is typical of a benzylic-type system.<sup>40</sup> An associated shortening of the 2C–CH<sub>2</sub> bond relative to **TEMPO-Vis**, indicates partial double bond character (Table 3.1).



**Scheme 3.10** Resonance stabilization of **TEMPO-Vis** derived alkyl radical (**QM-rad**).



**Figure 3.3** (A) DFT-derived atomic NBO spin densities; (B) Spin density distribution across **QM-rad** for three different isovalues with positive spin density appearing in purple and negative spin density in green. Geometry optimization performed in the gas phase using M06-2X/6-311++G (d,p), and NBO energy calculation performed using M06-2X/cc-pVTZ.

**Table 3.1** DFT-derived bond lengths in the benzimidazolequinone core of **TEMPO-Vis** and **QM-rad**.<sup>a</sup>

bond	TEMPO-Vis length (Å)	QM-rad length (Å)
1N—CH <sub>3</sub>	1.459	1.456
1N—2C	1.366	1.388
1N—7aC	1.366	1.361
2C—CH <sub>2</sub>	1.493	1.389
2C—3N	1.319	1.354
3N—3aC	1.359	1.333
3aC—4C	1.475	1.483
3aC—7aC	1.377	1.395
4C—O	1.206	1.205
4C—5C	1.504	1.499
5C—6C	1.336	1.336
6C—7C	1.495	1.496
7C—O	1.213	1.216
7C—7aC	1.462	1.458

<sup>a</sup>DFT geometry optimization performed in the gas phase using M06-2X/6-311++G (d,p), specifying singlet multiplicity for **TEMPO-Vis** and doublet multiplicity for **QM-rad**.

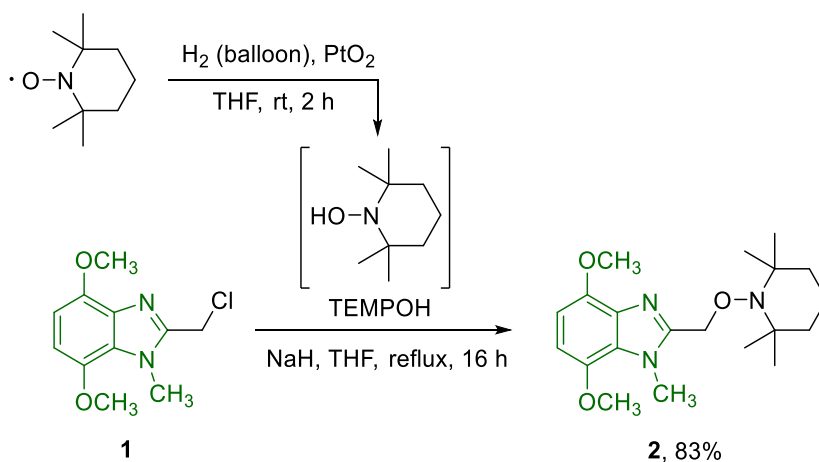


Given that photolysis of alkoxyamines occurs *via* triplet energy transfer to the H<sub>2</sub>C–O alkoxyamine bond,<sup>16,17,23,41</sup> DFT was used to estimate the bond dissociation energy (BDE), and the lowest triplet energy level ( $E_T$ ) of **TEMPO-Vis**. The model-alkoxyamine (**TEMPO-Vis**) was found to have a suitably low BDE (85.1 kJ·mol<sup>-1</sup>) compared to benzylic thermally labile (92.7–108.7 kJ·mol<sup>-1</sup>),<sup>42</sup> and UV-light activated (80–122 kJ·mol<sup>-1</sup>)<sup>16</sup> alkoxyamines, with enough driving force in the  $E_T$  to support the observed bond dissociation:  $\Delta G_d = \text{BDE} - E_T = -122.3 \text{ kJ}\cdot\text{mol}^{-1}$  (see section 3.3.3 later).

### 3.3.2 Synthesis

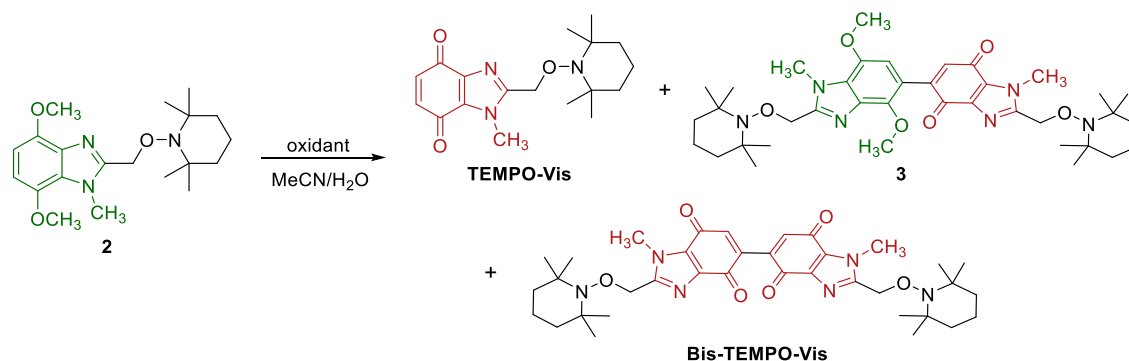
#### 3.3.2.1 Synthesis of benzimidazolequinone alkoxyamine and bis-alkoxyamines

The preparation of **TEMPO-Vis** and **Bis-TEMPO-Vis** from 4,7-dimethoxybenzimidazole alkoxyamine precursor **2**, using one-step oxidation was investigated. Alkoxyamine **2** was prepared in 83% yield from the substitution of 2-(chloromethyl)-4,7-dimethoxy-1-methyl-1*H*-benzimidazole (**1**) with the Na salt of *in situ* generated 2,2,6,6-tetramethylpiperidin-1-ol (TEMPOH<sup>43</sup>) (Scheme 3.11).



**Scheme 3.11** Synthesis of 4,7-dimethoxy-1-methyl-2-[(2,2,6,6-tetramethylpiperidin-1-yl)oxy]methyl-1*H*-benzimidazole **2**.

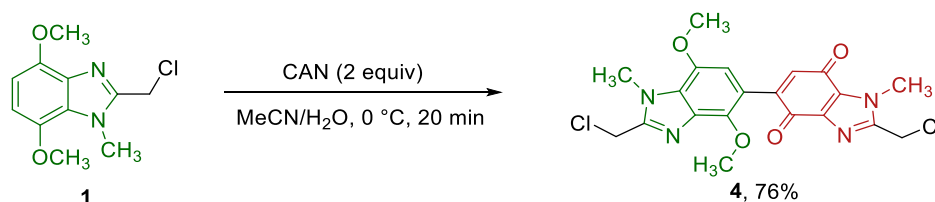
Previous work used NBS in combination with H<sub>2</sub>SO<sub>4</sub> to convert 4,7-dimethoxybenzimidazole into benzimidazolequinone.<sup>33</sup> In the present work, **TEMPO-Vis** was isolated in 52% yield (Table 3.2), with some undesirable bromination of **2** observed using HPLC-MS. PIFA [(CF<sub>3</sub>CO<sub>2</sub>)<sub>2</sub>IPh] improved the yield of **TEMPO-Vis** to

**Table 3.2** Oxidation of dimethoxybenzimidazoles to visible-light sensitive benzimidazolequinone-alkoxyamines<sup>a,b</sup>

oxidant (equiv)	TEMPO-Vis (%)	<b>3</b> (%)	Bis-TEMPO-Vis (%)
NBS (1.1) <sup>c</sup>	52 <sup>d</sup>	-	-
PIFA (1.5) <sup>e</sup>	78	-	-
CAN (2.0) <sup>f</sup>	-	86	-
CAN (3.2) <sup>f</sup>	-	-	82

<sup>a</sup>Isolated yields. <sup>b</sup>Experiments performed in the absence of light. <sup>c</sup>H<sub>2</sub>SO<sub>4</sub> (1.7 equiv), THF/H<sub>2</sub>O, rt, 10 min. <sup>d</sup>Brominated **2** and recovered **2** detected by HPLC-MS. <sup>e</sup>rt, 3 h. <sup>f</sup>0 °C, 20 min.

78%. Treatment with CAN (2 equiv) afforded bis-alkoxyamine **3** in 86% yield, as the product of oxidative coupling of benzimidazolequinone **TEMPO-Vis** with dimethoxybenzimidazole **2**. The analogous synthesis in 76% yield of bis-methylene chloride **4** (Scheme 3.11), provided X-ray crystallographic evidence of the regioselective dimethoxybenzimidazole-benzimidazolequinone C5-C5' bridge formation (Figure 3.4), with alternative couplings at C5-C6', C6-C5' and C6-C6' not observed.

**Scheme 3.11** Synthesis of bis-methylene chloride **4**.

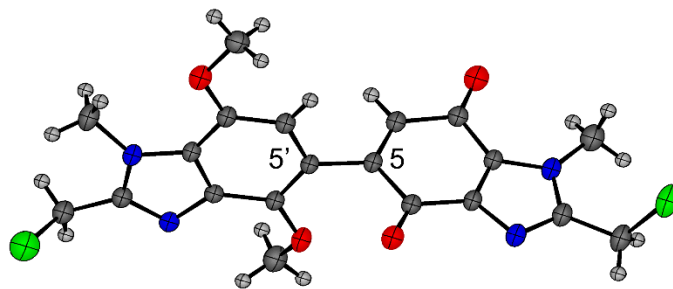


**Figure 3.4** X-ray crystal structure of 2,2'-bis(chloromethyl)-4',7'-dimethoxy-1,1'-dimethyl-1*H*,1'*H*-[5,5'-bibenzimidazole]-4,7-dione **4**.

Increased amounts of CAN (3.2 equiv) gave the fully oxidized **Bis-TEMPO-Vis** in 82% yield, with suitable crystals for X-ray crystallography obtained (Figure 3.5). During the dropwise addition of aq CAN for the synthesis of the intensely yellow-colored **Bis-TEMPO-Vis**, the transition through the intermediate deep-red solution of bis-alkoxyamine **3**, consisting of an electron-rich dimethoxybenzene attached to an electron-poor quinone moiety was observed.

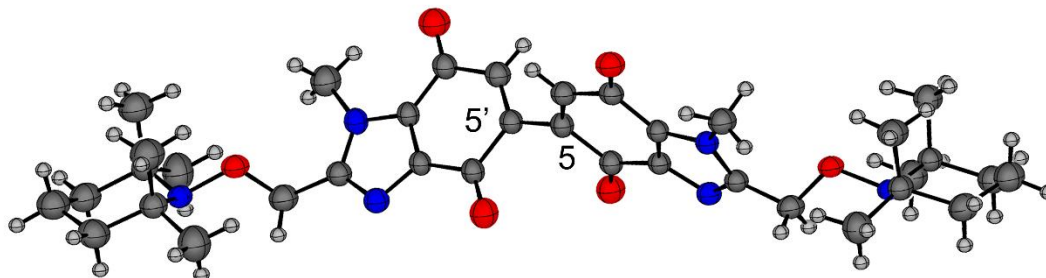


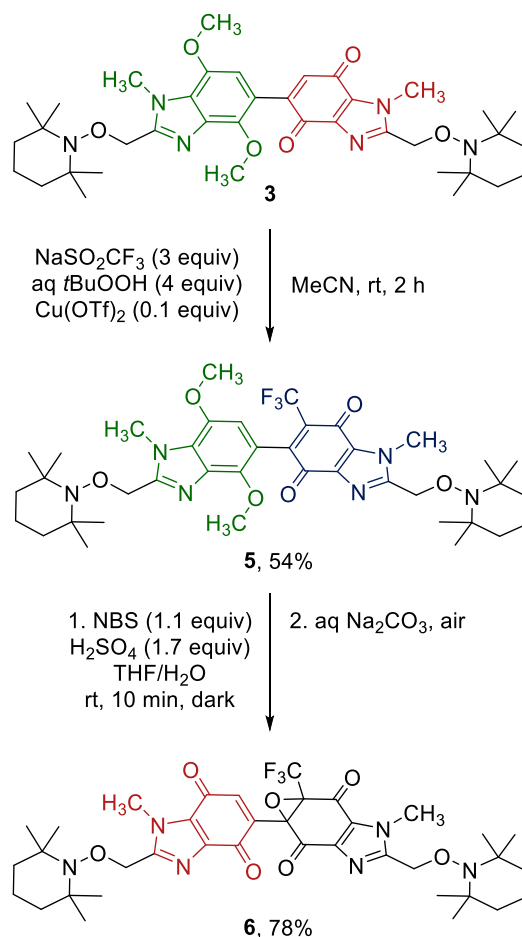
**Figure 3.5** X-ray crystal structure of **Bis-TEMPO-Vis**.

### 3.3.2.2 Synthetic chromophore deactivation

To investigate the necessity in **Bis-TEMPO-Vis** of the benzimidazolequinone chromophore for the release of both attached TEMPO residues, a selective epoxidation strategy was devised for single chromophore deactivation (Scheme 3.12). Given its asymmetric aromatic/non-aromatic nature, **3** was deemed a good substrate for selective quinone functionalization. Subjecting **3** to the Langlois reaction (using  $\text{NaSO}_2\text{CF}_3$ ),<sup>44</sup> gave the electrophilic trifluoromethylated quinone bis-alkoxyamine **5** in 54% yield. The oxidative demethylation of **5** using NBS and  $\text{H}_2\text{SO}_4$  (using Table 1 conditions), followed

## Chapter 3

by mild epoxidation at the CF<sub>3</sub>-containing quinone moiety, *via* air oxidation under basic conditions, furnished epoxide-quinone **6** in 78% yield. Trifluoromethylation and the mechanism of epoxidation will be discussed in more detail in Chapter 4 (section 4.2.1 and 4.2.2.1).

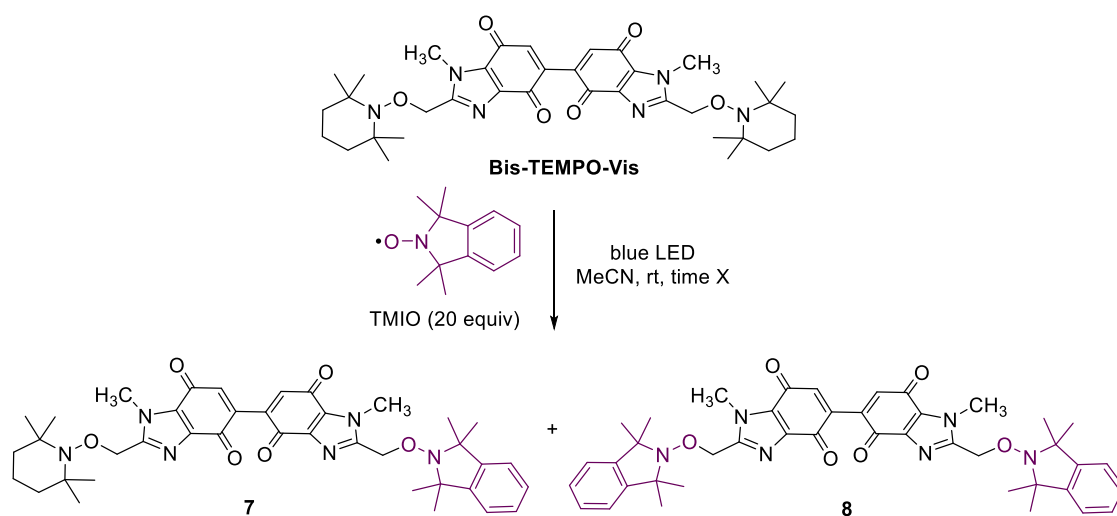


**Scheme 3.11** Chromophore deactivation *via* epoxidation.

### 3.3.3 Homolysis of alkoxyamines and bis-alkoxyamines

#### 3.3.3.1 Visible-light mediated nitroxide-exchange

The radical nature of the visible-light activated dissociation of **Bis-TEMPO-Vis** was confirmed through nitroxide-exchange experiments with excess 1,1,3,3-tetramethyl-2,3-dihydroisindol-2-ylloxyl (TMIO, Table 3.3). Irradiation with blue LED (420–520 nm) for 85 min showed sequential loss of TEMPO, leading to isolation of the mixed-nitroxide adduct **7** in 44% yield. Extending the reaction time to 720 min gave **8**, the product of double-TMIO exchange in 76% yield.

**Table 3.3** Visible-light mediated nitroxide-exchange.<sup>a</sup>

irradiation time X (min)	<b>Bis-TEMPO-Vis</b> (%) <sup>b</sup>	<b>7</b> (%) <sup>b</sup>	<b>8</b> (%) <sup>b</sup>
20	72	25	3
85	26	47 (44) <sup>c</sup>	27
720	1	19	80 (76) <sup>c</sup>

<sup>a</sup>Performed using one 9 W blue LED bulb and in the absence of O<sub>2</sub>. <sup>b</sup>Conversion determined by HPLC. <sup>c</sup>Isolated yield.

### 3.3.3.2 Kinetics of visible-light homolysis

While the nitroxide-exchange approach is used for the elucidation of alkoxyamine thermal homolysis rates,<sup>20,45</sup> it was deemed unsuitable for our present visible-light investigation. This is due to nitroxide absorption in the visible region, and electron transfer-induced quenching of excited states by the free nitroxide.<sup>41,46,47</sup> O<sub>2</sub> was the preferred radical trap,<sup>16,24,48</sup> and visible-light activated alkoxyamine homolysis was carried out under an O<sub>2</sub> atmosphere, while monitoring alkoxyamine decay and TEMPO release by HPLC (Table 3.4).<sup>20,45</sup> Under blue LED, 87% conversion of **TEMPO-Vis** to TEMPO was observed after 2.25 min. The decay of **TEMPO-Vis** alkoxyamine followed first-order kinetics (Figure 3.6A), from which the dissociation rate constant ( $k_d$ ) was determined, and corresponded to a half-life ( $t_{1/2}$ ) of 6 s. By monitoring [TEMPO] growth over time (Figure 3.6B), eq 3.1 may be fitted to the plot, to provide an alternative method to determine  $k_d$ , which also gave a  $t_{1/2}$  of 6 s.

$$[\text{TEMPO}] = [\text{TEMPO}]_{\text{max}}(1 - e^{-k_d t}) \quad (3.1)$$

**Table 3.4** Kinetics for alkoxyamine homolysis under visible-light,<sup>a</sup> and DFT-calculated homolysis parameters

alkoxyamine	LED color	$k_d$ via alkoxyamine decay ( $\text{min}^{-1}$ ) <sup>b</sup>	$k_d$ via TEMPO release ( $\text{min}^{-1}$ ) <sup>c</sup>	mol% TEMPO released (time, min) <sup>d</sup>	BDE ( $\text{kJ}\cdot\text{mol}^{-1}$ ) <sup>e</sup>	$E_T$ ( $\text{kJ}\cdot\text{mol}^{-1}$ ) <sup>e</sup>
<b>TEMPO-Vis</b>	blue	$6.71 \pm 0.21$	$7.29 \pm 0.26$	87 (2.25)	85.1	207.4
<b>Bis-TEMPO-Vis</b>	blue	$2.78 \pm 0.07$	$2.66 \pm 0.09$	175 (2.25)	104.9	215.5
<b>6</b>	blue	$1.27 \pm 0.16$	$1.41 \pm 0.24$	64 (2.25)	$99.7, ^f 104.6^g$	209.7
<b>3</b>	blue	$0.00313 \pm 0.00055$	$0.00417 \pm 0.00024$	78 (480)	$104.1, ^f 111.9^g$	176.8
<b>TEMPO-Vis</b>	green	$0.0948 \pm 0.0032$	$0.0993 \pm 0.0063$	80 (25)	-	-
<b>Bis-TEMPO-Vis</b>	green	$0.148 \pm 0.002$	$0.146 \pm 0.004$	162 (15)	-	-
<b>6</b>	green	$0.0321 \pm 0.0007$	$0.0346 \pm 0.0061$	43 (65)	-	-
<b>3</b>	green	$< 2 \times 10^{-4}$	-	$< 5$ (480)	-	-

<sup>a</sup>Conditions: alkoxyamine (0.25 mM, DCE) illuminated by blue ( $1 \times 9$  W) or green ( $2 \times 9$  W) LED bulbs under  $\text{O}_2$  balloon, with HPLC analysis. Experiments performed in triplicate. <sup>b</sup>Dissociation rate ( $k_d$ ) derived from slope of Figure 3.6A or 3.9A. <sup>c</sup>Derived from fit of eq 3.1 to Figure 3.6B or 3.9B. <sup>d</sup>HPLC yield based on starting alkoxyamine. <sup>e</sup>M06-2X/6-311++G (d,p). <sup>f</sup>BDE at benzimidazolequinone part. <sup>g</sup>BDE at epoxide/dimethoxybenzimidazole part.

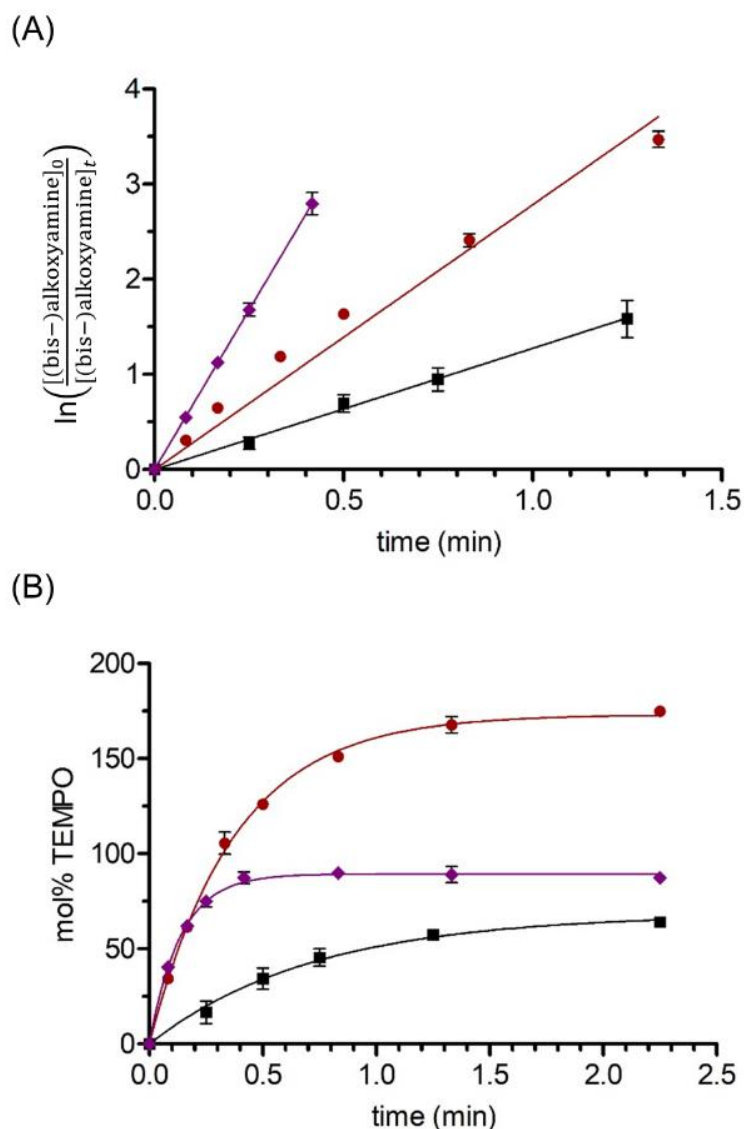


**Figure 3.6** Kinetics (at rt) of alkoxyamine and bis-alkoxyamine homolysis in blue LED according to (A) (bis-)alkoxyamine decay and (B) TEMPO release. Eq 3.1 was fitted to the plots in (B) using GraphPad Prism software. Key: **TEMPO-Vis** ( $\blacklozenge$ ), **Bis-TEMPO-Vis** ( $\bullet$ ) and **6** ( $\blacksquare$ ). Conditions: alkoxyamine (0.25 mM, DCE) illuminated by one blue LED bulb (9 W) under O<sub>2</sub> balloon, with HPLC analysis. Experiments performed in triplicate.

The on/off switchable nature of homolysis was demonstrated by alternating periods of light and dark for **TEMPO-Vis** using blue LED (Figure 3.7). Dissociation was halted by switching off the light, and indeed, solid samples and solutions of the alkoxyamines are indefinitely stable in the dark.

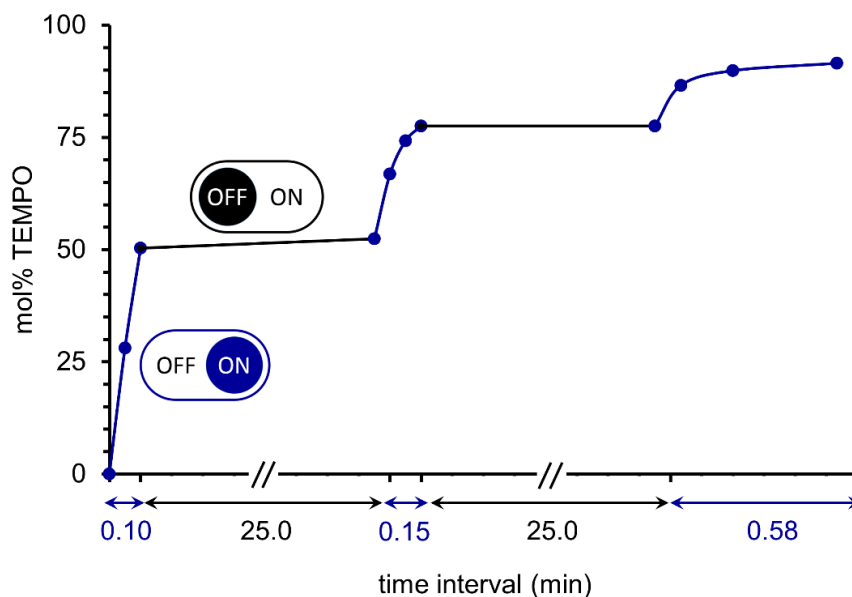


**Figure 3.7** On/off control in the blue LED-induced homolysis of **TEMPO-Vis**. Conditions: **TEMPO-Vis** (0.25 mM, DCE) illuminated by one blue LED bulb (9 W) under O<sub>2</sub> balloon, with HPLC analysis. Connecting lines drawn between data points.

For the bis-alkoxyamine, **Bis-TEMPO-Vis**, there are two possible dissociation rate constants,  $k_{d1}$  and  $k_{d2}$  corresponding to TEMPO release from the starting compound, and from the monoalkoxyamine O<sub>2</sub>-trapped intermediate(s), with hydroperoxide and aldehyde intermediates detected by HPLC-MS (Figure 3.8A). Just over twice as much TEMPO was released from **Bis-TEMPO-Vis** compared to **TEMPO-Vis**, with 175% released after the same period of 2.25 min. The  $k_{d1}$  was directly measured from the first-order decay plot of **Bis-TEMPO-Vis**, and corresponded to a  $t_{1/2}$  of 15 s in blue LED. The slower photolysis of **Bis-TEMPO-Vis**, was supported by the DFT-derived  $\Delta G_d$  being 11.7 kJ·mol<sup>-1</sup> less favorable compared to **TEMPO-Vis** (Table 3.4). The rate of overall TEMPO release attained by fitting eq 3.1 to the [TEMPO] vs time plot (Figure 3.6B), combines release from the starting bis-alkoxyamine ( $k_{d1}$ ), as well as from the O<sub>2</sub>-trapped intermediate alkoxyamine(s) ( $k_{d2}$ ). The rate constant derived in this way was in good agreement with the rate of **Bis-TEMPO-Vis** decay (Figure 3.6A and Table 3.4). This infers that for **Bis-TEMPO-Vis**,  $k_{d1} \approx k_{d2}$ , and the homolysis of the alkoxyamine in the O<sub>2</sub>-trapped intermediate(s) occurs at an almost identical rate to that of the starting bis-alkoxyamine.



## Chapter 3

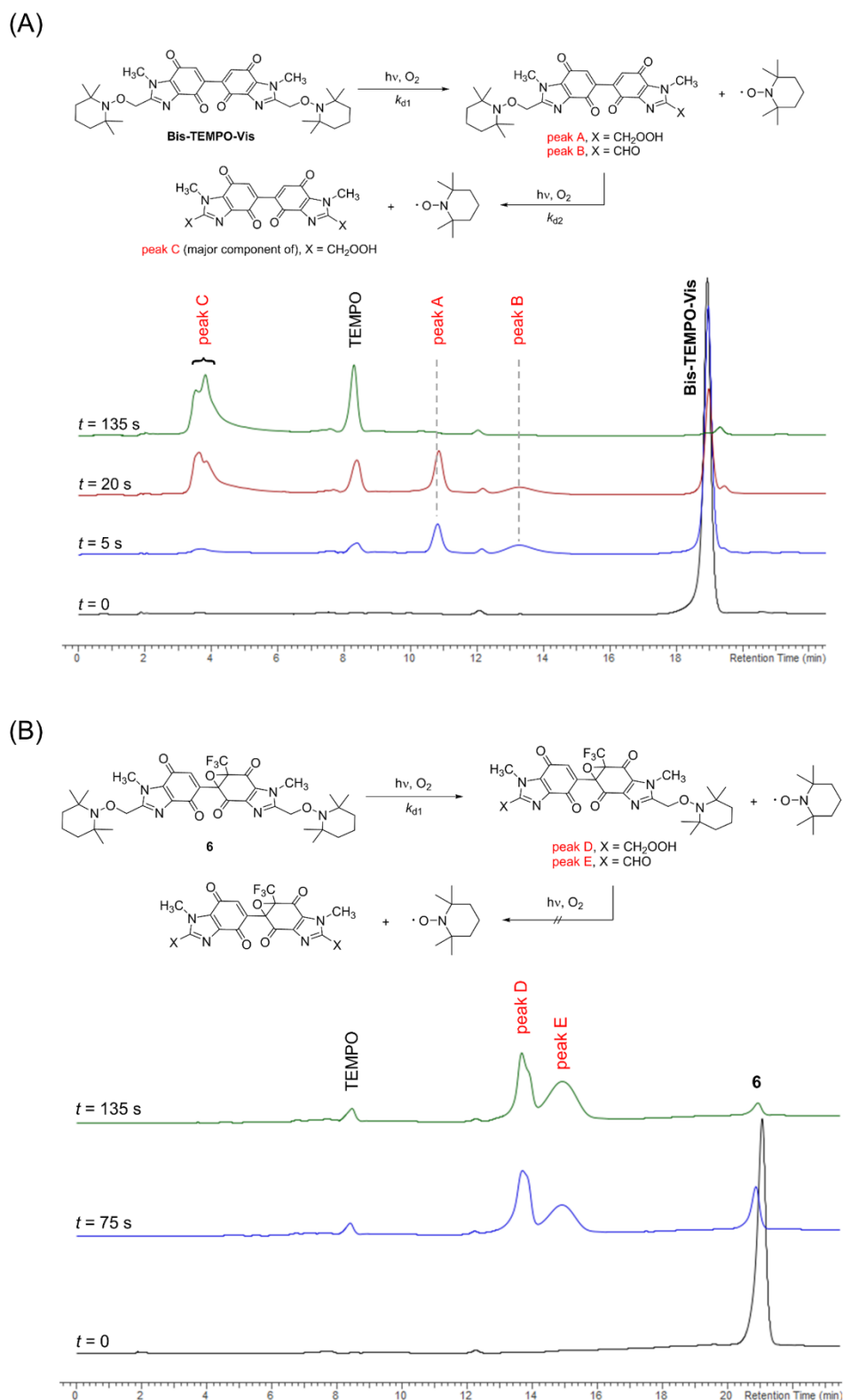


**Figure 3.8** HPLC-MS (ESI) monitoring of the blue LED homolysis of (A) **Bis-TEMPO-Vis** and (B) epoxide-quinone **6**. The  $[\text{M} + \text{H}]^+$  adducts were detected and used to assign the structures corresponding to peaks A, B, D and E. The  $[\text{M} + \text{Na} + \text{MeCN}]^+$  adduct was used to assign the major component of a complex mixture in peak C. The accuracy of all HRMS data was better than 5 ppm compared to the predicted masses.

By removing one of the chromophores of **Bis-TEMPO-Vis** in epoxide-quinone **6**, the release of < 1 equiv TEMPO occurred over the same time period (Table 3.4). The homolysis of one alkoxyamine of **6** was detected by HPLC-MS, with singly-homolyzed O<sub>2</sub>-trapped adducts observed (Figure 3.8B), and no products of double alkoxyamine homolysis detected. Single bond homolysis occurred despite the BDE of the alkoxyamine of the epoxide part mirroring the BDE of **Bis-TEMPO-Vis**. Time-dependent density functional theory (TD-DFT)<sup>49</sup> calculations supported the localization of the frontier molecular orbitals on only the fully-conjugated quinone moiety of **6** (Figure 3.9). The  $k_d$  of the labile alkoxyamine of **6** is less than half that of **Bis-TEMPO-Vis** in blue LED, and given that the  $\Delta G_d$  values of the quinone-alkoxyamine in **6** and **Bis-TEMPO-Vis** are similar (at about  $-110 \text{ kJ}\cdot\text{mol}^{-1}$ ), the observed reduction in rate may be attributed to the lower absorption of the partially deactivated **6** in the visible region (Figure 3.10).

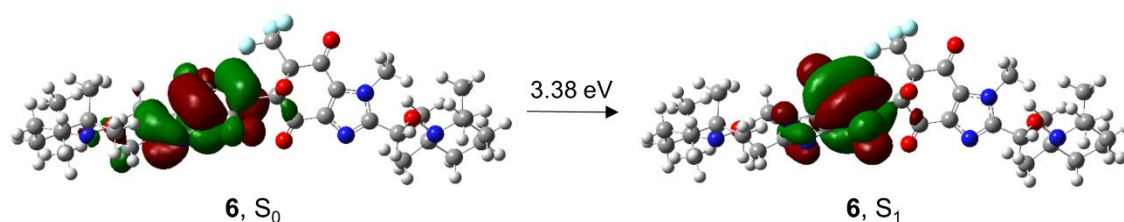


**Figure 3.9** TD-DFT analysis of ground and excited state orbital delocalization in epoxide-quinone **6**. Conditions: PCM/M06-2X/6-311++G (d,p), using DCE as solvent and the natural transition orbital (NTO)<sup>50</sup> method for visualization.

The rate of homolysis decreased using green LED (470–600 nm), by 71-, 19- and 40-fold for **TEMPO-Vis**, **Bis-TEMPO-Vis**, and **6** respectively (Figure 3.11), due to less absorption. Moreover, **Bis-TEMPO-Vis** underwent photolysis at a faster rate than **TEMPO-Vis** in green LED, in accordance with  $\lambda_{\text{max}}$  of the former being red-shifted by 12 nm (Figure 3.10). The result in green LED, is a reversal in the magnitude of  $k_d$  that was observed for blue LED for the two compounds. The same conclusion of  $k_{d1} \approx k_{d2}$  for **Bis-TEMPO-Vis** was reached for green LED activation.

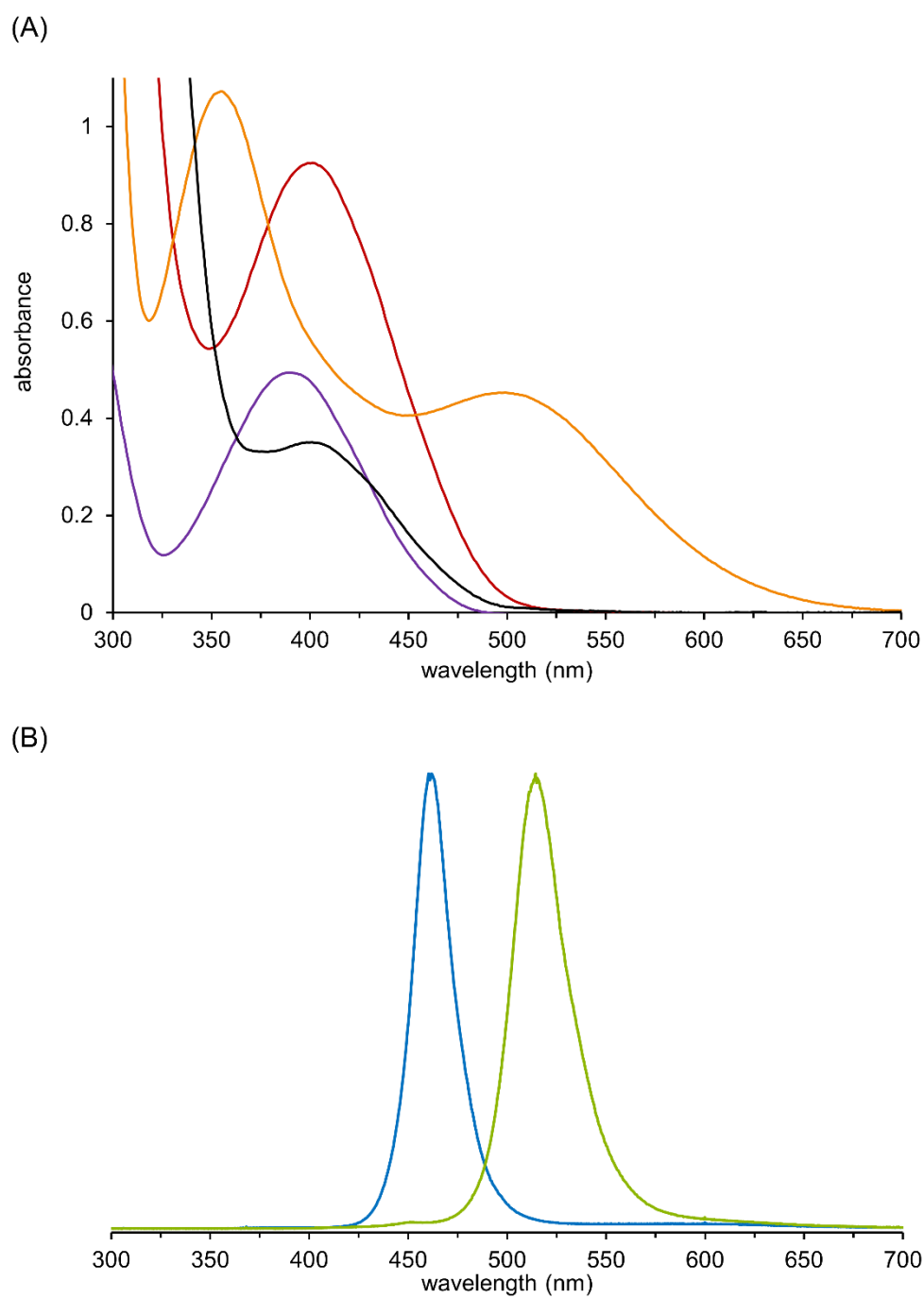


**Figure 3.10** (A) UV-visible light absorption spectra recorded in DCE (all  $3.75 \times 10^{-4}$  M) of **TEMPO-Vis** (purple), dimethoxybenzimidazole-benzimidazolequinone **3** (orange), **Bis-TEMPO-Vis** (red) and epoxide-quinone **6** (black). (B) Emission spectra for blue and green LEDs.

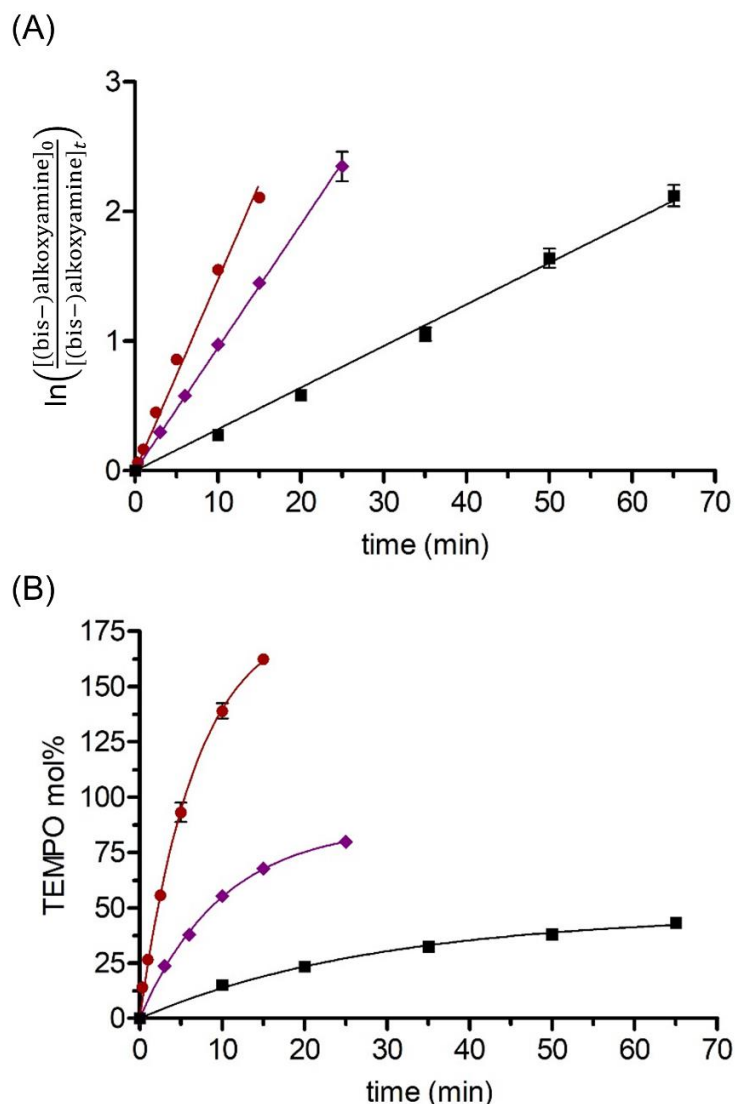
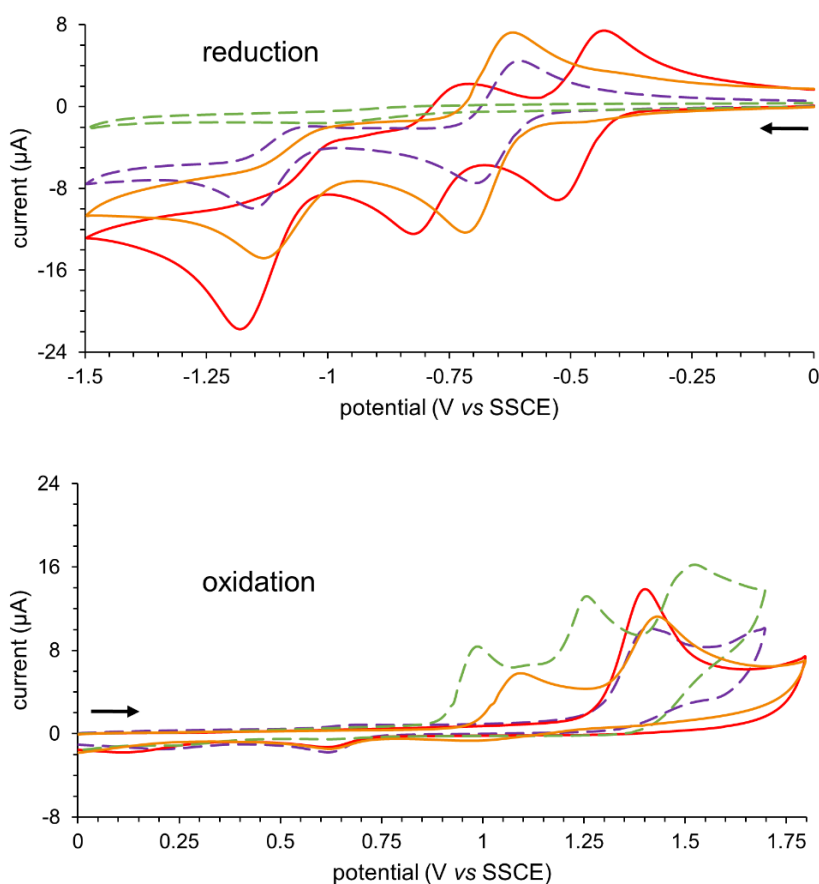


**Figure 3.11** Kinetics (at rt) of alkoxyamine and bis-alkoxyamine homolysis in green LED according to (A) (bis-)alkoxyamine decay and (B) TEMPO release. Eq 3.1 was fitted to the plots in (B) using GraphPad Prism software. Key: **TEMPO-Vis** (—◆—), **Bis-TEMPO-Vis** (—●—) and **6** (—■—). Conditions: alkoxyamine (0.25 mM, DCE) illuminated by two green LED bulbs (9 W each) under O<sub>2</sub> balloon, with HPLC analysis. Experiments performed in triplicate.

Dimethoxybenzene-coupled quinone bis-alkoxyamine **3** was found to be largely stable under visible-light, having a  $k_d$  three orders of magnitude smaller than its fully-oxidized derivative, **Bis-TEMPO-Vis**, in blue and green LED (Table 3.4). Although **3** possesses a similar first BDE to **Bis-TEMPO-Vis**, its  $E_T$  was more than 30 kJ·mol<sup>-1</sup> lower than the other alkoxyamines. The  $\lambda_{\text{max}}$  of **3** was red-shifted by 96 nm compared to **Bis-TEMPO-Vis**, suggesting the presence of a low-lying charge-transfer (CT) state. Given that **3** is comprised of a benzimidazolequinone and dimethoxybenzimidazole, the cyclic voltammetry of **3**, and those of its constituent alkoxyamines (**2** and **TEMPO-Vis**), proved the localization of the HOMO and LUMO to the dimethoxybenzimidazole and the

### Chapter 3

benzimidazolequinone motifs respectively (Figure 3.12). This is indicated by the first oxidation of **3** correlating well with the first oxidation of dimethoxybenzimidazole (DMB/DMB<sub>ox</sub>) **2**, and the first reduction of **3** correlating with the first quinone reduction (Q<sub>1</sub>/Q<sub>1</sub><sup>•-</sup>) of **TEMPO-Vis**. Cyclic voltammetry on **Bis-TEMPO-Vis** revealed electronic coupling of the two quinone moieties, resulting in two consecutive one-electron reductions (Q<sub>1</sub>/Q<sub>1</sub><sup>•-</sup> = - 0.48 V and Q<sub>2</sub>/Q<sub>2</sub><sup>•-</sup> = - 0.77 V), and a further two-electron reduction at - 1.18 V, which correlated to the second (Q<sup>•-</sup>/Q<sup>2-</sup>) one-electron reduction of **TEMPO-Vis**. The first oxidation of **Bis-TEMPO-Vis** correlates with the equivalent process in **TEMPO-Vis**.



	reduction			oxidation	
	Q <sub>1</sub> /Q <sub>1</sub> <sup>•-</sup>	Q <sub>2</sub> /Q <sub>2</sub> <sup>•-</sup>	Q <sup>•-</sup> /Q <sup>2-</sup>	DMB/DMB <sup>ox</sup>	Q/Q <sup>ox</sup>
<b>3</b>	- 0.67	-	- 1.13 (irrev)	1.09 (irrev)	1.43 (irrev)
<b>TEMPO-Vis</b>	- 0.65	-	- 1.16 (irrev)	-	1.41 (irrev)
<b>2</b>	-	-	-	0.99 (irrev)	-
<b>Bis-TEMPO-Vis</b>	- 0.48	- 0.77	- 1.18 (irrev)	-	1.40 (irrev)

**Figure 3.12** Cyclic voltammetry of **3** (—), **TEMPO-Vis** (---), **2** (- - -) and **Bis-TEMPO-Vis** (—) with associated table of redox potentials (all in V). Conditions: scan rate of 0.1 V/s, alkoxyamine (1 mM), anhydrous DCE (with Bu<sub>4</sub>NPF<sub>6</sub> as electrolyte, 0.2 M), arrow indicates direction of scan.

TD-DFT was used to provide graphical representation of the spatially-separated ground and excited state orbitals in CT compound **3** (Figure 3.13). The ground state ( $S_0$ ) of **3** is primarily localized on the dimethoxybenzimidazole, while the density of the first excited state ( $S_1$ ) is entirely localized on the quinone, with limited overlap between the two states. Such donor-acceptor processes have rendered photodeprotection inefficient for some photo-protecting groups.<sup>51</sup> In comparison, the CT effect is not observed in the analogous TD-DFT of **Bis-TEMPO-Vis**.

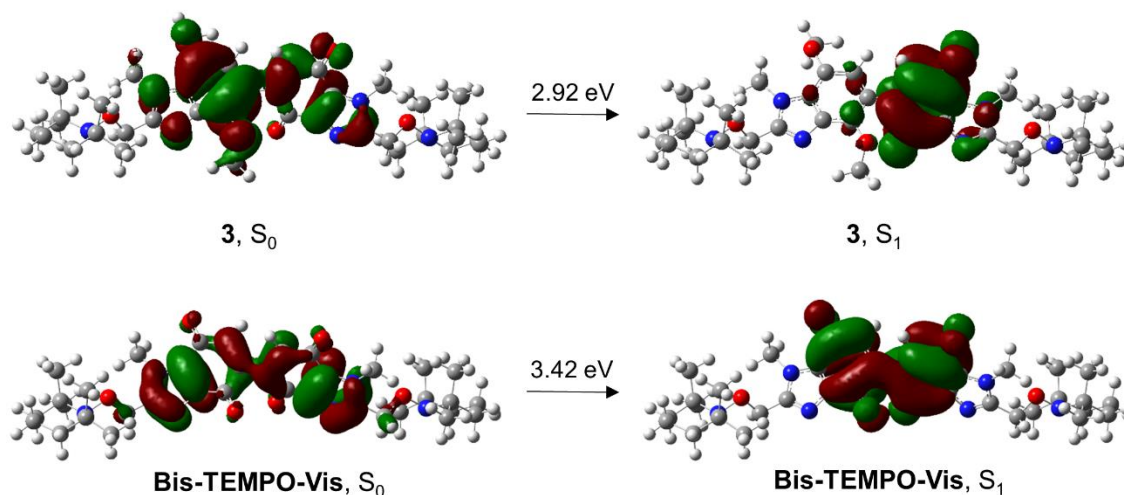


**Figure 3.13** TD-DFT analysis of ground and excited state orbital delocalization in *p*-dimethoxybenzene-coupled quinone **3** and **Bis-TEMPO-Vis**. Conditions as described in Figure 3.9.

### 3.4 Conclusions

Molecules with a diverse range of photochemical properties were prepared from a single dimethoxybenzimidazole precursor by variation of the oxidative reaction. The first alkoxyamine that can release up to two equivalents of nitroxide per molecule, using visible-light activation is established, and can do so sequentially with  $k_{d1} \approx k_{d2}$ . Synthetic deactivation of one chromophore in bis-benzimidazolequinone alkoxyamine limited TEMPO release to  $< 1$  equiv, despite the second alkoxyamine having a favorable BDE. For blue LED, the rates of bond homolysis can largely be rationalized by thermodynamics, while for green LED variations in absorbance become more important. The placement of an electron-rich substituent on the quinone gives a charge-transfer state that stabilizes the quinone under visible-light.

### 3.5 Future Work

The ability to unmask a reactive carbon-centred radical makes the benzimidazolequinone-alkoxyamines interesting candidates for photoactivated chemotherapy (PACT), with the visible-light trigger offering spatial and temporal cytotoxic control. In the field of materials science, the alkoxyamines are promising radical initiators for visible-light mediated vinyl monomer photopolymerizations, with the bis-alkoxyamines providing access to more exotic macromolecular architectures, including antibiotic end-functionalized polymers.

## 3.6 Experimental

### 3.6.1 Materials

(4,7-Dimethoxy-1*H*-benzimidazol-2-yl)methanol was synthesized from 2,3-diamino-1,4-dimethoxybenzene and glycolic acid (Sigma-Aldrich, 99%) in HCl (4 M, prepared from 37% reagent grade, Sigma-Aldrich) using the Phillips reaction.<sup>52</sup> 2,3-Diamino-1,4-dimethoxybenzene was synthesized according to the literature,<sup>53</sup> using 1,4-dimethoxybenzene (Sigma-Aldrich, 99%), nitric acid (Sigma-Aldrich, 70%), H<sub>2</sub> (BOC, 99.99%), Pd/C (ACROS Organics, 10%), and EtOAc (Fischer Scientific, ≥ 99%). 1,1,3,3-Tetramethyl-2,3-dihydroisoindol-2-ylloxyl (TMIO) was synthesized according to the literature,<sup>54,55</sup> using phthalic anhydride (TCI, > 98%), benzylamine (Sigma-Aldrich, 99%), AcOH (Sigma-Aldrich, ≥ 99.85%), Mg turnings (Sigma-Aldrich, 98%), MeI (Sigma-Aldrich, > 99%), Et<sub>2</sub>O [(Sigma-Aldrich, > 99.5%), dried and distilled over Na (Sigma-Aldrich, > 99.8%) and benzophenone (ACROS Organics, 99%)], toluene (Fischer Scientific, ≥ 99.8%), hexanes (Fischer Scientific, bp 40–60 °C), Celite® (Sigma-Aldrich), basic aluminium oxide (VWR), 3-chloroperoxybenzoic acid (Sigma-Aldrich, 57–86%), and CH<sub>2</sub>Cl<sub>2</sub> (Fischer Scientific, ≥ 99%). NaH (Sigma-Aldrich, 60% dispersion in mineral oil), SOCl<sub>2</sub> (Sigma-Aldrich, 97%), MgSO<sub>4</sub> (Alfa Aesar, 99.5%), Na<sub>2</sub>CO<sub>3</sub> (ACROS Organics, 99.5%), (2,2,6,6-tetramethylpiperidin-1-yl)oxyl (TEMPO, Sigma-Aldrich, 98%), PtO<sub>2</sub> (Sigma-Aldrich), *N*-bromosuccinimide (NBS, Lancaster, 99%), H<sub>2</sub>SO<sub>4</sub> (BDH, 98%), [bis(trifluoroacetoxy)iodo]benzene (PIFA, Sigma-Aldrich, 97%), MeCN (Sigma-Aldrich, HPLC Plus, ≥ 99.9%), cerium(IV) ammonium nitrate (CAN, Fischer Scientific, 99%), *t*BuOOH (ACROS Organics, 70% in H<sub>2</sub>O), sodium trifluoromethanesulfinate (Langlois reagent, TCI, > 95%), Ar (BOC, 99.8%), Cu(OTf)<sub>2</sub> (Sigma-Aldrich, 98%), 1,2-dichloroethane (DCE, Sigma-Aldrich, anhydrous, 99.8%) and Bu<sub>4</sub>NPF<sub>6</sub> (Sigma-Aldrich, for electrochemical analysis, ≥ 99%) were used as received. THF (Sigma-Aldrich, ≥ 99%) was freshly distilled over Na and benzophenone. CDCl<sub>3</sub> (Sigma-Aldrich, 99.8% atom D + 0.03% Si(CH<sub>3</sub>)<sub>4</sub> v/v) and CD<sub>2</sub>Cl<sub>2</sub> (Eurisotop, 99.9% atom D) were used as received. Thin layer chromatography (TLC) was performed on Merck TLC silica gel 60 F<sub>254</sub> plates using a UV lamp (254 nm) for visualization. Flash chromatography was performed using silica gel, pore size 60 Å, 230–400 mesh, and particle size 40–63 μm. Dry column vacuum chromatography (with Apollo Scientific silica gel ZEOprep 60 and 15–35 μm particle size),<sup>56</sup> was preferable for purification of



light-active compounds, due to the convenience of light exclusion by covering the apparatus with Al-foil during elution.

### 3.6.2 Measurements

**DFT calculations:** Geometry optimizations were performed using Gaussian 16,<sup>57</sup> installed at the Irish Centre for High-End Computing (ICHEC), using an M06-2X functional<sup>58</sup> with a 6-311++G (d,p) basis set. All structures were fully optimized in the gas phase and verified as local minima through frequency calculations. The natural bond orbital (NBO) energy calculation on **QM-rad** was performed using M06-2X with a cc-pVTZ basis set. TD-DFT was performed at the same level of theory as the geometry optimization, with 1,2-dichloroethane (DCE) as solvent using the polarizable continuum model (PCM).<sup>59</sup> Natural transition orbitals (NTOs) provided graphical representation of the ground and excited states.<sup>50</sup> Bond dissociation energies (BDEs) were calculated based on the free energy difference between the starting alkoxyamines and the radical products (thermal free energy correction was added). The lowest triplet energies ( $E_T$ ) of starting alkoxyamines are given relative to the optimized singlet ground state ( $S_0$ ) energies. A table of model energies (Table A4.1) and images of optimized models (Figure A4.1) are reported in the appendix.

**Melting points, ultraviolet-visible and infrared spectroscopy:** Melting points were measured on a Stuart Scientific melting point apparatus SMP3. Ultraviolet-visible (UV-vis) spectra were recorded using a Varian (Cary 100) UV-vis spectrometer. Infrared spectra were recorded using a Perkin-Elmer Spec 1 with ATR attached.

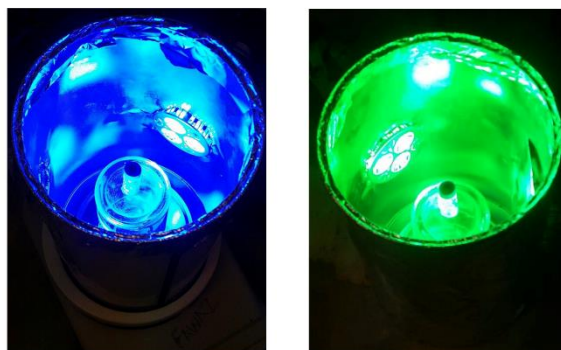
**Nuclear magnetic resonance (NMR spectroscopy):** NMR spectra were recorded using a JEOL ECX 400 MHz or a Varian 500 or 600 MHz instrument (the specific NMR frequency used is detailed in the characterization section and on spectra). The chemical shifts were in ppm relative to  $\text{Si}(\text{CH}_3)_4$  for recorded spectra in  $\text{CDCl}_3$ , and relative to  $\text{CH}_2\text{Cl}_2$  at 5.32 ppm for  $^1\text{H}$  NMR and 53.84 ppm for  $^{13}\text{C}$  NMR spectra recorded in  $\text{CD}_2\text{Cl}_2$ .  $^{13}\text{C}$  NMR data were collected at 100, 125 or 150 MHz with complete proton decoupling. NMR assignments were supported by DEPT and  $^1\text{H}$ - $^1\text{H}$  (COSY) and  $^1\text{H}$ - $^{13}\text{C}$  single bond correlation (HSQC). Multiple bond correlation of  $^1\text{H}$ - $^{13}\text{C}$  (HMBC) was used to characterize the aromatic CHs in benzimidazolequinone-dimethoxybenzimidazoles **3** and **5**, with through-space correlation (ROESY) supplementing the CH characterization

in trifluoromethylquinone **5**.  $^{19}\text{F}$  NMR data were collected at 470 MHz. NMR spectra for **4**, **7** and **8** are included in the appendix of this thesis. All other NMR spectra for this chapter are available on the RSC Publications website at <https://doi.org/10.1039/C9CC08261A>.<sup>60</sup>

**High resolution mass spectrometry (HRMS):** HRMS was carried out using ESI time-of-flight mass spectrometer (TOFMS) in positive mode using a Waters LCT Mass Spectrometry instrument. The precision of all accurate mass measurements was better than 5 ppm.

**Single crystal X-ray diffraction:** Single crystal data was collected using an Oxford Diffraction Xcalibur system operated using the CrysAlisPro software. The crystal structures were solved using ShelxT version 2014/55,<sup>61</sup> and refined using ShelxL version 2017/1,<sup>62</sup> both of which were operated within the Oscale software package.<sup>63</sup> Crystallographic data for **4** and **Bis-TEMPO-Vis** have been deposited with the Cambridge Crystallographic Data Centre with deposit numbers CCDC-1948449 and CCDC-1948448 respectively. This data is available free of charge *via* [www.ccdc.cam.ac.uk/data\\_request/cif](http://www.ccdc.cam.ac.uk/data_request/cif) (or from the Cambridge Crystallographic Data Centre, 12 Union Road, Cambridge CB2 1EZ, U.K.; fax +44 1223 336033; or e-mail [deposit@ccdc.cam.ac.uk](mailto:deposit@ccdc.cam.ac.uk)). Single crystal X-ray data and structure refinements are reported in the appendix.

**Visible-light photoreactor:** The reactor used green ( $2 \times 9$  W) or blue ( $1 \times 9$  W) LED bulb(s) placed inside an aluminium container of diameter 10 cm (below). A round-bottomed flask (25 mL capacity for TMIO-exchange experiment, Table 3.3) or a vial (1.5 mL capacity for homolysis kinetics experiments, Table 3.4) with a solution of alkoxyamine was placed in the centre of the reactor opposite the bulb. The bulb was air cooled using a 2.5 W fan, which ensured that the interior reactor temperature remained at ambient temperature. The emission spectra of the LEDs were narrow and confined to the visible region (Figure 3.10).



**Analytical HPLC:** The Agilent 1100 Series HPLC was equipped with a UV detector operating at 254 nm and a Phenomenex® BondClone™ 10  $\mu\text{m}$  C18, 250  $\times$  4.6 mm column. The sample was injected *via* automatic injector (see table below for injection volume). The flow rate of the mobile phase was 1 mL/min, and the composition depended on the experiment being performed (see below). Calibration curves were generated for [TEMPO] and [alkoxyamine] for the construction of rate plots, and for the determination of  $k_d$ .

experiment	injection volume ( $\mu\text{L}$ )	mobile phase program (%MeCN in $\text{H}_2\text{O}$ )
TMIO-exchange (Table 3.3)	5	time 0 = 45, 15 min = 95, 19 min = 95, 19.5 min = 45, 23 min = 45
<b>TEMPO-Vis</b> homolysis (Table 3.4)	5	time 0 = 45, 11.5 min = 45, 15 min = 75, 19.5 min = 75, 19.6 min = 45, 22 min = 45
<b>Bis-TEMPO-Vis</b> and <b>6</b> homolysis (Table 3.4)	10	time 0 = 45, 15 min = 95, 19 min = 95, 19.5 min = 45, 23 min = 45
<b>3</b> homolysis (Table 3.4)	5	time 0 = 45, 11.5 min = 45, 15 min = 95, 27 min = 95, 27.1 min = 45, 30 min = 45

**Preparative HPLC:** Preparative HPLC for purification of TMIO-coupled bis-alkoxyamines **7** and **8** was performed using the same equipment as above. Solutions of bis-alkoxyamines (30 mg/mL, MeCN) were injected (75  $\mu\text{L}$ ) onto the column. The mobile phase program was as follows (%MeCN in  $\text{H}_2\text{O}$ , 1 mL/min): time 0 = 70, time 17.5 min = 70, time 18 min = 98, time 23 min = 98. The eluent was collected at 16.2–

18.4 min for compound **7**, and at 13.5–15.8 min for compound **8**. Injections were repeated as required. The fractions were combined, extracted using CH<sub>2</sub>Cl<sub>2</sub>, dried (MgSO<sub>4</sub>) and evaporated to give **7** or **8**.

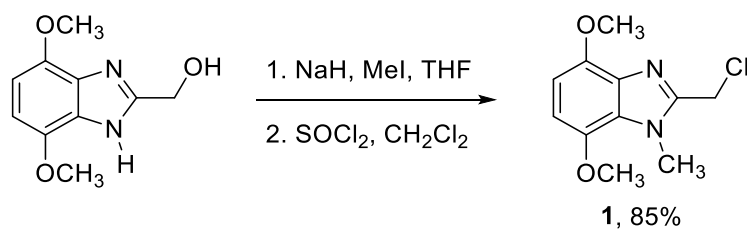
**Homolysis rates ( $k_d$ ):** A solution of alkoxyamine in DCE (1 mL, 0.25 mM) in a 1.5 mL clear glass vial was prepared in the absence of light. A sample was taken and analyzed by HPLC (representing time 0). The solution was subjected to either one blue (9 W) LED bulb or two green (9 W) LED bulbs under an O<sub>2</sub> balloon for a period of time. A sample was taken and [TEMPO] and [alkoxyamine] were measured by HPLC. During the run, the remainder of the solution was placed in the dark, which stopped the reaction, as evidenced by the on/off experiment (Figure 3.7). Illumination of the solution was resumed, with continued sampling over time. Experiments were performed in triplicate. Rate constants ( $k_d$ ) were derived using two equivalent methods: (1) using the first-order plot describing the decay of [alkoxyamine] over time and (2) using the growth of [TEMPO] and fitting eq 3.1 using the method of least squares within GraphPad Prism® software.

**Quantum yield of homolysis ( $\Phi_h$ ):** The  $\Phi_h$  was measured according to eq 3.2. The number of molecules converted was calculated based on the  $t_{1/2}$  of the alkoxyamine starting material measured by alkoxyamine decay (Table 3.4). The number of incident photons was measured using a Wavetek DM15XL multimeter connected to a calibrated Thorlabs FDS1010 Si photodiode (1 cm<sup>2</sup>), and was calculated based on the total light intensity falling on the surface of the reaction vessel from two directions: one direction measuring light emanating directly from the bulb, and the other direction being 180° opposite, accounting for any reflection from the photoreactor interior.

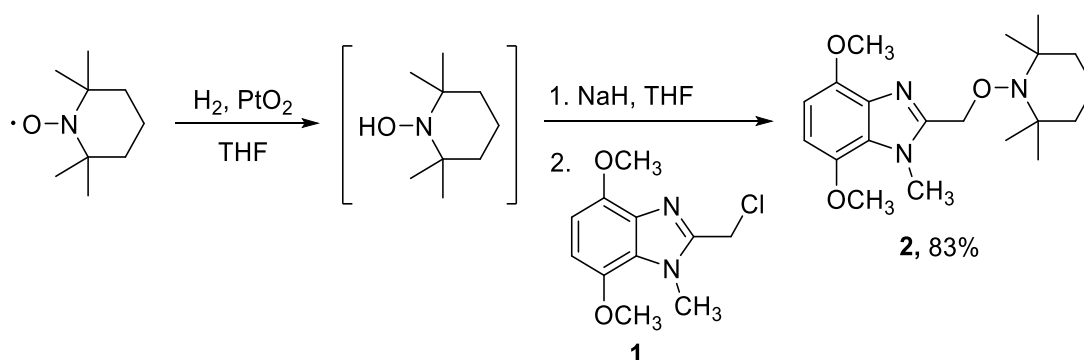
$$\Phi_h = 100 \times \frac{\text{number of molecules converted}}{\text{number of incident photons}} \quad (3.2)$$

**Cyclic voltammetry:** Cyclic voltammograms were recorded using a PalmSens3+ potentiostat equipped with a glassy carbon and Pt-wire electrode, using a sodium-saturated calomel electrode (SSCE) as reference. Cycles were performed on alkoxyamines (1 mM) at a scan rate of 0.1 V/s in anhydrous DCE using Bu<sub>4</sub>NPF<sub>6</sub> (0.2 M) as supporting electrolyte.

## 3.6.3 Synthetic procedures and characterization

**Synthesis of 2-(chloromethyl)-4,7-dimethoxy-1-methyl-1H-benzimidazole (1)**

NaH (0.212 g, 5.29 mmol, 60%) was added to (4,7-dimethoxy-1H-benzimidazol-2-yl)methanol (1.00 g, 4.81 mmol) in THF (100 mL). The mixture was stirred for 30 min at rt. MeI (0.33 mL, 5.29 mmol) was added dropwise, and the mixture stirred for 16 h. H<sub>2</sub>O (60 mL) was added, and the solution extracted with CH<sub>2</sub>Cl<sub>2</sub> (3 × 60 mL). The combined organic layers were dried (MgSO<sub>4</sub>), and evaporated to dryness. The brown solid was dissolved in CH<sub>2</sub>Cl<sub>2</sub> (30 mL), and SOCl<sub>2</sub> (1.40 mL, 19.2 mmol) added dropwise at 0 °C. The solution was stirred for 5 h, neutralized (sat. Na<sub>2</sub>CO<sub>3</sub>), and the organic layer separated. The aqueous layer was extracted with CH<sub>2</sub>Cl<sub>2</sub> (2 × 30 mL), and the combined organic layers were dried (MgSO<sub>4</sub>). The residue was purified by flash chromatography with EtOAc and hexanes as eluent to give **1** (0.983 g, 85%) as a white solid; mp 115–117 °C (mp<sup>31</sup> 114–116 °C), with spectral data in agreement with the literature.<sup>31</sup>

**Synthesis of 4,7-dimethoxy-1-methyl-2-[[2-(chloromethyl)-4,7-dimethoxy-1-methyl-1H-benzimidazol-2-yl]oxy]methyl-(2,2,6,6-tetramethylpiperidin-1-yl) (2)**

TEMPO (0.972 g, 6.23 mmol) and PtO<sub>2</sub> (28 mg, 0.12 mmol) in THF (15 mL) were stirred under a balloon of H<sub>2</sub> at rt, until the mixture turned colourless (~ 2 h). The mixture was filtered, NaH (83 mg, 2.08 mmol, 60%) added, and stirred at rt for 1 h. Chloride **1** (0.50 g,

2.08 mmol) was added, and the stirring continued at reflux for 16 h. H<sub>2</sub>O (50 mL) was added, and the solution extracted using CH<sub>2</sub>Cl<sub>2</sub> (3 × 40 mL). The combined organic layers were dried (MgSO<sub>4</sub>), evaporated, and the residue purified by flash chromatography using EtOAc and hexanes as eluent to give **2** (0.625 g, 83%) as a white solid; mp 114–116 °C; *R*<sub>f</sub> 0.40 (2 : 3 EtOAc : hexanes); *v*<sub>max</sub> (neat, cm<sup>-1</sup>) 2976, 2928, 1524, 1461, 1394, 1334, 1262, 1234, 1146, 1100, 1069, 1027; *δ*<sub>H</sub> (400 MHz, CDCl<sub>3</sub>) 1.05 (6H, s), 1.25 (6H, s), 1.29–1.31 (1H, m), 1.44–1.50 (5H, m), 3.85 (3H, s), 3.92 (3H, s), 4.11 (3H, s, NCH<sub>3</sub>), 5.02 (2H, s), 6.45 (1H, d, *J* = 8.5 Hz), 6.52 (1H, d, *J* = 8.5 Hz); *δ*<sub>C</sub> (100 MHz, CDCl<sub>3</sub>) 17.1 (CH<sub>2</sub>), 20.1 (CH<sub>3</sub>), 33.1 (NCH<sub>3</sub>), 33.5 (CH<sub>3</sub>), 39.8 (CH<sub>2</sub>), 55.8, 56.0 (both OCH<sub>3</sub>), 60.1 (C), 72.0 (CH<sub>2</sub>), 101.0, 103.3 (both CH), 126.9, 134.4, 141.8, 146.2, 149.8 (all C); HRMS (ESI) *m/z* [M + H]<sup>+</sup>, C<sub>20</sub>H<sub>32</sub>N<sub>3</sub>O<sub>3</sub> calcd. 362.2444, observed 362.2444.

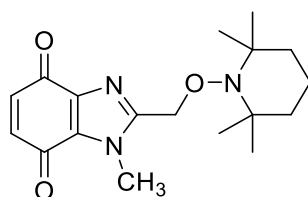
#### **General procedures (A-C) for the synthesis of benzimidazolequinones via dimethoxybenzimidazole oxidations**

**Procedure A:** *N*-Bromosuccinimide (NBS, 39 mg, 0.22 mmol) was added to dimethoxybenzimidazole (0.20 mmol), H<sub>2</sub>SO<sub>4</sub> (18 μL, 0.34 mmol) and THF/H<sub>2</sub>O (6 mL, 2/1) at rt, and stirred for 10 min in the absence of light. Aq Na<sub>2</sub>CO<sub>3</sub> (10 mL, sat.) was added, and the solution was extracted with CH<sub>2</sub>Cl<sub>2</sub> (2 × 20 mL). The combined organic layers were dried (MgSO<sub>4</sub>), evaporated, and the residue purified by dry column vacuum chromatography with EtOAc and hexanes as eluent.

**Procedure B:** Bis[(trifluoroacetoxy)iodo]benzene (PIFA, 0.129 g, 0.30 mmol) in MeCN/H<sub>2</sub>O (2 mL, 2/1) was added dropwise to dimethoxybenzimidazole (0.20 mmol) in MeCN/H<sub>2</sub>O (2 mL, 2/1) at rt, and stirred for 3 h in the absence of light. H<sub>2</sub>O (10 mL) was added, and the solution extracted with CH<sub>2</sub>Cl<sub>2</sub> (3 × 15 mL). The combined organic layers were dried (MgSO<sub>4</sub>), evaporated, and the residue purified by dry column vacuum chromatography with EtOAc and hexanes as eluent.

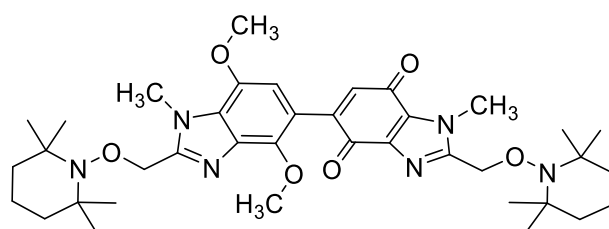
**Procedure C:** Cerium(IV) ammonium nitrate (CAN, X mmol, see Table 1) in H<sub>2</sub>O (5 mL) was added dropwise to dimethoxybenzimidazole (0.20 mmol) in MeCN (5 mL) at 0 °C, and stirred for 20 min in the absence of light. H<sub>2</sub>O (10 mL) was added, and the solution extracted with CH<sub>2</sub>Cl<sub>2</sub> (3 × 15 mL). The combined organic layers were dried

(MgSO<sub>4</sub>), evaporated, and the residue purified by dry column vacuum chromatography with EtOAc (or Et<sub>2</sub>O) and hexanes as eluent.



TEMPO-Vis

**1-Methyl-2-[(2,2,6,6-tetramethylpiperidin-1-yl)oxy]methyl-1H-benzimidazole-4,7-dione (TEMPO-Vis)**, according to Procedure B: 52 mg, 78%; yellow solid; mp 131–132 °C; *R<sub>f</sub>* 0.50 (2: 3 EtOAc : hexanes);  $\lambda_{\text{max}}$  (DCE, nm) 389 ( $\epsilon = 1.32 \times 10^3$ );  $\nu_{\text{max}}$  (neat, cm<sup>-1</sup>) 2974, 2931, 1661 (C=O), 1591, 1515, 1478, 1375, 1361, 1347, 1336, 1276, 1202, 1132;  $\delta_{\text{H}}$  (500 MHz, CDCl<sub>3</sub>) 1.09 (6H, s, CH<sub>3</sub>), 1.25 (6H, s, CH<sub>3</sub>), 1.34–1.36 (2H, m), 1.48–1.51 (4H, m), 4.09 (3H, s), 5.02 (2H, s), 6.62 (1H, d, *J* = 10.5 Hz), 6.69 (1H, d, *J* = 10.5 Hz);  $\delta_{\text{C}}$  (100 MHz, CDCl<sub>3</sub>) 17.0 (CH<sub>2</sub>), 20.2, 32.9, 33.3 (all CH<sub>3</sub>), 39.8 (CH<sub>2</sub>), 60.3 (C), 70.9 (CH<sub>2</sub>), 131.5 (C), 136.3, 136.6 (both CH), 141.0, 151.4 (both C), 178.8, 181.1 (both C=O); HRMS (ESI) *m/z* [M + H]<sup>+</sup>, C<sub>18</sub>H<sub>26</sub>N<sub>3</sub>O<sub>3</sub> calcd. 332.1974, observed 332.1971;  $\Phi_{\text{h}}$  (0.25 mM, DCE) 6.2% blue LED, 0.05% green LED.

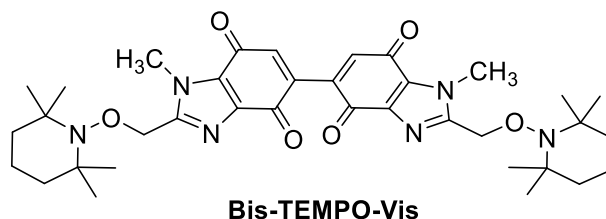


3

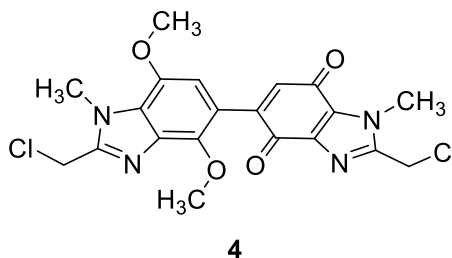
**4',7'-Dimethoxy-1,1'-dimethyl-2,2'-bis[(2,2,6,6-tetramethylpiperidin-1-yl)oxy]methyl-1H,1'H-[5,5'-bibenzimidazole]-4,7-dione (3)**, according to Procedure C using CAN (0.219 g, 0.40 mmol): 0.119 g, 86%; deep red solid; mp 127–129 °C; *R<sub>f</sub>* 0.25 (1 : 1 EtOAc : hexanes);  $\lambda_{\text{max}}$  (DCE, nm) 497 ( $\epsilon = 1.20 \times 10^3$ ), 355 ( $\epsilon = 2.87 \times 10^3$ );  $\nu_{\text{max}}$  (neat, cm<sup>-1</sup>) 2972, 2930, 1653 (C=O), 1532, 1463, 1277, 1150, 1103, 1037;  $\delta_{\text{H}}$  (400 MHz, CDCl<sub>3</sub>) 1.05–1.06 (12H, m, CH<sub>3</sub>), 1.23 (12H, s, CH<sub>3</sub>), 1.29–1.32 (2H, m), 1.45–1.50 (10H, m), 3.86 (3H, s, OCH<sub>3</sub>), 4.08 (3H, s, NCH<sub>3</sub>), 4.09 (3H, s, NCH<sub>3</sub>), 4.15 (3H, s, OCH<sub>3</sub>), 5.00 (2H, s), 5.01 (2H, s), 6.43 (1H, s, C6'-H), 6.66 (1H, s, C6-H);  $\delta_{\text{C}}$

### Chapter 3

(100 MHz, CDCl<sub>3</sub>) 17.0, 17.1 (both CH<sub>2</sub>), 20.2 (CH<sub>3</sub>), 32.9, 33.1 (both NCH<sub>3</sub>), 33.3, 33.4 (both CH<sub>3</sub>), 39.8 (CH<sub>2</sub>), 56.0 (OCH<sub>3</sub>), 60.1, 60.3 (C), 61.5 (OCH<sub>3</sub>), 71.0, 72.0 (both CH<sub>2</sub>), 105.4 (C6'-H), 116.8, 128.7, 131.5 (all C), 134.3 (C6-H), 136.4, 141.3, 142.7, 144.3, 147.0, 150.5, 151.1 (all C), 179.0, 180.1 (both C=O); HRMS (ESI) m/z [M + H]<sup>+</sup>, C<sub>38</sub>H<sub>55</sub>N<sub>6</sub>O<sub>6</sub> calcd. 691.4183, observed 691.4183; Φ<sub>h</sub> (0.25 mM, DCE) 0.003% blue LED, < 0.001% green LED.



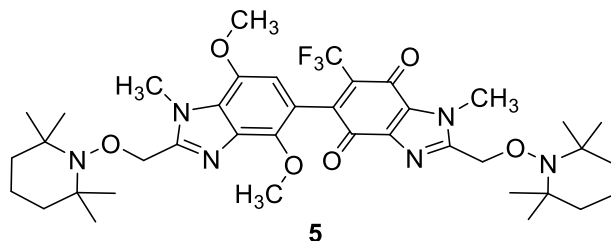
**1,1'-Dimethyl-2,2'-bis{[(2,2,6,6-tetramethylpiperidin-1-yl)oxy]methyl}-1*H*,1'*H*-5,5'-bibenzimidazole-4,4',7,7'-tetrone (Bis-TEMPO-Vis)**, according to Procedure C using CAN (0.350 g, 0.64 mmol): 0.108 g, 82%; yellow solid; mp 228–231 °C (deg); *R*<sub>f</sub> 0.28 (19 : 1 Et<sub>2</sub>O : hexanes); λ<sub>max</sub> (DCE, nm) 401 (ε = 2.35 × 10<sup>3</sup>), 273 (ε = 1.89 × 10<sup>4</sup>); ν<sub>max</sub> (neat, cm<sup>-1</sup>) 2975, 2934, 2870, 1662 (C=O), 1533, 1519, 1479, 1447, 1371, 1279, 1244, 1183, 1112, 1048; δ<sub>H</sub> (500 MHz, CD<sub>2</sub>Cl<sub>2</sub>) 1.12 (12H, s), 1.27 (12H, s), 1.35–1.37 (4H, m), 1.46–1.57 (8H, bs), 4.08 (6H, s, NCH<sub>3</sub>), 4.91–5.13 (4H, bs), 6.69 (2H, s); δ<sub>C</sub> (150 MHz, CD<sub>2</sub>Cl<sub>2</sub>) 16.9 (CH<sub>2</sub>), 19.8 (CH<sub>3</sub>), 32.7 (NCH<sub>3</sub>), 32.9 (CH<sub>3</sub>), 39.6 (CH<sub>2</sub>), 60.1 (C), 70.7 (CH<sub>2</sub>), 131.7 (C), 136.0 (CH), 140.4, 140.7, 151.7 (all C), 177.4, 178.5 (both C=O); HRMS (ESI) m/z [M + H]<sup>+</sup>, C<sub>36</sub>H<sub>49</sub>N<sub>6</sub>O<sub>6</sub> calcd. 661.3714, observed 661.3716; Φ<sub>h</sub> (0.25 mM, DCE) 2.56% blue LED, 0.07% green LED.



**2,2'-Bis(chloromethyl)-4',7'-dimethoxy-1,1'-dimethyl-1*H*,1'*H*-[5,5'-bibenzimidazole]-4,7-dione (4)**, according to Procedure C using CAN (0.219 g, 0.40 mmol): 68 mg, 76%; deep red solid; mp > 350 °C; *R*<sub>f</sub> 0.35 (4 : 1 EtOAc : hexanes); ν<sub>max</sub> (neat, cm<sup>-1</sup>) 3029, 2949, 1655 (C=O), 1498, 1379, 1280, 1245, 1119, 1039; δ<sub>H</sub>

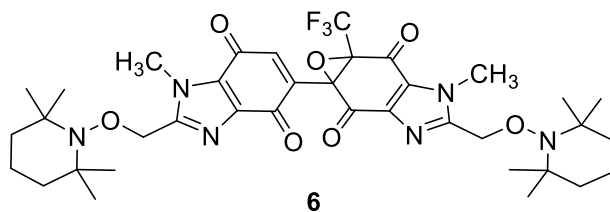


(400 MHz, CDCl<sub>3</sub>) 3.89 (3H, s, OCH<sub>3</sub>), 4.07 (3H, s, NCH<sub>3</sub>), 4.09 (3H, s, NCH<sub>3</sub>), 4.15 (3H, s, OCH<sub>3</sub>), 4.76 (2H, s), 4.79 (2H, s), 6.47 (1H, s), 6.70 (1H, s);  $\delta_C$  (100 MHz, CDCl<sub>3</sub>) 32.6, 33.0 (both NCH<sub>3</sub>), 35.6, 36.8 (both CH<sub>2</sub>), 56.1, 61.6 (both OCH<sub>3</sub>), 105.9 (CH), 117.1, 128.8, 131.8 (all C), 134.5 (CH), 136.1, 141.1, 142.7, 144.2, 147.0, 148.7, 149.6 (all C), 178.7, 179.7 (both C=O); HRMS (ESI) *m/z* [M + H]<sup>+</sup>, C<sub>20</sub>H<sub>19</sub>N<sub>4</sub>O<sub>4</sub><sup>35</sup>Cl<sub>2</sub> calcd. 449.0783, observed 449.0778.



**Synthesis of 4',7'-dimethoxy-1,1'-dimethyl-2,2'-bis[[2,2,6,6-tetramethylpiperidin-1-yl]oxy]methyl-6-(trifluoromethyl)-1H,1'H-[5,5'-bibenzimidazole]-4,7-dione (5)**

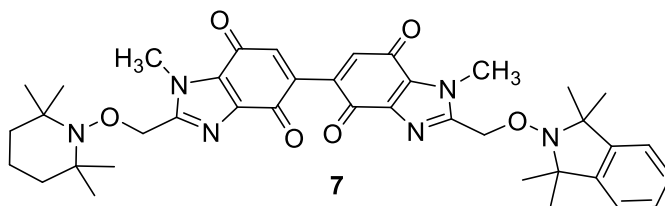
*t*BuOOH (133  $\mu$ L, 70% in H<sub>2</sub>O, 1.11 mmol) was added dropwise to 5,5'-dimethoxybenzimidazole-benzimidazolequinone **3** (0.18 g, 0.26 mmol), NaSO<sub>2</sub>CF<sub>3</sub> (0.122 g, 0.78 mmol), and Cu(OTf)<sub>2</sub> (9 mg, 0.03 mmol) in MeCN (3 mL) at rt under Ar. After 2 h of stirring, H<sub>2</sub>O (15 mL) was added, and the precipitate filtered. Purification of the precipitate by flash chromatography using EtOAc and hexanes as eluent gave trifluoromethylquinone **5** as a deep red oil (0.106 g, 54%); *R<sub>f</sub>* 0.43 (2 : 3 EtOAc : hexanes);  $\nu_{\max}$  (neat, cm<sup>-1</sup>) 2973, 2931, 1670 (C=O), 1611, 1502, 1466, 1375, 1361, 1297, 1262, 1245, 1175, 1130, 1041, 990;  $\delta_H$  (500 MHz, CDCl<sub>3</sub>) 1.09–1.11 (12H, m, CH<sub>3</sub>), 1.24–1.38 (14H, m), 1.49–1.55 (10H, m), 3.85 (3H, s, OCH<sub>3</sub>), 4.13 (3H, s, NCH<sub>3</sub>), 4.15 (3H, s, NCH<sub>3</sub>), 4.16 (3H, s, OCH<sub>3</sub>), 5.038 (2H, s), 5.043 (2H, s), 6.27 (1H, s);  $\delta_C$  (125 MHz, CDCl<sub>3</sub>) 16.9, 17.0 (both CH<sub>2</sub>), 20.1 (CH<sub>3</sub>), 32.9, 33.1 (both NCH<sub>3</sub>), 33.2 (CH<sub>3</sub>), 39.66, 39.72 (both CH<sub>2</sub>), 55.9 (OCH<sub>3</sub>), 60.1, 60.2 (both C), 61.1 (OCH<sub>3</sub>), 70.8, 71.7 (both CH<sub>2</sub>), 104.5 (CH), 113.8 (C), 121.7 (q, *J* = 276.6 Hz, CF<sub>3</sub>), 128.7 (C), 130.6 (q, *J* = 27.5 Hz, C6), 131.2, 135.4, 140.5, 142.1, 143.2, 147.84–147.85 (m), 150.2, 152.3 (all C), 174.6, 178.1 (both C=O);  $\delta_F$  (470 MHz, CDCl<sub>3</sub>) – 56.69; HRMS (ESI) *m/z* [M + H]<sup>+</sup>, C<sub>39</sub>H<sub>54</sub>N<sub>6</sub>O<sub>6</sub>F<sub>3</sub> calcd. 759.4057, observed 759.4066.



**3-Methyl-6a-(1-methyl-4,7-dioxo-2-[[2,2,6,6-tetramethylpiperidin-1-yl]oxy]methyl)-4,7-dihydro-1*H*-benzimidazol-5-yl)-4-[[2,2,6,6-tetramethylpiperidin-1-yl]oxy]methyl)-1a-(trifluoromethyl)-1a*H*-oxireno[*f*]benzimidazole-2,6(3*H*,6a*H*)-dione (6)**, according to procedure A: 116 mg, 78%; yellow solid; mp 150–152 °C (deg);  $R_f$  (0.56, 3 : 7 EtOAc : hexanes);  $\lambda_{\max}$  (DCE, nm) 400 ( $\epsilon = 9.31 \times 10^2$ ), 313 ( $\epsilon = 5.60 \times 10^3$ );  $\nu_{\max}$  (neat,  $\text{cm}^{-1}$ ) 2931, 1695 (C=O), 1664 (C=O), 1517, 1477, 1361, 1292, 1212, 1182, 1126, 1034;  $\delta_H$  (500 MHz,  $\text{CDCl}_3$ ) 1.10 (12H, s), 1.21–1.25 (12H, m), 1.33–1.36 (2H, m), 1.43–1.56 (10H, bs), 4.11 (3H, s, NCH<sub>3</sub>), 4.13 (3H, s, NCH<sub>3</sub>), 5.02 (2H, s), 5.03 (2H, s), 6.78 (1H, s);  $\delta_C$  (125 MHz,  $\text{CDCl}_3$ ) 16.90, 16.93 (both CH<sub>2</sub>), 20.08, 20.11 (both CH<sub>3</sub>), 32.9, 33.19, 33.25, 33.4 (all CH<sub>3</sub>), 39.67, 39.69 (both CH<sub>2</sub>), 60.2, 60.3 (both C), 63.4 (q,  $J = 33.9$  Hz, C-CF<sub>3</sub>), 65.6 (C), 70.72, 70.74 (both CH<sub>2</sub>), 120.4 (q,  $J = 280.7$  Hz, CF<sub>3</sub>), 131.3, 132.2 (both C), 135.1 (CH), 138.9, 140.2, 140.4, 151.8, 154.2 (all C), 176.1, 176.9, 178.1, 179.5 (all C=O);  $\delta_F$  (470 MHz,  $\text{CDCl}_3$ ) – 65.81; HRMS (ESI)  $m/z$  [M + H]<sup>+</sup>, C<sub>37</sub>H<sub>48</sub>N<sub>6</sub>O<sub>7</sub>F<sub>3</sub> calcd. 745.3537, observed 745.3547;  $\Phi_h$  (0.25 mM, DCE) 1.17% blue LED, 0.02% green LED.

#### General procedure for TMIO nitroxide-exchange with Bis-TEMPO-Vis

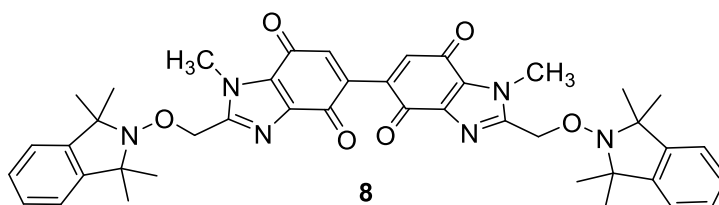
**Bis-TEMPO-Vis** (50 mg, 0.076 mmol) and TMIO (0.287 g, 1.51 mmol) were stirred in MeCN (20 mL) at rt under Ar with blue LED illumination (1 × 9 W bulb) for X min. The solution was evaporated and passed through a plug of silica using Et<sub>2</sub>O and hexanes to give a crude mixture of bis-alkoxyamines. The mixture was purified by preparative HPLC to give the desired TMIO-coupled bis-alkoxyamine.



**1,1'-Dimethyl-2-[[1,1,3,3-tetramethyl-1,3-dihydro-2*H*-isoindol-2-yl]oxy]methyl)-2'-[[2,2,6,6-tetramethylpiperidin-1-yl]oxy]methyl)-1*H*,1'*H*-[5,5'-bibenzimidazole]-**

### Chapter 3

**4,4',7,7'-tetrone (7)**, according to general procedure for TMIO nitroxide-exchange with a reaction time of 85 min: 23 mg, 44%; yellow solid; mp 195–200 °C (deg);  $R_f$  0.40 (Et<sub>2</sub>O);  $\nu_{\max}$  (neat, cm<sup>-1</sup>) 2964, 2929, 1659 (C=O), 1516, 1482, 1361, 1274, 1168, 1120, 1099;  $\delta_H$  (500 MHz, CD<sub>2</sub>Cl<sub>2</sub>) 1.11 (6H, s, TEMPO-CH<sub>3</sub>), 1.26 (6H, s, TEMPO-CH<sub>3</sub>), 1.35–1.38 (12H, m, TMIO-CH<sub>3</sub>), 1.50–1.55 (6H, m), 4.09 (3H, s), 4.15 (3H, s), 5.02 (2H, s), 5.14 (2H, s), 6.71 (1H, s), 6.72 (1H, s), 7.12 (2H, dd,  $J = 3.2, 5.6$  Hz), 7.25 (2H, dd,  $J = 3.2, 5.6$  Hz);  $\delta_C$  (125 MHz, CD<sub>2</sub>Cl<sub>2</sub>) 17.0 (CH<sub>2</sub>), 19.8 (TEMPO-CH<sub>3</sub>), 24.8, 29.7 (both TMIO-CH<sub>3</sub>), 32.7, 32.8 (both NCH<sub>3</sub>), 33.0 (TEMPO-CH<sub>3</sub>), 39.7 (CH<sub>2</sub>), 60.1, 67.7 (both C), 69.7, 70.8 (both CH<sub>2</sub>), 121.4, 127.4 (both CH), 131.6, 131.7 (both C), 136.16, 136.17 (both CH), 140.2, 140.3, 140.7, 140.8, 144.5, 151.8, 151.9 (all C), 177.41, 177.44, 178.47, 178.51 (all C=O); HRMS (ESI)  $m/z$  [M + H]<sup>+</sup>, C<sub>39</sub>H<sub>47</sub>N<sub>6</sub>O<sub>6</sub> calcd. 695.3557, observed 695.3552.



**1,1'-Dimethyl-2,2'-bis[[1,1,3,3-tetramethyl-1,3-dihydro-2H-isoindol-2-yl]oxy]methyl]-1H,1'H-[5,5'-bibenzimidazole]-4,4',7,7'-tetrone (8)**, according to general procedure for TMIO nitroxide-exchange with a reaction time of 720 min: 42 mg, 76%; yellow solid; mp 135–138 °C (deg);  $R_f$  0.28 (19 : 1 Et<sub>2</sub>O : hexanes);  $\nu_{\max}$  (neat, cm<sup>-1</sup>) 2974, 2925, 1660 (C=O), 1531, 1483, 1375, 1361, 1275, 1166, 1117, 1098, 1036;  $\delta_H$  (500 MHz, CDCl<sub>3</sub>) 1.32–1.52 (24H, bs), 4.17 (6H, s, NCH<sub>3</sub>), 5.15 (4H, s), 6.76 (2H, s), 7.09 (4H, dd,  $J = 3.2, 5.5$  Hz), 7.24 (4H, dd,  $J = 3.2, 5.5$  Hz);  $\delta_C$  (125 MHz, CDCl<sub>3</sub>) 25.1, 30.0, 33.0 (all CH<sub>3</sub>), 67.7 (C), 69.8 (CH<sub>2</sub>), 121.5, 127.5 (both CH), 131.5 (C), 136.8 (CH), 139.3, 140.9, 144.4, 151.8 (all C), 177.5, 178.2 (both C=O); HRMS (ESI)  $m/z$  [M + H]<sup>+</sup>, C<sub>42</sub>H<sub>45</sub>N<sub>6</sub>O<sub>6</sub> calcd. 729.3401, observed 729.3413.

### 3.7 Chapter 3 Contributions

Sincere thanks to the following workers at NUI Galway: Prof. Patrick McArdle for X-ray crystallography, to Dr. Benjamin A. Chalmers for assistance in the preparation of TMIO nitroxide, and to Dr. John O'Reilly for consultation on HPLC.

### 3.8 Chapter 3 References

1. Karoui, H.; Le Moigne, F.; Ouari, O.; Tordo, P. Nitroxide Radicals: Properties, Synthesis and Applications. In *Stable Radicals: Fundamentals and Applied Aspects of Odd-Electron Compounds*, R. G. Hicks, Ed.; John Wiley and Sons: Chichester, **2010**, pp 173–229. <https://doi.org/10.1002/9780470666975.ch5>.
2. Keana, J. F. W. *Chem. Rev.* **1978**, *78*, 37–64. <https://doi.org/10.1021/cr60311a004>.
3. Amar, M.; Bar, S.; Iron, M. A.; Toledo, H.; Tumanskii, B.; Shimon, L. J. W.; Botoshansky, M.; Fridman, N.; Szpilman, A. M. *Nat. Commun.* **2015**, *6*, 6070. <https://doi.org/10.1038/ncomms7070>.
4. Nicolas, J.; Guillaneuf, Y.; Lefay, C.; Bertin, D.; Gigmes, D.; Charleux, B. *Prog. Polym. Sci.* **2013**, *38*, 63–235. <https://doi.org/10.1016/j.progpolymsci.2012.06.002>.
5. Fischer, H. *Chem. Rev.*, **2001**, *101*, 3581–3610. <https://doi.org/10.1021/cr990124y>.
6. Beejapur, H. A.; Zhang, Q.; Hu, K.; Zhu, L.; Wang, J.; Ye, Z. *ACS Catal.* **2019**, *9*, 2777–2830. <https://doi.org/10.1021/acscatal.8b05001>.
7. Leifert, D.; Studer, A. *Angew. Chem. Int. Ed.* **2019**, Accepted Author Manuscript. <https://doi.org/10.1002/anie.201903726>.
8. Haugland, M. M.; Lovett, J. E.; Anderson, E. A. *Chem. Soc. Rev.* **2018**, *47*, 668–680. <https://doi.org/10.1039/C6CS00550K>.
9. Kaur, A.; Kolanowski, J. L.; New, E. J. *Angew. Chem. Int. Ed.* **2016**, *55*, 1602–1613. <https://doi.org/10.1002/anie.201506353>.
10. Wahsner, J.; Gale, E. M.; Rodríguez-Rodríguez, A.; Caravan, P. *Chem. Rev.* **2019**, *119*, 957–1057. <https://doi.org/10.1021/acs.chemrev.8b00363>.

### Chapter 3

---

11. Nutting, J. E.; Rafiee, M.; Stahl, S. S. *Chem. Rev.* **2018**, *118*, 4834–4885. <https://doi.org/10.1021/acs.chemrev.7b00763>.
12. Ding, Y.; Zhang, C.; Zhang, L.; Zhou, Y.; Yu, G. *Chem. Soc. Rev.* **2018**, *47*, 69–103. <https://doi.org/10.1039/C7CS00569E>.
13. Hansen, K.-A.; Blinco, J. P. *Polym. Chem.* **2018**, *9*, 1479–1516. <https://doi.org/10.1039/C7PY02001E>.
14. Bagryanskaya, E. G.; Marque, S. R. A. *Chem. Rev.* **2014**, *114*, 5011–5056. <https://doi.org/10.1021/cr4000946>.
15. Fukuda, T.; Terauchi, T.; Goto, A.; Ohno, K.; Tsujii, Y.; Miyamoto, T.; Kobatake, S.; Yamada, B. *Macromolecules* **1996**, *29*, 6393–6398. <https://doi.org/10.1021/ma960552v>.
16. Versace, D.-L.; Guillaneuf, Y.; Bertin, D.; Fouassier, J. P.; Lalevée, J.; Gigmes, D. *Org. Biomol. Chem.* **2011**, *9*, 2892–2898. <https://doi.org/10.1039/C0OB01207F>.
17. Guillaneuf, Y.; Bertin, D.; Gigmes, D.; Versace, D.-L.; Lalevée, J.; Fouassier, J.-P. *Macromolecules* **2010**, *43*, 2204–2212. <https://doi.org/10.1021/ma902774s>.
18. Hu, S.; Malpert, J. H.; Yang, X.; Neckers, D. C. *Polymer* **2000**, *41*, 445–452. [https://doi.org/10.1016/S0032-3861\(99\)00188-3](https://doi.org/10.1016/S0032-3861(99)00188-3).
19. Li, I. Q.; Howell, B. A.; Koster, R. A.; Priddy, D. B. *Macromolecules* **1996**, *29*, 8554–8555. <https://doi.org/10.1021/ma9610121>.
20. Ananchenko, G.; Matyjaszewski, K. *Macromolecules* **2002**, *35*, 8323–8329. <https://doi.org/10.1021/ma020733z>.
21. Ruehl, J.; Nilsen, A.; Born, S.; Thoniyot, P.; Xu, L.; Chen, S.; Braslau, R. *Polymer* **2007**, *48*, 2564–2571. <https://doi.org/10.1016/j.polymer.2007.03.008>.
22. Ruehl, J.; Hill, N. L.; Walter, E. D.; Millhauser, G.; Braslau, R. *Macromolecules* **2008**, *41*, 1972–1982. <https://doi.org/10.1021/ma702358c>.
23. Herder, M.; Lehn, J.-M. *J. Am. Chem. Soc.* **2018**, *140*, 7647–7657. <https://doi.org/10.1021/jacs.8b03633>.
24. Baron, M.; Morris, J. C.; Telitel, S.; Clément, J.-L.; Lalevée, J.; Morlet-Savary, F.; Spangenberg, A.; Malval, J.-P.; Soppera, O.; Gigmes, D.; Guillaneuf, Y. *J. Am. Chem. Soc.* **2018**, *140*, 3339–3344. <https://doi.org/10.1021/jacs.7b12807>.
25. Goto, A.; Scaiano, J. C.; Maretti, L. *Photochem. Photobiol. Sci.* **2007**, *6*, 833–835. <https://doi.org/10.1039/B705671K>.

### Chapter 3

---

26. Bass, P. D.; Gubler, D. A.; Judd, T. C.; Williams, R. M. *Chem. Rev.* **2013**, *113*, 6816–6863. <https://doi.org/10.1021/cr3001059>.
27. Tomasz, M.; Lipman, R.; Chowdary, D.; Pawlak, J.; Verdine, G. L.; Nakanishi, K. *Science* **1987**, *235*, 1204–1208. <https://doi.org/10.1126/science.3103215>.
28. Wolkenberg, S. E.; Boger, D. L. *Chem. Rev.* **2002**, *102*, 2477–2496. <https://doi.org/10.1021/cr010046q>.
29. Kalyanaraman, B.; Perez-Reyes, E.; Mason, R. P. *Biochim. Biophys. Acta, Gen. Subj.* **1980**, *630*, 119–130. [https://doi.org/10.1016/0304-4165\(80\)90142-7](https://doi.org/10.1016/0304-4165(80)90142-7).
30. Schulz, W. G.; Nieman, R. A.; Skibo, E. B. *Proc. Ntnl. Acad. Sci., U. S. A.* **1995**, *92*, 11854–11858. <https://doi.org/10.1073/pnas.92.25.11854>.
31. Skibo, E. B. *J. Org. Chem.* **1992**, *57*, 5874–5878. <https://doi.org/10.1021/jo00048a020>.
32. Sweeney, M.; Gurry, M.; Keane, L.-A. J.; Aldabbagh, F. *Tetrahedron Lett.* **2017**, *58*, 3565–3567. <https://doi.org/10.1016/j.tetlet.2017.07.102>.
33. O'Donovan, L.; Carty, M. P.; Aldabbagh, F. *Chem. Commun.* **2008**, 5592–5594. <https://doi.org/10.1039/b814706j>.
34. Marminon, C.; Gentili, J.; Barret, R.; Nebois, P. *Tetrahedron* **2007**, *63*, 735–739. <https://doi.org/10.1016/j.tet.2006.10.086>.
35. Tohma, H.; Morioka, H.; Harayama, Y.; Hashizume, M.; Kita, Y. *Tetrahedron Lett.* **2001**, *42*, 6899–6902. [https://doi.org/10.1016/S0040-4039\(01\)01407-1](https://doi.org/10.1016/S0040-4039(01)01407-1).
36. Love, B. E.; Bonner-Stewart, J.; Forrest, L. A. *Synlett*, **2009**, 2009, 813–817. <https://doi.org/10.1055/s-0028-1087937>.
37. Gellis, A.; Kovacic, H.; Boufatah, N.; Vanelle, P. *Eur. J. Med. Chem.* **2008**, *43*, 1858–1864. <http://doi.org/10.1016/j.ejmech.2007.11.020>.
38. Love, B. E.; Simmons, A. L. *Tetrahedron Lett.* **2016**, *57*, 5712–5715. <https://doi.org/10.1016/j.tetlet.2016.11.042>.
39. Sweeney, M.; Keane, L.-A. J.; Gurry, M.; Aldabbagh, F. *Org. Lett.* **2018**, *20*, 6970–6974. <https://doi.org/10.1021/acs.orglett.8b03135>.
40. Van Hoomissen, D. J.; Vyas, S. *J. Org. Chem.* **2017**, *82*, 5731–5742. <https://doi.org/10.1021/acs.joc.7b00549>.
41. Scaiano, J. C.; Connolly, T. J.; Mohtat, N.; Pliva, C. N. *Can. J. Chem.* **1997**, *75*, 92–97. <https://doi.org/10.1139/v97-014>.
42. Hodgson, J. L.; Roskop, L. B.; Gordon, M. S.; Lin, C. Y.; Coote, M. L. *J Phys. Chem. A* **2010**, *114*, 10458–10466. <https://doi.org/10.1021/jp1064165>.

### Chapter 3

---

43. Aldabbagh, F.; Busfield, W. K.; Jenkins, I. D.; Thang, S. H. *Tetrahedron Lett.* **2000**, *41*, 3673–3676. [https://doi.org/10.1016/S0040-4039\(00\)00440-8](https://doi.org/10.1016/S0040-4039(00)00440-8).
44. Langlois, B. R. In *Modern Synthesis Processes and Reactivity of Fluorinated Compounds*; Groult, H., Leroux, F. R., Tressaud, A., Eds.; Elsevier: **2017**, p 125–140. <https://doi.org/10.1016/B978-0-12-803740-9.00005-6>.
45. Moad, G.; Rizzardo, E. *Macromolecules* **1995**, *28*, 8722–8728. <https://doi.org/10.1021/ma00130a003>.
46. Versace, D.-L.; Lalevée, J.; Fouassier, J.-P.; Gigmès, D.; Guillaeneuf, Y.; Bertin, D. *J. Polym. Sci., Part A: Polym. Chem.* **2010**, *48*, 2910–2915. <https://doi.org/10.1002/pola.24071>.
47. Scaiano, J. C. *Chem. Phys. Lett.* **1981**, *79*, 441–443. [https://doi.org/10.1016/0009-2614\(81\)85010-5](https://doi.org/10.1016/0009-2614(81)85010-5).
48. Grattan, D. W.; Carlsson, D. J.; Howard, J. A.; Wiles, D. M. *Can. J. Chem.* **1979**, *57*, 2834–2842. <https://doi.org/10.1139/v79-460>.
49. Laurent, A. D.; Jacquemin, D. *Int. J. Quantum Chem.* **2013**, *113*, 2019–2039. <https://doi.org/10.1002/qua.24438>.
50. Martin, R. L. *J. Chem. Phys.* **2003**, *118*, 4775–4777. <https://doi.org/10.1063/1.1558471>.
51. Klán, P.; Šolomek, T.; Bochet, C. G.; Blanc, A.; Givens, R.; Rubina, M.; Popik, V.; Kostikov, A.; Wirz, J. *Chem. Rev.* **2013**, *113*, 119–191. <https://doi.org/10.1021/cr300177k>.
52. Phillips, M. A. *J. Chem. Soc.* **1928**, 2393–2399. <https://doi.org/10.1039/JR9280002393>.
53. Hammershøj, P.; Reenberg, T. K.; Pittelkow, M.; Nielsen, C. B.; Hammerich, O.; Christensen, J. B. *Eur. J. Org. Chem.* **2006**, *2006*, 2786–2794. <https://doi.org/10.1002/ejoc.200600081>.
54. Griffiths, P. G.; Moad, G.; Rizzardo, E. *Aust. J. Chem.* **1983**, *36*, 397–401. <https://doi.org/10.1071/CH9830397>.
55. Chan, K. S.; Li, X. Z.; Lee, S. Y. *Organometallics* **2010**, *29*, 2850–2856. <https://doi.org/10.1021/om1000869>.
56. Harwood, L. M. *Aldrichim. Acta* **1985**, *18*, 25.
57. Frisch, M. J.; Trucks, G. W.; Schlegel, H. B.; Scuseria, G. E.; Robb, M. A.; Cheeseman, J. R.; Scalmani, G.; Barone, V.; Petersson, G. A.; Nakatsuji, H.; Li, X.; Caricato, M.; Marenich, A. V.; Bloino, J.; Janesko, B. G.; Gomperts, R.;

- Mennucci, B.; Hratchian, H. P.; Ortiz, J. V.; Izmaylov, A. F.; Sonnenberg, J. L.; Williams-Young, D.; Ding, F.; Lipparini, F.; Egidi, F.; Goings, J.; Peng, B.; Petrone, A.; Henderson, T.; Ranasinghe, D.; Zakrzewski, V. G.; Gao, J.; Rega, N.; Zheng, G.; Liang, W.; Hada, M.; Ehara, M.; Toyota, K.; Fukuda, R.; Hasegawa, J.; Ishida, M.; Nakajima, T.; Honda, Y.; Kitao, O.; Nakai, H.; Vreven, T.; Throssell, K.; Montgomery, J. A., Jr.; Peralta, J. E.; Ogliaro, F.; Bearpark, M. J.; Heyd, J. J.; Brothers, E. N.; Kudin, K. N.; Staroverov, V. N.; Keith, T. A.; Kobayashi, R.; Normand, J.; Raghavachari, K.; Rendell, A. P.; Burant, J. C.; Iyengar, S. S.; Tomasi, J.; Cossi, M.; Millam, J. M.; Klene, M.; Adamo, C.; Cammi, R.; Ochterski, J. W.; Martin, R. L.; Morokuma, K.; Farkas, O.; Foresman, J. B.; Fox, D. J. Gaussian 16, Revision B.01, Gaussian, Inc., Wallingford CT, 2016.
58. Zhao, Y.; Truhlar, D. G. *Theor. Chem. Acc.* **2008**, *120*, 215–241. <https://doi.org/10.1007/s00214-007-0310-x>.
59. Amovilli, C.; Barone, V.; Cammi, R.; Cancès, E.; Cossi, M.; Mennucci, B.; Pomelli, C. S.; Tomasi, J. *J. Adv. Quant. Chem.* **1998**, *32*, 227–261. [https://doi.org/10.1016/S0065-3276\(08\)60416-5](https://doi.org/10.1016/S0065-3276(08)60416-5).
60. Kielty, P.; Farràs, P.; McArdle, P.; Smith, D. A.; Aldabbagh, F. *Chem. Commun.* **2019**, Advance Article. <https://doi.org/10.1039/C9CC08261A>.
61. Sheldrick, G. *Acta Crystallogr. Sect. A: Found. Crystallogr.* **2015**, *71*, 3–8. <https://doi.org/10.1107/S2053273314026370>.
62. Sheldrick, G. *Acta Crystallogr. Sect. C: Cryst. Struct. Commun.* **2015**, *71*, 3–8. <https://doi.org/10.1107/S2053229614024218>.
63. McArdle, P. *J. Appl. Crystallogr.* **2017**, *50*, 320–326. <https://doi.org/10.1107/S1600576716018446>.



# Chapter 4

***Part 1: The Chemistry of TMIO-Vis***

***Part 2: The Chemistry of CF<sub>3</sub>-Bis-TEMPO-Vis***

***Part 3: 2-(Fluoromethyl)-4,7-dimethoxy-1-methyl-1H-benzimidazole***

## Chapter 4

---

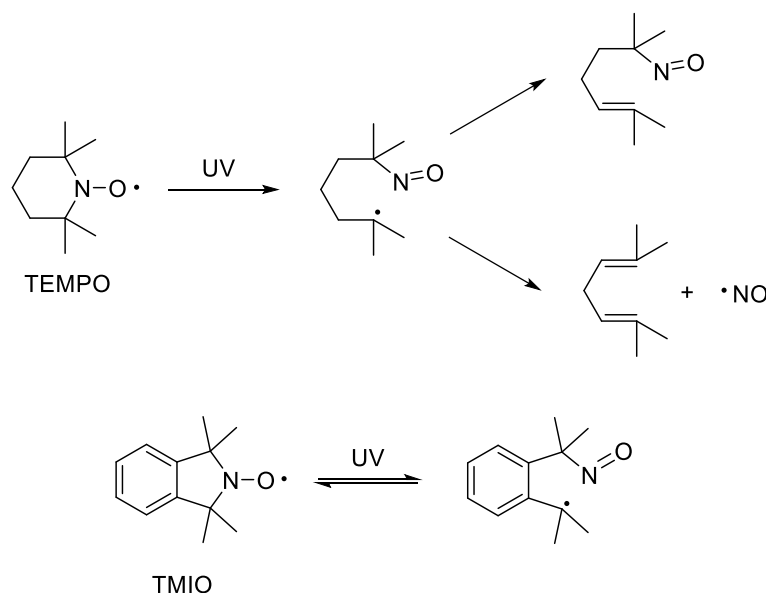
### Chapter 4 Layout

Chapter 4 continues from the substantive work in Chapter 3. At the time of writing this thesis, most of the content of Chapter 3 was being readied for publication. Please note that this Chapter (4), is arranged in three disparate parts, which will be readied for publication at a later date, and are planned to appear, as two or three separate research articles. Parts 1 and/or 2 are intended for the Special Issue of *Molecules* (Basel, MDPI) on “*Advances in Radical Chemistry*” (Ed. John C. Walton). Part 3 is intended for the Special Issue of *Molbank* (Basel, MDPI), entitled, “*Heterocycle Reactions*” (Ed. Fawaz Aldabbagh). Compound numbering has continued from Chapter 3.

## Part 1: The Chemistry of TMIO-Vis

## 4.1.1 Introduction

The synthesis of the isoindoline-based nitroxide, 1,1,3,3-tetramethyl-2,3-dihydroisoindol-2-yloxy (TMIO), was first described by Griffiths *et al.* in 1983,<sup>1</sup> and is an alternative to commercial TEMPO. TMIO has a number of advantages over its piperidine-based counterpart. Its aromatic ring enables further functionalization<sup>2-4</sup> and provides a UV chromophore, which is useful for the detection of trapped, non-UV-active carbon-centred radical intermediates.<sup>5,6</sup> TMIO is a superior radical trap to TEMPO,<sup>7</sup> and does not undergo UV-induced  $\alpha$ -cleavage like TEMPO,<sup>8</sup> due to recombination in TMIO of the tertiary radical with the nitrene (Scheme 4.1).<sup>9</sup>



**Scheme 4.1** UV-induced irreversible and reversible  $\alpha$ -cleavage of TEMPO and TMIO respectively.<sup>8,9</sup>

In recent years, TMIO has found most use in fluorescent probes to measure the redox status of a cellular environment.<sup>10</sup> Reduction of the nitroxide switches on fluorescence, and oxidation back to the free radical results in fluorescence quenching by the unpaired electron. Successful TMIO-based probes have attached chromophores including fluorescein,<sup>11</sup> coumarin *via* a triazole linker,<sup>12</sup> and boron-dipyrromethene (BODIPY, Figure 4.1).<sup>13</sup>

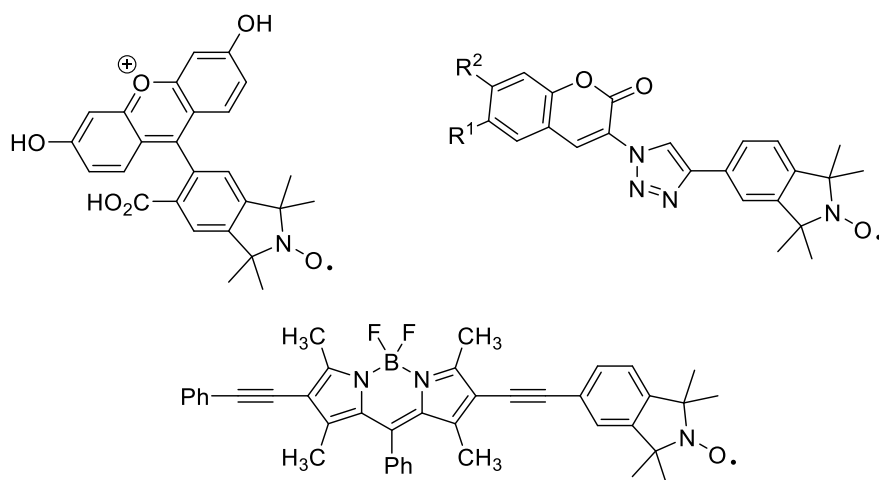


**Figure 4.1** Fluorescein-,<sup>11</sup> coumarin-<sup>12</sup> and BODIPY-based<sup>13</sup> TMIO fluorescent probes.

The thermally-induced homolysis rates of TEMPO- and TMIO-based 2-methylpropanenitrile alkoxyamines (PCN-TEMPO and PCN-TMIO, Figure 4.2) have been reported. PCN-TMIO dissociated 12-fold and 6.8-fold slower than the TEMPO nitroxide analogue in ethyl acetate (60 °C)<sup>14</sup> and *tert*-butylbenzene (120 °C) respectively.<sup>15</sup> The slower homolysis was attributed to less steric influence on the alkoxyamine C-O bond by the five-membered ring-containing TMIO compared to the six-membered piperidine ring of TEMPO. DFT predicted a 4 kJ·mol<sup>-1</sup> decrease in the bond dissociation energy (BDE) of PCN-TEMPO compared to PCN-TMIO.<sup>16</sup> Semi-empirical calculations (AM1-CI) predicted an increasing disparity in the bond dissociation energies (BDEs) of TEMPO- and TMIO-based alkoxyamines, when the steric bulk of the O-alkyl group increased.<sup>14</sup> When the alkyl group was methyl (Figure 4.2), the BDEs for TEMPO- and TMIO-alkoxyamine homolysis were similar (at 162.5 and 165.8 kJ·mol<sup>-1</sup> respectively), however when the alkyl group was *tert*-butyl, the BDE difference was significantly larger at 56.5 and 75.9 kJ·mol<sup>-1</sup> respectively.

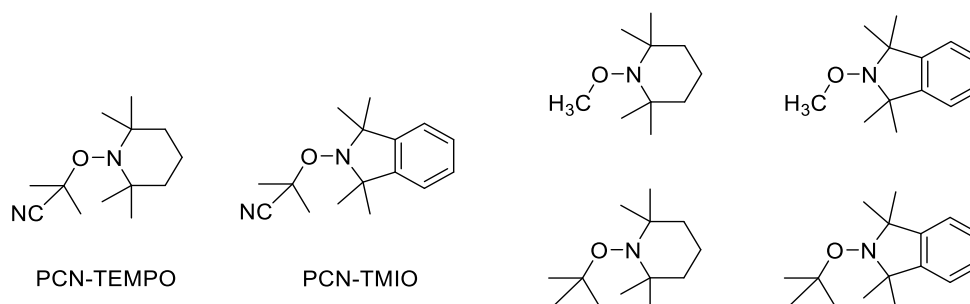


**Figure 4.2** Thermally labile alkoxyamines of TEMPO and TMIO used in theoretical BDE calculations (AM1-CI).

The UV-light activated, xanthone-containing alkoxyamine **PhEt-TMIOX** homolyzed two times slower than the TEMPO-based analogue, **XEt-TEMPO**, where xanthone was attached on the alkyl fragment of the alkoxyamine (Figure 4.3).<sup>17</sup> The difference in photolytic efficiency was rationalised by the greater distance between the triplet-sensitizing chromophore and alkoxyamine bond for the TMIO analogue.

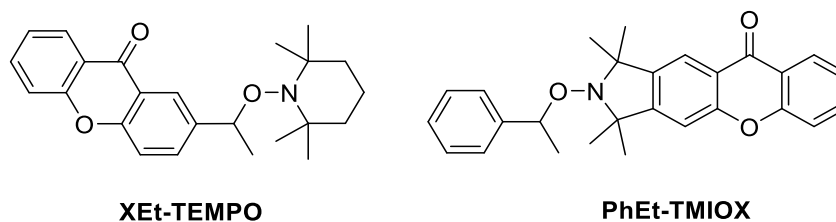


**Figure 4.3** UV-light responsive TEMPO- and TMIO-alkoxyamines.<sup>17</sup>

Given that there is no fundamental comparison of the photolysis of TEMPO- vs TMIO-alkoxyamines using visible light; in this chapter, benzimidazolequinone-based **TMIO-Vis** is prepared, as the TMIO analogue of **TEMPO-Vis** (Figure 4.4). The kinetics of homolysis of the two alkoxyamines are compared, and an investigation into the effect of oxygen and excess TEMPO, as radical scavengers for **TMIO-Vis** photolysis is provided.

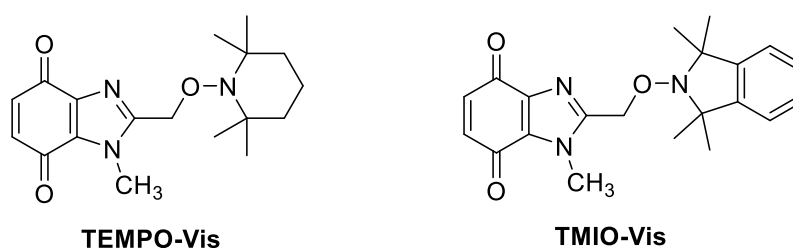


**Figure 4.4** Visible-light responsive **TEMPO-Vis** and **TMIO-Vis**.

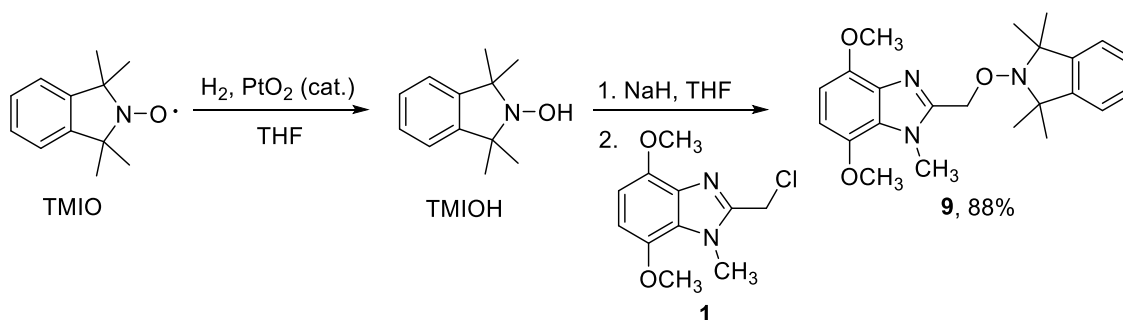
## 4.1.2 Results and Discussion

### 4.1.2.1 Synthesis of TMIO-coupled benzimidazolequinones

Analogous to the TEMPO-benzimidazolequinone syntheses in Chapter 3, 4,7-dimethoxy-1-methyl-2-[[[(1,1,3,3-tetramethyl-1,3-dihydro-2*H*-isoindol-2-yl)oxy]methyl]-1*H*-

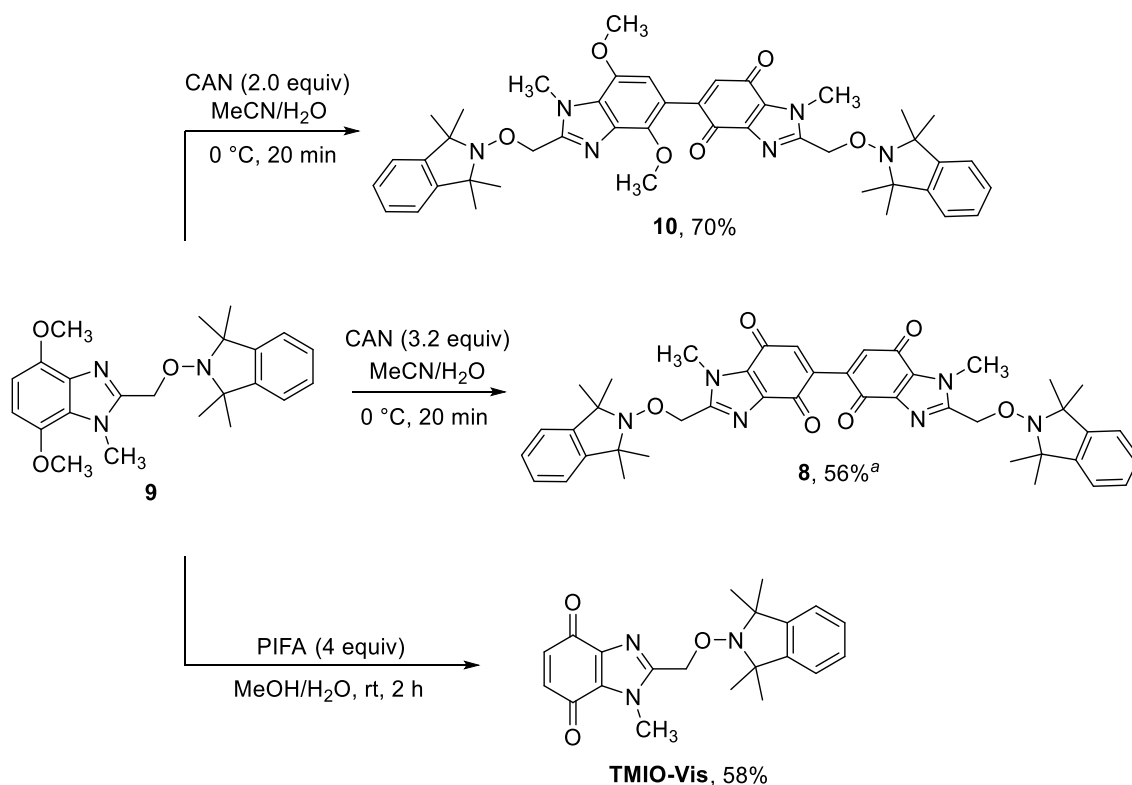
## Chapter 4

benzimidazole **9** was prepared in 88% yield by nucleophilic substitution onto dimethoxybenzimidazole methylene chloride **1**, using the pre-prepared hydroxylamine of TMIO (TMIOH, Scheme 4.2).<sup>18</sup> TMIOH was prepared by hydrogenation of TMIO over Adams' catalyst (PtO<sub>2</sub>). Completion was denoted by transition of the solution from the yellow TMIO colour to colourless of TMIOH.



**Scheme 4.2** Synthesis of 4,7-dimethoxy-1-methyl-2-[(1,1,3,3-tetramethyl-1,3-dihydro-2H-isoindol-2-yl)oxy]methyl}-1H-benzimidazole (**9**).

For oxidation of dimethoxybenzimidazole **9**, the NBS/H<sub>2</sub>SO<sub>4</sub> method<sup>19</sup> was avoided due to observed undesirable bromination of the TEMPO analogue.<sup>20</sup> Oxidation of dimethoxybenzimidazole **9** using Ce(NH<sub>4</sub>)<sub>2</sub>(NO<sub>3</sub>)<sub>6</sub> (CAN, 2.0 equiv) delivered the deeply red-coloured charge-transfer type benzimidazolequinone-dimethoxybenzimidazole **10**, in 70% yield (Scheme 4.3). As expected from Chapter 3 results for the TEMPO analogue,<sup>20</sup> adding increased amounts of CAN (3.2 equiv) to **9** gave the fully oxidized bis-benzimidazolequinone **8**, in 56% HPLC conversion. Using (CF<sub>3</sub>CO<sub>2</sub>)<sub>2</sub>IPh (PIFA)<sup>21</sup> for the oxidative-demethylation of light-insensitive **9** gave the desired light-sensitive benzimidazolequinone, **TMIO-Vis**, in 58% yield, with exclusion of light during the 2 h reaction achieved by covering of the vessel with Al-foil.



**Scheme 4.3** Synthesis of TMIO-coupled benzimidazolequinones in the absence of light. <sup>a</sup>HPLC conversion, with **9** (11%) and **10** (18%) also detected.

The <sup>1</sup>H NMR spectra of each of the TMIO-alkoxyamines **9**, **10** and **TMIO-Vis** each bear the characteristic broad signals of the TMIO-methyl groups in the 1.2–1.6 ppm region. The integration of this signal in dimer **10** amounts to 24H, confirming the presence of two TMIO moieties (Figure 4.5). The broadness of the methyl signals arises from the slow rate of *N*-inversion and N–O bond rotation relative to the NMR timescale.<sup>22</sup> Oxidative demethylation of **9** to **TMIO-Vis** is evidenced by the loss of the OCH<sub>3</sub> signals, and the downfield shift of the aromatic benzimidazole CHs in **9** at 6.51 and 6.58 ppm to 6.64 and 6.71 ppm in **TMIO-Vis**. In **10**, two of the OCH<sub>3</sub> signals appear, one at 3.91 ppm and one which overlaps with the two NCH<sub>3</sub> signals at ~ 4.19 ppm. The oxidative coupling giving **10** results in the collapse of the dimethoxybenzene and quinone CH signals to singlets at 6.51 and 6.74 ppm respectively, with the unsymmetrical nature of the dimer noted by the presence of two non-equivalent methylene singlets at 5.16 and 5.19 ppm. The location of the bridge at C5–C5' is indicated using the <sup>13</sup>C NMR spectrum with the 6-CH and 6'-CH signals at 134 and 105 ppm for **3** appearing at almost identical chemical shifts to the di-TEMPO analogue (Figure 4.6), for which the C5–C5' designation was confirmed by the X-ray crystal structure of the product of oxidative demethylation, **Bis-**

## Chapter 4

**TEMPO-Vis.** The major difference in  $^{13}\text{C}$  NMR spectrum arises from the signals associated with the TMIO aromatics rings i.e. CHs at 121.5, 127.3 and 127.4 ppm and quaternary carbons at 144.5 and 144.7 ppm.

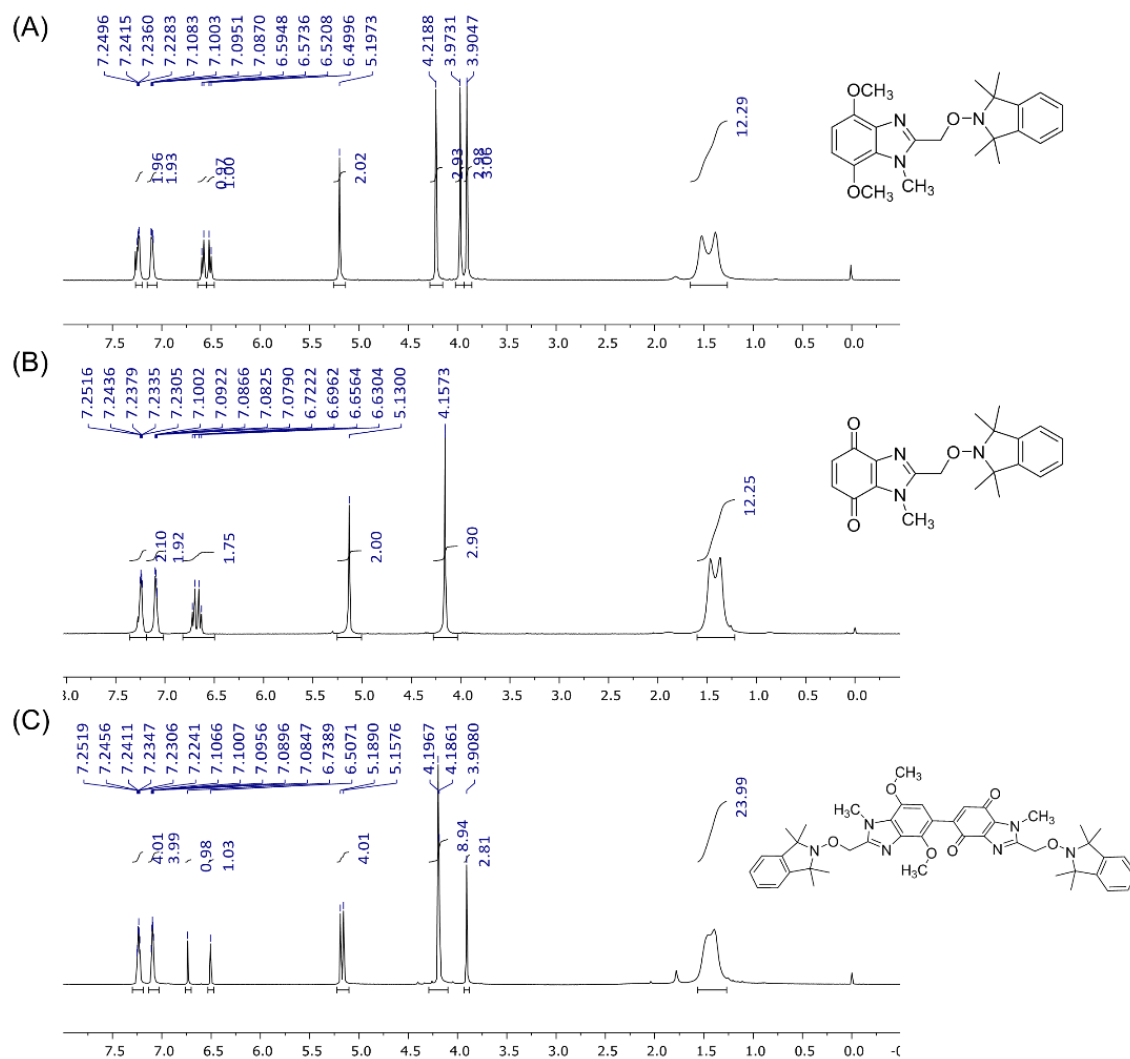


**Figure 4.5**  $^1\text{H}$  NMR spectra of (a) 4,7-dimethoxy-1-methyl-2-[[1,1,3,3-tetramethyl-1,3-dihydro-2H-isoindol-2-yl]oxy]methyl]-1H-benzimidazole (**9**), (b) **TMIO-Vis** and (c) 4',7'-dimethoxy-1,1'-dimethyl-2,2'-bis[[1,1,3,3-tetramethyl-1,3-dihydro-2H-isoindol-2-yl]oxy]methyl]-1H,1'H-[5,5'-bibenzimidazole]-4,7-dione (**10**).



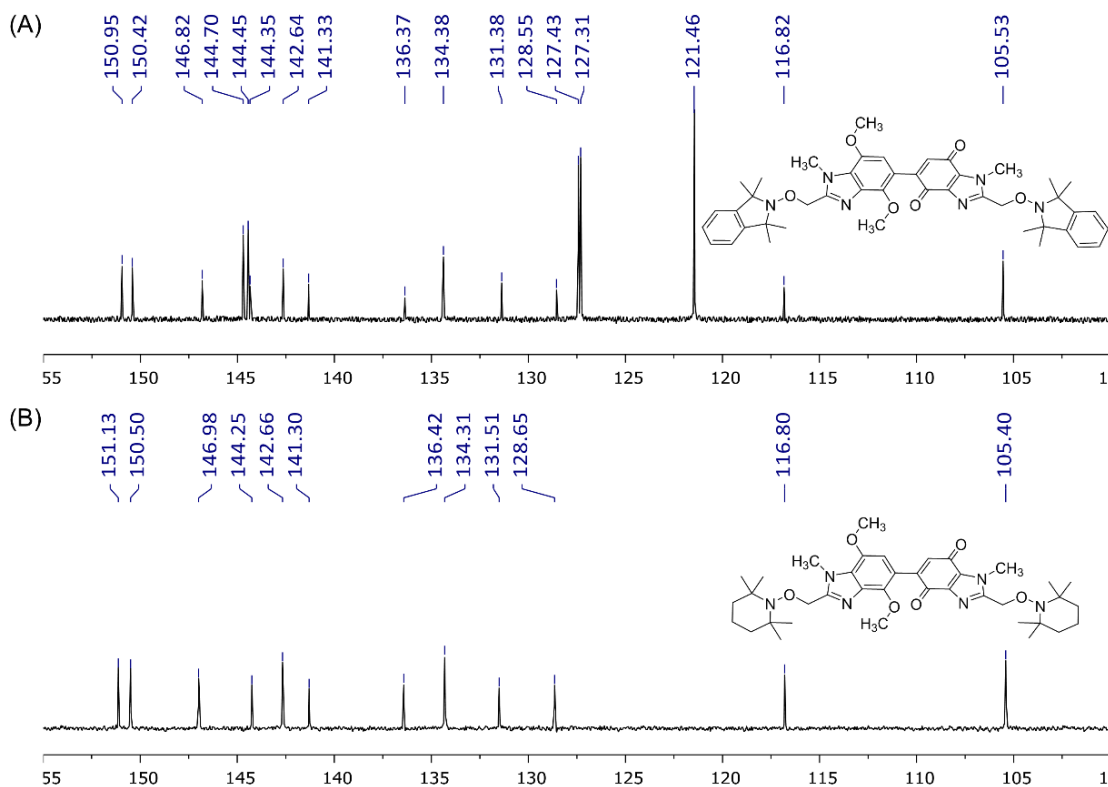


**Figure 4.6**  $^{13}\text{C}$  NMR spectra (aromatic region) in  $\text{CDCl}_3$  of (a) 4',7'-dimethoxy-1,1'-dimethyl-2,2'-bis[[(1,1,3,3-tetramethyl-1,3-dihydro-2*H*-isoindol-2-yl)oxy]methyl]-1*H*,1'*H*-[5,5'-bibenzimidazole]-4,7-dione (**10**) and (b) the bis-TEMPO analogue (**3** from Chapter 3).

#### 4.1.2.2 Kinetics of homolysis for TMIO-Vis

TMIO-based bis-alkoxyamine **10** (with coupled dimethoxybenzimidazole and benzimidazolequinone motifs), like its TEMPO analogue, is stable under visible-light. The photolytic stability of **10** is explained by the low energy charge-transfer state evidenced by the long wavelength absorbance band at  $\lambda_{\text{max}} = 486 \text{ nm}$  (Figure 4.7) (red-shifted by 104 nm compared to **TMIO-Vis**), and the low energy (DFT-derived) triplet state ( $E_{\text{T}}$ ) of  $180.5 \text{ kJ}\cdot\text{mol}^{-1}$  (which is comparable to the TEMPO analogue in Chapter 3:  $E_{\text{T}} = 176.8 \text{ kJ}\cdot\text{mol}^{-1}$ ) (Table 4.1). For **3**,  $\Delta G_{\text{d}} = \text{BDE} - E_{\text{T}} = -92.7 \text{ kJ}\cdot\text{mol}^{-1}$ , a less favourable reaction compared to the more exothermic homolysis of **TMIO-Vis**, with  $\Delta G_{\text{d}} = -118.6 \text{ kJ}\cdot\text{mol}^{-1}$ . The low energy  $E_{\text{T}}$  renders the molecule stable despite both alkoxyamine functionalities having similar and favourable BDEs comparable to light-sensitive **TMIO-Vis**.

The rate equation for the decay of labile alkoxyamines depends on the [alkoxyamine], and the [scavenger] used to prevent the reverse reaction (radical

combination) to the original alkoxyamine. The rate equation (eq 4.1) is second order in nature, however, using an excess scavenger ensures that [scavenger] is effectively constant, and the rate equation is pseudo-first-order (eq 4.2) with rate constant of homolysis,  $k_d$ . Thus, the plot of equation 4.4 will be linear, if first-order kinetics are followed, having slope =  $k_d$ .

$$\frac{d[\text{alkoxyamine}]}{dt} = -k[\text{scavenger}][\text{alkoxyamine}] \quad (4.1)$$

$$\frac{d[\text{alkoxyamine}]}{dt} = -k_d[\text{alkoxyamine}] \quad (4.2)$$

$$-\frac{d[\text{alkoxyamine}]}{[\text{alkoxyamine}]} = k_d dt \quad (4.3)$$

$$\ln\left(\frac{[\text{alkoxyamine}]_0}{[\text{alkoxyamine}]_t}\right) = k_d t \quad (4.4)$$

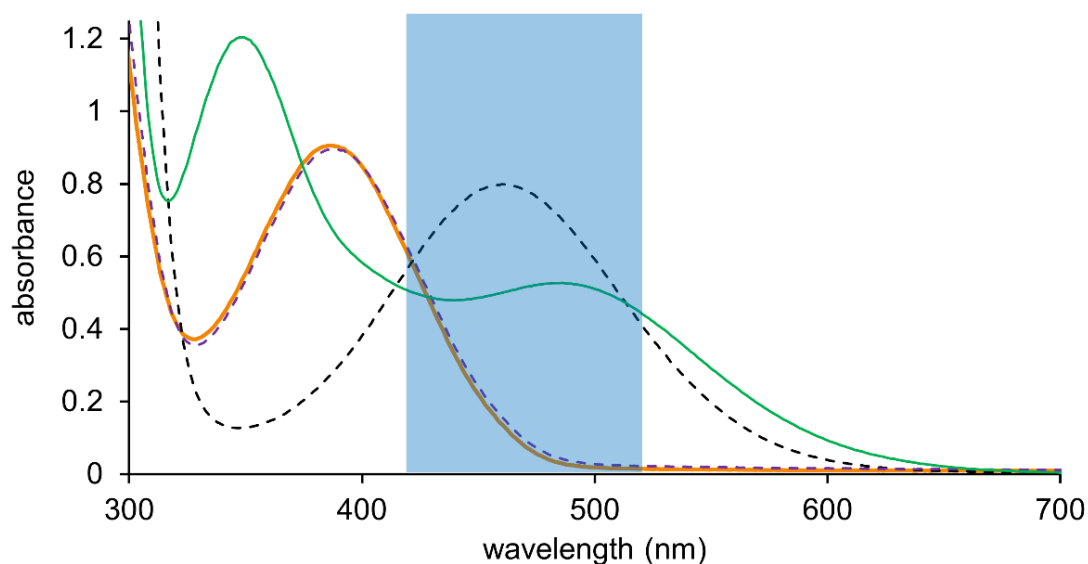


**Figure 4.7** UV-visible absorbance spectra in MeCN of 4',7'-dimethoxy-1,1'-dimethyl-2,2'-bis[[(1,1,3,3-tetramethyl-1,3-dihydro-2*H*-isoindol-2-yl)oxy]methyl]-1*H*,1'*H*-[5,5'-bibenzimidazole]-4,7-dione (**10**) (green continuous, 0.375 mM), **TMIO-Vis** (orange continuous, 0.75 mM), **TEMPO-Vis** (purple dash, 0.75 mM) and TEMPO (black dashed, 75.0 mM) with blue LED emission region (420–520 nm) shaded in blue.

Under blue LED illumination (9 W) and using oxygen as radical scavenger,<sup>23–25</sup> the visible-light homolysis of **TMIO-Vis** and **TEMPO-Vis** followed first-order decay kinetics (Figure 4.8). The first order rate plot of alkoxyamines were virtually superimposable, with the TMIO- and TEMPO-benzimidazolequinones having identical (within experimental error)  $k_d$  values of  $0.73 \text{ min}^{-1}$  each (Table 4.1).

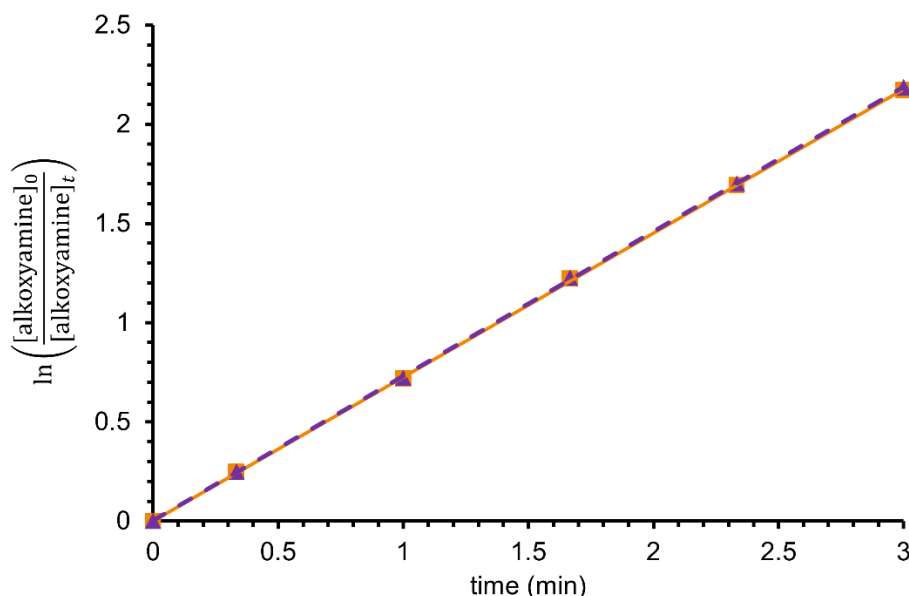


**Figure 4.8** Kinetics of room temperature blue-LED (9 W) induced **TEMPO-Vis** (purple dashed line) and **TMIO-Vis** (orange continuous line) alkoxyamine (5 mM, MeCN) homolysis, using  $\text{O}_2$  as the radical trap. Alkoxyamine decay was monitored by HPLC at 254 nm. Experiments were performed in triplicate.

**Table 4.1** Kinetics of alkoxyamine homolysis using visible-light,<sup>a</sup> and DFT-calculated homolysis parameters

alkoxyamine	$k_d$ ( $\text{min}^{-1}$ ) <sup>b</sup>	BDE ( $\text{kJ}\cdot\text{mol}^{-1}$ ) <sup>c</sup>	$E_T$ ( $\text{kJ}\cdot\text{mol}^{-1}$ ) <sup>c</sup>
<b>10</b>	-	87.8, 87.7 <sup>d</sup>	180.5
<b>TMIO-Vis</b>	$0.725 \pm 0.012$	89.1	207.7
<b>TEMPO-Vis</b>	$0.730 \pm 0.011$	85.1	207.4
<b>TMIO-Vis</b> + 10 equiv TEMPO	$0.334 \pm 0.004$	-	-
<b>TMIO-Vis</b> + 100 equiv TEMPO	$0.0532 \pm 0.0012$	-	-

<sup>a</sup>Conditions: alkoxyamine (MeCN, 5 mM) using a blue (9 W) LED bulb in the presence of  $\text{O}_2$ .

<sup>b</sup>Dissociation rate ( $k_d$ ) derived from slope of Figure 4.8 or 4.9. <sup>c</sup>M06-2X/6-311++G (d,p). <sup>d</sup>BDE values at benzimidazolequinone and dimethoxybenzimidazole part respectively.

In contrast to the literature thermal dissociation of TEMPO and TMIO alkoxyamines (see above), the photolysis of **TEMPO-Vis** and **TMIO-Vis** occurred at the same rate. This is supported by DFT calculations predicting only a marginal a  $4 \text{ kJ}\cdot\text{mol}^{-1}$  drop in BDE for **TEMPO-Vis** vs **TMIO-Vis**, but perhaps more significantly, there was sufficient energy in the triplet states ( $E_T$ ) to give highly exothermic free energies of dissociation ( $\Delta G_d = \text{BDE} - E_T$ ) of  $-122.3$  and  $-118.6 \text{ kJ}\cdot\text{mol}^{-1}$  for **TEMPO-Vis** and **TMIO-Vis** respectively. As a consequence of both compounds bearing the same benzimidazolequinone chromophore, the UV-visible spectra of **TMIO-Vis** and **TEMPO-Vis** (Figure 4.7) were almost identical with a  $\lambda_{\text{max}}$  of 382 nm for both, and molar absorptivity values ( $\epsilon$ ) in good agreement at  $1.17 \times 10^3$  for **TMIO-Vis** and  $1.16 \times 10^3$  for **TEMPO-Vis**. Despite the photolysis being performed at 20 times higher concentration (5 mM compared to 0.25 mM in Chapter 3), no quenching of the homolytic process by liberated nitroxide was observed, as evidenced by the alkoxyamine decay following first-order kinetics for the duration of the experiment. Indeed, the higher alkoxyamine concentration is primarily responsible for the 9-fold decrease in  $k_d$  of **TEMPO-Vis** compared with the lower alkoxyamine concentration used in Chapter 3, which leads to a relative decrease in light intensity (overall absorption). Two different concentrations of free TEMPO nitroxide were added to the aerated **TMIO-Vis** solution experiment under blue LED (Figure 4.9).

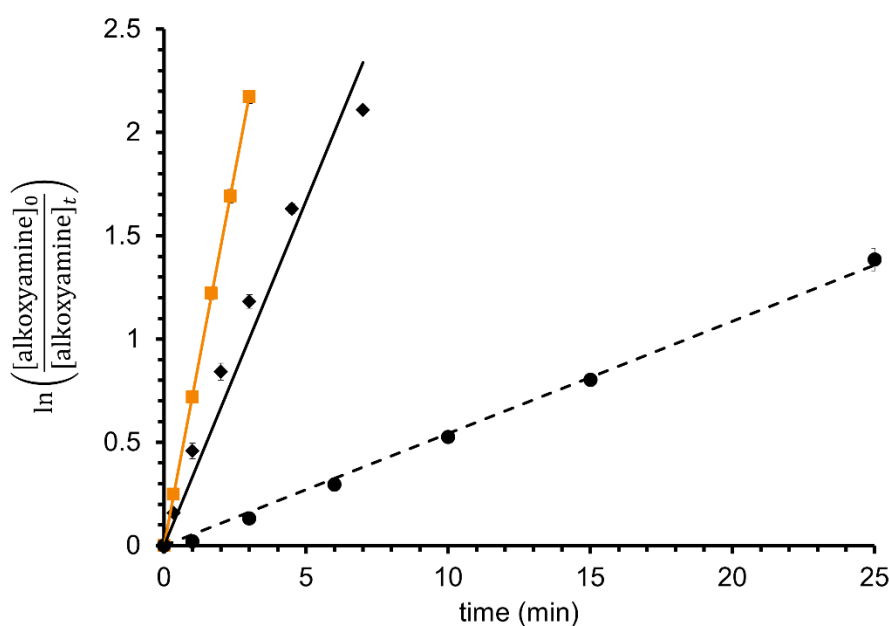


**Figure 4.9** The effect of added free TEMPO (10 equiv solid line and 100 equiv dashed line) on the kinetics of room temperature blue-LED (9 W) induced **TMIO-Vis** alkoxyamine (5 mM) homolysis in MeCN (orange line), under oxygenated conditions. Alkoxyamine decay was monitored by HPLC at 254 nm.

The product of radical trapping was thus the product of nitroxide exchange, **TEMPO-Vis**, as monitored by HPLC (Figure 4.10), with no products of O<sub>2</sub>-trapping observed. The decay of **TMIO-Vis** in this nitroxide-exchange experiment followed first-order kinetics, as for the O<sub>2</sub>-trapped experiment, but the  $k_d$  decreased by 2.2 and 13.6 times, when the sample was spiked with 10 and 100 equiv TEMPO respectively.

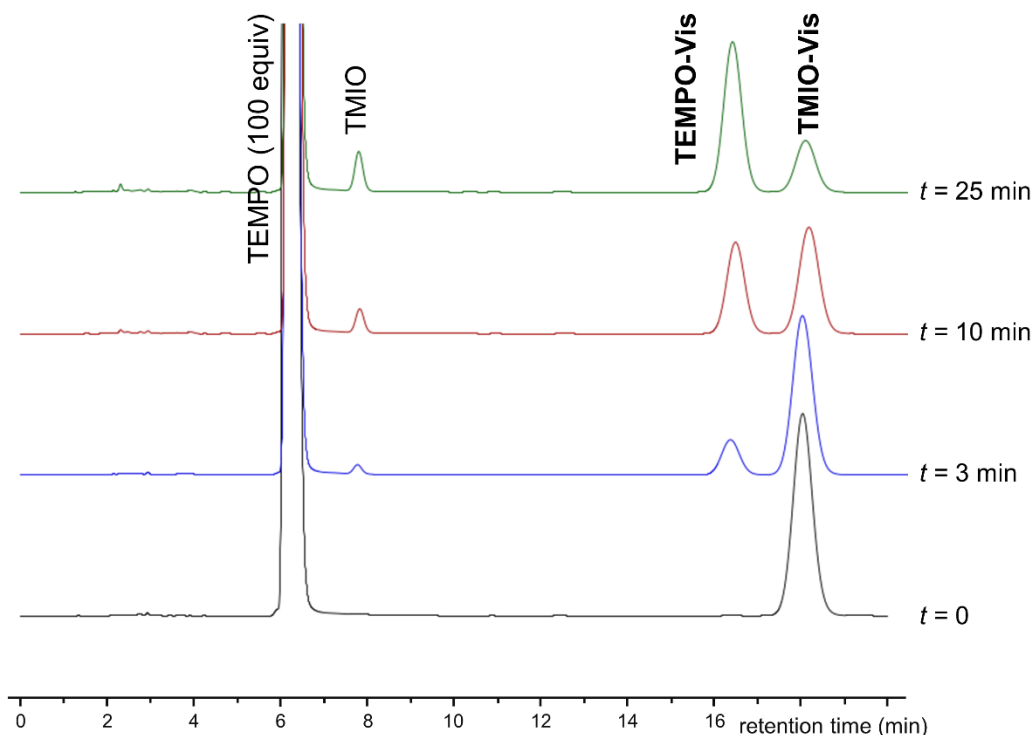
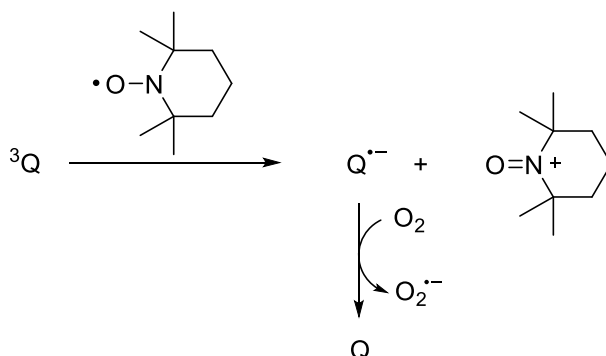


**Figure 4.10** HPLC monitoring of the room temperature blue LED homolysis of **TMIO-Vis** in the presence of excess free TEMPO (100 equiv).

Such TEMPO-induced quenching may proceed *via* electron transfer from the nitroxide to the benzimidazolequinone excited state of **TMIO-Vis**, with similar processes demonstrated for the TEMPO-induced reduction of triplet excited states of C<sub>60</sub> fullerene<sup>26</sup> and isopropylthioxanthone and/or benzophenone photosensitizers.<sup>27</sup> In our case, TEMPO is expected to reduce the quinone triplet state to give an oxoammonium cation and a quinone radical anion (semiquinone), which is easily re-oxidized to the singlet quinone under oxygenated conditions (Scheme 4.5).



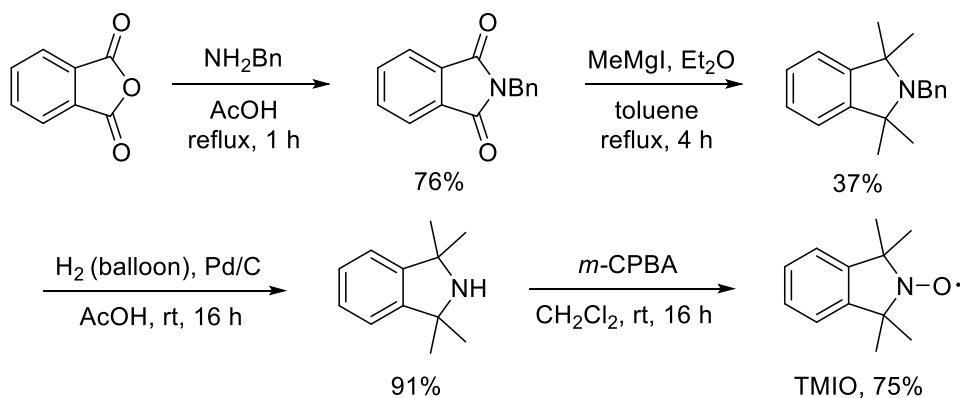
**Scheme 4.5** Proposed excited quinone (Q) triplet state quenching by TEMPO.

The UV-visible absorption spectrum shows the strong absorbance of TEMPO in the blue region (420–520 nm, Figure 4.7), thus competitive absorption by free TEMPO plays a role in the decreased **TMIO-Vis** homolysis rate, particularly when TEMPO is present at 100-fold excess. For thermal processes, nitroxide-trapping is well-established as a reliable method for the determination of  $k_d$ ,<sup>14,28–30</sup> however, the quenching effects of TEMPO means that oxygen is the preferred trap for photolytic processes.

### 4.1.3 Experimental

#### 4.1.3.1 Materials

1,1,3,3-Tetramethyl-2,3-dihydroisindol-2-ylloxyl (TMIO) was synthesized in four steps according to the literature (Scheme 4.6).<sup>1,31</sup> Reaction of phthalic anhydride (TCI, > 98%) with benzylamine (Sigma-Aldrich, 99%) in AcOH (Sigma-Aldrich,  $\geq 99.85\%$ ) at reflux for 1 h gave *N*-benzylphthalimide in 76% yield, after recrystallization in Et<sub>2</sub>O (Sigma-



**Scheme 4.6** Synthesis of TMIO nitroxide.

Aldrich, > 99.5%).<sup>31</sup> Reaction of *N*-benzylphthalimide with MeMgI {prepared *in situ* from Mg turnings (Sigma-Aldrich, 98%), MeI (Sigma-Aldrich, > 99%), Et<sub>2</sub>O [(Sigma-Aldrich, > 99.5%), dried and distilled over Na (Sigma-Aldrich, > 99.8%) and benzophenone (ACROS Organics, 99%)]} in toluene (Fischer Scientific, ≥ 99.8%) at reflux for 4 h gave 2-benzyl-1,1,3,3-tetramethylisoindoline in 37% yield, after purification by passing through basic aluminium oxide (VWR) using hexanes (Fischer Scientific, bp 40–60 °C) as eluent.<sup>1</sup> Reduction of 2-benzyl-1,1,3,3-tetramethylisoindoline using a balloon of H<sub>2</sub> (BOC, 99.99%) over Pd/C (ACROS Organics, 10%) in AcOH for 16 h gave 1,1,3,3-tetramethylisoindoline in 91% yield.<sup>1</sup> Oxidation of 1,1,3,3-tetramethylisoindoline using 3-chloroperoxybenzoic acid (*m*-CPBA, Sigma-Aldrich, 57–86%), in CH<sub>2</sub>Cl<sub>2</sub> (Fischer Scientific, ≥ 99%) for 16 h gave TMIO in 75% yield after recrystallization from aq EtOH (70% EtOH, prepared using EtOH, Fischer Scientific, 96%).<sup>31</sup> 2-(Chloromethyl)-4,7-dimethoxy-1-methyl-1*H*-benzimidazole **1** was prepared according to Chapter 3 (section 3.6.3) in 85% overall yield by *N*-methylation and benzyl-chlorination of (4,7-dimethoxy-1*H*-benzimidazol-2-yl)methanol. Selectfluor (Sigma-Aldrich, > 95% F<sup>+</sup> active), MeCN (Sigma-Aldrich, HPLC Plus, ≥ 99.9%), CH<sub>2</sub>Cl<sub>2</sub> (Fischer Scientific, ≥ 99%), MgSO<sub>4</sub> (Alfa Aesar, 99.5%) were used as received. PtO<sub>2</sub> (Sigma-Aldrich), NaH (Sigma-Aldrich, 60% dispersion in mineral oil), [bis(trifluoroacetoxy)iodo]benzene (PIFA, Sigma-Aldrich, 97%), cerium(IV) ammonium nitrate (CAN, Fischer Scientific, 99%), MeCN (Sigma-Aldrich, HPLC Plus, ≥ 99.9%), MeOH (Fischer Scientific, ≥ 99.8%) and MgSO<sub>4</sub> (Alfa Aesar, 99.5%) were used as received. Thin layer chromatography (TLC) was performed on Merck TLC silica gel 60 F<sub>254</sub> plates using a UV lamp (254 nm) for visualization. Flash chromatography was performed using silica gel, pore size 60 Å, 230–400 mesh, and particle size 40–63 μm (Sigma-Aldrich) using EtOAc (Fischer Scientific, ≥ 99%) and hexanes (Fischer Scientific, bp 40–60 °C). Dry column vacuum chromatography (with Apollo Scientific silica gel ZEOprep 60 and 15–35 μm particle size),<sup>32</sup> was preferable for purification of light-active compounds, due to the convenience of light exclusion by covering the apparatus with Al-foil during elution.

#### 4.1.3.2 Measurements

**DFT calculations:** Geometry optimizations were performed using Gaussian 16,<sup>33</sup> installed at the Irish Centre for High-End Computing (ICHEC), using an M06-2X functional<sup>34</sup> with a 6-311++G (d,p) basis set. All structures were fully optimized in the

gas phase and verified as local minima through frequency calculations. Bond dissociation energies (BDEs) were calculated based on the free energy difference between the starting alkoxyamines and the radical products (thermal free energy correction was added). The lowest triplet energies ( $E_T$ ) of starting alkoxyamines are given relative to the optimized singlet ground state ( $S_0$ ) energies. A table of model energies and images of optimized geometries are reported in the appendix (Table A4.1).

**Melting points, ultraviolet-visible and infrared spectroscopy:** Melting points were measured on a Stuart Scientific melting point apparatus SMP3. Ultraviolet-visible (UV-vis) spectra were recorded using a Varian (Cary 100) UV-vis spectrometer. Spectra are reported in Figure 4.7, which depicts **TMIO-Vis** and **TEMPO-Vis** at the same concentration (0.75 mM) and compound **10** is at half concentration (0.375 mM) due to stronger absorbance. The UV-vis spectrum of TEMPO is depicted at  $100 \times$  concentration (75.0 mM) compared to **TMIO-Vis** to provide insight into the **TMIO-Vis** homolysis experiment with added TEMPO (100 equiv). Infrared spectra were recorded using a Perkin-Elmer Spec 1 with ATR attached.

**Nuclear magnetic resonance (NMR spectroscopy):** NMR spectra were recorded using a JEOL 400 MHz or a Varian 500 MHz instrument. The chemical shifts were in ppm relative to  $\text{Si}(\text{CH}_3)_4$  for recorded spectra in  $\text{CDCl}_3$ .  $^{13}\text{C}$  NMR data were collected at 100 or 125 MHz with complete proton decoupling. NMR assignments were supported by DEPT and  $^1\text{H}$ - $^1\text{H}$  (COSY) and  $^1\text{H}$ - $^{13}\text{C}$  correlation. NMR spectra are included in the appendix of this thesis.

**High resolution mass spectrometry (HRMS):** HRMS was carried out using ESI time-of-flight mass spectrometer (TOFMS) in positive mode using a Waters LCT Mass Spectrometry instrument.

**Visible-light homolysis:** The photoreactor was set up and homolysis kinetics were measured according to alkoxyamine decay as described in Chapter 3 (section 3.6.2).<sup>20</sup>

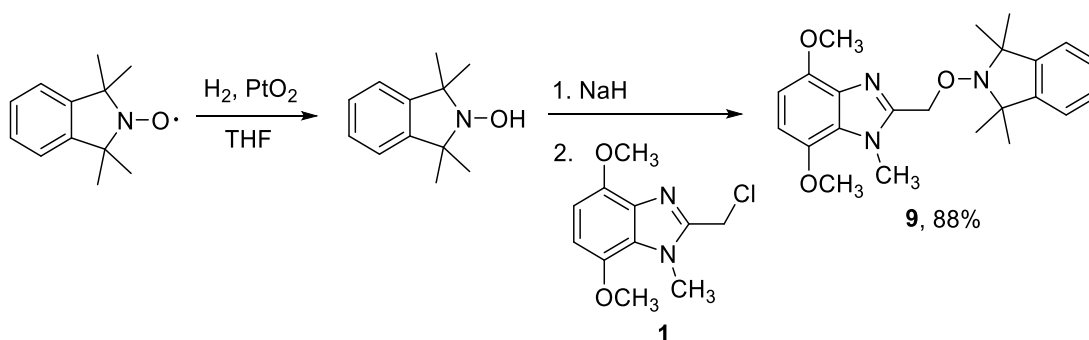
**Analytical HPLC:** The Agilent 1100 Series HPLC was equipped with a UV detector operating at 254 nm and a Phenomenex® BondClone™ 10  $\mu\text{m}$  C18,  $250 \times 4.6$  mm column. Calibration curves were generated for [alkoxyamine] for the construction of rate plots. The mobile phase comprised of 55% MeCN in  $\text{H}_2\text{O}$  at a flow rate of 1.5 mL/min for 12 min in the cases of **TEMPO-Vis** and **TMIO-Vis** homolyses in the presence of  $\text{O}_2$  scavenger, and the mobile phase was 48% MeCN in  $\text{H}_2\text{O}$  at a flow rate of 1.5 mL/min



for 22 min in the case of **TMIO-Vis** homolysis in the presence of TEMPO scavenger (Figure 4.8). Analysis of the reaction mixture of 4,7-dimethoxy-1-methyl-2-[[[(1,1,3,3-tetramethyl-1,3-dihydro-2*H*-isoindol-2-yl)oxy]methyl]-1*H*-benzimidazole **2** with CAN (3.2 equiv) was performed using the following mobile phase program (all %MeCN in H<sub>2</sub>O, 1.5 mL/min): time 0 = 45, 15 min = 95, 30 min = 95.

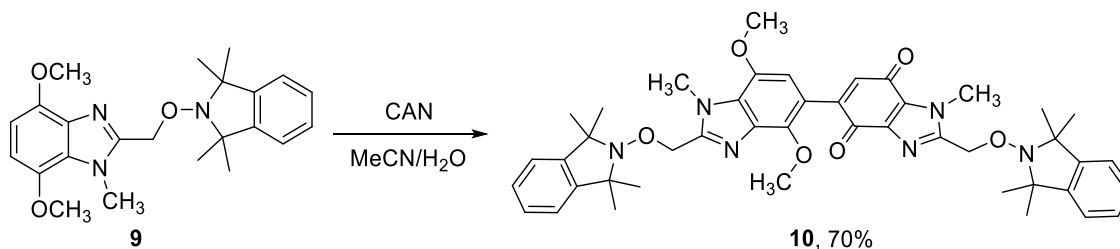
#### 4.1.3.3 Synthetic procedures and characterization

##### Synthesis of 4,7-dimethoxy-1-methyl-2-[[[(1,1,3,3-tetramethyl-1,3-dihydro-2*H*-isoindol-2-yl)oxy]methyl]-1*H*-benzimidazole (**9**)



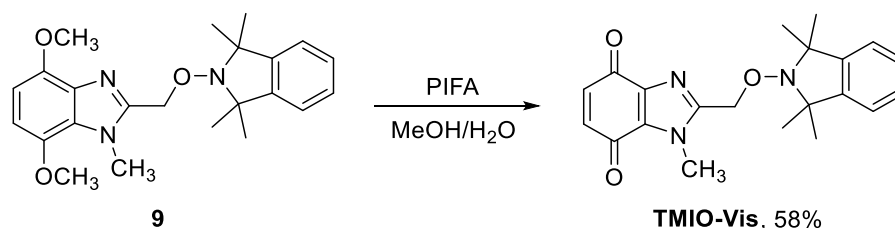
TMIO (0.340 g, 1.79 mmol) and PtO<sub>2</sub> (7 mg, 0.03 mmol) in THF (10 mL) were stirred under a balloon of H<sub>2</sub> at rt, until the mixture turned colourless (~1 h). The mixture was filtered, NaH (27 mg, 0.66 mmol, 60%) added, and the stirring continued at rt for 1 h. Chloride **1** (0.143 g, 0.60 mmol) was added, and the stirring continued at reflux for 16 h. H<sub>2</sub>O (50 mL) was added and extracted using CH<sub>2</sub>Cl<sub>2</sub> (3 × 40 mL). The combined organic layers were dried (MgSO<sub>4</sub>), evaporated, and the residue purified by flash chromatography using EtOAc and hexanes as eluent to give **9** (0.209 g, 88%), as a white solid; mp 162–164 °C; *R*<sub>f</sub> 0.37 (2 : 3 EtOAc : hexanes);  $\nu_{\text{max}}$  (neat, cm<sup>-1</sup>) 1041, 1073, 1100, 1145, 1164, 1190, 1210, 1233, 1264, 1338, 1362, 1392, 1463, 1532, 2223, 2837, 2954;  $\delta_{\text{H}}$  (400 MHz, CDCl<sub>3</sub>) 1.19–1.62 (12H, bs), 3.91 (3H, s), 3.97 (3H, s), 4.22 (3H, s, NCH<sub>3</sub>), 5.20 (2H, s), 6.51 (1H, d, *J* = 8.5 Hz), 6.59 (1H, d, *J* = 8.5 Hz), 7.10 (2H, dd, *J* = 3.2, 5.3 Hz), 7.24 (2H, dd, *J* = 3.2, 5.3 Hz);  $\delta_{\text{C}}$  (100 MHz, CDCl<sub>3</sub>) 25.1, 30.1 (both CH<sub>3</sub>), 33.2 (NCH<sub>3</sub>), 55.8, 56.0 (both OCH<sub>3</sub>), 67.6 (C), 71.3 (CH<sub>2</sub>), 101.2, 103.5, 121.5 (all CH), 126.9 (C), 127.4 (CH), 134.4, 141.9, 144.9, 146.3, 149.5 (all C); HRMS (ESI) *m/z* [M + H]<sup>+</sup>, C<sub>23</sub>H<sub>30</sub>N<sub>3</sub>O<sub>3</sub> calcd. 396.2284, observed 396.2287.

**Synthesis of 4',7'-dimethoxy-1,1'-dimethyl-2,2'-bis{[(1,1,3,3-tetramethyl-1,3-dihydro-2*H*-isoindol-2-yl)oxy]methyl}-1*H*,1'*H*-[5,5'-bibenzimidazole]-4,7-dione (10)**



Cerium(IV) ammonium nitrate (CAN) (0.194 g, 0.36 mmol) in H<sub>2</sub>O (2.5 mL) was added dropwise to 4,7-dimethoxy-1-methyl-2-[[1,1,3,3-tetramethyl-1,3-dihydro-2*H*-isoindol-2-yl)oxy]methyl]-1*H*-benzimidazole **9** (70 mg, 0.18 mmol) in MeCN (10 mL) at 0 °C, and stirred for 20 min in the absence of light. H<sub>2</sub>O (10 mL) was added, and the solution extracted with CH<sub>2</sub>Cl<sub>2</sub> (3 × 15 mL). The combined organic layers were dried (MgSO<sub>4</sub>), evaporated, and the residue purified by dry column vacuum chromatography with EtOAc and hexanes as eluent to give **10** (47 mg, 70%) as a deep red oil; *R*<sub>f</sub> 0.21 (2 : 3 EtOAc : hexanes); λ<sub>max</sub> (MeCN, nm) 486 (ε = 1.41 × 10<sup>3</sup>), 348 (ε = 3.21 × 10<sup>3</sup>), 231 (ε = 5.31 × 10<sup>4</sup>); ν<sub>max</sub> (neat, cm<sup>-1</sup>) 2972, 2927, 1682, 1654 (C=O), 1500, 1483, 1459, 1375, 1361, 1279, 1166, 1127, 1104; δ<sub>H</sub> (500 MHz, CDCl<sub>3</sub>) 1.26–1.57 (24H, bs), 3.91 (3H, s, OCH<sub>3</sub>), 4.19 (3H, s, NCH<sub>3</sub>), 4.20 (6H, s), 5.16 (2H, s), 5.19 (2H, s), 6.51 (1H, s), 6.74 (1H, s), 7.08–7.11 (4H, m), 7.22–7.25 (4H, m); δ<sub>C</sub> (125 MHz, CDCl<sub>3</sub>) 25.1, 30.0 (both CH<sub>3</sub>), 32.8, 33.1 (both NCH<sub>3</sub>), 55.9, 61.6 (both OCH<sub>3</sub>), 67.6, 67.7 (both C), 70.0, 71.1 (both CH<sub>2</sub>), 105.5 (CH), 116.8 (C), 121.5, 127.3, 127.4 (all CH), 128.6, 131.4 (both C), 134.4 (CH), 136.4, 141.3, 142.6, 144.4, 144.5, 144.7, 146.9, 150.4, 151.0 (all C), 178.9, 180.1 (both C=O); HRMS (ESI) *m/z* [M + H]<sup>+</sup>, C<sub>44</sub>H<sub>51</sub>N<sub>6</sub>O<sub>6</sub> calcd. 759.3870, observed 759.3873.

**Synthesis of 1-methyl-2-[[1,1,3,3-tetramethyl-1,3-dihydro-2*H*-isoindol-2-yl)oxy]methyl]-1*H*-benzimidazole-4,7-dione (TMIO-Vis)**



Bis(trifluoroacetoxy)iodo]benzene (PIFA, 0.65 g, 1.51 mmol) was added to a suspension of 4,7-dimethoxy-1-methyl-2-[[1,1,3,3-tetramethyl-1,3-dihydro-2*H*-isoindol-2-yl)oxy]methyl]-1*H*-benzimidazole **9** (0.15 g, 0.38 mmol) in aq MeOH (2.5%, 4.5 mL) at rt, and stirred for 2 h in the absence of light. H<sub>2</sub>O (10 mL) was added, and the solution extracted with CH<sub>2</sub>Cl<sub>2</sub> (3 × 20 mL). The combined organic layers were dried (MgSO<sub>4</sub>), evaporated, and the residue purified by dry column vacuum chromatography with EtOAc and hexanes as eluent to give **TMIO-Vis** (80 mg, 58%), as a yellow solid; mp 169–170 °C (deg); *R*<sub>f</sub> 0.47 (2 : 3 EtOAc : hexanes); λ<sub>max</sub> (MeCN, nm) 382 (ε = 1.17 × 10<sup>3</sup>), 248 (ε = 1.82 × 10<sup>4</sup>), 223 (ε = 2.36 × 10<sup>4</sup>); ν<sub>max</sub> (neat, cm<sup>-1</sup>) 2977, 2929, 1666 (C=O), 1592, 1515, 1478, 1451, 1376, 1361, 1332, 1273, 1195, 1163, 1104, 1051, 1038; δ<sub>H</sub> (400 MHz, CDCl<sub>3</sub>) 1.20–1.57 (12H, bs), 4.16 (3H, s), 5.13 (2H, s), 6.64 (1H, d, *J* = 10.4 Hz), 6.71 (1H, d, *J* = 10.4 Hz), 7.08–7.10 (2H, m), 7.23–7.25 (2H, m); δ<sub>C</sub> (100 MHz, CDCl<sub>3</sub>) 25.2, 30.0 (both CH<sub>3</sub>), 32.9 (NCH<sub>3</sub>), 67.8 (C), 69.8 (CH<sub>2</sub>), 121.5, 127.6 (both CH), 131.4 (C), 136.3, 136.6 (both CH), 141.0, 144.4, 151.3 (all C), 178.7, 181.0 (both C=O); HRMS (ESI) *m/z* [M + H]<sup>+</sup>, C<sub>21</sub>H<sub>24</sub>N<sub>3</sub>O<sub>3</sub> calcd. 366.1818, observed 366.1825.

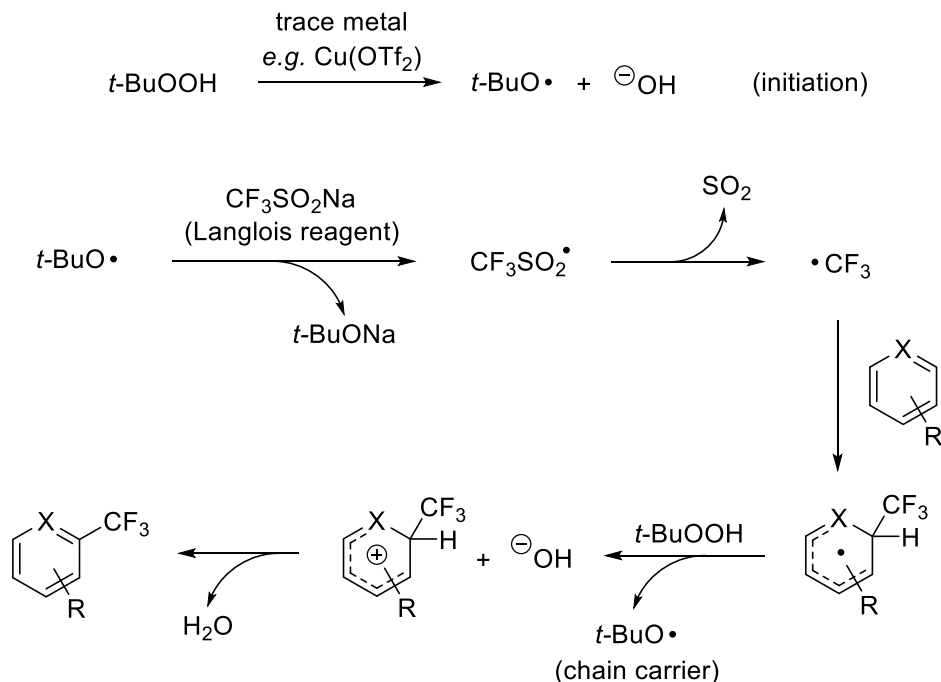
#### 4.1.4 Conclusions

**TMIO-Vis** has been introduced as a room-temperature visible-light activated source of radicals, with a rate of dissociation mirroring **TEMPO-Vis**. The almost identical observed rates of homolysis for **TMIO-Vis** and **TEMPO-Vis** using blue LED were supported by similar absorptivity and favourable DFT-derived Δ*G*<sub>d</sub> (Δ*G*<sub>d</sub> = BDE – *E*<sub>T</sub>) values of –118.6 and –122.3 kJ·mol<sup>-1</sup> respectively. The stability of dimethoxybenzene-coupled quinone **10** was rationalized by a higher DFT-derived Δ*G*<sub>d</sub> for homolysis. TEMPO significantly absorbs in the visible-region and quenches chromophore excited states, so the addition of free TEMPO significantly lowers the dissociation rate of **TMIO-Vis** under blue LED. Nitroxide-exchange to **TEMPO-Vis** during the photolysis of **TMIO-Vis** was conveniently monitored by HPLC connected to a UV-detector at 254 nm.

Part 2: The Chemistry of CF<sub>3</sub>-Bis-TEMPO-Vis

## 4.2.1 Introduction

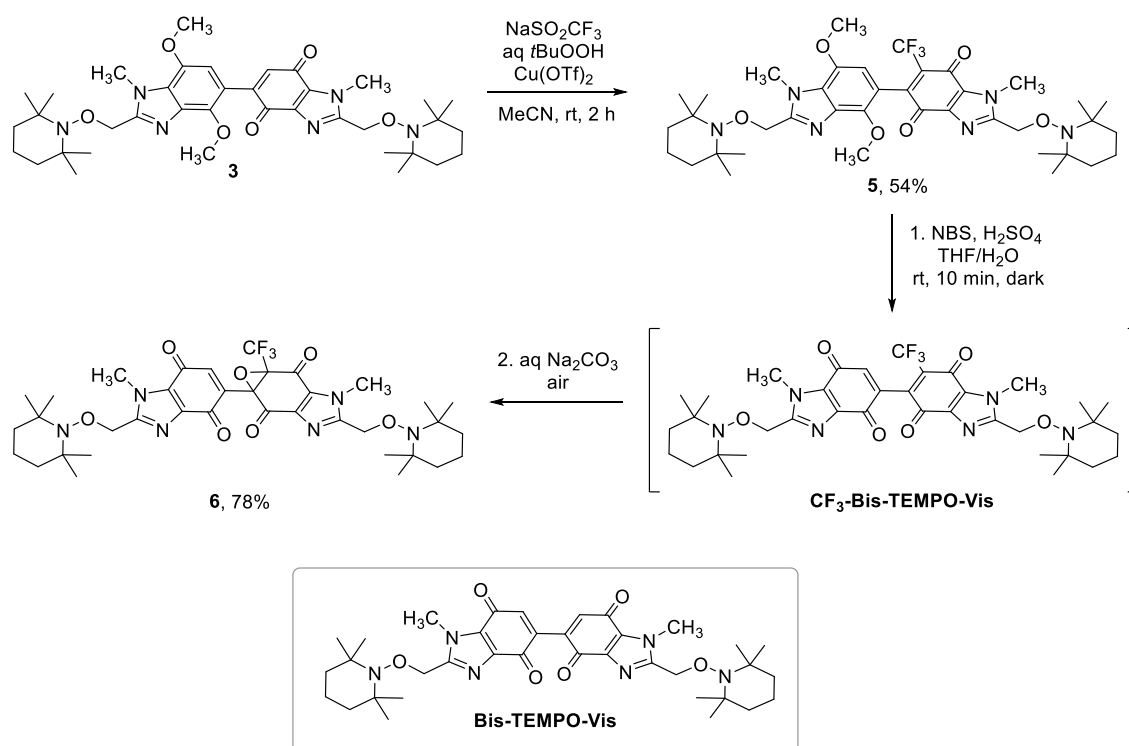
The trifluoromethyl group is a strong inductively electron-withdrawing group that holds special value in medicinal chemistry,<sup>35</sup> agrochemicals<sup>36</sup> and materials science.<sup>37</sup> The electronegativity of CF<sub>3</sub> is 3.5 on the Pauling scale,<sup>38</sup> a value that lies between Cl and F with respective values of 3.0 and 3.98.<sup>39,40</sup> The CF<sub>3</sub> group is similar in size to the methyl group, with unique solubility properties which enhance bioavailability.<sup>35</sup> The Langlois reagent (NaSO<sub>2</sub>CF<sub>3</sub>), in combination with a transition metal catalyst, is a source of •CF<sub>3</sub> for efficient CH trifluoromethylation of aromatics (Scheme 4.7).<sup>40-43</sup> The process is initiated by *t*-butoxyl radicals produced from the metal catalysed reduction of *t*-BuOOH, which oxidizes the Langlois reagent to give the CF<sub>3</sub>SO<sub>2</sub>•. Elimination of SO<sub>2</sub> gives •CF<sub>3</sub> which adds to the arene. Oxidation of the adduct by *t*-BuOOH gives the chain propagating *t*-butoxyl radical and a cyclohexadienyl cation, which is deprotonated and rearomatized to give the trifluoromethylated arene.<sup>40,43</sup>



**Scheme 4.7** Mechanism of aromatic trifluoromethylation using the Langlois reagent.<sup>40,43</sup>

## Chapter 4

In Chapter 3 of this thesis, the trifluoromethylation of dimethoxybenzimidazole-benzimidazolequinone **3** gave trifluoromethylquinone **5** (Scheme 4.8). Bis-alkoxyamine **5** was subjected to oxidative demethylation of the dimethoxybenzene moiety using NBS/H<sub>2</sub>SO<sub>4</sub>, and base/O<sub>2</sub>-mediated epoxidation of the highly electrophilic trifluoromethylquinone part to give epoxide-quinone **6**. Herein, the intermediate, **CF<sub>3</sub>-Bis-TEMPO-Vis**, is isolated by adding water rather than aq Na<sub>2</sub>CO<sub>3</sub>. The homolysis kinetics of this new visible-light active bis-alkoxyamine are disclosed, with attention paid to the effects of bis-alkoxyamine concentration on decomposition.



**Scheme 4.8** Formation of **CF<sub>3</sub>-Bis-TEMPO-Vis**, in the absence of light during the synthesis of epoxide-quinone **6**.

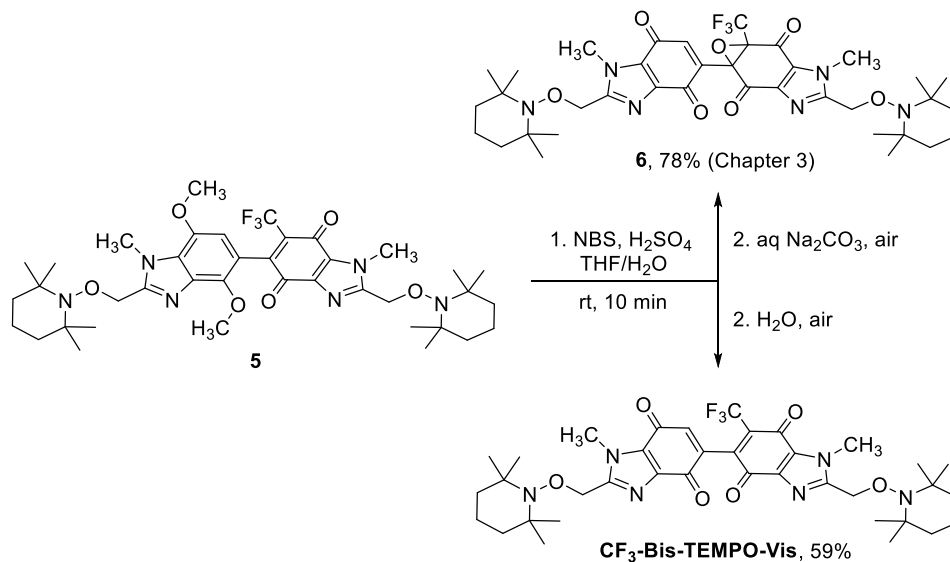
## 4.2.2 Results and Discussion

### 4.2.2.1 Synthesis of **CF<sub>3</sub>-Bis-TEMPO-Vis**

The oxidative demethylation and epoxidation of dimethoxybenzimidazole-trifluoromethylquinone **5** was demonstrated using NBS/H<sub>2</sub>SO<sub>4</sub> followed by aq Na<sub>2</sub>CO<sub>3</sub> workup in air (section 3.3.3.2). By using water for workup, epoxidation was avoided, furnishing the intermediate trifluoromethyl-bis-benzimidazolequinone **CF<sub>3</sub>-Bis-TEMPO-Vis** in 59% yield, with both quinone chromophores intact (Scheme 4.9). The key spectral

## Chapter 4

difference between the epoxide-quinone and the fully conjugated **CF<sub>3</sub>-Bis-TEMPO-Vis** is the downfield shift of the C-CF<sub>3</sub> quartet on the <sup>13</sup>C NMR spectrum from 63.4 ppm in the epoxide-quinone to 132.3 ppm in **CF<sub>3</sub>-Bis-TEMPO-Vis** (Figure 4.9).



**Scheme 4.9** Workup-dependant synthesis of epoxide **6** or **CF<sub>3</sub>-Bis-TEMPO-Vis**.

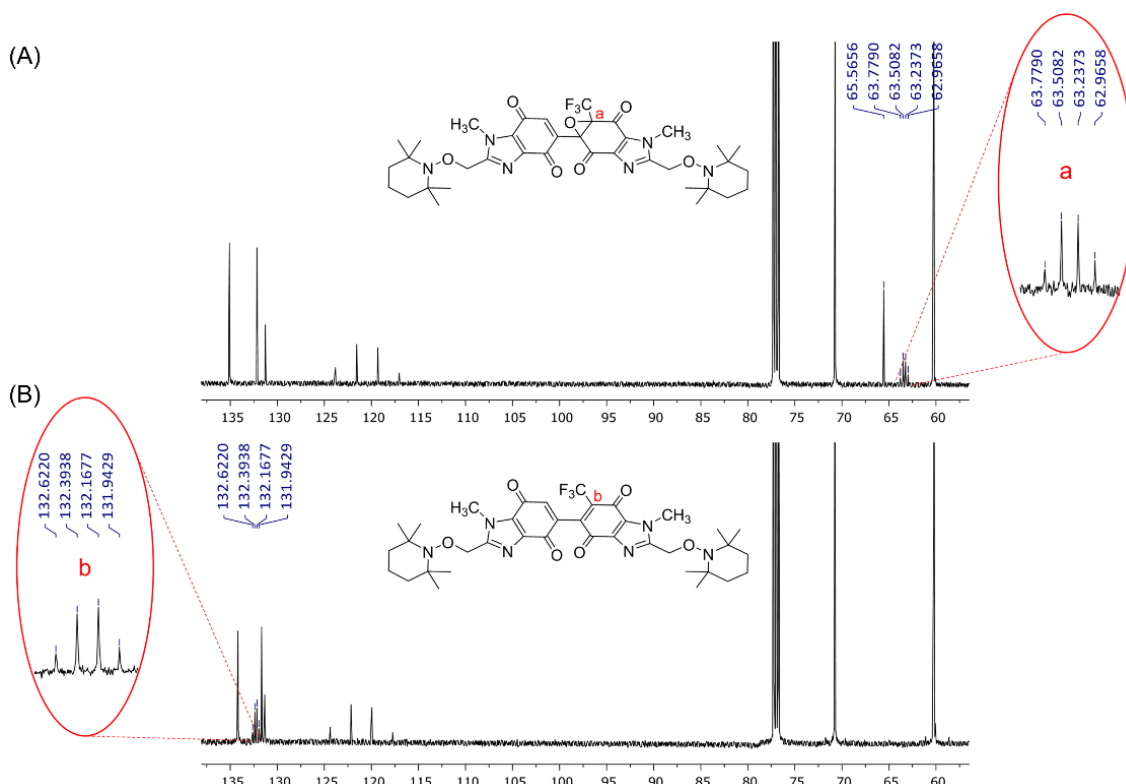
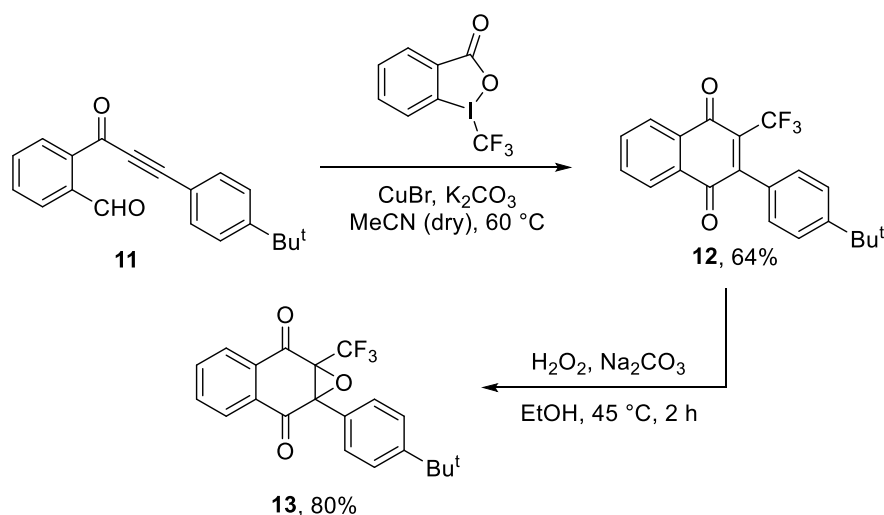


**Figure 4.9** <sup>13</sup>C NMR spectra of (a) epoxide-quinone **6** and (b) bis-benzimidazolequinone **CF<sub>3</sub>-Bis-TEMPO-Vis**.

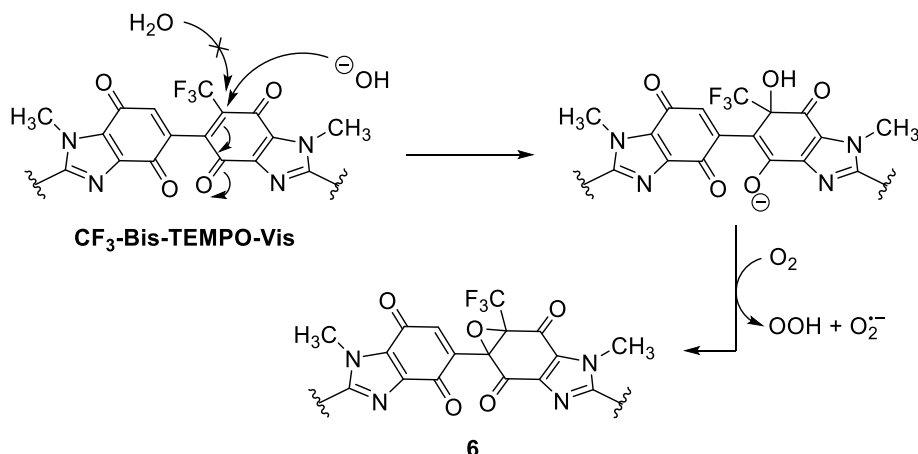
## Chapter 4

The mild epoxidation strategy contrasts with literature reported syntheses of naphthoquinone epoxides, which require  $\text{H}_2\text{O}_2$  as an oxidant in combination with  $\text{Na}_2\text{CO}_3$ .<sup>44,45</sup> Zhu and co-workers prepared trifluoromethylated naphthoquinone **12** in 64% yield from 2-(3-arylpropioloyl)benzaldehyde **11**, and using 3,3-dimethyl-1-(trifluoromethyl)-1,2-benziodoxole as a source of  $\cdot\text{CF}_3$  (Scheme 4.10).<sup>46</sup> It is worth noting their use of dry MeCN as solvent, and that aqueous workup was not performed, with the reaction mixture simply concentrated and purified using column chromatography. Epoxidation of the trifluoromethylquinone to give **13** was performed using  $\text{H}_2\text{O}_2$  and  $\text{Na}_2\text{CO}_3$ .



**Scheme 4.10** The use of  $\text{H}_2\text{O}_2$ /base in trifluoromethyl epoxide formation.<sup>46</sup>

In our case, the Michael-addition of hydroxide to give the highly electrophilic  $\text{CF}_3$ -quinone is the likely first step, with pH neutral water being an insufficient nucleophile (Scheme 4.11). Oxidation by dissolved  $\text{O}_2$  promotes the effective loss of hydride necessary to give epoxide-quinone **6**.



**Scheme 4.11** Proposed mechanism of **CF<sub>3</sub>-Bis-TEMPO-Vis** epoxidation under basic oxygenated conditions.

#### 4.2.2.2 Kinetics of homolysis for **CF<sub>3</sub>-Bis-TEMPO-Vis**

The rate of visible-light induced homolysis of **CF<sub>3</sub>-Bis-TEMPO-Vis** was examined and compared to the other light-active bis-alkoxyamines, **Bis-TEMPO-Vis** and epoxide-quinone **6** using green LED illumination (18 W). Using bis-alkoxyamine at 5 mM concentration in DCE, 130% and 152% TEMPO (based on starting bis-alkoxyamine) is released from **CF<sub>3</sub>-Bis-TEMPO-Vis** and **Bis-TEMPO-Vis** respectively, after 348 min (Table 4.2). However, the decay of **CF<sub>3</sub>-Bis-TEMPO-Vis** and **Bis-TEMPO-Vis**

**Table 4.2** Kinetics of bis-alkoxyamine homolysis using visible-light,<sup>a</sup> and DFT homolysis parameters.

bis-alkoxyamine (concentration, mM)	$k_d$ ( $\text{min}^{-1}$ ) <sup>b</sup>	mol% TEMPO released (time, min) <sup>c</sup>	BDE ( $\text{kJ}\cdot\text{mol}^{-1}$ ) <sup>d</sup>	$E_T$ ( $\text{kJ}\cdot\text{mol}^{-1}$ ) <sup>d</sup>
<b>CF<sub>3</sub>-Bis-TEMPO-Vis</b> (5.0)	-	130 (348)	104.6, <sup>e</sup> 105.7 <sup>f</sup>	215.6
<b>Bis-TEMPO-Vis</b> (5.0)	-	152 (348)	104.9	215.5
<b>6</b> (5.0)	$0.0162 \pm 0.0010$	73 (180)	104.6, <sup>e</sup> 99.7 <sup>f</sup>	209.7
<b>CF<sub>3</sub>-Bis-TEMPO-Vis</b> (0.25)	$0.0472 \pm 0.0018$	125 (80)	-	-
<b>Bis-TEMPO-Vis</b> (0.25)	$0.148 \pm 0.002$	162 (15)	-	-
<b>6</b> (0.25)	$0.0321 \pm 0.007$	43 (65)	-	-

<sup>a</sup>Conditions: bis-alkoxyamine homolysis in DCE using green LED illumination ( $2 \times 9$  W bulbs) in the presence of  $\text{O}_2$ . <sup>b</sup>Dissociation rate ( $k_d$ ) derived from slope of first-order decay plot (Figure 4.10). <sup>c</sup>HPLC yield based on starting alkoxyamine. <sup>d</sup>M06-2X/6-311++G (d,p). <sup>e</sup>BDE at  $\text{CF}_3$ -quinone/epoxide part. <sup>f</sup>BDE at quinone part.



deviated from first-order kinetics after about 20 min (Figure 4.10A). The rate of decay continues to be non-linear with increasing conversion to TEMPO free radical. Indeed, when TEMPO (1.3 equiv) was added to the **Bis-TEMPO-Vis** homolysis experiment, the initial bis-alkoxyamine decay was slowed in comparison to the uninhibited experiment. TEMPO quenches excited states *via* electron-transfer,<sup>47,48</sup> and its propensity for quenching increases with the electron-accepting potential of the chromophore.<sup>23</sup> When a quinone moiety is removed as in the case of epoxide-quinone **6**, first-order decay in green

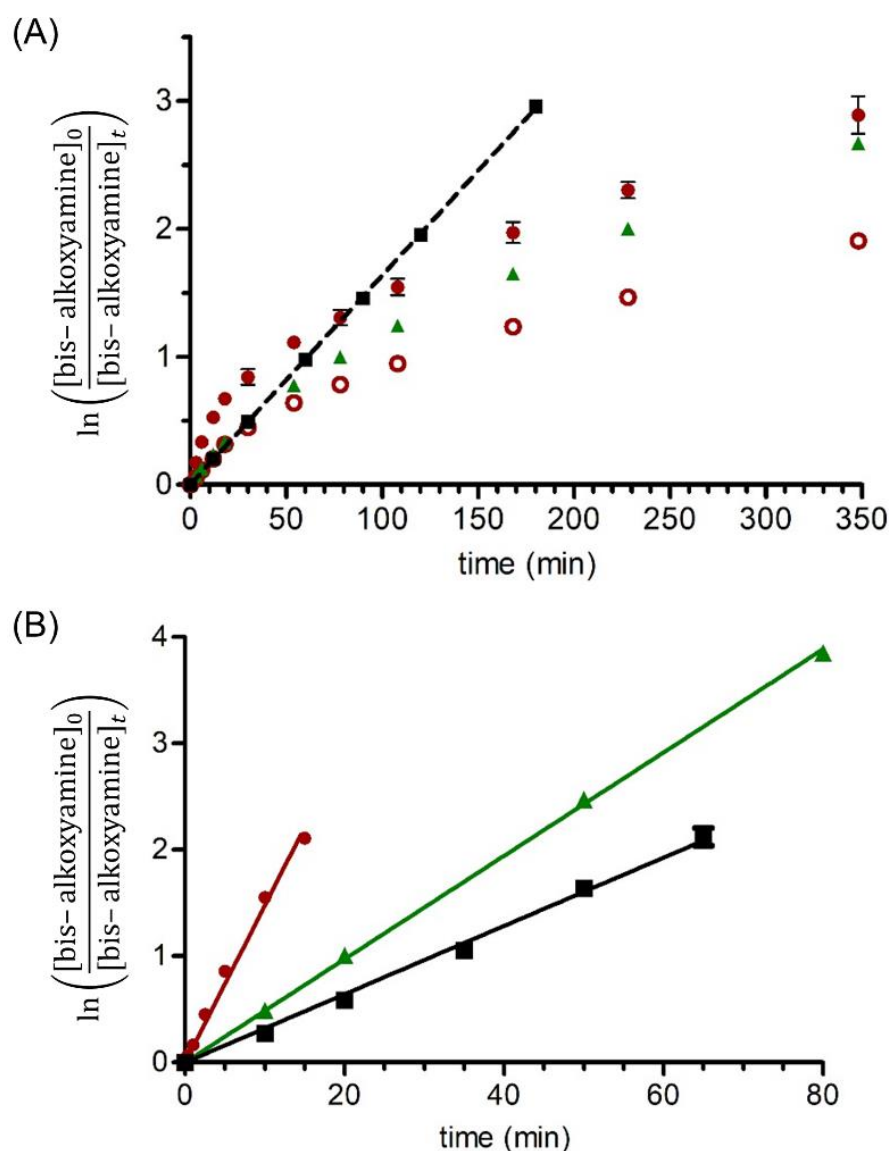


**Figure 4.10** Kinetics of room temperature green-LED ( $2 \times 9 \text{ W}$  bulbs) induced decomposition in DCE at (A)  $[\text{bis-alkoxyamine}] = 5 \text{ mM}$  and (B)  $[\text{bis-alkoxyamine}] = 0.25 \text{ mM}$ , where **CF<sub>3</sub>-Bis-TEMPO-Vis** (green triangles, green line), **Bis-TEMPO-Vis** (red filled circles, red line), **Bis-TEMPO-Vis** with added TEMPO free radical (1.3 equiv, red open circles), and epoxide-quinone **6** (black squares and black line). Conditions as described in Table 4.2.

LED is observed, with the slope of the linear decay plot corresponding to a  $k_d$  of  $0.0162 \text{ min}^{-1}$ . As expected from Chapter 3 results (section 3.3.3), less than 1 equiv of TEMPO is released from **6** due the presence of one chromophore. By diluting the starting concentrations of the bis-alkoxyamines 20-fold, the effects of quenching by released TEMPO is nullified with decay plots now following first-order kinetics (Figure 4.10B). By limiting the potential of intermolecular quenching, first order rate constants for homolysis ( $k_d$ ) may be obtained for **Bis-TEMPO-Vis** and **CF<sub>3</sub>-Bis-TEMPO-Vis**. The CF<sub>3</sub> group is found to have a clear stabilizing effect on the alkoxyamine bond under green LED, with the homolysis rate being 3 times slower compared to its non-functionalized counterpart **Bis-TEMPO-Vis**. The slower rate of homolysis occurs despite the bis-alkoxyamines having similar DFT-derived BDE and  $E_T$  values. The BDE of the alkoxyamine attached to the CF<sub>3</sub>-quinone in **CF<sub>3</sub>-Bis-TEMPO-Vis** is marginally lower by  $1.1 \text{ kJ}\cdot\text{mol}^{-1}$  than the BDE of the alkoxyamine bond at the non-functionalized part of the molecule. For thermal alkoxyamine homolyses, strongly electron-withdrawing groups (EWGs), including CF<sub>3</sub>,<sup>49</sup> stabilize the alkyl radical fragment promoting alkoxyamine bond homolysis.<sup>50</sup> Our observation is a reversal of the observed thermal trend using photolysis. The slower rate of homolysis compared to **Bis-TEMPO-Vis** may be explained by the marginally lower absorbance of **CF<sub>3</sub>-Bis-TEMPO-Vis** in the green region of the visible spectrum (Figure 4.11). Although, it is apparent from the UV-Vis

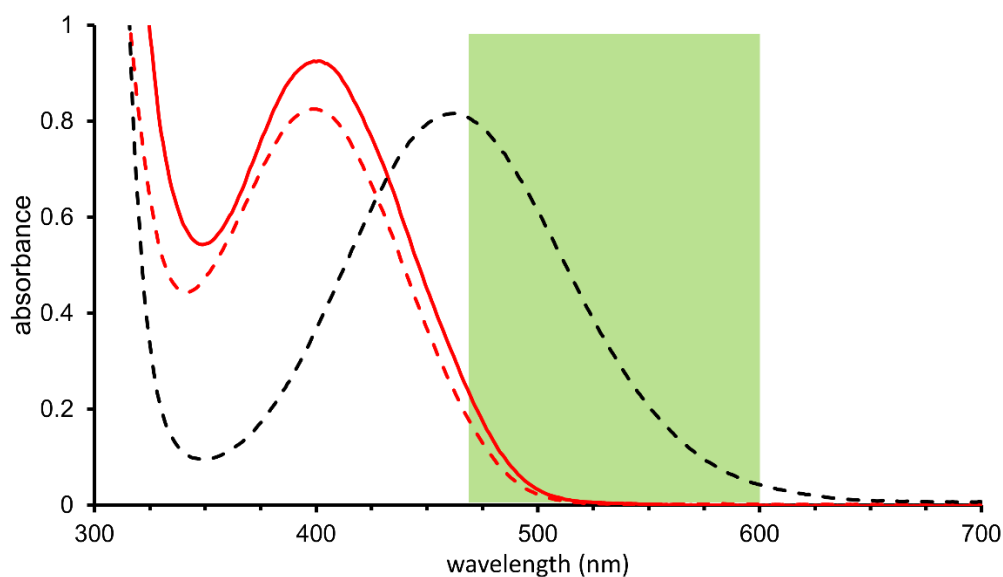


**Figure 4.11** UV-Visible absorbance spectra in DCE of **Bis-TEMPO-Vis** (red continuous, 0.33 mM), and **CF<sub>3</sub>-Bis-TEMPO-Vis** (red dashed, 0.33 mM) and TEMPO (75.0 mM) with green LED emission region (470–600 nm) shaded.

spectrum, that both bis-alkoxyamines weakly absorb green light. A more likely scenario, is that the CF<sub>3</sub> group modifies the redox properties of the quinone, making **CF<sub>3</sub>-Bis-TEMPO-Vis** more easily reduced.<sup>51–53</sup> Thus, an enhancement in the reductive quenching of **CF<sub>3</sub>-Bis-TEMPO-Vis** excited triplet state by released TEMPO leads to the lower observed *k<sub>d</sub>*. The decay of epoxide-quinone **6** remains first-order, and the *k<sub>d</sub>* increases 2-fold when the homolysis solution is diluted 20-fold, as expected due to the relative increase in photon to molecule ratio using the same LED setup.

## 4.2.3 Experimental

### 4.2.3.1 Materials

4',7'-Dimethoxy-1,1'-dimethyl-2,2'-bis{[(2,2,6,6-tetramethylpiperidin-1-yl)oxy]methyl}-6-(trifluoromethyl)-1*H*,1'*H*-[5,5'-bibenzimidazole]-4,7-dione (**5**), 3-methyl-6a-(1-methyl-4,7-dioxo-2-[(2,2,6,6-tetramethylpiperidin-1-yl)oxy]methyl)-4,7-dihydro-1*H*-benzimidazol-5-yl)-4-[(2,2,6,6-tetramethylpiperidin-1-yl)oxy]methyl}-1a-(trifluoromethyl)-1a*H*-oxireno[*f*]benzimidazole-2,6(3*H*,6a*H*)-dione (**6**) and 1,1'-dimethyl-2,2'-bis{[(2,2,6,6-tetramethylpiperidin-1-yl)oxy]methyl}-1*H*,1'*H*-5,5'-bibenzimidazole-4,4',7,7'-tetrone (**Bis-TEMPO-Vis**) were synthesized according to the procedures in Chapter 3 (section 3.6.3).<sup>20</sup> *N*-bromosuccinimide (NBS, Lancaster, 99%), H<sub>2</sub>SO<sub>4</sub> (BDH, 98%), THF (Sigma-Aldrich, ≥ 99%), CH<sub>2</sub>Cl<sub>2</sub> (Fischer Scientific, ≥ 99%), MgSO<sub>4</sub> (Alfa Aesar, 99.5%), EtOAc (Fischer Scientific, ≥ 99%), hexanes (Fischer Scientific, bp 40–60 °C) and 1,2-dichloroethane (DCE, Sigma-Aldrich, anhydrous, 99.8%) were used as received. Dry column vacuum chromatography (with Apollo Scientific silica gel ZEOprep 60 and 15–35 μm particle size),<sup>32</sup> was preferable for purification of light-active compounds, due to the convenience of light exclusion by covering the apparatus with Al-foil during elution.

### 4.2.3.2 Measurements

**DFT calculations:** Geometry optimizations were performed using Gaussian 16,<sup>33</sup> installed at the Irish Centre for High-End Computing (ICHEC), using an M06-2X functional<sup>34</sup> with a 6-311++G (d,p) basis set. All structures were fully optimized in the gas phase and verified as local minima through frequency calculations. Bond dissociation energies (BDEs) were calculated based on the free energy difference between the starting alkoxyamines and the radical products (thermal free energy correction was added). The

lowest triplet energies ( $E_T$ ) of starting alkoxyamines are given relative to the optimized singlet ground state ( $S_0$ ) energies. A table of model energies (Table A4.1) and images of optimized geometries (Figure A4.1) are reported in the appendix.

**Melting points, ultraviolet-visible and infrared spectroscopy:** Melting point was measured on a Stuart Scientific melting point apparatus SMP3. Ultraviolet-visible (UV-vis) spectra were recorded using a Varian (Cary 100) UV-vis spectrometer. Spectra are reported in Figure 4.11, which depicts **Bis-TEMPO-Vis** and **CF<sub>3</sub>-Bis-TEMPO-Vis** at the same concentration (0.33 mM) and TEMPO is at 200 × concentration (75.0 mM). Infrared spectra were recorded using a Perkin-Elmer Spec 1 with ATR attached.

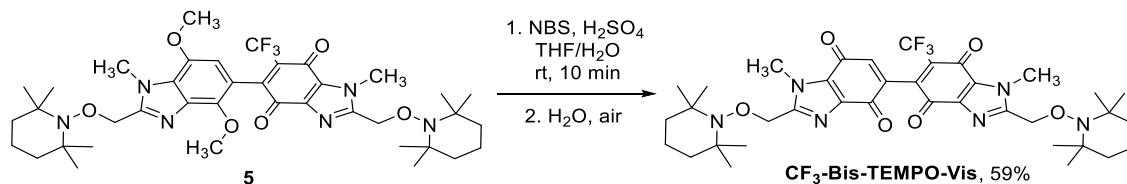
**Nuclear magnetic resonance (NMR spectroscopy):** NMR spectra were recorded using a Varian 500 MHz instrument. The chemical shifts were in ppm relative to Si(CH<sub>3</sub>)<sub>4</sub>. <sup>13</sup>C NMR data were collected at 125 MHz with complete proton decoupling. NMR assignments were supported by DEPT and <sup>1</sup>H-<sup>13</sup>C correlation. <sup>19</sup>F NMR data were collected at 470 MHz. NMR spectra are reported in the appendix of this thesis.

**High resolution mass spectrometry (HRMS):** HRMS was carried out using ESI time-of-flight mass spectrometer (TOFMS) in positive mode using a Waters LCT Mass Spectrometry instrument.

**Visible-light homolysis:** The photoreactor was set up and homolysis kinetics were measured according to alkoxyamine decay as described in Chapter 3 (section 3.6.2).<sup>20</sup>

**Analytical HPLC:** The Agilent 1100 Series HPLC was equipped with a UV detector operating at 254 nm and a Phenomenex® BondClone™ 10 μm C18, 250 × 4.6 mm column. Calibration curves were generated for [alkoxyamine] and [TEMPO] for the construction of rate plots. The mobile phase programs for **Bis-TEMPO-Vis** and epoxide-quinone **6** were applied as outlined in Chapter 3 (section 3.6.2),<sup>20</sup> with analysis of **CF<sub>3</sub>-Bis-TEMPO-Vis** homolysis in O<sub>2</sub> performed using the same conditions as for **Bis-TEMPO-Vis** homolysis in O<sub>2</sub>.

### 4.2.3.2 Synthesis of 1,1'-dimethyl-2,2'-bis{[(2,2,6,6-tetramethylpiperidin-1-yl)oxy]methyl}-6-(trifluoromethyl)-1*H*,1'*H*-[5,5'-bibenzimidazole]-4,4',7,7'-tetrone (**CF<sub>3</sub>-Bis-TEMPO-Vis**)



*N*-Bromosuccinimide (NBS, 39 mg, 0.22 mmol) was added to 4,7'-dimethoxy-1,1'-dimethyl-2,2'-bis{[(2,2,6,6-tetramethylpiperidin-1-yl)oxy]methyl}-6-(trifluoromethyl)-1*H*,1'*H*-[5,5'-bibenzimidazole]-4,7-dione **5** (0.152 g, 0.20 mmol), H<sub>2</sub>SO<sub>4</sub> (18 μL, 0.34 mmol) and THF/H<sub>2</sub>O (6 mL, 2/1) at rt, and stirred for 10 min in the absence of light. H<sub>2</sub>O (10 mL) was added, and the solution was extracted with CH<sub>2</sub>Cl<sub>2</sub> (2 × 20 mL). The combined organic layers were dried (MgSO<sub>4</sub>), evaporated, and the residue purified by dry column vacuum chromatography with EtOAc and hexanes as eluent to give **CF<sub>3</sub>-Bis-TEMPO-Vis** (86 mg, 59%) as a yellow solid; mp 136–140 °C (deg); *R*<sub>f</sub> 0.31 (3 : 1 EtOAc : hexanes); λ<sub>max</sub> (DCE, nm) 399 (ε = 2.21 × 10<sup>3</sup>), 252 (ε = 1.89 × 10<sup>4</sup>); ν<sub>max</sub> (neat, cm<sup>-1</sup>) 2974, 2932, 1665, 1518, 1479, 1361, 1334, 1276, 1252, 1207, 1181, 1151, 1122, 1100, 1032; δ<sub>H</sub> (500 MHz, CDCl<sub>3</sub>) 1.10 (12H, s, CH<sub>3</sub>), 1.23-1.25 (12H, m, CH<sub>3</sub>), 1.34-1.38 (2H, m), 1.44-1.57 (10H, bs), 4.12 (3H, s, NCH<sub>3</sub>), 4.13 (3H, s, NCH<sub>3</sub>), 5.03 (2H, s), 5.04 (2H, s), 6.45 (1H, s); δ<sub>C</sub> (125 MHz, CDCl<sub>3</sub>) 16.9 (CH<sub>2</sub>), 20.1 (CH<sub>3</sub>), 32.9 (CH<sub>3</sub>), 33.2 (CH<sub>3</sub>), 39.7 (CH<sub>2</sub>), 60.2 (C), 70.7 (CH<sub>2</sub>), 121.1 (q, <sup>1</sup>J<sub>C-F</sub> = 276.3 Hz, CF<sub>3</sub>), 131.3, 131.7 (both C), 132.3 (q, <sup>2</sup>J<sub>C-F</sub> = 28.3 Hz, C6), 134.2 (CH), 140.0, 140.1, 140.3, 140.8, 151.7, 153.0 (all C), 172.8, 176.6, 176.8, 177.5 (all C=O); δ<sub>F</sub> (470 MHz, CDCl<sub>3</sub>) – 56.83; HRMS (ESI) *m/z* [M + H]<sup>+</sup>, C<sub>37</sub>H<sub>48</sub>N<sub>6</sub>O<sub>6</sub>F<sub>3</sub> calcd. 729.3587, observed 729.3581.

### 4.2.4 Conclusions

The intermediate CF<sub>3</sub>-quinone (**CF<sub>3</sub>-Bis-TEMPO-Vis**) from the NBS/H<sub>2</sub>SO<sub>4</sub> oxidative demethylation reaction was isolated by performing a pH neutral workup. Green LED-induced photolysis of bibenzimidazolequinone bis-alkoxyamines **Bis-TEMPO-Vis** and **CF<sub>3</sub>-Bis-TEMPO-Vis** did not follow first-order decay kinetics at high bis-alkoxyamine concentration (5 mM) with proposed intermolecular quenching by liberated TEMPO inhibiting the process. Dilution of the bis-alkoxyamines 20-times prevented

intermolecular quenching, by reducing the concentration of liberated TEMPO, resulting in first-order kinetics. The trifluoromethylated bis-alkoxyamine exhibited slower photolytic kinetics than its non-functionalized counterpart, contrasting with the expected thermal homolysis rate increase under the influence of electron withdrawing groups. The reaction order of epoxide-quinone **6** homolysis was independent of concentration, and first-order behaviour was observed at 0.25 mM and 5 mM with no observed quenching by liberated TEMPO.

**Part 3: 2-(Fluoromethyl)-4,7-dimethoxy-1-methyl-1*H*-benzimidazole****4.3.1 Introduction**

Traditionally, alkoxyamines thermally release bench-stable nitroxide radicals, such as commercial TEMPO, at 80–140 °C.<sup>54,55</sup> This thesis has established visible-light room-temperature controlled nitroxide release from alkoxyamines. The alkoxyamines are benzimidazolequinones, and the simplest is **TEMPO-Vis** (Figure 4.12), which forms a thermodynamically stable methide radical on exposure to blue or green LED (see Chapter 3). Benzimidazolequinones are well-known bioreductive anti-tumour agents.<sup>19,58–64</sup> Fluorinated benzimidazolequinones are however yet to be reported, and we predict that a highly electronegative fluorine substituent on the quinone would increase the tendency for reduction, thus impacting cytotoxicity.<sup>61,65</sup> Furthermore, the inclusion of fluorine in drug molecules leads to improvements in the therapeutic index.<sup>35,66</sup> The synthetic substrate, which is oxidized to give **TEMPO-Vis**, is 4,7-dimethoxy-1-methyl-2-[[2,2,6,6-tetramethylpiperidin-1-yl]oxy]methyl]-1*H*-benzimidazole (**2**). Alkoxyamine **2** is light-insensitive and indefinitely bench-stable.

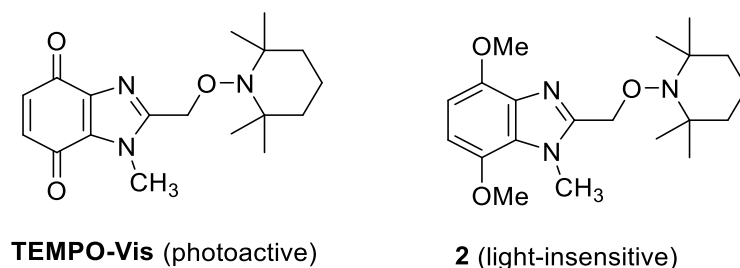
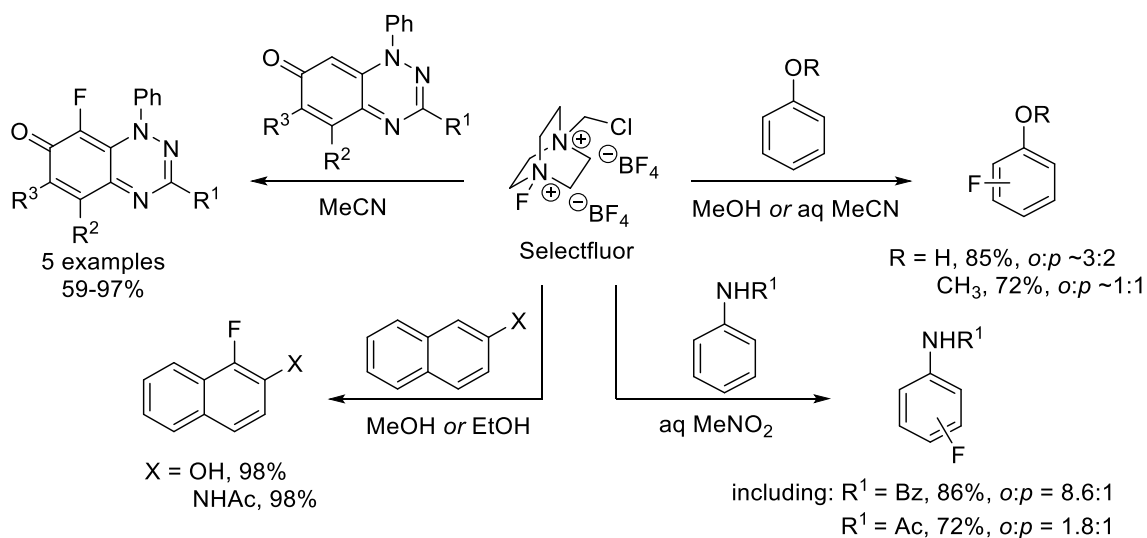


**Figure 4.12** TEMPO-Vis and synthetic substrate **2**.

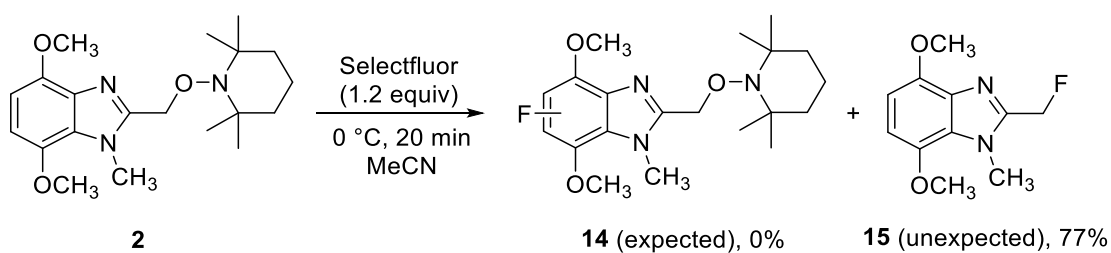
Disclosed herein is the unexpected outcome of the reaction of **2** with the most popular and convenient electrophilic fluorination reagent, Selectfluor.<sup>67,68</sup> Fluorinations using Selectfluor have been described onto activated aromatics including anisoles,<sup>69</sup> phenols,<sup>69,70</sup> protected anilines,<sup>70</sup> and benzamides,<sup>71</sup> and recently onto the enamine-activated position of benzotriazines<sup>72</sup> (Scheme 4.12).



**Scheme 4.12** Examples of heterocyclic and aromatic fluorinations using Selectfluor.<sup>69–72</sup>

### 4.3.2 Results and Discussion

Treatment of alkoxyamine **2** with Selectfluor (1.2 equiv) at 0 °C led to rapid liberation of TEMPO free radical and benzylic fluorination to give 2-(fluoromethyl)-4,7-dimethoxy-1-methyl-1*H*-benzimidazole **15** (Scheme 4.13) as indicated by GC-MS (Figure 4.13). 2-Fluoromethylbenzimidazole **15** was isolated in 77% yield. The expected electrophilic aromatic fluorination of the electron-rich *p*-dimethoxybenzene part to give **14** was not observed.



**Scheme 4.13** Synthesis of fluorinated benzimidazole **15**.



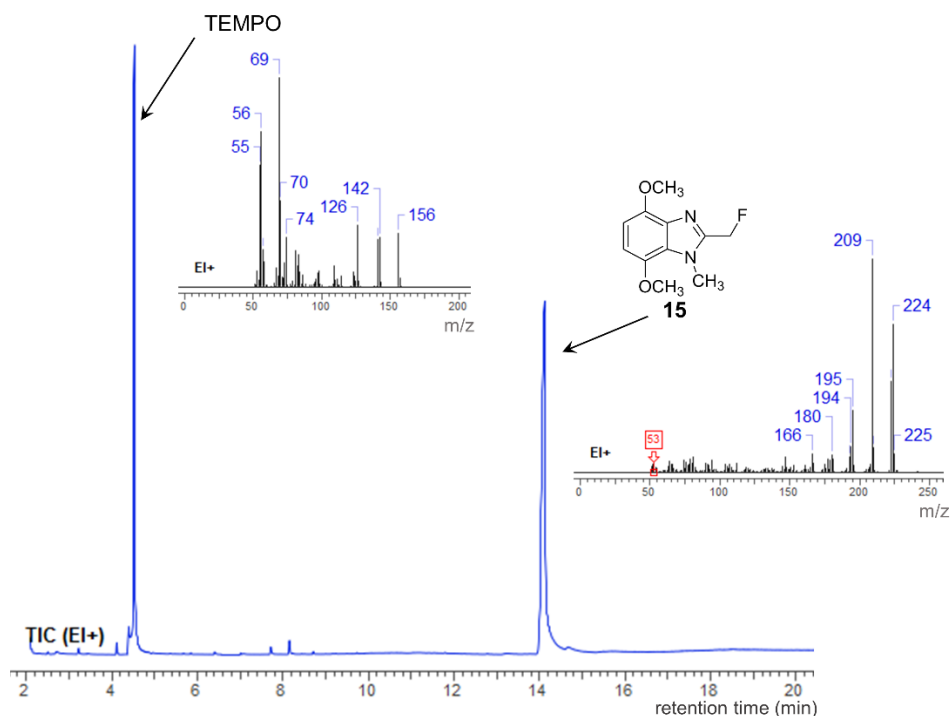
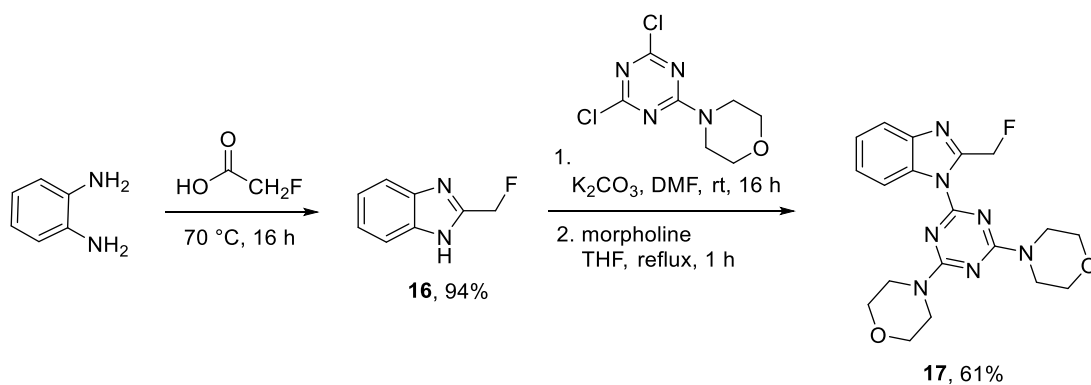


**Figure 4.13** GC-MS analysis of the fluorination reaction mixture.

Previously, 2-fluoromethylbenzimidazole **16** was synthesized *via* condensation of 1,2-phenylenediamine and trifluoroacetic acid,<sup>73</sup> and *N*-functionalization with dimorpholine-substituted 1,3,5-triazine to give **17**, a phosphatidylinositol 3-kinase inhibitor (Scheme 4.14).<sup>74</sup> The displacement of TEMPO from our benzimidazole-alkoxyamine is apparent in differences in the <sup>1</sup>H NMR spectra (Figure 4.14). There are no TEMPO-based peaks in the spectrum of **15**, and the methylene signal has shifted downfield to 5.61 ppm with splitting of this signal into a doublet ( $J = 48.2$  Hz) due to <sup>1</sup>H-<sup>19</sup>F coupling. The location and multiplicity of the methylene signal is in good agreement with signals reported for 2-(fluoromethyl)-1*H*-benzimidazole in DMSO-*d*<sub>6</sub> (5.64 ppm, d,  $J =$



**Scheme 4.14** Literature synthesis and *N*-functionalization of 2-fluoromethylbenzimidazole.<sup>73,74</sup>

47.5 Hz),<sup>73</sup> and *N*-triazine substituted 2-(fluoromethyl)-benzimidazole in CDCl<sub>3</sub> (5.98 ppm, d,  $J = 47.3$  Hz).<sup>74</sup> The methylene signal in the <sup>13</sup>C NMR shifted downfield from 72.0 ppm in the alkoxyamine to 76.8 ppm in the methylene fluoride, with splitting of this signal into a doublet ( $J = 165.5$  Hz) due to <sup>13</sup>C-<sup>19</sup>F coupling (Figure 4.15). <sup>13</sup>C-<sup>19</sup>F coupling was also observed for the C-2 (147.1 ppm, d,  $J = 19.0$  Hz), in good agreement with literature data on 2-(fluoromethyl)-1*H*-benzimidazole C-2 (148.6 ppm, d,  $J = 19.7$  Hz),<sup>73</sup> and the N-CH<sub>3</sub> signal was also split due to <sup>13</sup>C-<sup>19</sup>F coupling (32.6 ppm, d,  $J = 2.5$  Hz). The <sup>19</sup>F NMR signal for **15** at -214.93 ppm was similar to the literature value of -213.92 ppm for 2-(fluoromethyl)-1*H*-benzimidazole in DMSO-d<sub>6</sub>. The signal appeared as a triplet ( $J = 48.0$  Hz) due to two-bond <sup>19</sup>F-<sup>1</sup>H coupling with the two <sup>1</sup>H atoms of the adjacent methylene group (Figure 4.16).

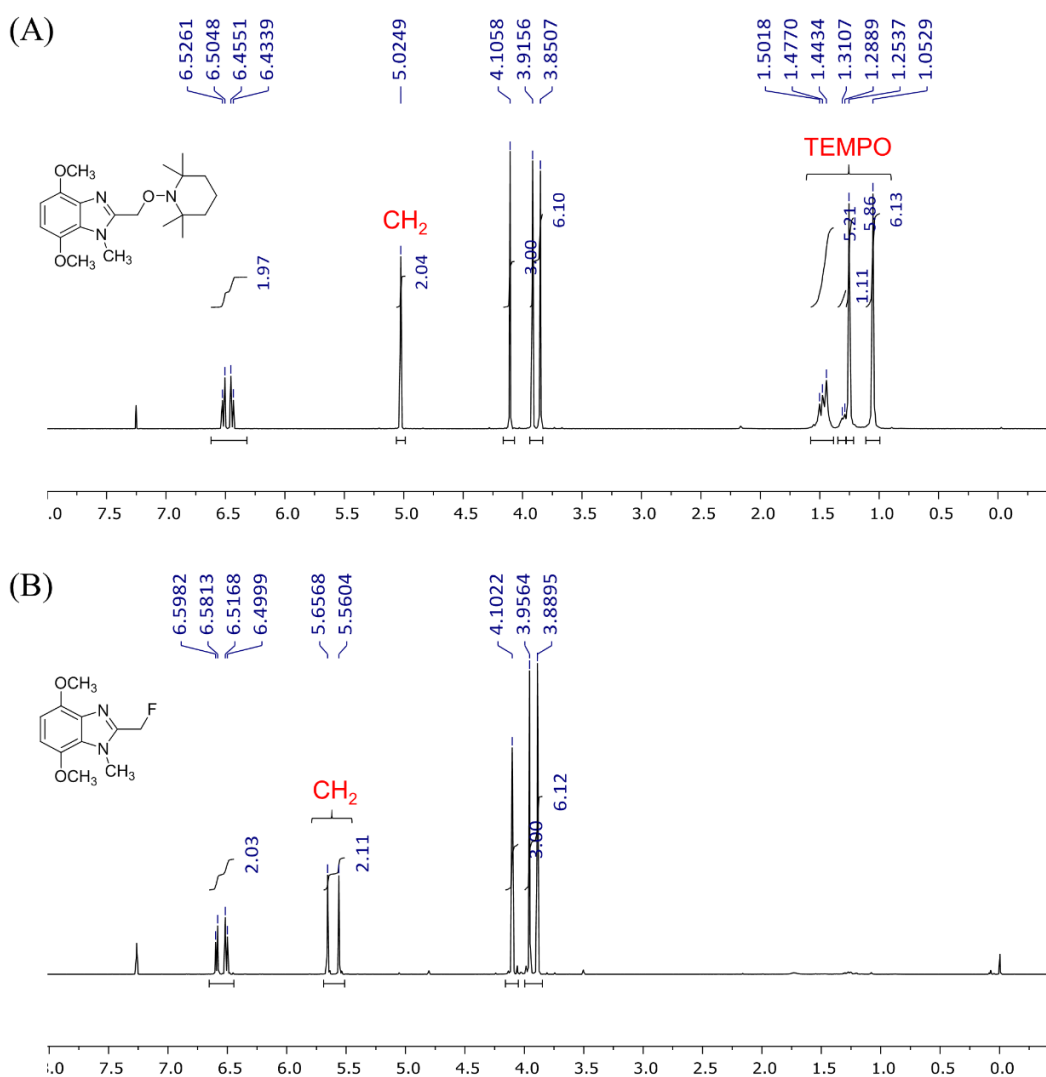


**Figure 4.14** <sup>1</sup>H NMR spectra in CDCl<sub>3</sub> of: (a) 4,7-dimethoxy-1-methyl-2-[(2,2,6,6-tetramethylpiperidin-1-yl)oxy]methyl-1*H*-benzimidazole (**2**) and (b) 2-(fluoromethyl)-4,7-dimethoxy-1-methyl-1*H*-benzimidazole (**15**).

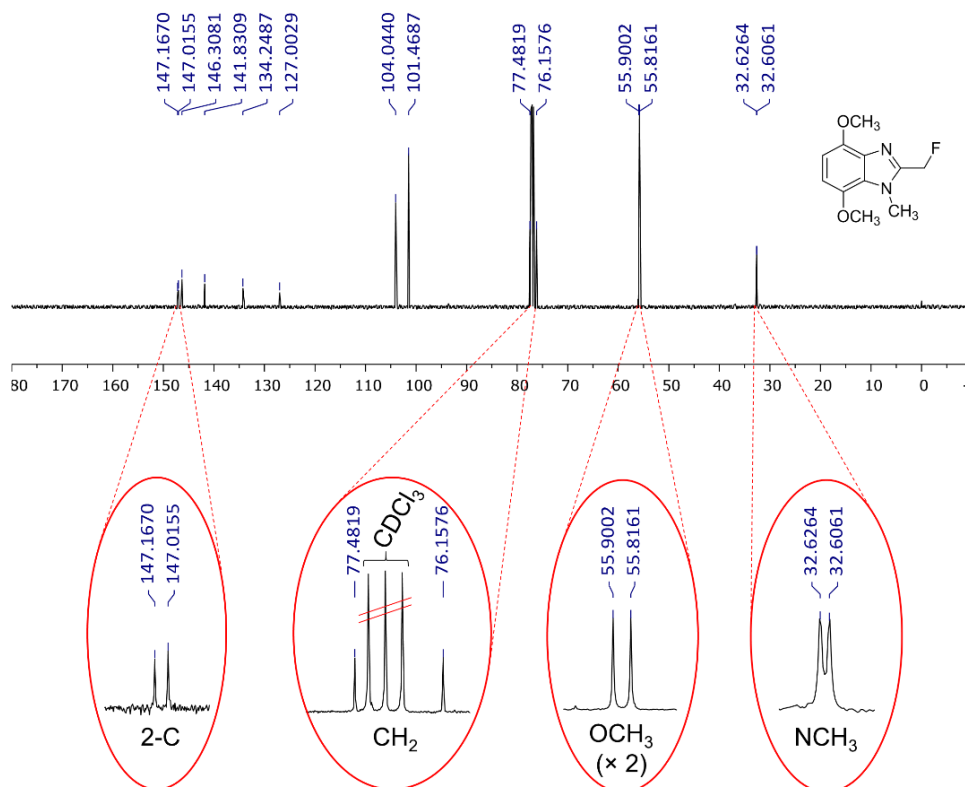


**Figure 4.15**  $^{13}\text{C}$  NMR spectrum in  $\text{CDCl}_3$  of 2-(fluoromethyl)-4,7-dimethoxy-1-methyl-1H-benzimidazole (**15**).

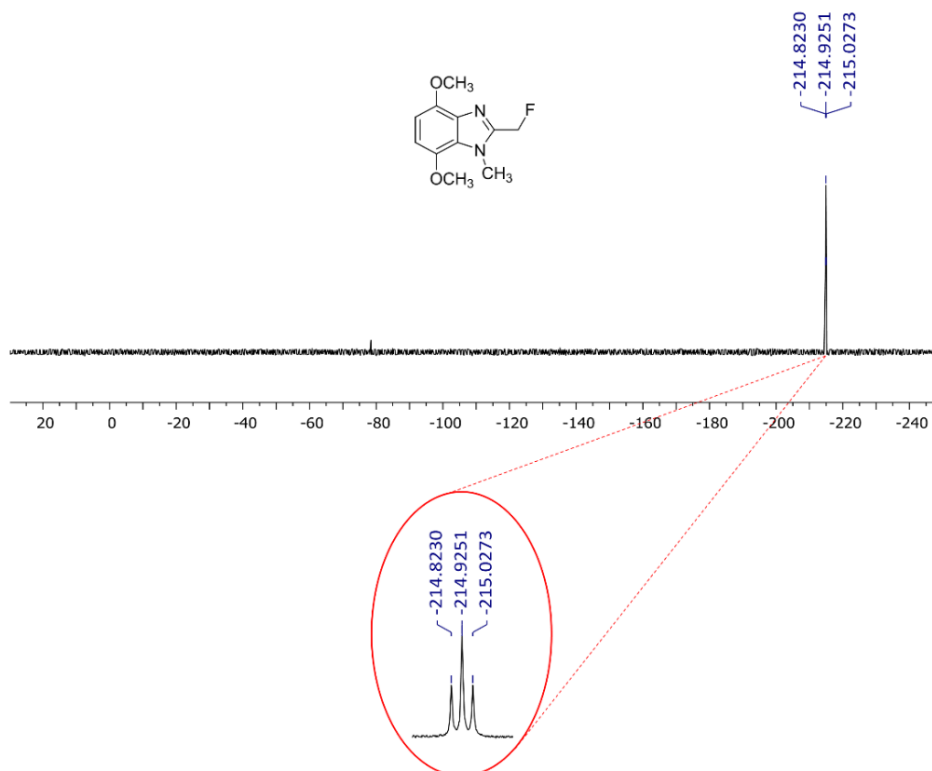
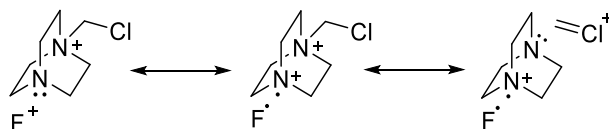


**Figure 4.16**  $^{19}\text{F}$  NMR spectrum in  $\text{CDCl}_3$  of 2-(fluoromethyl)-4,7-dimethoxy-1-methyl-1H-benzimidazole (**15**).

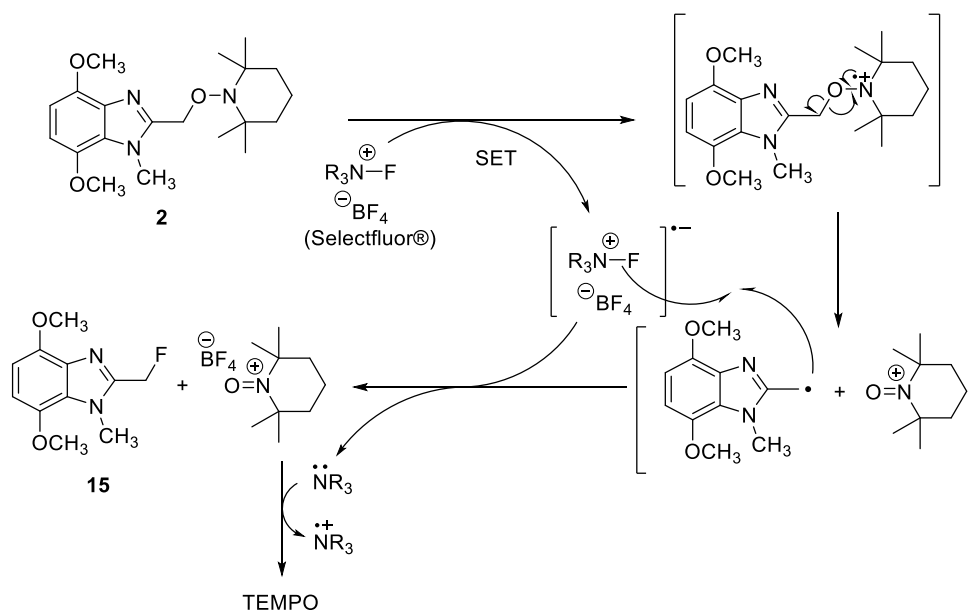
## Chapter 4

The reactions of Selectfluor can proceed either *via* electrophilic fluorination or a single electron-transfer (SET) pathway, or both.<sup>67,75</sup> Selectfluor is a well-established oxidant,<sup>68</sup> and a source of electrophilic F<sup>•</sup>, possibly courtesy of favoured resonance structures (Scheme 4.15).<sup>67</sup> The S<sub>H</sub>2 mechanism is considered unlikely due to the incompatible polarization of the alkoxyamine C–O bond for substitution by the electrophilic F<sup>•</sup>.



**Scheme 4.15** Resonance structures of Selectfluor.<sup>67</sup>

Given that alkoxyamine **2** is stable under visible-light conditions and the reaction is performed at 0 °C; a fluorination mechanism *via* homolysis of the alkoxyamine bond is not possible. The SET pathway is now proposed, and is supported by electrochemical oxidations of TEMPO-alkoxyamines (TEMPO-R).<sup>76</sup> These have recently shown to induce mesolytic cleavage of the alkoxyamine bond to form either TEMPO<sup>•</sup> and an R<sup>+</sup> carbocation or TEMPO<sup>+</sup> oxoammonium cation and R<sup>•</sup>, depending on the nature of the R group. When R is a benzylic or allylic group, cleavage tends to produce R<sup>•</sup>, due to the resonance stabilization of the carbon-centred radical. In our case (Scheme 4.16), SET is proposed to induce mesolytic cleavage of benzimidazole-alkoxyamine **2** to produce TEMPO<sup>+</sup>, and a methylene radical, which is thermodynamically stabilized by resonance onto the benzimidazole system. Abstraction of F<sup>•</sup> gives the methylene fluoride, while reduction of the oxoammonium cation by the Selectfluor-derived DABCO derivative gives TEMPO free radical.



**Scheme 4.16** Proposed SET-mechanism of Selectfluor-induced TEMPO displacement by fluorine.

### 4.3.3 Materials and Methods

#### 4.3.3.1 General Information

4,7-Dimethoxy-1-methyl-2-[[2,2,6,6-tetramethylpiperidin-1-yl]oxy]methyl]-1H-benzimidazole **2** was synthesized according to Chapter 3 (section 3.6.3) in 83% yield by the base-mediated substitution of 2-(chloromethyl)-4,7-dimethoxy-1-methyl-1H-benzimidazole by TEMPO hydroxylamine (prepared *in situ* via PtO<sub>2</sub> catalysed hydrogenation of TEMPO).<sup>18</sup> 2-(Chloromethyl)-4,7-dimethoxy-1-methyl-1H-benzimidazole was prepared according to Chapter 3 (section 3.6.3) in 85% overall yield by *N*-methylation and benzyl-chlorination of (4,7-dimethoxy-1H-benzimidazol-2-yl)methanol. Selectfluor (Sigma-Aldrich, > 95% F<sup>+</sup> active), MeCN (Sigma-Aldrich, HPLC Plus, ≥ 99.9%), CH<sub>2</sub>Cl<sub>2</sub> (Fischer Scientific, ≥ 99%) and MgSO<sub>4</sub> (Alfa Aesar, 99.5%) were used as received. GC-MS analysis was performed on an Agilent 7890A GC system equipped with an Agilent 5975C inert XL Mass Selective Detector (EI) and a RTX-1, 30 m, ID 0.25 mm, FD 0.25 μm column (Restek Corporation, Bellefonte, PA., USA). Helium was used as carrier gas at a flow rate of 0.7 mL/min. The injector was heated to 250 °C and the oven temperature was increased from 75 to 250 °C at the rate of 10 °C/min and was then further increased to 350 °C at 50 °C/min. Thin layer chromatography (TLC) was performed on Merck TLC silica gel 60 F<sub>254</sub> plates using a UV lamp (254 nm) for visualization. Flash chromatography was performed using silica

gel, pore size 60 Å, 230–400 mesh, and particle size 40–63 μm (Sigma-Aldrich) using EtOAc (Fischer Scientific, ≥ 99%) and hexanes (Fischer Scientific, bp 40–60 °C). Melting point was measured on a Stuart Scientific melting point apparatus SMP3. Infrared spectrum was recorded using a Perkin-Elmer Spec 1 with ATR attached. CDCl<sub>3</sub> (Sigma-Aldrich, 99.8% atom D + 0.03% Si(CH<sub>3</sub>)<sub>4</sub> v/v) was used as received. NMR spectra were recorded using a Varian 500 MHz instrument. The chemical shifts were in ppm relative to Si(CH<sub>3</sub>)<sub>4</sub>. <sup>13</sup>C NMR data were collected at 125 MHz with complete proton decoupling. NMR assignments were supported by DEPT and <sup>1</sup>H-<sup>1</sup>H (COSY) and <sup>1</sup>H-<sup>13</sup>C correlation. <sup>19</sup>F NMR data were collected at 470 MHz. NMR spectra are included in the appendix of this thesis. HRMS was carried out using ESI time-of-flight mass spectrometer (TOFMS) in positive mode using a Waters LCT Mass Spectrometry instrument.

### 4.3.3.2 Synthesis of 2-(fluoromethyl)-4,7-dimethoxy-1-methyl-1*H*-benzimidazole (15)

Selectfluor (0.118 g, 0.33 mmol) was added to TEMPO-dimethoxybenzimidazole-alkoxyamine **2** (0.100 g, 0.28 mmol) in MeCN (5 mL) at 0 °C, and stirred for 20 min. H<sub>2</sub>O (10 mL) was added and the mixture was extracted with CH<sub>2</sub>Cl<sub>2</sub> (3 × 20 mL). The combined organic layers were dried (MgSO<sub>4</sub>), evaporated, and the residue purified by flash chromatography with EtOAc and hexanes, as eluent to give **15** (48 mg, 77%) as a white solid; mp 90–92 °C; *R*<sub>f</sub> 0.33 (1 : 1 EtOAc : hexanes); *v*<sub>max</sub> (neat, cm<sup>-1</sup>) 3001, 2936, 2838, 1525, 1465, 1392, 1263, 1238, 1221, 1174, 1100, 1070, 1001; *δ*<sub>H</sub> (500 MHz, CDCl<sub>3</sub>) 3.89 (3H, s), 3.96 (3H, s), 4.10 (3H, s, NCH<sub>3</sub>), 5.61 (2H, d, <sup>2</sup>*J*<sub>H-F</sub> = 48.2 Hz), 6.51 (1H, d, <sup>1</sup>*J*<sub>H-H</sub> = 8.5 Hz), 6.59 (1H, d, <sup>1</sup>*J*<sub>H-H</sub> = 8.5 Hz); *δ*<sub>C</sub> (125 MHz, CDCl<sub>3</sub>) 32.6 (d, <sup>4</sup>*J*<sub>C-F</sub> = 2.5 Hz, NCH<sub>3</sub>), 55.8, 55.9 (both OCH<sub>3</sub>), 76.8 (d, <sup>1</sup>*J*<sub>C-F</sub> = 165.5 Hz, CH<sub>2</sub>), 101.5, 104.0 (both CH), 127.0, 134.2, 141.8, 146.3 (all C), 147.1 (d, <sup>2</sup>*J*<sub>C-F</sub> = 19.0 Hz, C2); *δ*<sub>F</sub> (470 MHz, CDCl<sub>3</sub>) - 214.93 (t, <sup>2</sup>*J*<sub>F-H</sub> = 48.0 Hz); HRMS (ESI) *m/z* [M + H]<sup>+</sup>, C<sub>11</sub>H<sub>14</sub>N<sub>2</sub>O<sub>2</sub>F calcd. 225.1039, observed 225.1040.

### 4.3.3 Conclusion

Selectfluor reaction with 4,7-dimethoxy-1-methyl-2-[(2,2,6,6-tetramethylpiperidin-1-yl)oxy]methyl}-1*H*-benzimidazole **2** gave the unexpected fluorine substitution of the TEMPO moiety in high isolated yield. TEMPO free radical was liberated in the reaction, and a mechanism based on SET from the alkoxyamine to Selectfluor is proposed.

### 4.4 Chapter 4 References

1. Griffiths, P. G.; Moad, G.; Rizzardo, E. *Aust. J. Chem.* **1983**, *36*, 397–401. <https://doi.org/10.1071/CH9830397>.
2. Reid, D. A.; Bottle, S. E. *Chem. Commun.* **1998**, 1907–1908. <https://doi.org/10.1039/A805228J>.
3. Micallef, A. S.; Bott, R. C.; Bottle, S. E.; Smith, G.; White, J. M.; Matsuda, K.; Iwamura, H. *J. Chem. Soc., Perkin Trans. 2* **1999**, 65–72. <https://doi.org/10.1039/A806884D>.
4. Fairfull-Smith, K. E.; Brackmann, F.; Bottle, S. E. *Eur. J. Org. Chem.* **2009**, *2009*, 1902–1915. <https://doi.org/10.1002/ejoc.200801255>.
5. Griffiths, P. G.; Rizzardo, E.; Solomon, D. H. *J. Macromol. Sci., Part A* **1982**, *17*, 45–50. <https://doi.org/10.1080/00222338208056464>.
6. Solomon, D. H. *J. Polym. Sci., Part A: Polym. Chem.* **2005**, *43*, 5748–5764. <https://doi.org/10.1002/pola.21067>.
7. Bowry, V. W.; Ingold, K. U. *J. Am. Chem. Soc.* **1992**, *114*, 4992–4996. <https://doi.org/10.1021/ja00039a006>.
8. Blinco, J. P. *PhD Thesis* **2008**, Queensland University of Technology.
9. Bottle, S. E.; Chand, U.; Micallef, A. S. *Chem. Lett.* **1997**, *26*, 857–858. <https://doi.org/10.1246/cl.1997.857>.
10. Blinco, J. P.; Fairfull-Smith, K. E.; Morrow, B. J.; Bottle, S. E. *Aust. J. Chem.* **2011**, *64*, 373–389. <https://doi.org/10.1071/CH10442>.
11. Morrow, B. J.; Keddie, D. J.; Gueven, N.; Lavin, M. F.; Bottle, S. E. *Free Radical Biol. Med.* **2010**, *49*, 67–76. <https://doi.org/10.1016/j.freeradbiomed.2010.03.019>.
12. Morris, J. C.; McMurtrie, J. C.; Bottle, S. E.; Fairfull-Smith, K. E. *J. Org. Chem.* **2011**, *76*, 4964–4972. <https://doi.org/10.1021/jo200613r>.
13. Allen, J. P.; Pfrunder, M. C.; McMurtrie, J. C.; Bottle, S. E.; Blinco, J. P.; Fairfull-Smith, K. E. *Eur. J. Org. Chem.* **2017**, *2017*, 476–483. <https://doi.org/10.1002/ejoc.201601280>.
14. Moad, G.; Rizzardo, E. *Macromolecules* **1995**, *28*, 8722–8728. <https://doi.org/10.1021/ma00130a003>.
15. Marque, S.; Le Mercier, C.; Tordo, P.; Fischer, H. *Macromolecules* **2000**, *33*, 4403–4410. <https://doi.org/10.1021/ma9918452>.

## Chapter 4

---

16. Gaudel-Siri, A.; Siri, D.; Tordo, P. *ChemPhysChem* **2006**, *7*, 430–438. <https://doi.org/10.1002/cphc.200500308>.
17. Herder, M.; Lehn, J.-M. *J. Am. Chem. Soc.* **2018**, *140*, 7647–7657. <https://doi.org/10.1021/jacs.8b03633>.
18. Aldabbagh, F.; Busfield, W. K.; Jenkins, I. D.; Thang, S. H. *Tetrahedron Lett.* **2000**, *41*, 3673–3676. [http://doi.org/10.1016/S0040-4039\(00\)00440-8](http://doi.org/10.1016/S0040-4039(00)00440-8).
19. O'Donovan, L.; Carty, M. P.; Aldabbagh, F. *Chem. Commun.* **2008**, 5592–5594. <https://doi.org/10.1039/b814706j>.
20. KIELTY, P.; FARRÀS, P.; McARDLE, P.; SMITH, D. A.; ALDABBAGH, F. *Chem. Commun.* **2019**, Advance Article. <https://doi.org/10.1039/C9CC08261A>.
21. Tohma, H.; Morioka, H.; Harayama, Y.; Hashizume, M.; Kita, Y. *Tetrahedron Lett.* **2001**, *42*, 6899–6902. [https://doi.org/10.1016/S0040-4039\(01\)01407-1](https://doi.org/10.1016/S0040-4039(01)01407-1).
22. Busfield, W. K.; Jenkins, I. D.; Thang, S. H.; Moad, G.; Rizzardo, E.; Solomon, D. H. *J. Chem. Soc., Chem. Commun.* **1985**, 1249–1250. <https://doi.org/10.1039/C39850001249>.
23. Versace, D.-L.; Guillaneuf, Y.; Bertin, D.; Fouassier, J. P.; Lalevée, J.; Gigmès, D. *Org. Biomol. Chem.* **2011**, *9*, 2892–2898. <https://doi.org/10.1039/C0OB01207F>.
24. Baron, M.; Morris, J. C.; Telitel, S.; Clément, J.-L.; Lalevée, J.; Morlet-Savary, F.; Spangenberg, A.; Malval, J.-P.; Soppera, O.; Gigmès, D.; Guillaneuf, Y. *J. Am. Chem. Soc.* **2018**, *140*, 3339–3344. <https://doi.org/10.1021/jacs.7b12807>.
25. Grattan, D. W.; Carlsson, D. J.; Howard, J. A.; Wiles, D. M. *Can. J. Chem.* **1979**, *57*, 2834–2842. <https://doi.org/10.1139/v79-460>.
26. Araki, Y.; Luo, H.; Islam, S. D. M.; Ito, O.; Matsushita, M. M.; Iyoda, T. *J. Phys. Chem. A* **2003**, *107*, 2815–2820. <https://doi.org/10.1021/jp0273373>.
27. Versace, D.-L.; Lalevée, J.; Fouassier, J.-P.; Gigmès, D.; Guillaneuf, Y.; Bertin, D. *J. Polym. Sci., Part A: Polym. Chem.* **2010**, *48*, 2910–2915. <https://doi.org/10.1002/pola.24071>.
28. Skene, W. G.; Belt, S. T.; Connolly, T. J.; Hahn, P.; Scaiano, J. C. *Macromolecules* **1998**, *31*, 9103–9105. <https://doi.org/10.1021/ma9812229>.
29. Cresidio, S. P.; Aldabbagh, F.; Busfield, W. K.; Jenkins, I. D.; Thang, S. H.; Zayas-Holdsworth, C.; Zetterlund, P. B. *J. Polym. Sci., Part A: Polym. Chem.* **2001**, *39*, 1232–1241. <https://doi.org/10.1002/pola.1100>.



## Chapter 4

---

30. Hawker, C. J.; Bosman, A. W.; Harth, E. *Chem. Rev.* **2001**, *101*, 3661–3688.  
<https://doi.org/10.1021/cr990119u>.
31. Chan, K. S.; Li, X. Z.; Lee, S. Y. *Organometallics* **2010**, *29*, 2850–2856.  
<https://doi.org/10.1021/om1000869>.
32. Harwood, L. M. *Aldrichim. Acta* **1985**, *18*, 25.
33. Frisch, M. J.; Trucks, G. W.; Schlegel, H. B.; Scuseria, G. E.; Robb, M. A.; Cheeseman, J. R.; Scalmani, G.; Barone, V.; Petersson, G. A.; Nakatsuji, H.; Li, X.; Caricato, M.; Marenich, A. V.; Bloino, J.; Janesko, B. G.; Gomperts, R.; Mennucci, B.; Hratchian, H. P.; Ortiz, J. V.; Izmaylov, A. F.; Sonnenberg, J. L.; Williams-Young, D.; Ding, F.; Lipparini, F.; Egidi, F.; Goings, J.; Peng, B.; Petrone, A.; Henderson, T.; Ranasinghe, D.; Zakrzewski, V. G.; Gao, J.; Rega, N.; Zheng, G.; Liang, W.; Hada, M.; Ehara, M.; Toyota, K.; Fukuda, R.; Hasegawa, J.; Ishida, M.; Nakajima, T.; Honda, Y.; Kitao, O.; Nakai, H.; Vreven, T.; Throssell, K.; Montgomery, J. A., Jr.; Peralta, J. E.; Ogliaro, F.; Bearpark, M. J.; Heyd, J. J.; Brothers, E. N.; Kudin, K. N.; Staroverov, V. N.; Keith, T. A.; Kobayashi, R.; Normand, J.; Raghavachari, K.; Rendell, A. P.; Burant, J. C.; Iyengar, S. S.; Tomasi, J.; Cossi, M.; Millam, J. M.; Klene, M.; Adamo, C.; Cammi, R.; Ochterski, J. W.; Martin, R. L.; Morokuma, K.; Farkas, O.; Foresman, J. B.; Fox, D. J. Gaussian 16, Revision B.01, Gaussian, Inc., Wallingford CT, 2016.
34. Zhao, Y.; Truhlar, D. G. *Theor. Chem. Acc.* **2008**, *120*, 215–241.  
<https://doi.org/10.1007/s00214-007-0310-x>.
35. Müller, K.; Faeh, C.; Diederich, F. *Science* **2007**, *317*, 1881–1886.  
<https://doi.org/10.1126/science.1131943>.
36. Fujiwara, T.; O'Hagan, D. *J. Fluorine Chem.* **2014**, *167*, 16–29.  
<https://doi.org/10.1016/j.jfluchem.2014.06.014>.
37. Furuya, T.; Kamlet, A. S.; Ritter, T. *Nature* **2011**, *473*, 470–477.  
<https://doi.org/10.1038/nature10108>.
38. McClinton, M. A.; McClinton, D. A. *Tetrahedron* **1992**, *48*, 6555–6666.  
[https://doi.org/10.1016/S0040-4020\(01\)80011-9](https://doi.org/10.1016/S0040-4020(01)80011-9).
39. Sen, K. D.; Jørgensen, C. K. *Electronegativity* New York, 1987.
40. Langlois, B. R. In *Modern Synthesis Processes and Reactivity of Fluorinated Compounds*; Groult, H., Leroux, F. R., Tressaud, A., Eds.; Elsevier: 2017, p 125–140. <https://doi.org/10.1016/B978-0-12-803740-9.00005-6>.

## Chapter 4

---

41. Langlois, B. R.; Laurent, E.; Roidot, N. *Tetrahedron Lett.* **1991**, *32*, 7525–7528. [https://doi.org/10.1016/0040-4039\(91\)80524-A](https://doi.org/10.1016/0040-4039(91)80524-A).
42. Ji, Y.; Brueckl, T.; Baxter, R. D.; Fujiwara, Y.; Seiple, I. B.; Su, S.; Blackmond, D. G.; Baran, P. S. *Proc Natl. Acad. Sci., U. S. A.* **2011**, *108*, 14411–14415. <https://doi.org/10.1073/pnas.1109059108>.
43. Studer, A. *Angew. Chem. Int. Ed.* **2012**, *51*, 8950–8958. <https://doi.org/10.1002/anie.201202624>.
44. Henderson, D. A.; Collier, P. N.; Pavé, G.; Rzepa, P.; White, A. J. P.; Burrows, J. N.; Barrett, A. G. M. *J. Org. Chem.* **2006**, *71*, 2434–2444. <https://doi.org/10.1021/jo052637c>.
45. Cheng, X.; Zhang, G.; Seupel, R.; Feineis, D.; Brünnert, D.; Chatterjee, M.; Schlosser, A.; Bringmann, G. *Tetrahedron* **2018**, *74*, 5102–5112. <https://doi.org/10.1016/j.tet.2018.04.056>.
46. Zhang, Y.; Guo, D.; Ye, S.; Liu, Z.; Zhu, G. *Org. Lett.* **2017**, *19*, 1302–1305. <https://doi.org/10.1021/acs.orglett.7b00095>.
47. Scaiano, J. C.; Connolly, T. J.; Mohtat, N.; Pliva, C. N. *Can. J. Chem.* **1997**, *75*, 92–97. <https://doi.org/10.1139/v97-014>.
48. Scaiano, J. C. *Chem. Phys. Lett.* **1981**, *79*, 441–443. [https://doi.org/10.1016/0009-2614\(81\)85010-5](https://doi.org/10.1016/0009-2614(81)85010-5).
49. Bertin, D.; Gigmes, D.; Marque, S. R. A.; Milardo, S.; Peri, J.; Tordo, P. *Collect. Czech. Chem. Commun.* **2004**, *69*, 2223–2238. <https://doi.org/10.1135/cccc20042223>.
50. Audran, G.; Brémond, P.; Joly, J.-P.; Marque, S. R. A.; Yamasaki, T. *Org. Biomol. Chem.* **2016**, *14*, 3574–3583. <https://doi.org/10.1039/C6OB00384B>.
51. Hünig, S.; Bau, R.; Kemmer, M.; Meixner, H.; Metzenthin, T.; Peters, K.; Sinzger, K.; Gulbis, J. *Eur. J. Org. Chem.* **1998**, *1998*, 335–348. [https://doi.org/10.1002/\(SICI\)1099-0690\(199802\)1998:2<335::AID-EJOC335>3.0.CO;2-A](https://doi.org/10.1002/(SICI)1099-0690(199802)1998:2<335::AID-EJOC335>3.0.CO;2-A).
52. Matsubara, H.; Maegawa, T.; Kita, Y.; Yokoji, T.; Nomoto, A. *Org. Biomol. Chem.* **2014**, *12*, 5442–5447. <https://doi.org/10.1039/C4OB00783B>.
53. Yokoji, T.; Matsubara, H.; Satoh, M. *J. Mater. Chem. A* **2014**, *2*, 19347–19354. <https://doi.org/10.1039/C4TA02812K>.
54. Tebben, L.; Studer, A. *Angew. Chem. Int. Ed.* **2011**, *50*, 5034–5068. <https://doi.org/10.1002/anie.201002547>.

## Chapter 4

---

55. Nicolas, J.; Guillaneuf, Y.; Lefay, C.; Bertin, D.; Gignes, D.; Charleux, B. *Prog. Polym. Sci.* **2013**, *38*, 63–235. <https://doi.org/10.1016/j.progpolymsci.2012.06.002>.
56. Antonini, I.; Claudi, F.; Cristalli, G.; Franchetti, P.; Grifantini, M.; Martelli, S. *J. Med. Chem.* **1988**, *31*, 260–264. <https://doi.org/10.1021/jm00396a041>.
57. Fahey, K.; Aldabbagh, F. *Tetrahedron Lett.* **2008**, *49*, 5235–5237. <https://doi.org/10.1016/j.tetlet.2008.06.121>.
58. Fahey, K.; O'Donovan, L.; Carr, M.; Carty, M. P.; Aldabbagh, F. *Eur. J. Med. Chem.* **2010**, *45*, 1873–1879. <https://doi.org/10.1016/j.ejmech.2010.01.026>
59. Skibo, E. B. *J. Org. Chem.* **1992**, *57*, 5874–5878. <https://doi.org/10.1021/jo00048a020>.
60. Schulz, W. G.; Nieman, R. A.; Skibo, E. B. *Proc. Natl. Acad. Sci., U. S. A.* **1995**, *92*, 11854–11858. <https://doi.org/10.1073/pnas.92.25.11854>.
61. Lynch, M.; Hehir, S.; Kavanagh, P.; Leech, D.; O'Shaughnessy, J.; Carty, M. P.; Aldabbagh, F. *Chem. Eur. J.* **2007**, *13*, 3218–3226. <https://doi.org/10.1002/chem.200601450>.
62. Moriarty, E.; Carr, M.; Bonham, S.; Carty, M. P.; Aldabbagh, F. *Eur. J. Med. Chem.* **2010**, *45*, 3762–3769. <https://doi.org/10.1016/j.ejmech.2010.05.025>.
63. Gellis, A.; Kovacic, H.; Boufatah, N.; Vanelle, P. *Eur. J. Med. Chem.* **2008**, *43*, 1858–1864. <https://doi.org/10.1016/j.ejmech.2007.11.020>.
64. Garuti, L.; Roberti, M.; Malagoli, M.; Rossi, T.; Castelli, M. *Bioorg. Med. Chem. Lett.* **2000**, *10*, 2193–2195. [https://doi.org/10.1016/S0960-894X\(00\)00429-7](https://doi.org/10.1016/S0960-894X(00)00429-7).
65. Kunz, K. R.; Iyengar, B. S.; Dorr, R. T.; Alberts, D. S.; Remers, W. A. *J. Med. Chem.* **1991**, *34*, 2281–2286. <https://doi.org/10.1021/jm00111a051>.
66. Purser, S.; Moore, P. R.; Swallow, S.; Gouverneur, V. *Chem. Soc. Rev.* **2008**, *37*, 320–330. <https://doi.org/10.1039/B610213C>.
67. Nyffeler, P. T.; Duron, S. G.; Burkart, M. D.; Vincent, S. P.; Wong, C.-H. *Angew. Chem., Int. Ed.* **2005**, *44*, 192–212. <https://doi.org/10.1002/anie.200400648>.
68. Stavber, S. *Molecules* **2011**, *16*, 6432–6464. <https://doi.org/10.3390/molecules16086432>.
69. Banks, R. E.; Besheesh, M. K.; Mohialdin-Khaffaf, S. N.; Sharif, I. *J. Chem. Soc., Perkin Trans. 1* **1996**, 2069–2076. <https://doi.org/10.1039/P19960002069>.
70. Heravi, M. R. P. *J. Fluorine Chem.* **2008**, *129*, 217–221. <https://doi.org/10.1016/j.jfluchem.2007.11.006>.

## Chapter 4

---

71. Liang, D.; Li, Y.; Gao, S.; Li, R.; Li, X.; Wang, B.; Yang, H. *Green Chem.* **2017**, *19*, 3344–3349. <https://doi.org/10.1039/C7GC00356K>.
72. Mirallai, S. I.; Koutentis, P. A.; Aldabbagh, F. *Molecules* **2019**, *24*, 282. <https://doi.org/10.3390/molecules24020282>.
73. René, O.; Souverneva, A.; Magnuson, S. R.; Fauber, B. P. *Tetrahedron Lett.* **2013**, *54*, 201–204. <https://doi.org/10.1016/j.tetlet.2012.09.069>.
74. Rewcastle, G. W.; Gamage, S. A.; Flanagan, J. U.; Frederick, R.; Denny, W. A.; Baguley, B. C.; Kestell, P.; Singh, R.; Kendall, J. D.; Marshall, E. S.; Lill, C. L.; Lee, W.-J.; Kolekar, S.; Buchanan, C. M.; Jamieson, S. M. F.; Shepherd, P. R. *J. Med. Chem.* **2011**, *54*, 7105–7126. <https://doi.org/10.1021/jm200688y>.
75. Rueda-Becerril, M.; Chatalova Sazepin, C.; Leung, J. C. T.; Okbinoglu, T.; Kennepohl, P.; Paquin, J.-F.; Sammis, G. M. *J. Am. Chem. Soc.* **2012**, *134*, 4026–4029. <https://doi.org/10.1021/ja211679v>.
76. Hammill, C. L.; Noble, B. B.; Norcott, P. L.; Ciampi, S.; Coote, M. L. *J. Phys. Chem. C* **2019**, *123*, 5273–5281. <https://doi.org/10.1021/acs.jpcc.8b12545>.

# Appendix

## Supplementary Data for Chapter 2

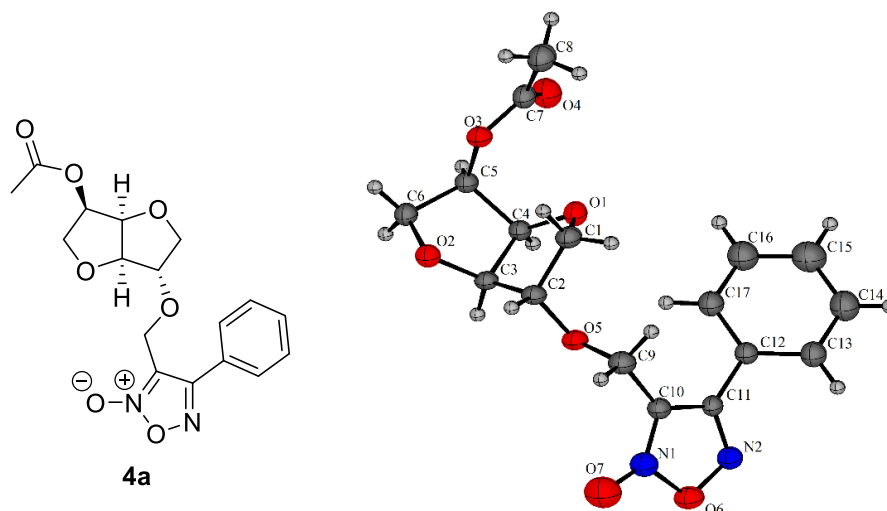
## Chapter 2 Supporting Tables

Table A2.1 DFT model energies for Scheme 2.7, 2.8 and Figure 2.6.

structure	EE + thermal free energy correction (Hartrees)
<b>1</b> (minimum)	- 535.540814
<b>1</b> (alternative conformer)	- 535.539262
<b>6a</b>	- 1195.430560
<b>6b</b>	- 1195.416160
<b>6c</b>	- 1195.411911
<b>6d</b>	- 1855.299059
<b>6e</b>	- 1855.302255
<b>6f</b>	- 1348.109210
<b>6g</b>	- 1348.083919
CH <sub>4</sub>	- 40.509724
MeMgCl	- 700.33001

## Appendix (Chapter 2)

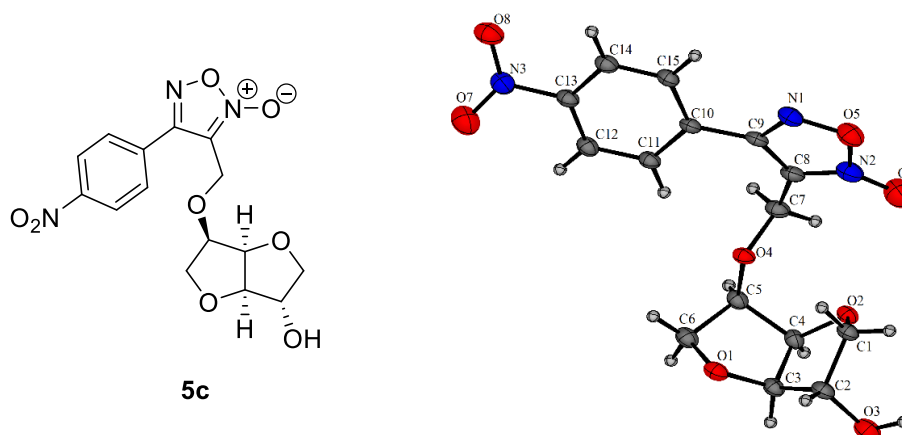
**Table A2.2** Single crystal X-ray data and structure refinement for **4a**.



Empirical formula	C <sub>17</sub> H <sub>18</sub> N <sub>2</sub> O <sub>7</sub>	
Formula weight	362.33	
Temperature	300.4(3) K	
Wavelength	0.71073 Å	
Crystal system	Orthorhombic	
Space group	P2 <sub>1</sub> 2 <sub>1</sub> 2 <sub>1</sub>	
Unit cell dimensions	a = 8.4273(6) Å	α = 90°
	b = 8.8552(4) Å	β = 90°
	c = 23.0068(12) Å	γ = 90°
Volume	1716.89(17) Å <sup>3</sup>	
Z	4	
Density (calculated)	1.402 Mg/m <sup>3</sup>	
Absorption coefficient	0.110 mm <sup>-1</sup>	
F(000)	760	
Crystal size	0.50 x 0.40 x 0.20 mm <sup>3</sup>	
Theta range for data collection	3.592 to 29.214°	
Index ranges	-5 ≤ h ≤ 10, -11 ≤ k ≤ 6, -31 ≤ l ≤ 31	
Reflections collected	5090	
Independent reflections	3415 [R(int) = 0.0180]	
Completeness to theta = 25.242°	99.5%	
Absorption correction	Semi-empirical from equivalents	
Max. and min. transmission	1.00000 and 0.89536	
Refinement method	Full-matrix least-squares on F <sup>2</sup>	
Data / restraints / parameters	3415 / 0 / 237	
Goodness-of-fit on F <sup>2</sup>	0.999	
Final R indices [I > 2 sigma(I)]	R1 = 0.0409, wR2 = 0.0869	
R indices (all data)	R1 = 0.0566, wR2 = 0.0977	
Absolute structure parameter	0.3(6)	
Extinction coefficient	0.035(3)	
Largest diff. peak and hole	0.134 and -0.130 e.Å <sup>-3</sup>	

## Appendix (Chapter 2)

**Table A2.3** Single crystal X-ray data and structure refinement for **5c**.



Empirical formula	C <sub>15</sub> H <sub>16</sub> N <sub>3</sub> O <sub>8</sub>	
Formula weight	374.31	
Temperature	150.0(1) K	
Wavelength	0.71073 Å	
Crystal system	Triclinic	
Space group	P1	
Unit cell dimensions	a = 7.3453(4) Å	α = 85.258(5)°.
	b = 8.0481(6) Å	β = 76.390(4)°.
	c = 14.5503(7) Å	γ = 74.825(6)°.
Volume	806.64(9) Å <sup>3</sup>	
Z	2	
Density (calculated)	1.541 Mg/m <sup>3</sup>	
Absorption coefficient	0.128 mm <sup>-1</sup>	
F(000)	390	
Crystal size	0.50 x 0.40 x 0.20 mm <sup>3</sup>	
Theta range for data collection	3.854 to 29.070°.	
Index ranges	-10 ≤ h ≤ 9, -10 ≤ k ≤ 9, -19 ≤ l ≤ 19	
Reflections collected	6143	
Independent reflections	4783 [R(int) = 0.0158]	
Completeness to theta = 25.242°	99.6%	
Absorption correction	Semi-empirical from equivalents	
Max. and min. transmission	1.00000 and 0.95047	
Refinement method	Full-matrix least-squares on F <sup>2</sup>	
Data / restraints / parameters	4783 / 7 / 494	
Goodness-of-fit on F <sup>2</sup>	1.028	
Final R indices [I > 2σ(I)]	R1 = 0.0329, wR2 = 0.0742	
R indices (all data)	R1 = 0.0382, wR2 = 0.0777	
Absolute structure parameter	-0.4(6)	
Extinction coefficient	n/a	
Largest diff. peak and hole	0.208 and -0.212 e.Å <sup>-3</sup>	



## Appendix (Chapter 2)

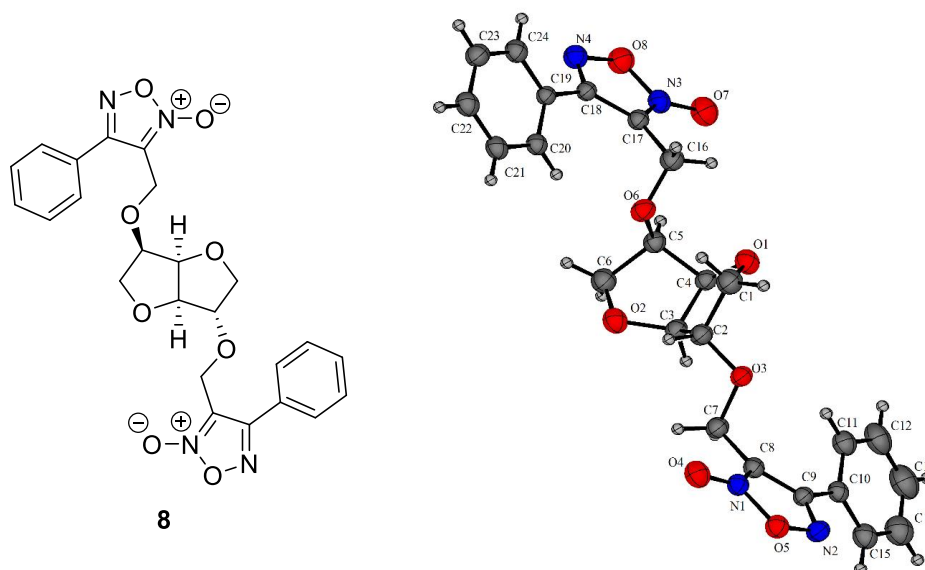
---

**Table A2.4** H-bond lengths and angles for **5c** [ $\text{\AA}$  and  $^\circ$ ] as depicted in Figure A2.1.

D-H...A	d(D-H)	d(H...A)	d(D...A)	angle (DHA)
O(17)-H(17A)...O(9)#1	0.88(2)	1.97(2)	2.823(3)	162.3
O(17)-H(17B)...O(10)	0.87(2)	1.89(2)	2.752(3)	169.4
O(3)-H(103)...O(17)	0.89(2)	1.82(2)	2.704(3)	170.4
O(12)-H(12A)...O(3)#2	0.86(2)	1.91(2)	2.772(3)	176.4

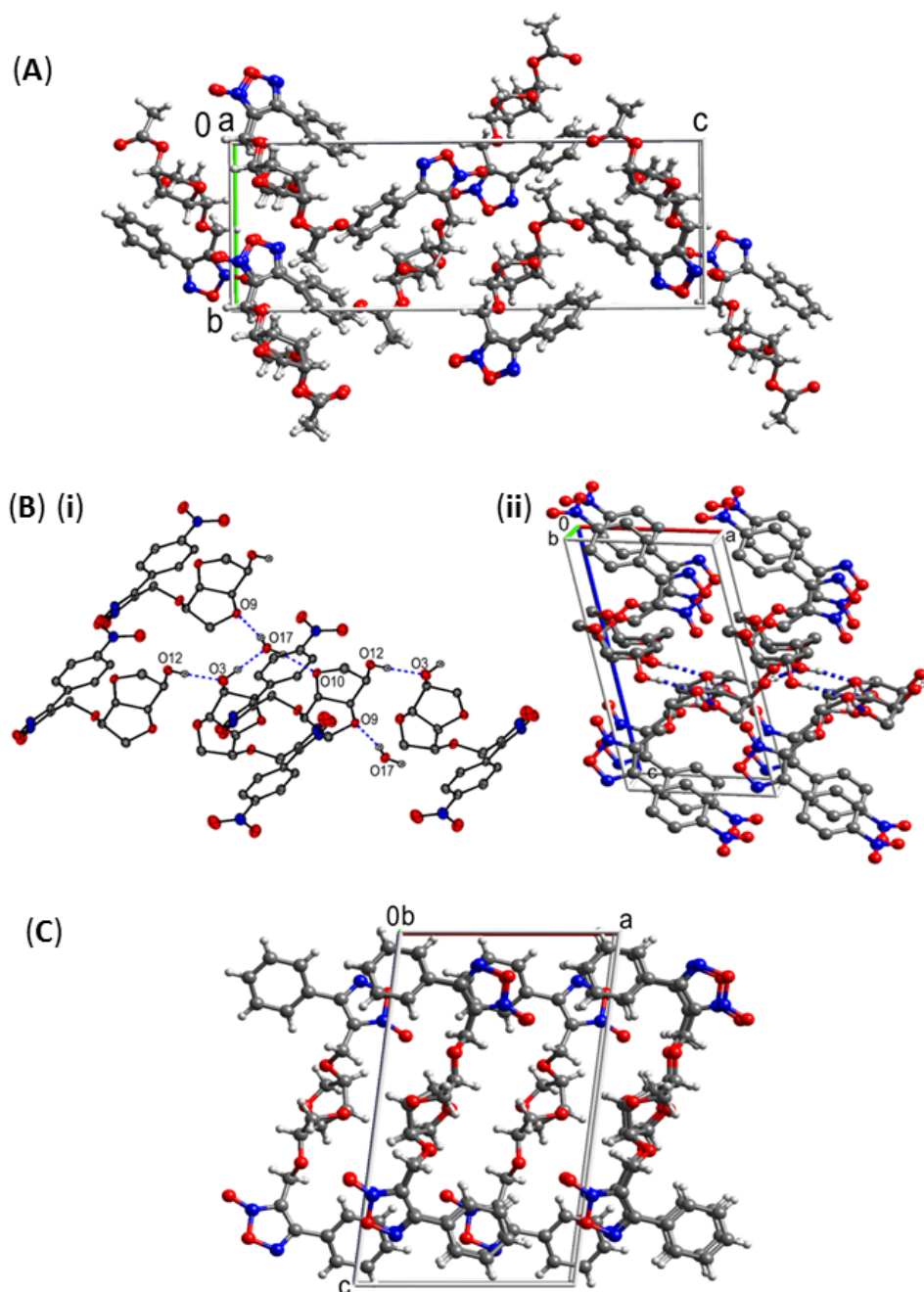
## Appendix (Chapter 2)

**Table A2.5** Single crystal X-ray data and structure refinement for **8**.



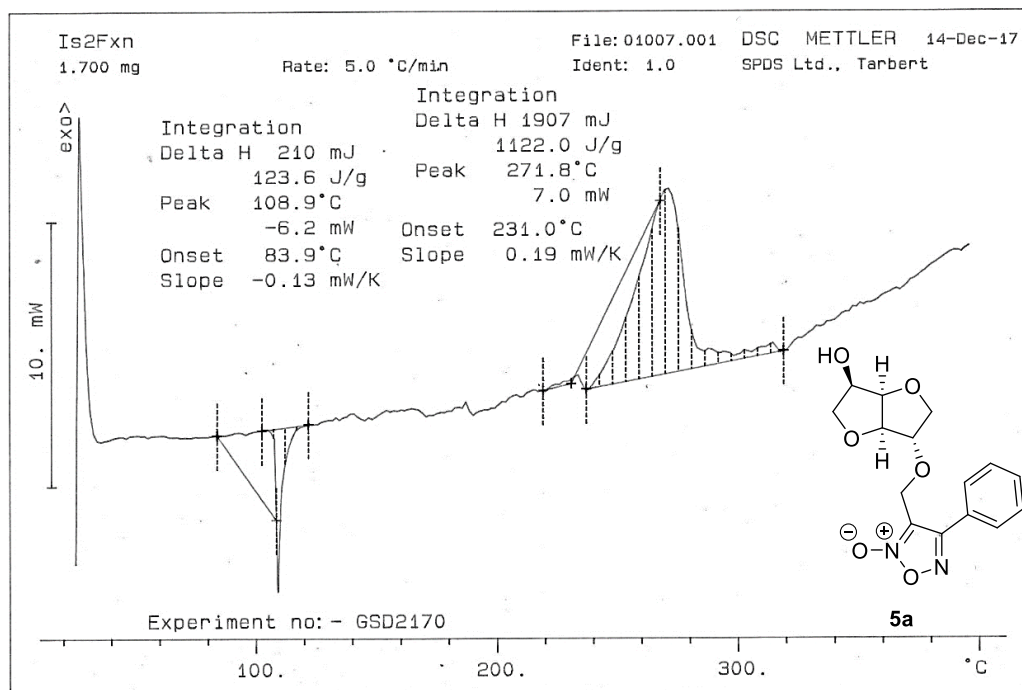
Empirical formula	C <sub>24</sub> H <sub>22</sub> N <sub>4</sub> O <sub>8</sub>	
Formula weight	494.45	
Temperature	298.0(1) K	
Wavelength	0.71073 Å	
Crystal system	Monoclinic	
Space group	P21	
Unit cell dimensions	a = 9.7477(15) Å	α = 90°.
	b = 6.9314(17) Å	β = 96.616(13)°.
	c = 17.336(3) Å	γ = 90°.
Volume	1163.5(4) Å <sup>3</sup>	
Z	2	
Density (calculated)	1.411 Mg/m <sup>3</sup>	
Absorption coefficient	0.108 mm <sup>-1</sup>	
F(000)	516	
Crystal size	0.50 x 0.40 x 0.08 mm <sup>3</sup>	
Theta range for data collection	3.549 to 25.348°.	
Index ranges	-10 ≤ h ≤ 11, -8 ≤ k ≤ 8, -20 ≤ l ≤ 12	
Reflections collected	4765	
Independent reflections	3306 [R(int) = 0.0506]	
Completeness to theta = 25.242°	99.7%	
Absorption correction	Semi-empirical from equivalents	
Max. and min. transmission	1.00000 and 0.19370	
Refinement method	Full-matrix least-squares on F <sup>2</sup>	
Data / restraints / parameters	3306 / 1 / 325	
Goodness-of-fit on F <sup>2</sup>	0.936	
Final R indices [I > 2σ(I)]	R1 = 0.0653, wR2 = 0.1426	
R indices (all data)	R1 = 0.1136, wR2 = 0.1716	
Absolute structure parameter	0.9(10)	
Extinction coefficient	n/a	
Largest diff. peak and hole	0.236 and -0.183 e.Å <sup>-3</sup>	

## Chapter 2 Supporting Figures

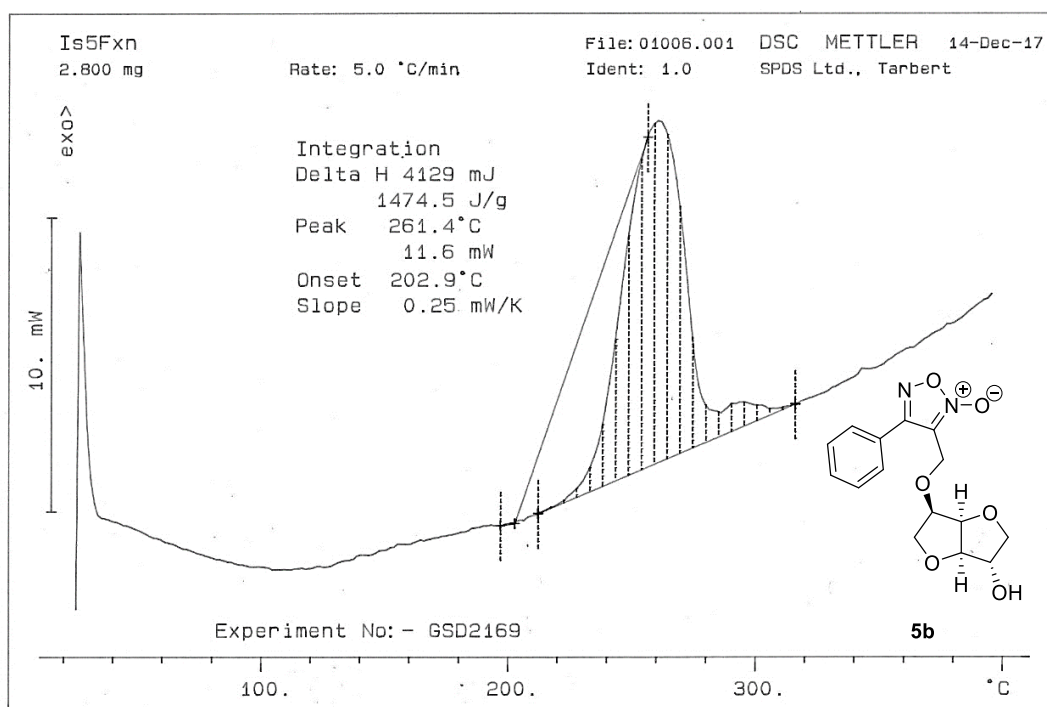


**Figure A2.1** Intermolecular interactions within the crystal lattice with the repeating unit cell outlined in grey: (A) View down the axis of the **4a** unit cell (B) (i) Hydrogen bonding (O-H $\cdots$ O) in the crystal structure of **5c**. (ii) The hydrogen bonds in **5c** forming sheets which are parallel to the *ab* face. Hydrogen atoms not involved in hydrogen bonding have been omitted for clarity. (C) View of the unit cell structure of **8** down the *b* axis.

## Appendix (Chapter 2)

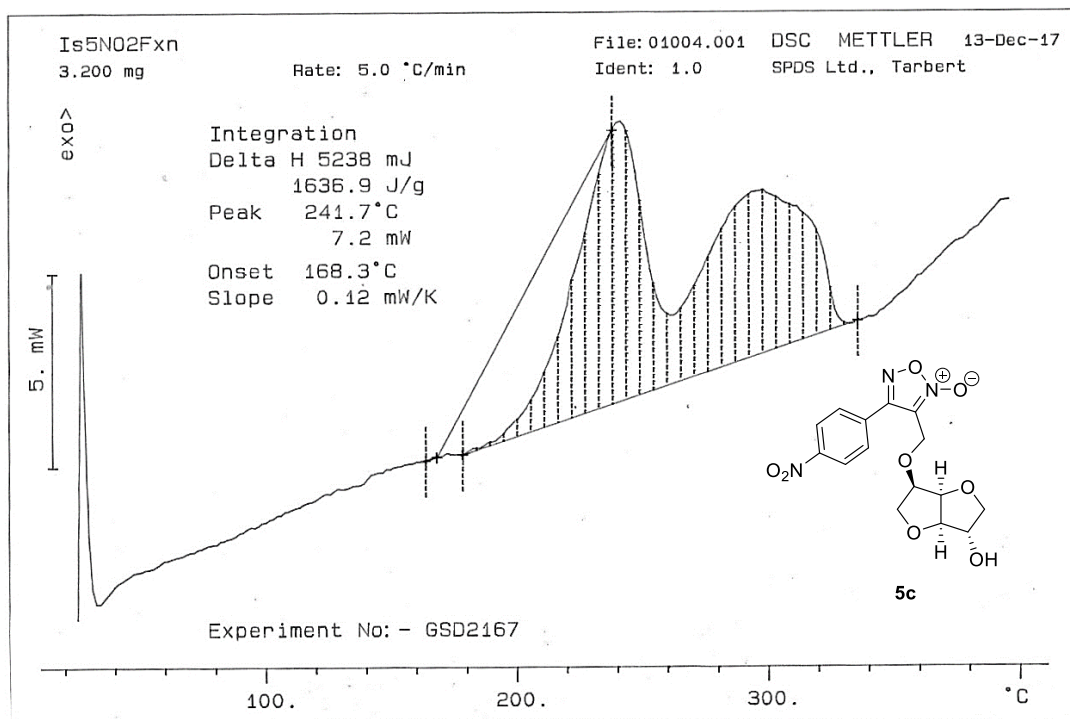


**Figure A2.2** DSC of **5a** depicting endothermic melting point (peak = 109 °C) and exothermic degradation (peak = 271.8 °C).

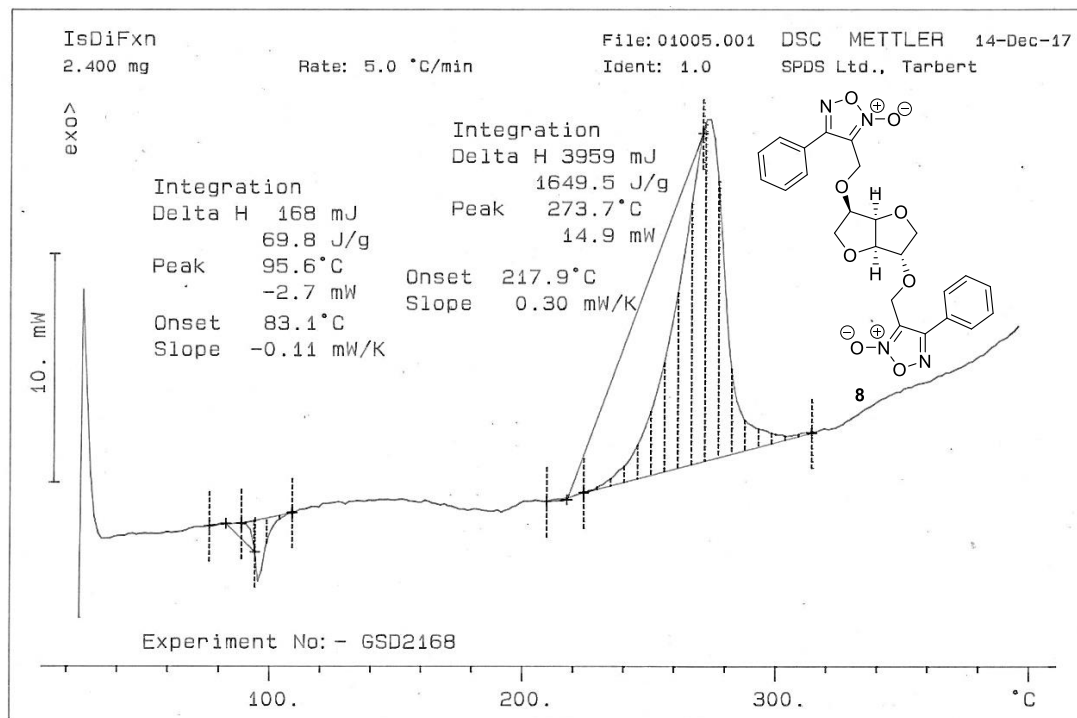


**Figure A2.3** DSC of **5b** depicting exothermic degradation (peak = 261.4 °C).

## Appendix (Chapter 2)

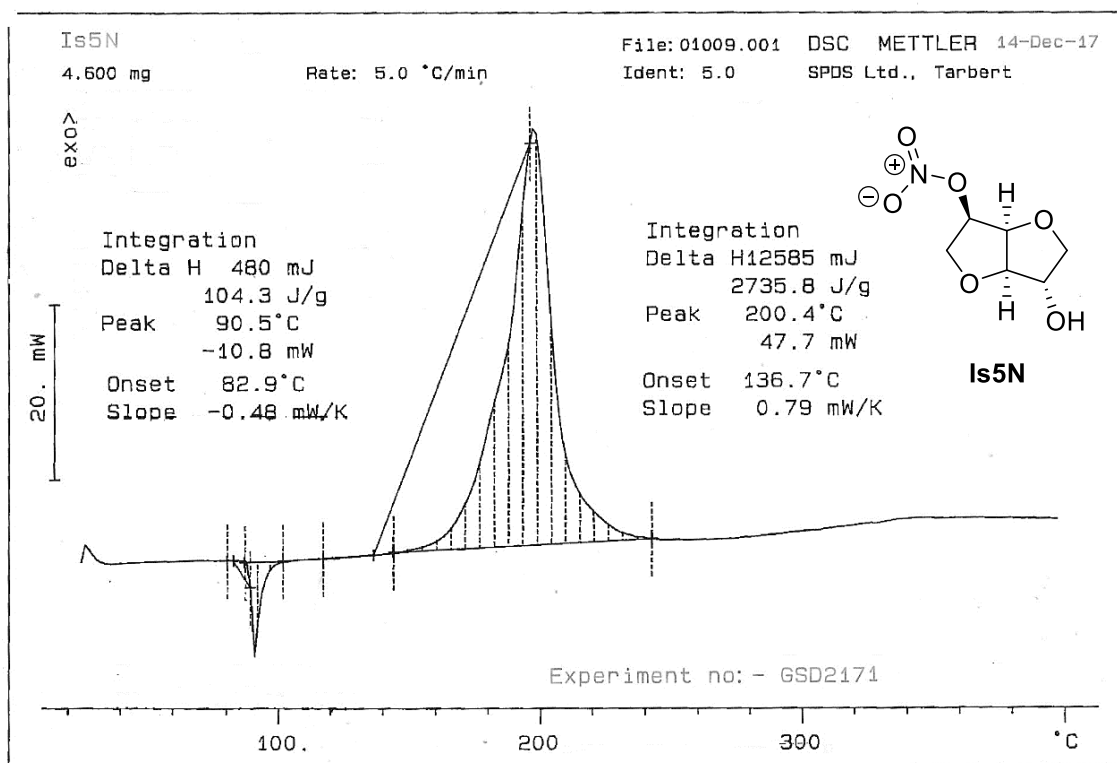


**Figure A2.4** DSC of **5c** depicting exothermic degradation (peak = 241.7 °C).



**Figure A2.5** DSC of **8** depicting endothermic melting point (peak = 95.6 °C) and exothermic degradation (peak = 273.7 °C).

## Appendix (Chapter 2)

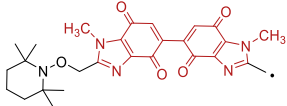
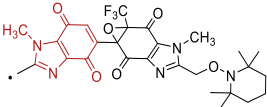
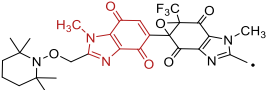
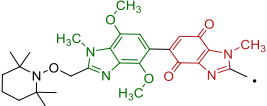
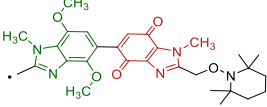


**Figure A2.6** DSC of Is5N depicting endothermic melting point (peak = 90.5 °C) and exothermic degradation (peak = 200.4 °C).

## Supplementary Data for Chapter 3

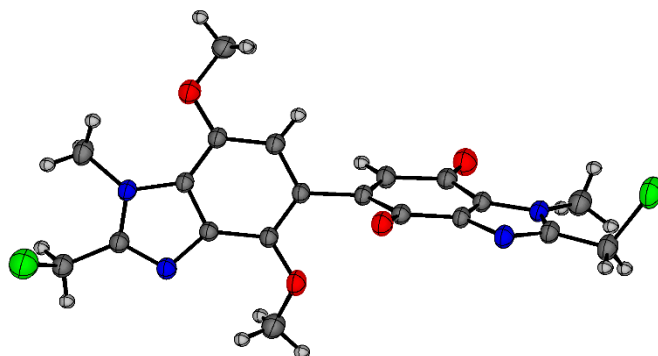
## Chapter 3 Supporting Tables

Table A3.1 DFT model energies associated with Table 3.4.

compd	multiplicity	EE (Hartrees)	EE + thermal free energy correction (Hartrees)
<b>TEMPO-Vis</b>	singlet	- 1090.676089	- 1090.311417
<b>TEMPO-Vis</b>	triplet	- 1090.594405	- 1090.232441
<b>QM-rad</b>	doublet	- 606.984531	- 606.875713
TEMPO	doublet	- 483.631085	- 483.403280
<b>Bis-TEMPO-Vis</b>	singlet	- 2180.186815	- 2179.453072
<b>Bis-TEMPO-Vis</b>	triplet	- 2180.103807	- 2179.371002
 <b>Bis-TEMPO-Vis radical</b>	doublet	- 1696.486519	- 1696.009845
<b>6</b>	singlet	- 2592.424110	- 2591.685608
<b>6</b>	triplet	- 2592.339550	- 2591.605755
 <b>6 quinone-radical</b>	doublet	- 2108.723751	- 2108.244338
 <b>6 epoxide-radical</b>	doublet	- 2108.723151	- 2108.242497
<b>3</b>	singlet	- 2259.989495	- 2259.180506
<b>3</b>	triplet	- 2259.921214	- 2259.113174
 <b>3 quinone-radical</b>	doublet	- 1776.289571	- 1775.737561
 <b>3 dimethoxy-radical</b>	doublet	- 1776.289116	- 1775.734596

## Appendix (Chapter 3)

**Table A3.2** Single crystal X-ray data and structure refinement for benzimidazolequinone-dimethoxybenzimidazole **4** (thermal ellipsoids set at 50% probability). The dihedral angle defined by C6-C5-C5'-C6' is 60.7°.

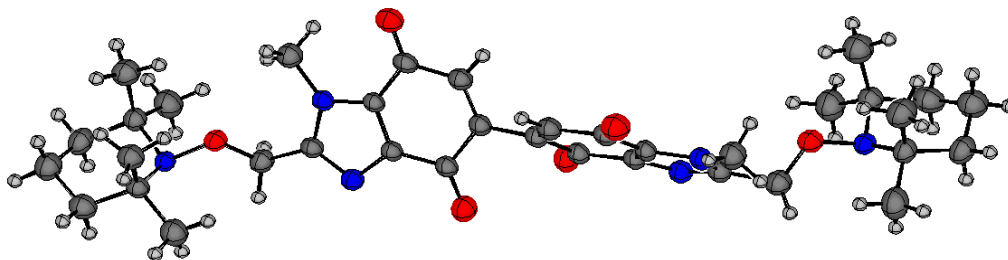


Empirical formula	$C_{20}H_{18}Cl_2N_4O_4$	
Formula weight	449.28	
Temperature	299.0(1) K	
Wavelength	0.71073 Å	
Crystal system	Monoclinic	
Space group	$P2_1/n$	
Unit cell dimensions	$a = 10.7210(7)$ Å	$\alpha = 90^\circ$ .
	$b = 14.6163(11)$ Å	$\beta = 97.406(7)^\circ$ .
	$c = 12.7288(11)$ Å	$\gamma = 90^\circ$ .
Volume	$1978.0(3)$ Å <sup>3</sup>	
Z	4	
Density (calculated)	$1.509$ Mg/m <sup>3</sup>	
Absorption coefficient	$0.365$ mm <sup>-1</sup>	
F(000)	928	
Crystal size	$0.50 \times 0.30 \times 0.20$ mm <sup>3</sup>	
Theta range for data collection	$3.383$ to $29.242^\circ$ .	
Index ranges	$-7 \leq h \leq 14$ , $-18 \leq k \leq 18$ , $-16 \leq l \leq 16$	
Reflections collected	9557	
Independent reflections	4593 [R(int) = 0.0320]	
Completeness to theta = $25.242^\circ$	99.7 %	
Absorption correction	Semi-empirical from equivalents	
Max. and min. transmission	1.00000 and 0.93128	
Refinement method	Full-matrix least-squares on F <sup>2</sup>	
Data / restraints / parameters	4593 / 0 / 275	
Goodness-of-fit on F <sup>2</sup>	1.027	
Final R indices [I > 2σ(I)]	R1 = 0.0599, wR2 = 0.1393	
R indices (all data)	R1 = 0.1107, wR2 = 0.1726	
Extinction coefficient	n/a	
Largest diff. peak and hole	$0.383$ and $-0.335$ e.Å <sup>-3</sup>	



## Appendix (Chapter 3)

**Table A3.3** Single crystal X-ray data and structure refinement for **Bis-TEMPO-Vis** (thermal ellipsoids set at 50% probability). The dihedral angle defined by C6-C5-C5'-C6' is 55.6°.



Empirical formula	C <sub>36</sub> H <sub>48</sub> N <sub>6</sub> O <sub>6</sub>	
Formula weight	660.80	
Temperature	298.9(5) K	
Wavelength	0.71073 Å	
Crystal system	Orthorhombic	
Space group	P2 <sub>1</sub> 2 <sub>1</sub> 2 <sub>1</sub>	
Unit cell dimensions	a = 6.0407(3) Å	α = 90°.
	b = 21.1209(12) Å	β = 90°.
	c = 27.1076(14) Å	γ = 90°.
Volume	3458.5(3) Å <sup>3</sup>	
Z	4	
Density (calculated)	1.269 Mg/m <sup>3</sup>	
Absorption coefficient	0.087 mm <sup>-1</sup>	
F(000)	1416	
Crystal size	0.50 x 0.40 x 0.20 mm <sup>3</sup>	
Theta range for data collection	3.455 to 29.311°.	
Index ranges	-6 <= h <= 8, -28 <= k <= 21, -32 <= l <= 35	
Reflections collected	28054	
Independent reflections	8461 [R(int) = 0.0449]	
Completeness to theta = 25.242°	99.6 %	
Absorption correction	Semi-empirical from equivalents	
Max. and min. transmission	1.00000 and 0.62048	
Refinement method	Full-matrix least-squares on F <sup>2</sup>	
Data / restraints / parameters	8461 / 0 / 443	
Goodness-of-fit on F <sup>2</sup>	1.002	
Final R indices [I > 2σ(I)]	R1 = 0.0519, wR2 = 0.1002	
R indices (all data)	R1 = 0.0942, wR2 = 0.1188	
Absolute structure parameter	0.7(5)	
Extinction coefficient	n/a	
Largest diff. peak and hole	0.167 and -0.196 e.Å <sup>-3</sup>	

Chapter 3 Supporting Figure

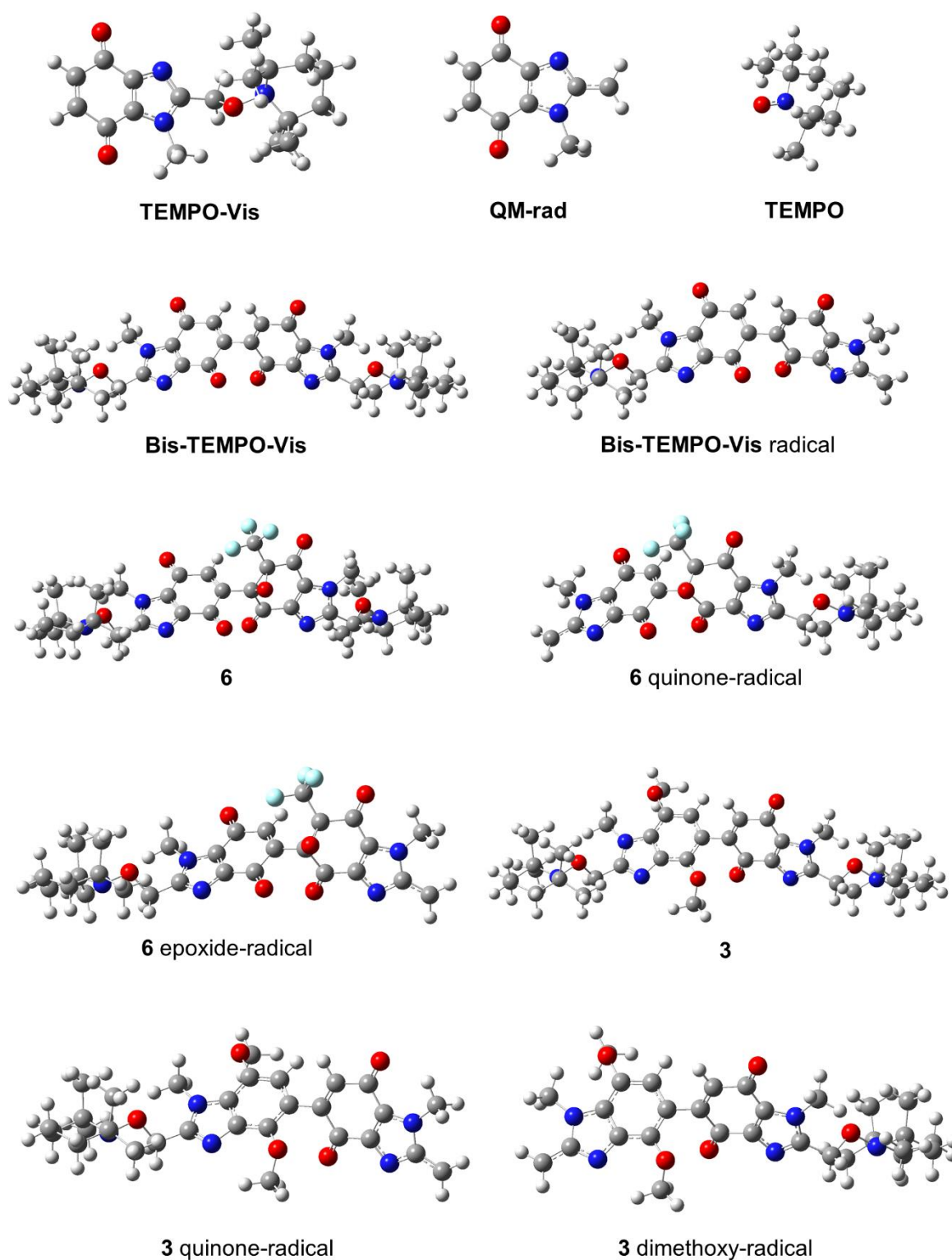
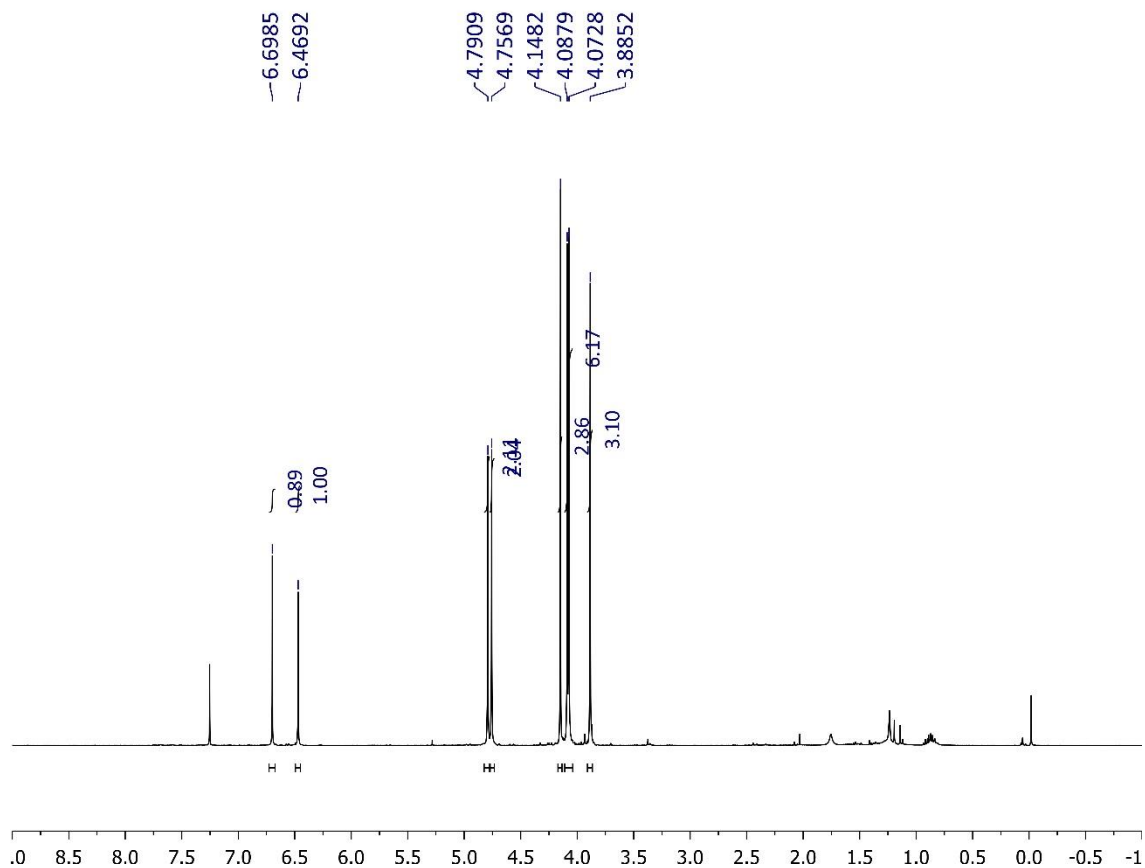
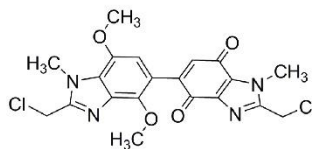


**Figure A3.1** Optimized geometries of alkoxyamines (singlet) and radicals (doublet).

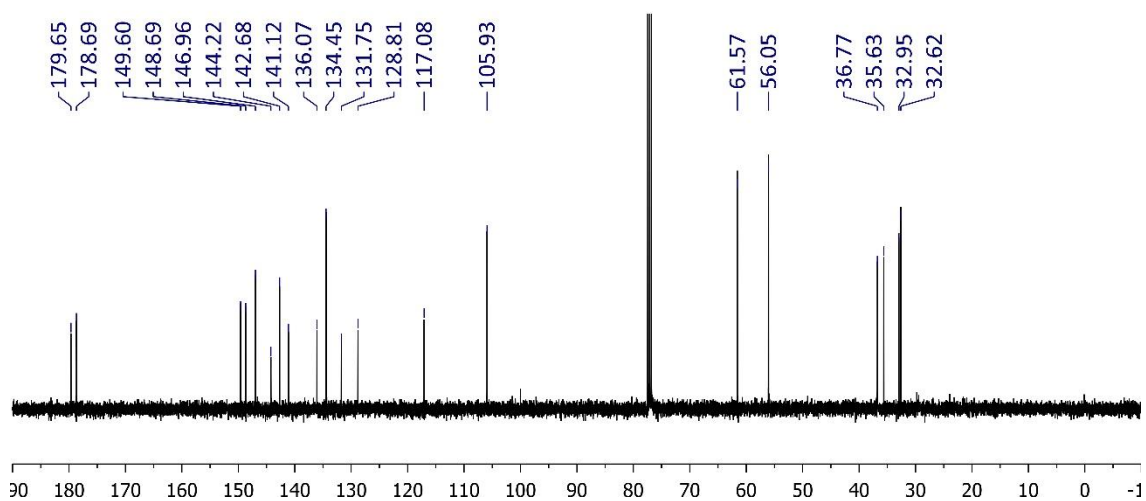
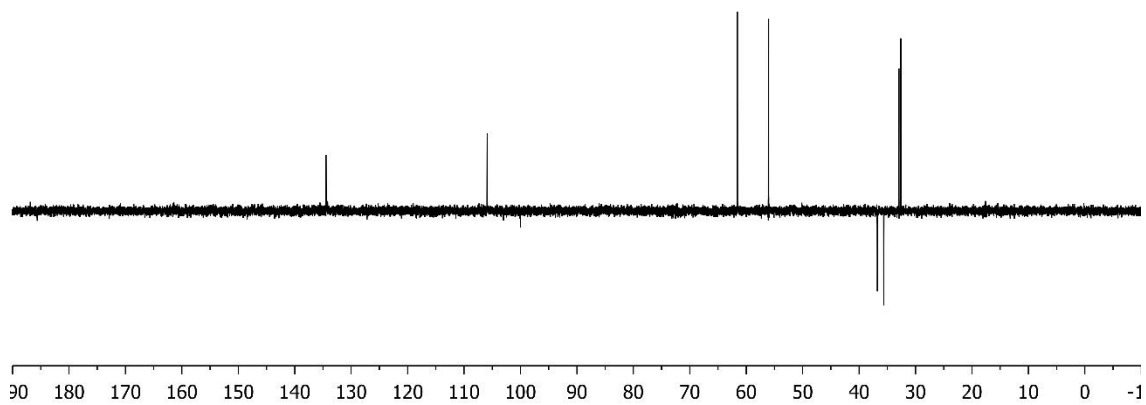
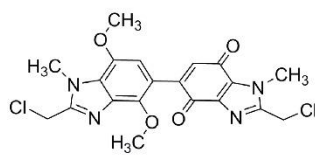
Chapter 3 NMR Spectra

$^1\text{H}$  NMR (400 MHz) of **4** in  $\text{CDCl}_3$



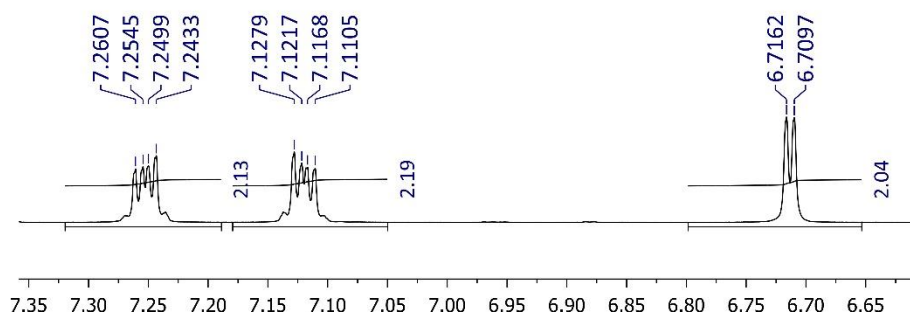
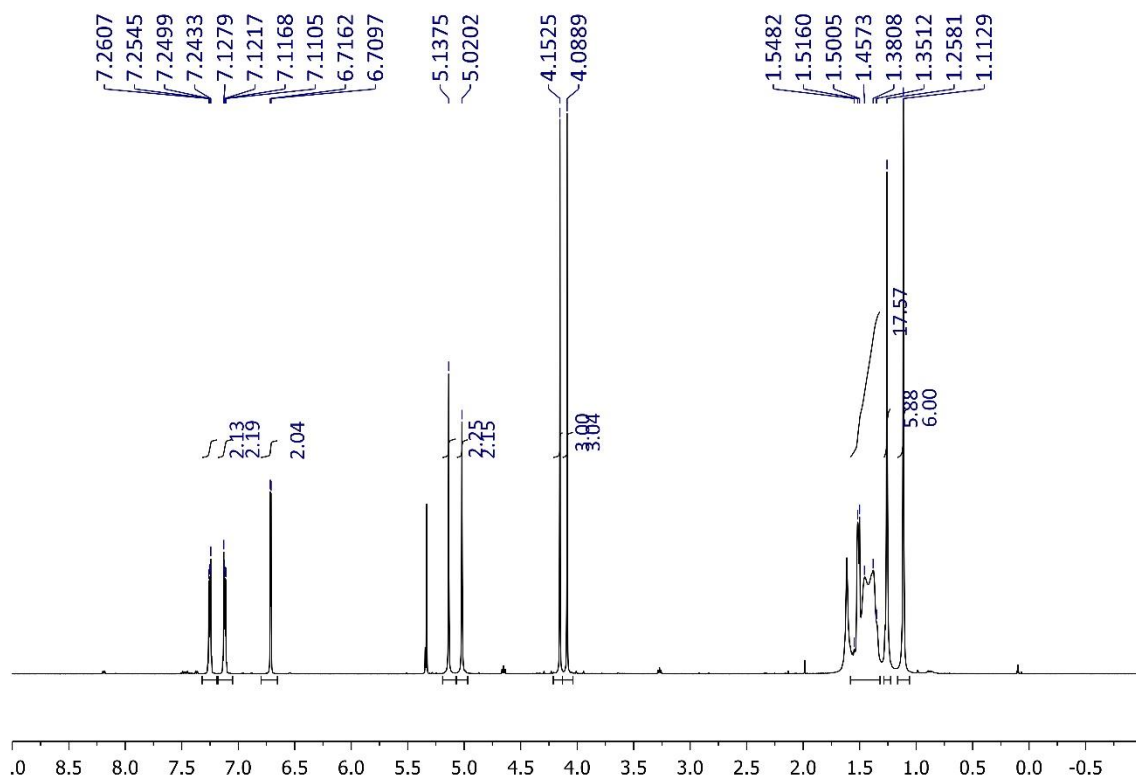
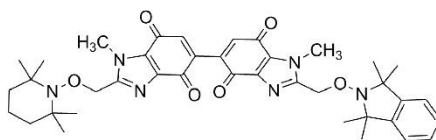
## Appendix (Chapter 3)

$^{13}\text{C}$  NMR (100 MHz) of **4** in  $\text{CDCl}_3$



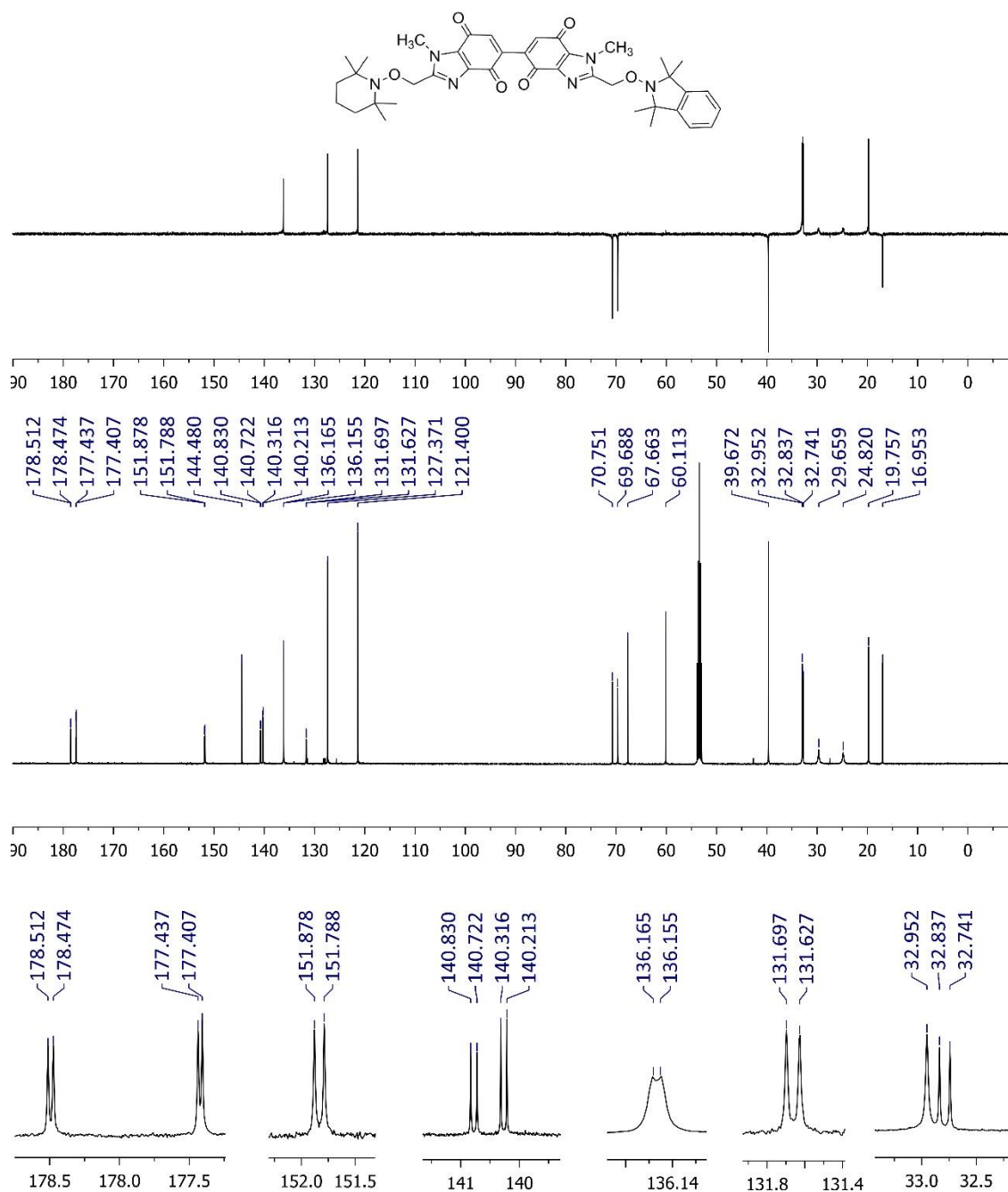
## Appendix (Chapter 3)

$^1\text{H}$  NMR (500 MHz) of **7** in  $\text{CD}_2\text{Cl}_2$



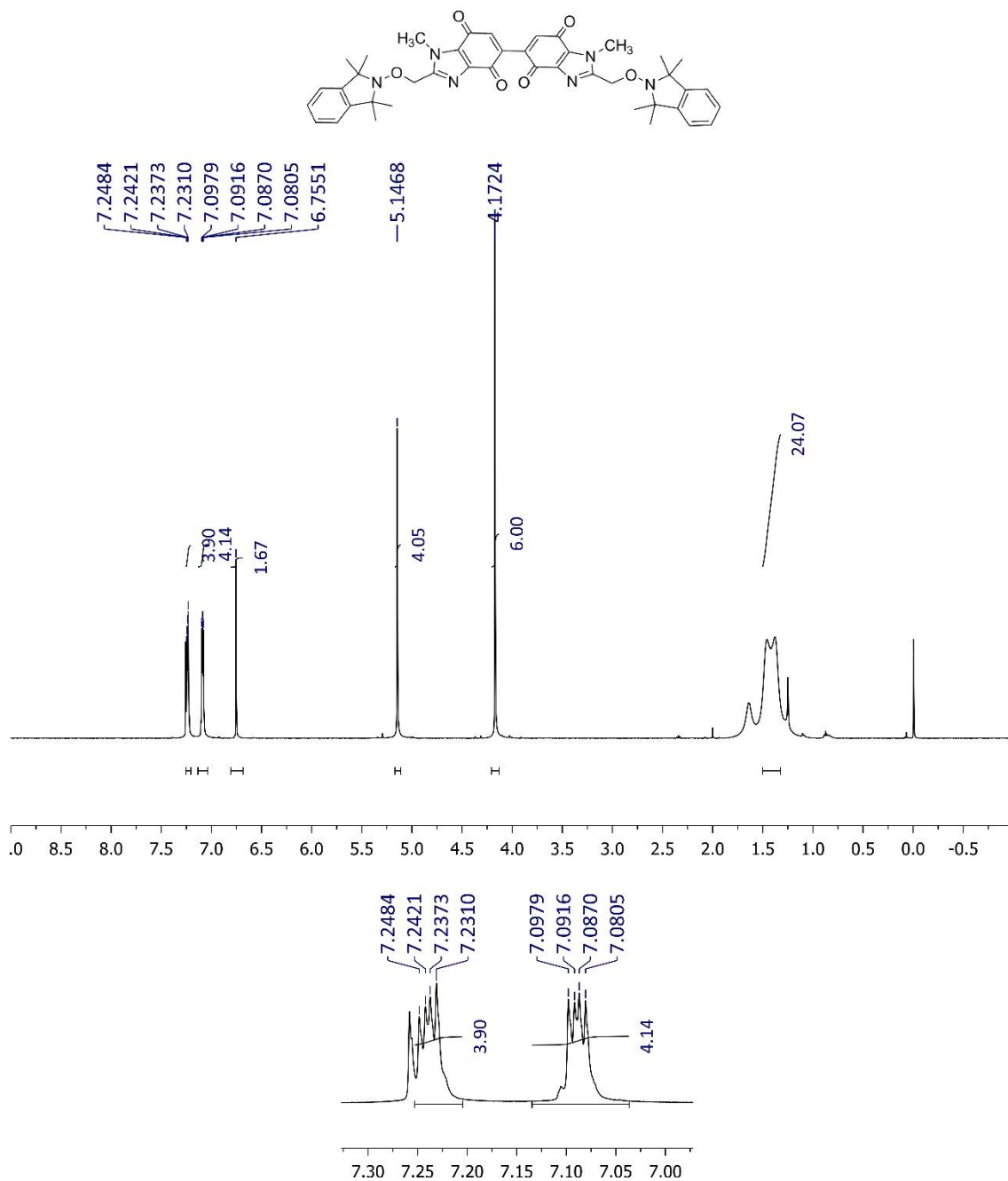
## Appendix (Chapter 3)

$^{13}\text{C}$  NMR (125 MHz) of **7** in  $\text{CD}_2\text{Cl}_2$



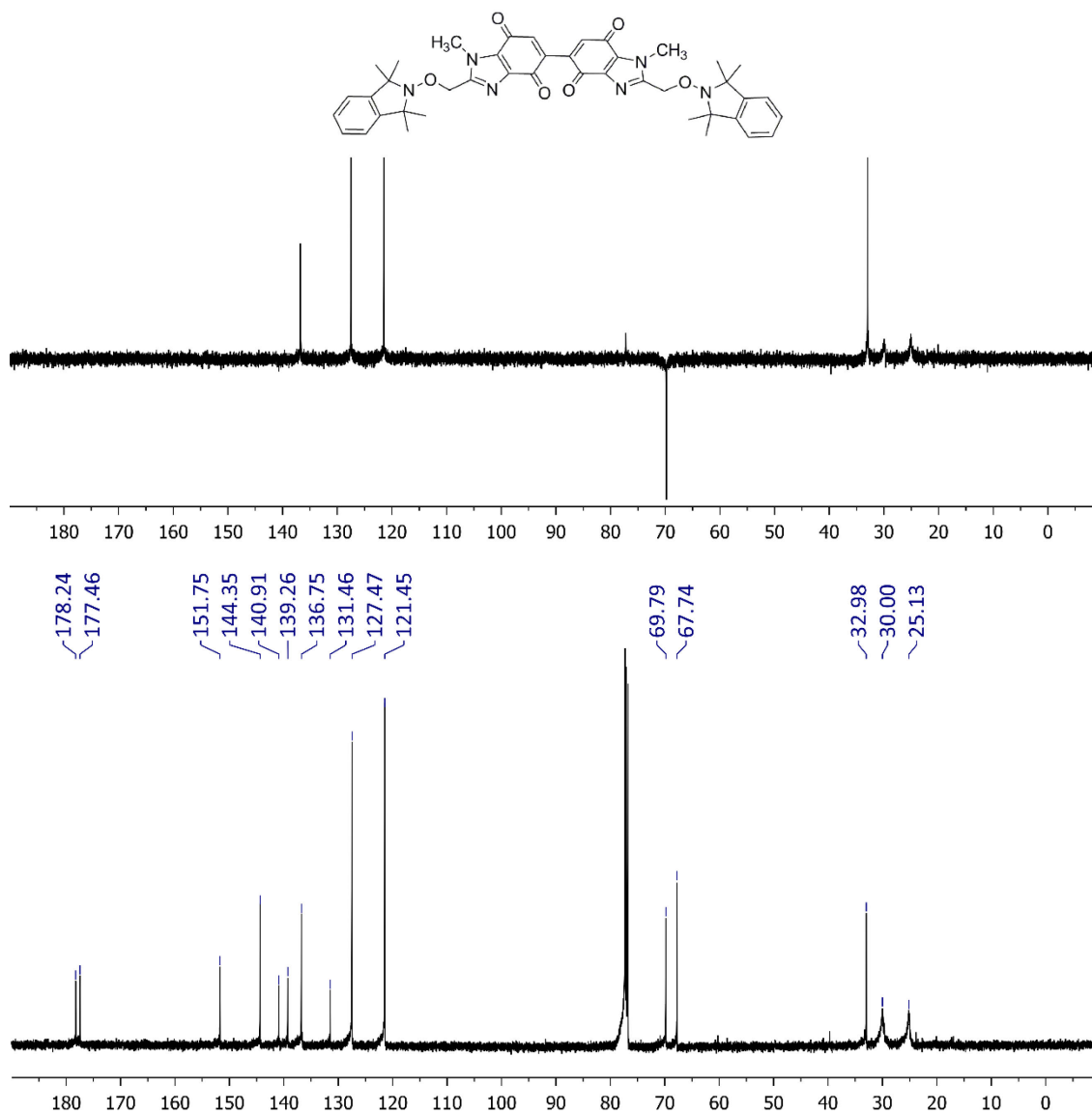
## Appendix (Chapter 3)

$^1\text{H}$  NMR (500 MHz) of **8** in  $\text{CDCl}_3$



## Appendix (Chapter 3)

$^{13}\text{C}$  NMR (125 MHz) of **8** in  $\text{CDCl}_3$

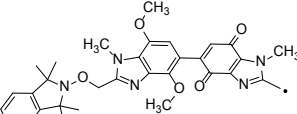
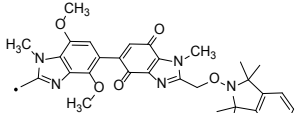
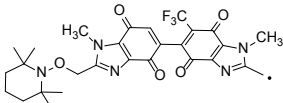
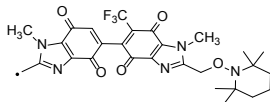




## Supplementary Data for Chapter 4

## Chapter 4 Supporting Table

Table A4.1 DFT model energies associated with Table 3.4.

compd	multiplicity	EE (Hartrees)	EE + thermal free energy correction (Hartrees)
<b>10</b>	singlet	- 2486.192247	- 2485.401233
<b>10</b>	triplet	- 2486.120124	- 2485.332486
 <b>10 quinone-radical</b>	doublet	- 1889.392895	- 1888.848546
 <b>10 dimethoxy-radical</b>	doublet	- 1889.391894	- 1888.848596
<b>TMIO-Vis</b>	singlet	- 1203.784153	- 1203.428900
<b>TMIO-Vis</b>	triplet	- 1203.702507	- 1203.349776
TMIO	doublet	- 596.736157	- 596.519239
<b>CF<sub>3</sub>-Bis-TEMPO-Vis</b>	singlet	- 2517.227738	- 2516.494899
<b>CF<sub>3</sub>-Bis-TEMPO-Vis</b>	triplet	- 2517.142635	- 2516.412787
 <b>CF<sub>3</sub>-Bis-TEMPO-Vis</b> <b>CF<sub>3</sub>-quinone-radical</b>	doublet	- 2033.526752	- 2033.051761
 <b>CF<sub>3</sub>-Bis-TEMPO-Vis</b> <b>quinone-radical</b>	doublet	- 2033.527297	- 2033.051375

Chapter 4 Supporting Figure

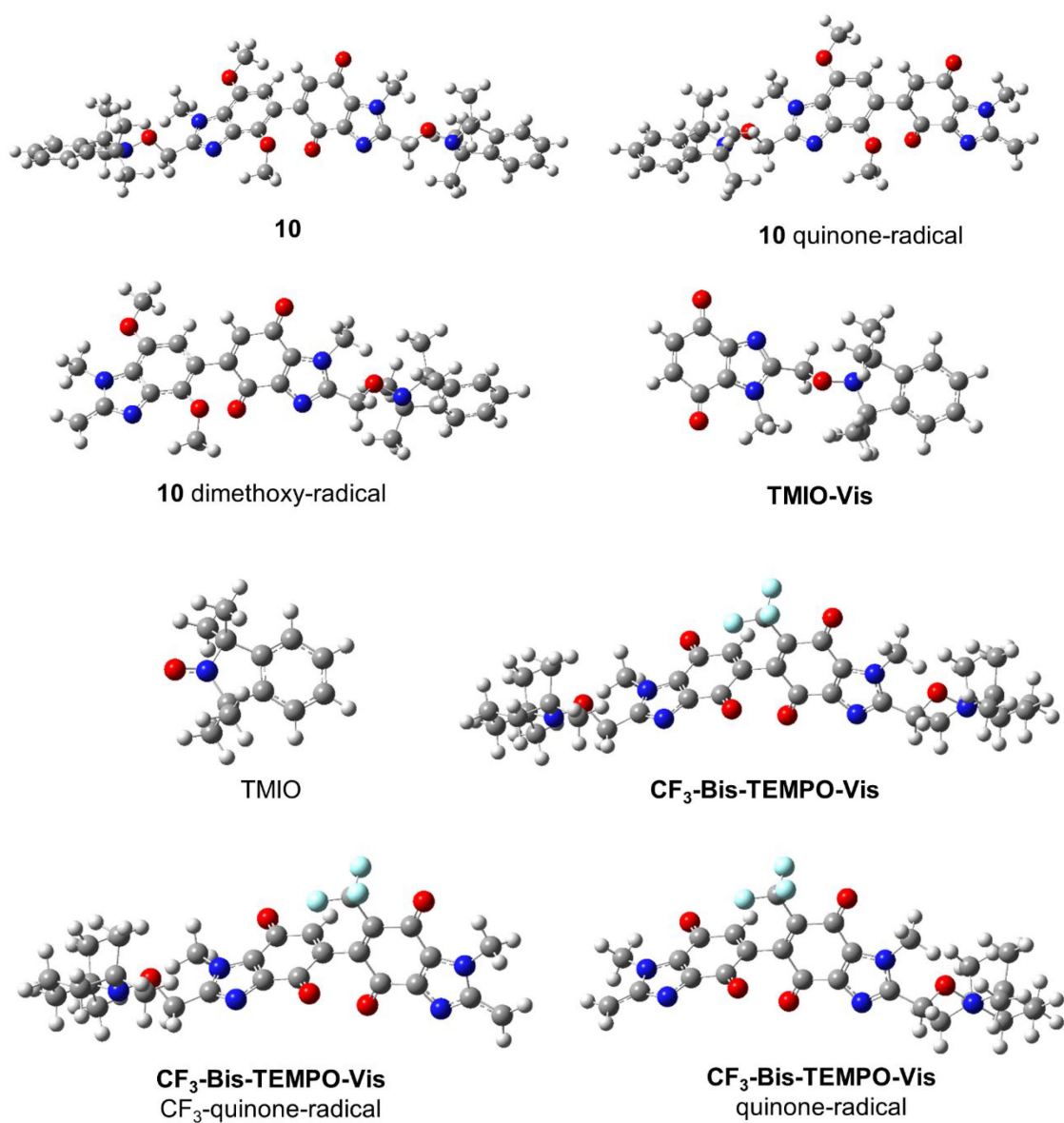
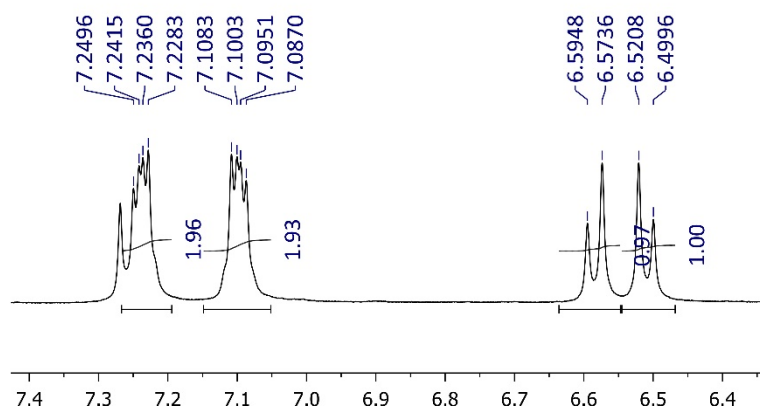
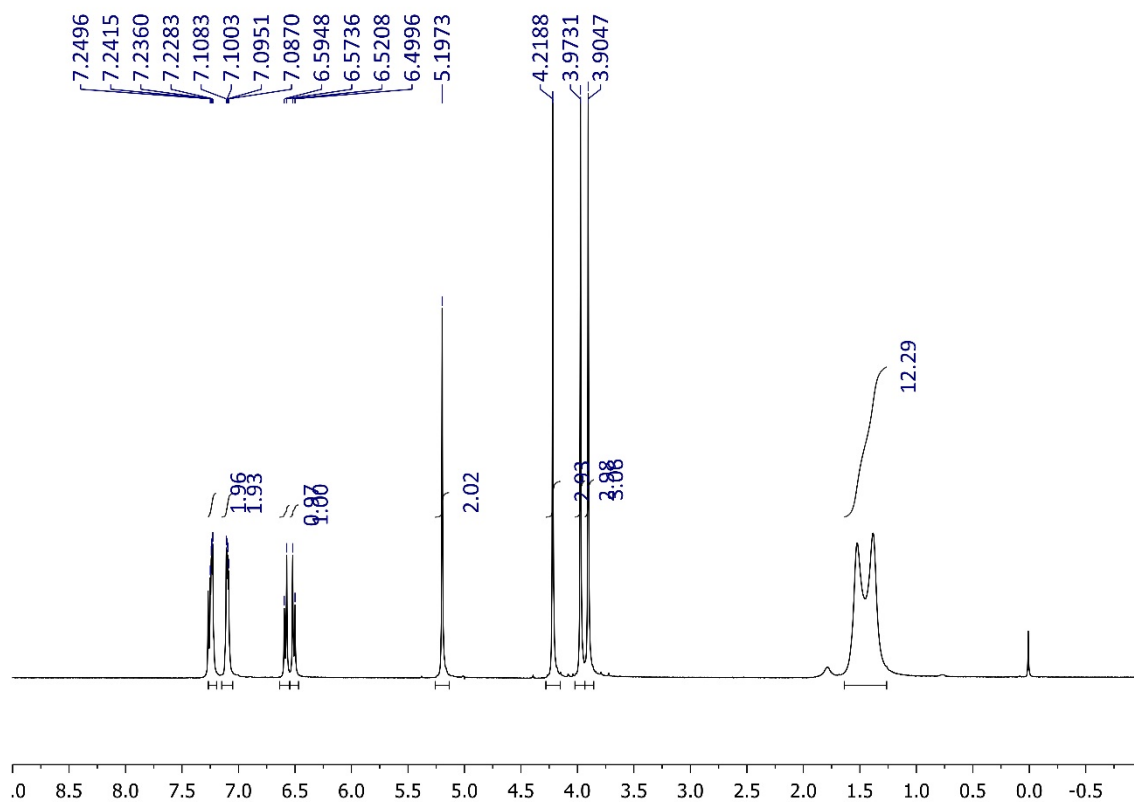
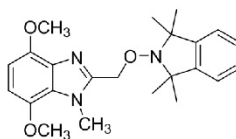


Figure A4.1 Optimized geometries of alkoxyamines (singlet) and radicals (doublet).

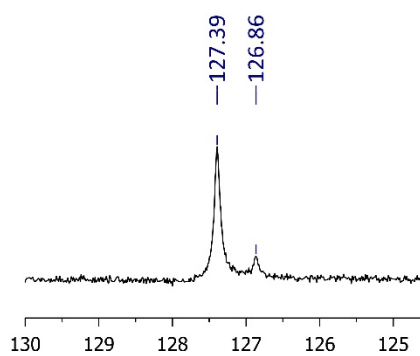
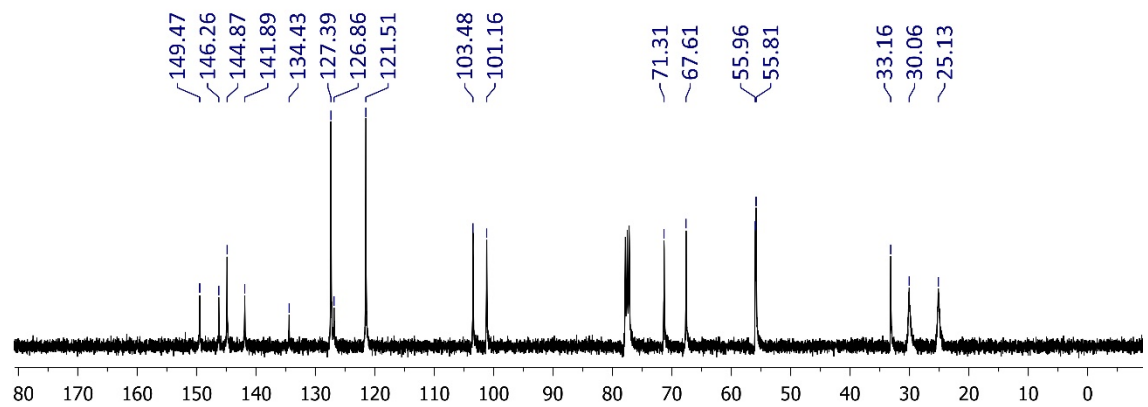
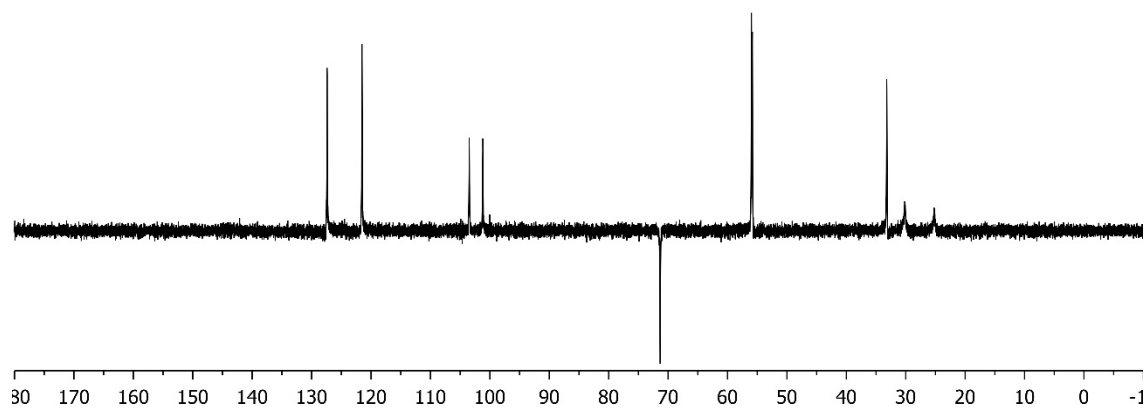
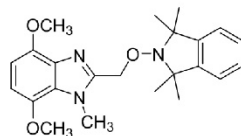
Chapter 4 NMR Spectra

$^1\text{H}$  NMR (400 MHz) of **9** in  $\text{CDCl}_3$



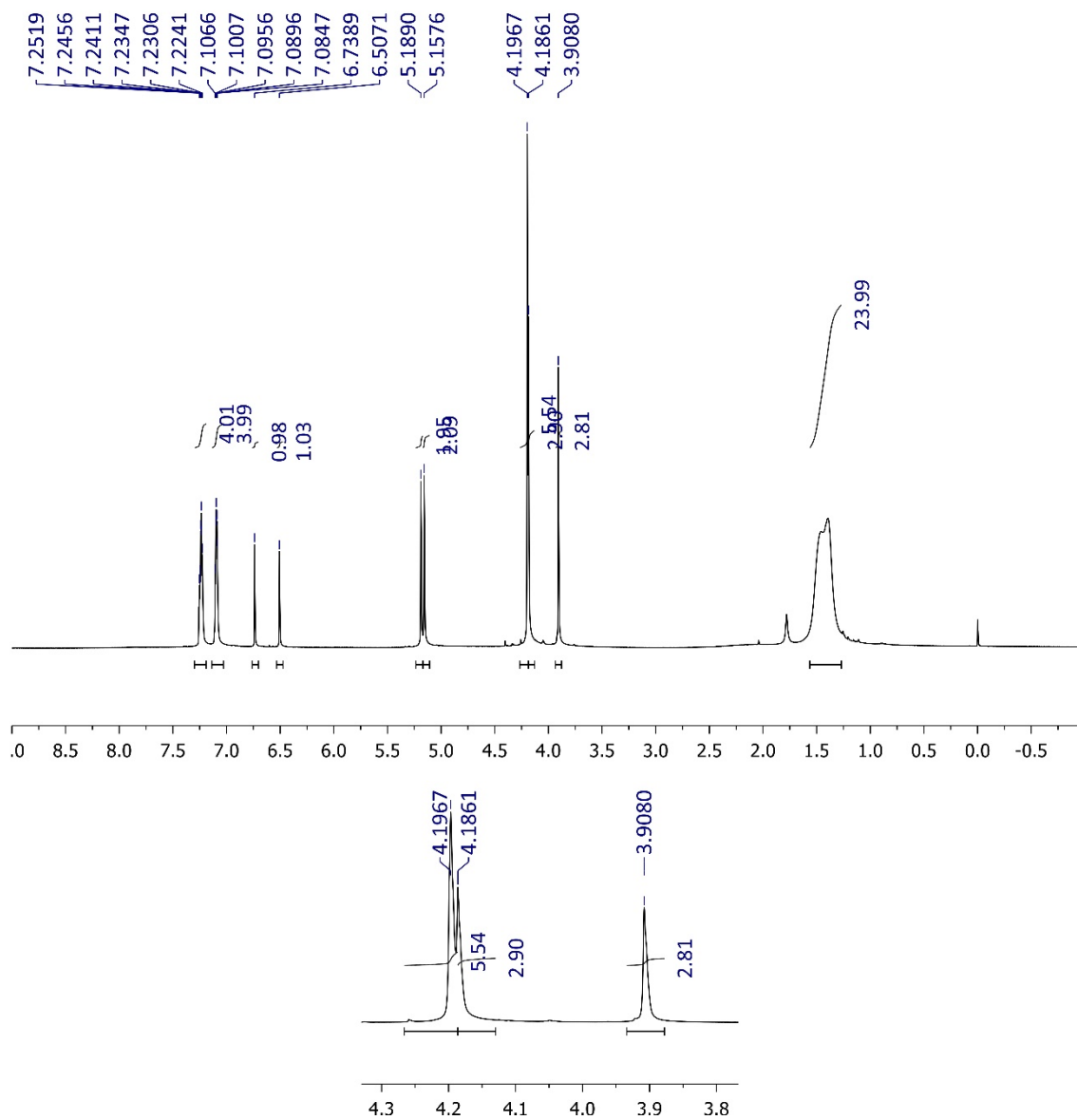
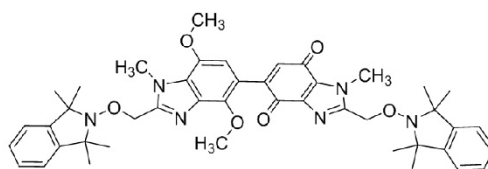
## Appendix (Chapter 4)

$^{13}\text{C}$  NMR (100 MHz) of **9** in  $\text{CDCl}_3$



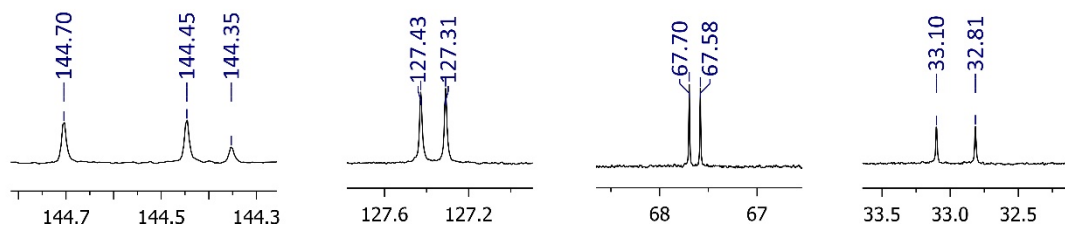
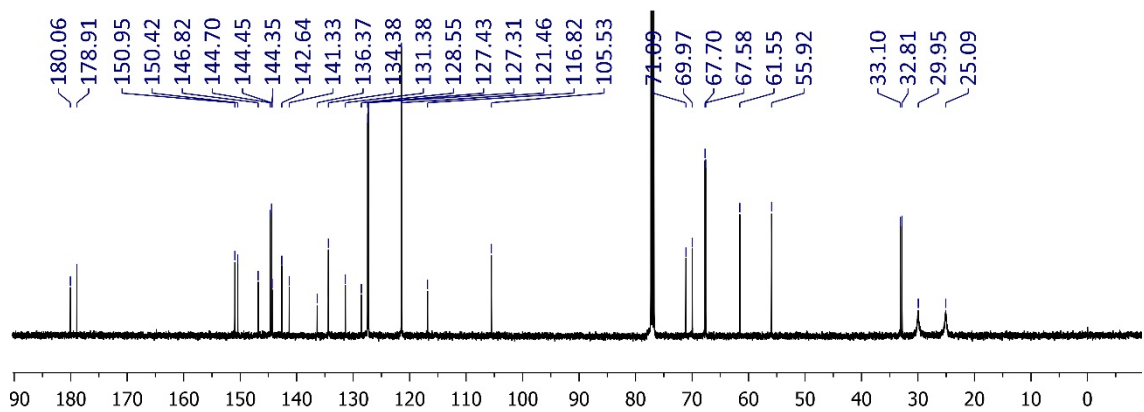
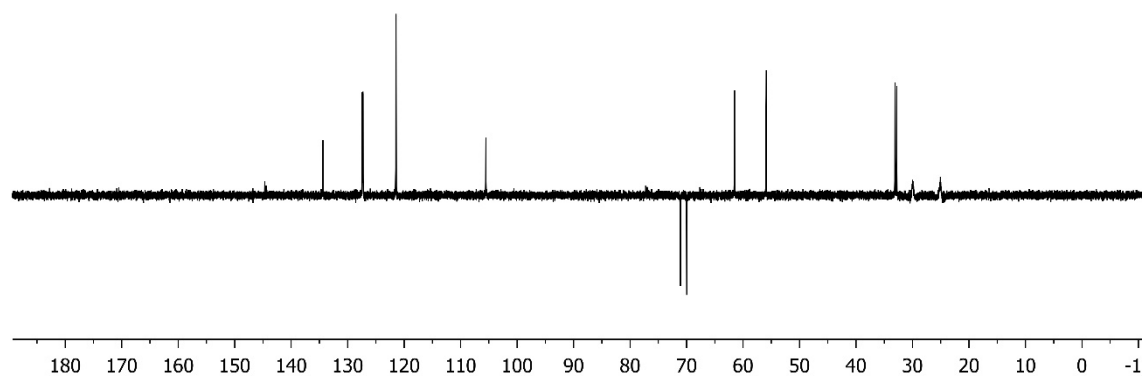
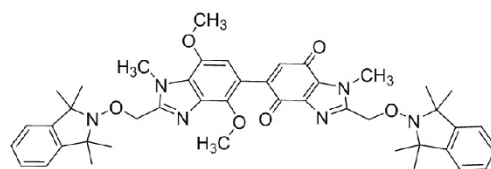
## Appendix (Chapter 4)

$^1\text{H}$  NMR (500 MHz) of **10** in  $\text{CDCl}_3$



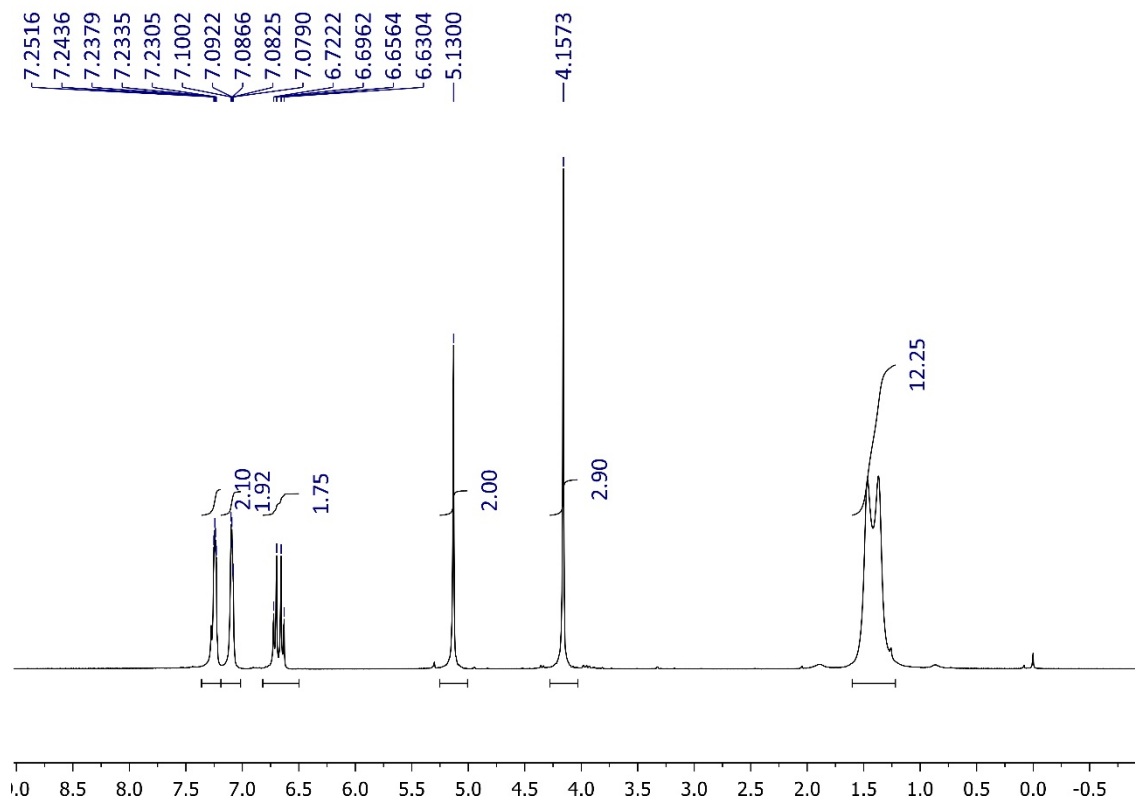
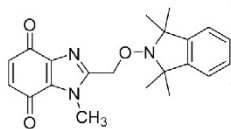
## Appendix (Chapter 4)

$^{13}\text{C}$  NMR (125 MHz) of **10** in  $\text{CDCl}_3$



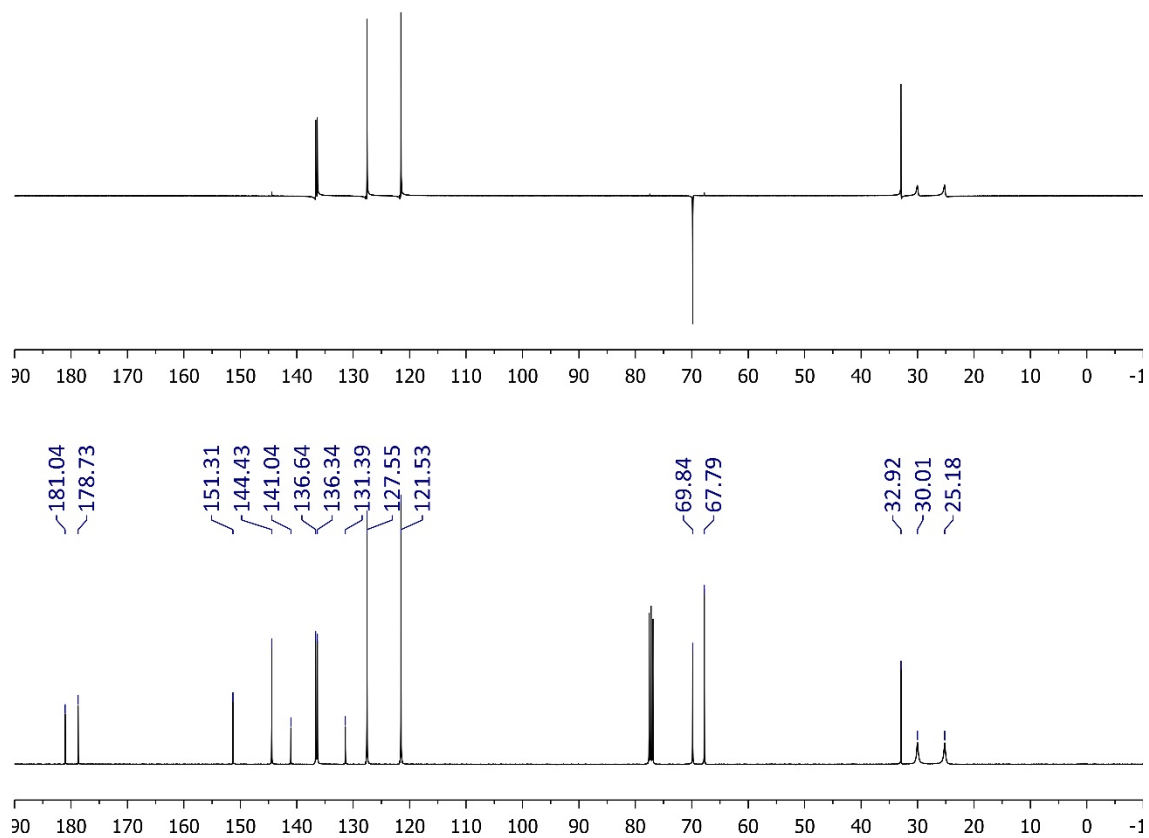
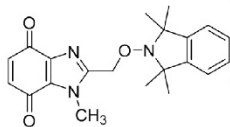
## Appendix (Chapter 4)

$^1\text{H}$  NMR (400 MHz) of **TMIO-Vis** in  $\text{CDCl}_3$



## Appendix (Chapter 4)

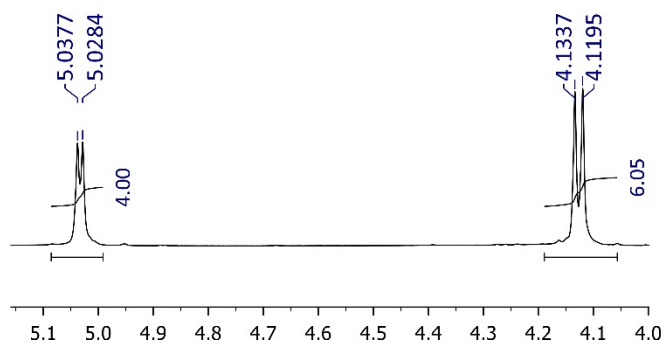
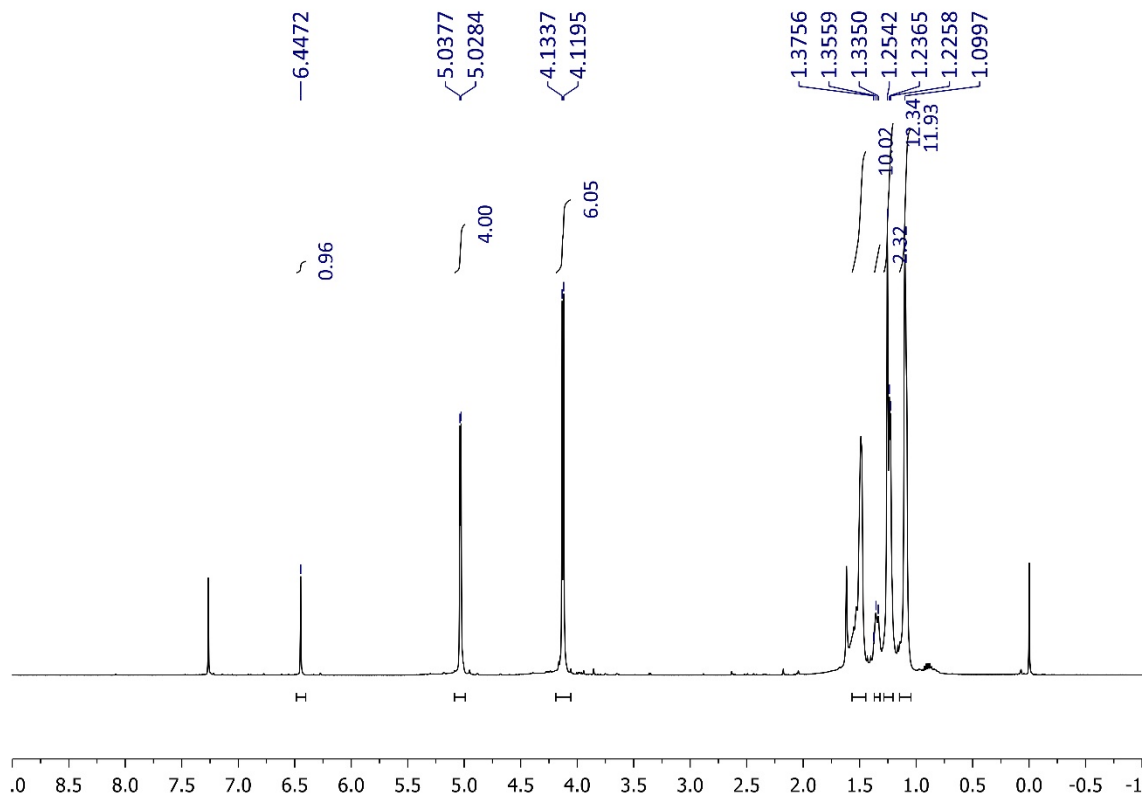
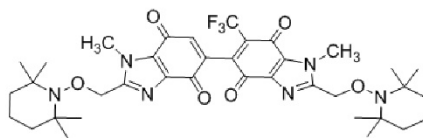
$^{13}\text{C}$  NMR (100 MHz) of **TMIO-Vis** in  $\text{CDCl}_3$





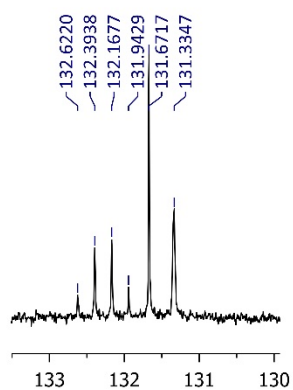
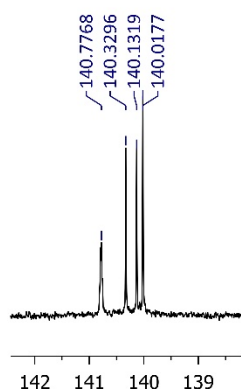
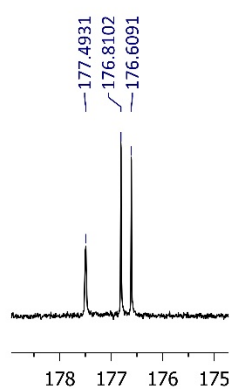
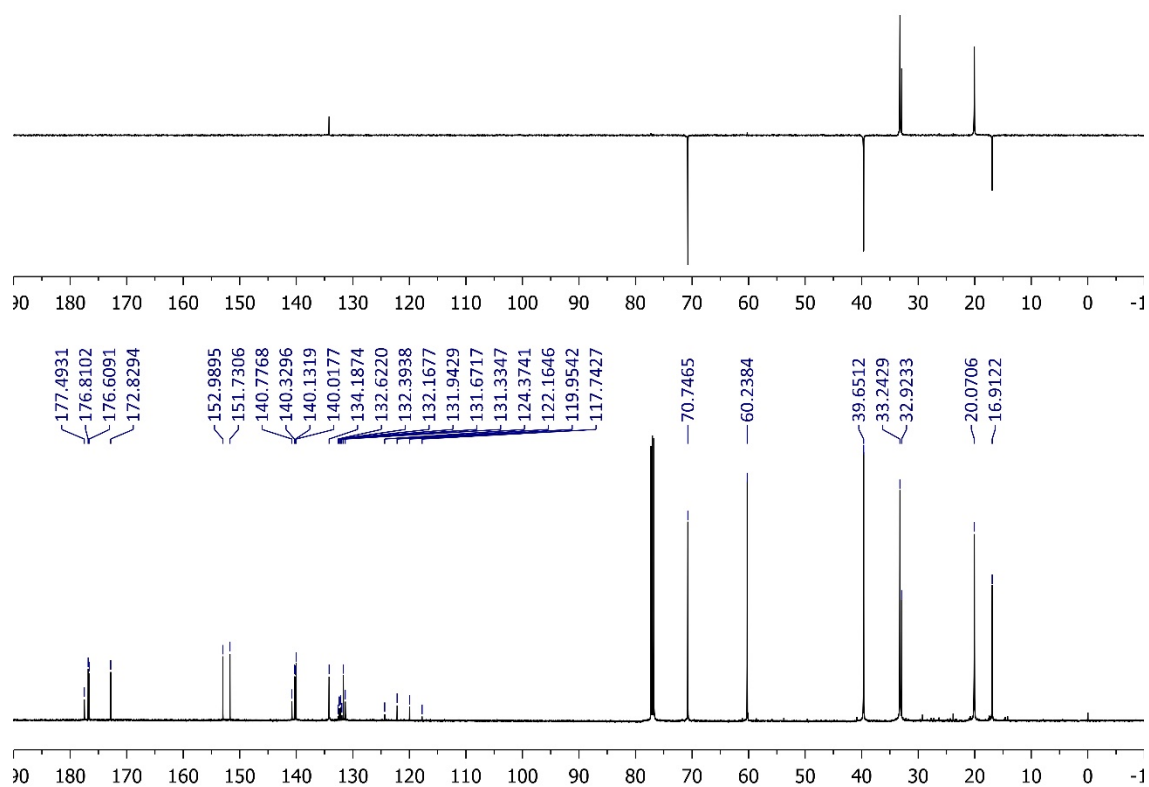
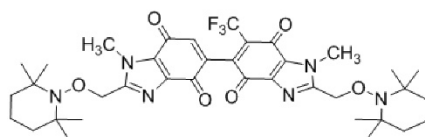
## Appendix (Chapter 4)

$^1\text{H}$  NMR (500 MHz) of **CF<sub>3</sub>-Bis-TEMPO-Vis** in  $\text{CDCl}_3$



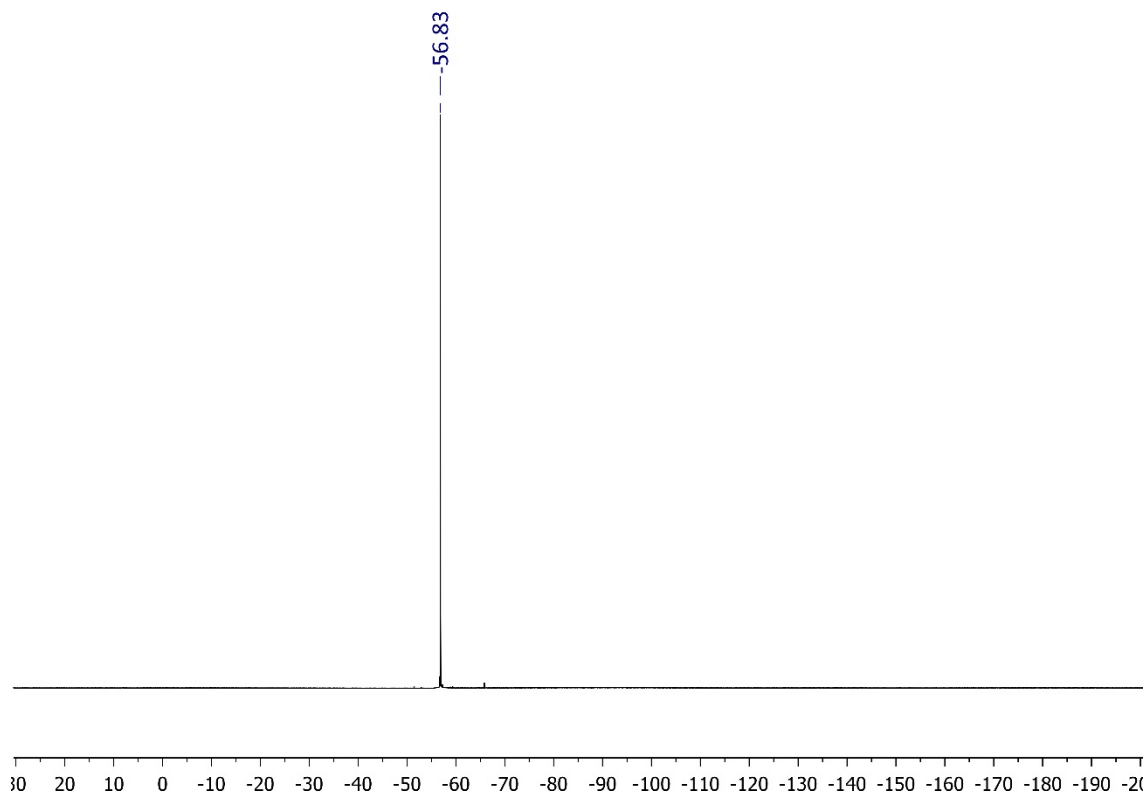
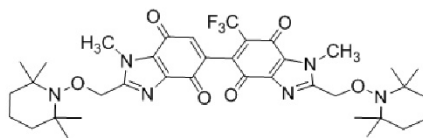
## Appendix (Chapter 4)

$^{13}\text{C}$  NMR (125 MHz) of **CF<sub>3</sub>-Bis-TEMPO-Vis** in  $\text{CDCl}_3$



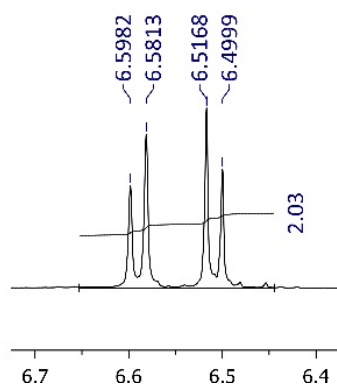
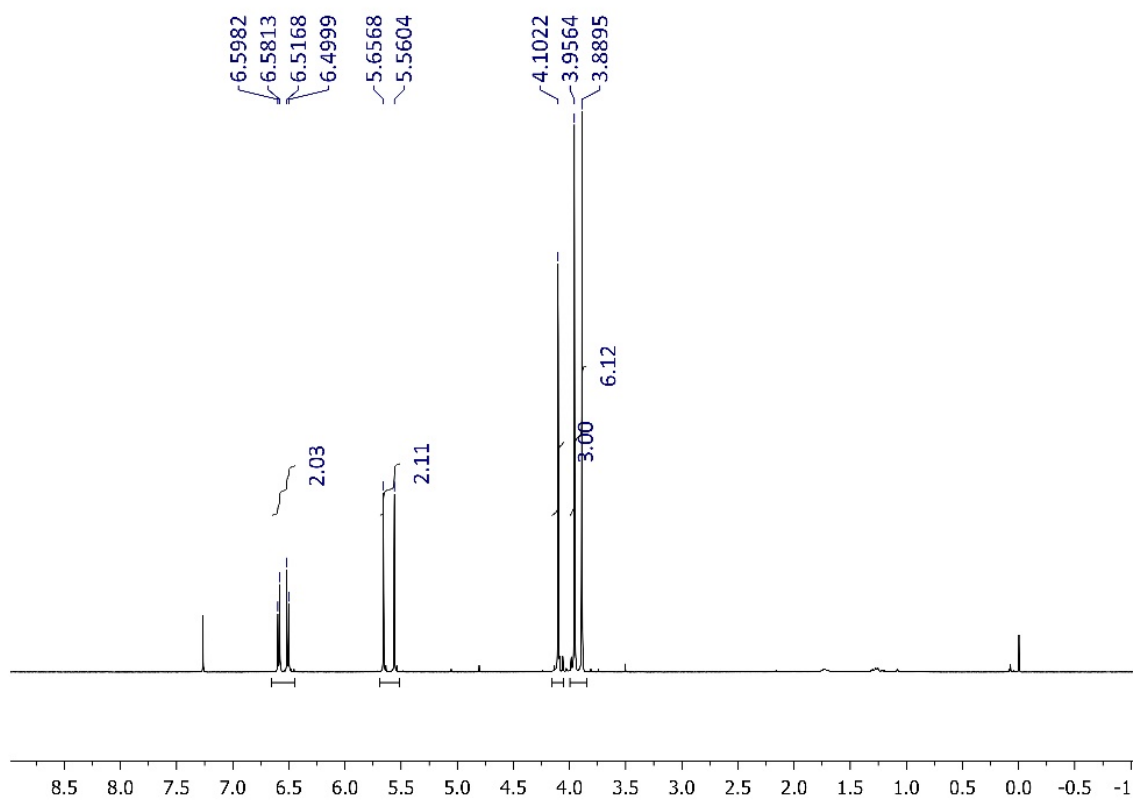
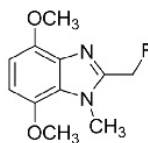
## Appendix (Chapter 4)

$^{19}\text{F}$  NMR (470 MHz) of **CF<sub>3</sub>-Bis-TEMPO-Vis** in CDCl<sub>3</sub>



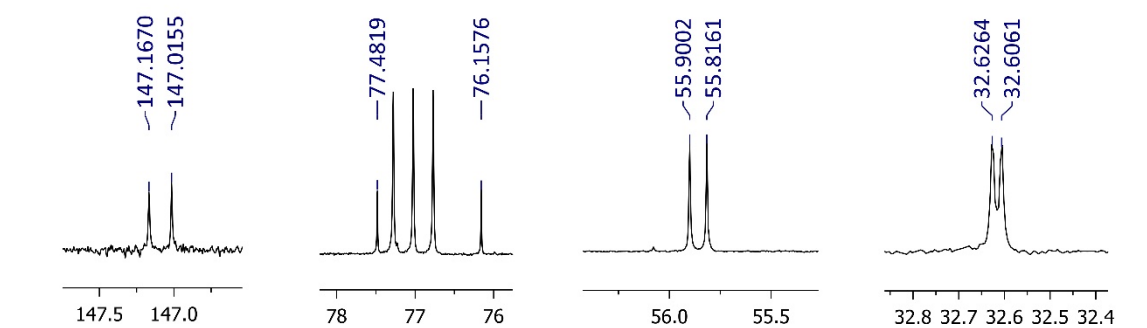
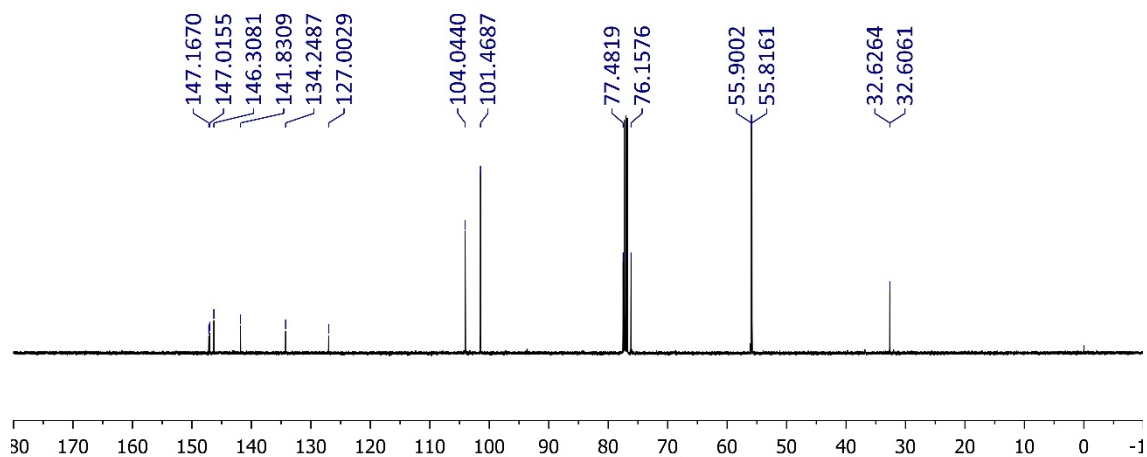
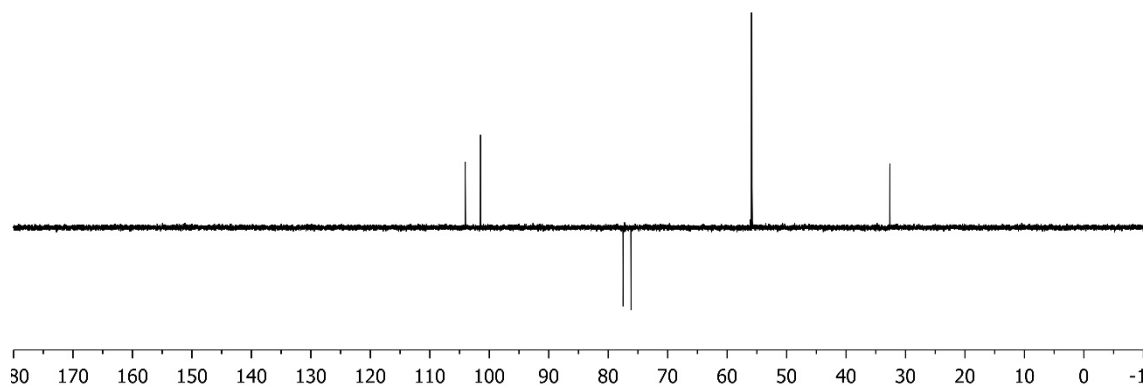
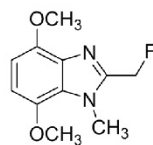
## Appendix (Chapter 4)

$^1\text{H}$  NMR (500 MHz) of **15** in  $\text{CDCl}_3$



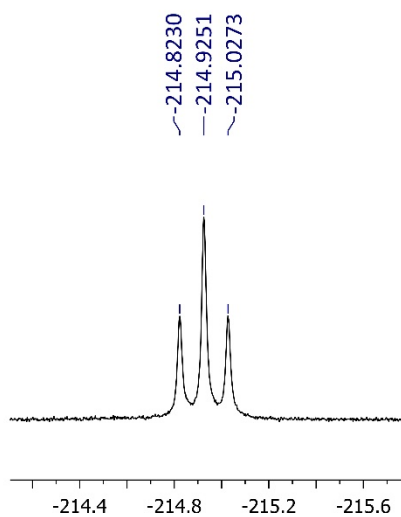
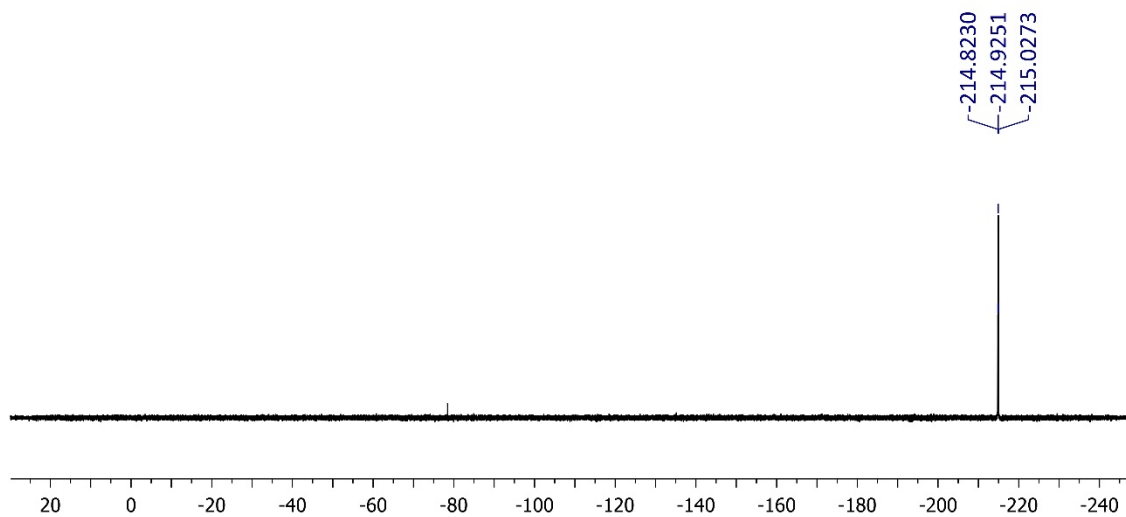
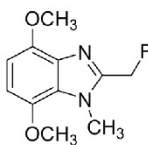
## Appendix (Chapter 4)

$^{13}\text{C}$  NMR (125 MHz) of **15** in  $\text{CDCl}_3$



## Appendix (Chapter 4)

$^{19}\text{F}$  NMR (470 MHz) of **15** in  $\text{CDCl}_3$



## Conference Proceedings

*Presenting author underlined*

1. **Nitric Oxide Donor Furoxans *via* MeMgCl-Mediated Acetylations of Isosorbide**

Patrick Kielty, Dennis A. Smith, Peter Cannon, Michael P. Carty, Michael Kennedy, Patrick McArdle, Richard J. Singer and Fawaz Aldabbagh

RSC London & South East Organic Division Regional Meeting 2019

The University of Greenwich, London, U.K.

13 February 2019

Oral Communication

2. **Nitric Oxide Donor Furoxans *via* MeMgCl-Mediated Acetylations of Isosorbide**

Patrick Kielty, Dennis A. Smith, Peter Cannon, Michael P. Carty, Michael Kennedy, Patrick McArdle, Richard J. Singer and Fawaz Aldabbagh

RSC Heterocyclic and Synthesis Group 33<sup>rd</sup> Postgraduate Symposium

GSK, Stevenage, U.K.

20 September 2018

Oral Communication

3. **Nitric Oxide Donor Furoxans *via* MeMgCl-Mediated Acetylations of Isosorbide**

Patrick Kielty, Dennis A. Smith, Peter Cannon, Michael P. Carty, Michael Kennedy, Patrick McArdle, Richard J. Singer and Fawaz Aldabbagh

70<sup>th</sup> Irish Universities Chemistry Research Colloquium

Queen's University Belfast, U.K.

21 June 2018

Oral Communication (Flash) and Poster Presentation

4. **Improving the Industrial Manufacture of Isosorbide-5-Mononitrate**  
Patrick Kielty, Dennis A. Smith, Peter Cannon and Fawaz Aldabbagh  
XVII International Conference on Heterocycles in Bioorganic Chemistry  
Bioheterocycles 2017, NUI Galway  
30 May 2017  
Oral Communication
  
5. **Visible-Light Nitroxide-Releasing Anti-Cancer Agents**  
Patrick Kielty, Dennis A. Smith, Peter Cannon and Fawaz Aldabbagh  
Eli Lilly Postgraduate Chemistry Research Symposium  
School of Chemistry, NUI Galway  
20 January 2017  
Oral Communication, *1<sup>st</sup> Prize*





# Nitric Oxide Donor Furoxans via Methylmagnesium Chloride Mediated Acetylations of Isosorbide

Patrick KIELTY,<sup>a</sup> Dennis A. Smith,<sup>a</sup> Peter Cannon,<sup>b</sup> Michael P. Carty,<sup>c</sup>  
Michael Kennedy,<sup>a</sup> Patrick McArdle,<sup>a</sup> Richard J. Singer<sup>d</sup> and Fawaz Aldabbagh<sup>a,d</sup>

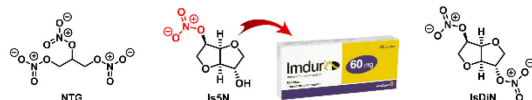
<sup>a</sup>School of Chemistry, National University of Ireland Galway, Ireland; <sup>b</sup>Avara Pharmaceutical Services, Shannon, Co. Clare, Ireland;

<sup>c</sup>School of Natural Sciences, National University of Ireland Galway, Ireland; <sup>d</sup>Penrhyn Road Campus, Kingston University, London, U.K.

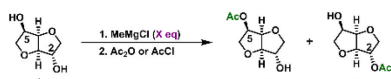


## Introduction

Clinically, nitrate ester drugs are used to effect vasodilation via nitric oxide (NO) release. Nitroglycerin (NTG), isosorbide dinitrate (IsDIN), and isosorbide-5-mononitrate (Is5N, Imdur<sup>®</sup>) are prescribed to patients with angina. These nitrate esters are well-known explosives presenting a substantial industrial hazard. Herein, the  $-ONO_2$  explosophore on Is5N is replaced by the alternative NO donating group, furoxan. To selectively functionalise sustainable isosorbide, we have developed a simple and selective acetylation protection-deprotection protocol mediated by inexpensive MeMgCl.

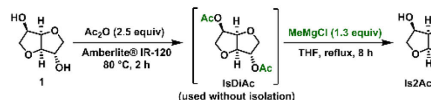


## Selective Protection of Isosorbide



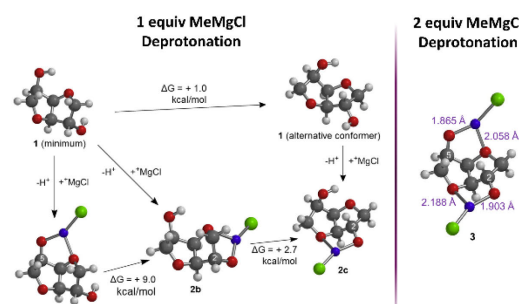
MeMgCl, rt-reflux (for Is5Ac) or 0 °C (for Is2Ac), THF, 0.5 h then Ac<sub>2</sub>O, reflux (for Is5Ac), or AcCl, 0 °C (for Is2Ac), 2h.

- Acetylation of isosorbide (**1**) to selectively give isosorbide-5-acetate (Is5Ac) or isosorbide-2-acetate (Is2Ac) was achieved by varying the amount of MeMgCl.



- Is2Ac could also be selectively formed on multigram scale via IsDIAC without the requirement for column chromatography.

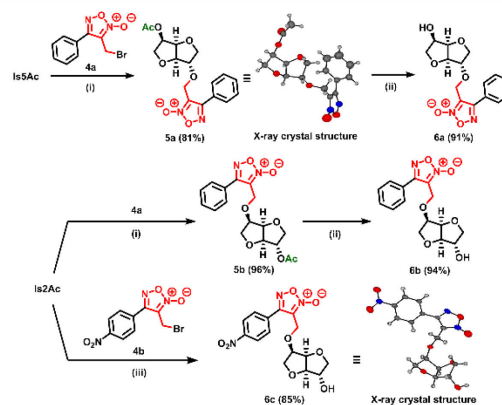
## DFT Modeling of Selective Protection



DFT B3LYP/6311G (2d,p) basis set. Mg and Cl atoms depicted in blue and green, respectively.

- Selective 5-acetylation was rationalised by a more stable 5-alkoxide due to effective <sup>+</sup>MgCl coordination to the oxygen of the adjacent ring (**2a**). Steric hindrance from the isosorbide junction 3,4-hydrogens destabilised complex **2c**.
- Longer, less stable Mg<sup>+</sup>...OR(alkoxide) and Mg<sup>+</sup>...OR(ether) bond lengths at the 2-alkoxide of dialkoxide **3** rationalises selective 2-acetylation.

## Synthesis of Isosorbide-furoxans

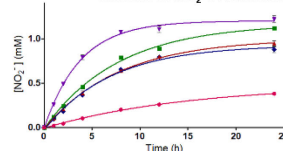


(i) **4a** (4 equiv), Ag<sub>2</sub>O (3 equiv), CH<sub>2</sub>Cl<sub>2</sub>, reflux, 3 days; (ii) aq K<sub>2</sub>CO<sub>3</sub> (1 equiv), MeOH, rt, 1 h; (iii) **4b** (4 equiv), Ag<sub>2</sub>O (3 equiv), CH<sub>2</sub>Cl<sub>2</sub>, reflux, 3 days, then aq K<sub>2</sub>CO<sub>3</sub> (1 equiv), MeOH/CH<sub>2</sub>Cl<sub>2</sub>, rt, 1 h.

- The protection strategy facilitated the selective synthesis of isosorbide-2-furoxan (**6a**), and isosorbide-5-furoxans (**6b-6c**).

## Measurement of NO Release

### Kinetics of NO<sub>x</sub> Production



- The isosorbide-furoxans showed far superior rates and extents of NO release compared to the clinically used Is5N, with the electron deficient **6c** offering the fastest rate of NO release.
- Isosorbide-2-furoxan (**6a**) has higher activity than 5-furoxan **6b**, in line with the higher potency (*in vivo*) of Is2N relative to Is5N.

## Thermal Stability

### Exothermic Events

NO Donor	Onset Temp (°C)	Energy Release (J/g)
Is5N	136.7	2735.8
<b>6a</b>	231.0	1122.0
<b>6b</b>	202.9	1474.5
<b>6c</b>	168.3	1636.9

- The onset temperature for thermal degradation of furoxans (DSC) is less accessible than that of the explosive Is5N, and the energy released from such exothermic events was considerably lower and safer.

## Conclusion

MeMgCl mediated acetylation has afforded an effective and simple protection-deprotection for both hydroxyls of isosorbide. Subsequent functionalization with furoxan gave powerful NO donors with vastly higher rates and amounts of NO<sub>x</sub> produced compared to the commercial vasodilator, Is5N. Isosorbide-furoxans are safer to handle than Is5N.

P. Kielty, D. A. Smith, P. Cannon, M. P. Carty, M. Kennedy, P. McArdle, R. J. Singer, F. Aldabbagh, *Org. Lett.* **2018**, *20*, 3025-3029.



We thank the Irish Research Council (IRC) for awarding Patrick Kielty an Enterprise Partnership Postgraduate Scholarship in association with Avara Pharmaceutical Services. p.kielty2@nuigalway.ie; f.aldbagh@kingston.ac.uk



## Peer-Reviewed Publications

1. **Selective Methylmagnesium Chloride Mediated Acetylations of Isosorbide: A Route to Powerful Nitric Oxide Donor Furoxans**

Patrick Kielty, Dennis A. Smith, Peter Cannon, Michael P. Carty, Michael Kennedy, Patrick McArdle, Richard J. Singer and Fawaz Aldabbagh\*

*Organic Letters*, **2018**, *20*, 3025–3029

DOI: [10.1021/acs.orglett.8b01060](https://doi.org/10.1021/acs.orglett.8b01060)

2. **Visible-Light Unmasking of Heterocyclic Quinone Methide Radicals from Alkoxyamines**

Patrick Kielty, Pau Farràs, Patrick McArdle, Dennis A. Smith and Fawaz Aldabbagh\*

*Chemical Communications*, **2019**, Advance article

DOI: [10.1039/C9CC08261A](https://doi.org/10.1039/C9CC08261A)